The energy calibration for the solar neutrino analysis of all three phases of the Sudbury Neutrino Observatory

by

Ryan Francis MacLellan

A thesis submitted to the
Department of Physics, Engineering Physics, and Astronomy
in conformity with the requirements for
the degree of Doctor of Philosophy

Queen's University
Kingston, Ontario, Canada
September 2009

Abstract

This work presents the calibration of the energy response of the Sudbury Neutrino Observatory (SNO). The development of the energy response processor RSP and its use in setting the energy scale of the SNO detector and reconstructing the energy of neutrino-like events is presented for each of the three phases of SNO: the pure D_2O phase, the salt phase, and the neutral current detector phase. A ^{16}N calibration source, producing mainly 6.13 MeV γ-rays, is the primary energy calibration source. It is used to set the energy scale of the detector and to test for errors in the energy calibration and reconstruction process. The errors associated with energy reconstruction in the pure D_2O and salt phase data, that to be used in a low energy threshold solar ^8B neutrino analysis, are derived for the RSP energy response processor and shown to be in agreement with other analyses. The largest of the errors, that associated with using the ^{16}N source to set the energy scale of the detector, is improved through a detailed and thorough analysis.

The calibration of the energy scale of the photomultiplier tube array in the third phase, with an array of ^3He proportional counters (NCDs) distributed within the D_2O, is presented. The event energy reconstruction errors in the NCD phase are reassessed with more precise measurements and shown to be in agreement with the conservative estimates used by Aharmim et al. [1]. The implications of the improvements in the error are assessed and the solar ^8B neutrino fluxes—charged current (CC), elastic scattering (ES), and neutral current (NC)—are determined to be:

$$\begin{aligned} \phi_{\mathrm{CC}} &= 1.68^{+0.09}_{-0.07}, \\ \phi_{\mathrm{ES}} &= 1.79^{+0.25}_{-0.22}, \text{ and} \\ \phi_{\mathrm{NC}} &= 5.52^{+0.48}_{-0.45}, \end{aligned}$$

in units of $10^6\,\mathrm{cm}^{-2}\mathrm{s}^{-1}$. The errors quoted are the combined statistical and systematic uncertainties. These results are in good agreement with those published by Aharmim et al. [1] with a modest improvement in the CC measurement.

Acknowledgments

I would first like to thank all those that I am about to slight by neglecting to acknowledge their contribution to either my graduate work or my life as a graduate student. After such a long haul there are certainly more than I can recognize here and, at the age I have attained, certainly those whom I have merely forgotten.

To begin with, I had the good fortune of having two of the finest physicists for supervisors: Art McDonald and Aksel Hallin. Many thanks to Aksel for my having something to write about in my thesis and equally many to Art for seeing I get to the end of it. I would also like to single out Kevin Graham as another strong influence on this work whereas more recently I have relied on the likes of Christine and Carsten (Kraus and Krauss respectively) and Bei Cai for advice, insight, and generally someone to gripe to. Of the many fellow graduate students I have worked with at Queen's I would especially like to thank Mark Kos, Ryan Martin, and Alex Wright for our discussions on just about everything with some physics mixed in too.

I would like to thank Paradorn, Tim, and Nicole's supervisor for each providing me with lodgings from which to finish writing. And Nicole for providing me with someone I could actually best in a race to finish; for those were no easy shoes to fill. For Wolfgang the unfailing Grad Club companion, and Peter for solving problems that were not his, and Phil's comprehensive programming genius (and inspiration to play lunchtime soccer), and José for being not so bad of an office mate, I am also thankful. And of course I cannot forget to thank the original Oxford girls for, among many other things, the Queen's Inn, clean pants, and Charlotte for some reason too.

A few experiences that I will be eternally grateful for include being a part of the Softball Nerds Organization (SNO), adventures in pig roasting; learning how to ski and play hockey; fresh baked blueberry pie in the old SNO control room at 2 AM; shoveling three feet of SNO from the entire length of the SNOLAB parking lot, after a graveyard; and every one of the 2000 miles traveled on the 2002 summer road trip. I will miss Kingston and, yes, even Sudbury for all the fond memories to go along with all the interesting people I have come to know.

Last, and probably least, I would like to thank my parents for patiently waiting, and continuing to wait, for their son to return home.

Statement of Originality

The Sudbury Neutrino Observatory (SNO) was designed and constructed before any participation by the author in the Collaboration. Data taking, maintenance, and data analysis have been the goals of the SNO Collaboration over the course of three separate data taking phases: the pure D_2O phase, the salt phase, and the neutral current detector phase. The author has contributed to data collection and analysis since the beginning of the salt phase, primarily with respect to detector calibrations.

The work presented in this thesis is the work of the author except as noted here and where the work of others has been cited.

Chapters 1 and 2 are reviews of past results published by the SNO Collaboration (including the author in many cases) and a review of the function and calibration of the different elements of the detector.

Chapter 3 borrows heavily from the work of previous Collaboration members that have assessed the many facets of the detector response; the works of Bryce Moffat (formerly of Queen's University) and Olivier Simard (Carleton University) are particularly relevant in regard to characterizing the optical response of the detector. However, the evolution of the optical model is from the perspective of the author.

The work of Mark Boulay (formerly and currently of Queen's University) on the application of the detector energy response to energy reconstruction is the basis for the energy response processor RSP. However, the new RSP algorithm and its application to data from each of the three phases of SNO in this work is the work of the author.

Chapter 7 is a reassessment of energy scale error originally performed by Mike Lay and Andre Hamer. Comparisons to and utilization of their work is explicitly cited in the text.

The majority of the results presented in chapter 8 are the work of the SNO Collaboration as a whole. The signal extraction routines used by the author to reproduce and improve the solar ^8B neutrino fluxes were developed by Blair Jamieson (University of British Columbia).

Table of Contents

List of Tables

List of Figures

Chapter 1

Introduction

The Sudbury Neutrino Observatory (SNO) was proposed in 1984 [2] to solve the long standing solar neutrino problem whereby experiments, sensitive solely or primarily to electron neutrinos, observed a flux smaller than that predicted by solar models. The electron neutrino spectra from the dominant nuclear reactions in the Sun are shown in figure 1.1. The scale of each spectrum is as predicted by the solar model of Bahcall et al. [3], which reproduces well all other observable solar parameters. Previous measurements [4–8][1], with neutrino energy thresholds ranging from 233 keV and 814 keV up to 7 MeV, observed fewer, by a factor of two to three, electron neutrinos than predicted by the solar models [12]. The SNO experiment was designed primarily to observe neutrinos from the decay of ^{8}B in the Sun; specifically, to solve the solar neutrino problem by measuring separately the flux of electron neutrinos and of all active neutrino flavours to test whether neutrino flavour change is occurring.

With a proposed detection medium comprised of 1000 tonnes of ultra-pure $D_2O$the possible neutrino interactions are

$$\begin{aligned} \nu_e + d &\rightarrow e^- + p + p - 1.442\,\text{MeV} && \text{(CC)} \\ \nu_x + d &\rightarrow \nu_x + p + n - 2.224\,\text{MeV} && \text{(NC)} \\ \nu_x + e^- &\rightarrow \nu_x + e^- && \text{(ES)} \end{aligned}$$

where ν_x can be any flavour of active neutrino. The charged-current (CC) reaction,

[1] The results presented in [5, 6, 8] have been most recently updated in [9–11].

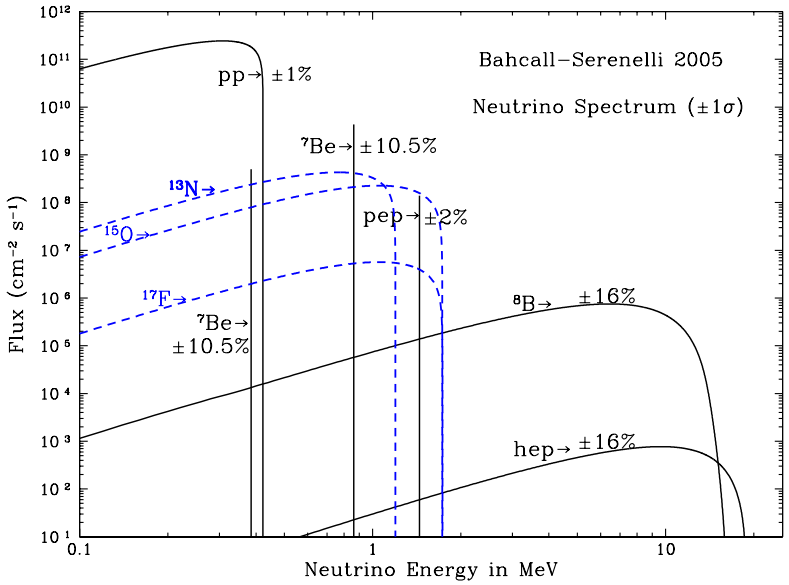

Figure 1.1: Solar neutrino spectra as predicted by Bahcall et al. [3]. SNO was designed to detect ^{8}B neutrinos but is also sensitive to *hep* neutrinos given their energy.

is sensitive only to electron flavour neutrinos. The neutral-current (NC) reaction is equally sensitive to all active neutrino flavours. Neutrino-electron elastic scattering (ES) is also sensitive to all active neutrino flavours but more so to ν_e than ν_μ or ν_τ by a factor of about six. All three neutrino signals can be observed by the detection of Čerenkov radiation, emitted by fast electrons, in an array of photomultiplier tubes. In the case of the NC reaction, this occurs via a process of neutron capture with the subsequent γ-ray Compton scattering an electron. The different signals are not distinguishable on an event-by-event basis, except in the third phase of the experiment when the neutrons are detected in an array of ^{3}He filled proportional counters. The number of each signal, however, can be statistically separated based on the expected probability distributions of event characteristics including reconstructed energy, position, and direction.

The ES of neutrinos has been thoroughly reported on by the Kamiokande and Super-Kamiokande experiment. The ES interaction cannot alone discriminate between the ν_e flavour content and that of ν_μ and ν_τ. The number of CC events

observed is a measure of the ν_e flavour content of solar neutrinos while the number of NC events is a direct measure of the total flux of active neutrinos. The ratio of these fluxes can be used to determine if electron neutrinos change flavour while the total flux of neutrinos is representative of the total flux of neutrinos produced by the Sun, independent of neutrino flavour change model[2]. In summary, the fluxes of the three neutrino signals in SNO are related to the flux of the different flavours of neutrinos via

$$\begin{aligned}\phi_{\mathrm{CC}} &= \phi_{\nu_e} \\ \phi_{\mathrm{ES}} &= \phi_{\nu_e} + \sim 0.16\left(\phi_{\nu_\mu} + \phi_{\nu_\tau}\right) \\ \phi_{\mathrm{NC}} &= \phi_{\nu_e} + \phi_{\nu_\mu} + \phi_{\nu_\tau}\end{aligned}$$

The CC reaction can occur for ν_e with a minimum energy of 1.442 MeV. The energy of the resultant electron is strongly correlated with that of the incident neutrino providing a measure of the incident ν_e energy spectrum. The ES of neutrinos also directly produces a Čerenkov electron. The two electron signals can be separated based on the direction of the scattered electron. The direction of ES electrons is highly correlated with that of the incident neutrino while the direction of CC electrons is anti-correlated with the neutrino direction. Since the direction of the incident neutrino is from the direction of the Sun, ES electrons pointing away from the Sun provide a strong indication that the neutrinos observed by SNO originate in the Sun.

The NC reaction has an energy threshold of 2.225 MeV; the binding energy of the deuteron. SNO measured the rate of NC events in three progressively more complex, yet sensitive phases of operation.

1.1 Phase I: The pure D_2O phase

During the first operational phase of SNO, the signal for NC neutrino reactions was observed by capturing the free neutron on deuterium. Neutron capture by deuterium produces a single 6.25 MeV γ-ray that can subsequently Compton scatter one or more electrons. The first solar neutrino flux analysis was presented in [13] with an

[2]This is assuming there are no sterile neutrinos or at least no oscillations to sterile neutrinos.

imposed 6.75 MeV electron kinetic energy threshold; this being above the expected energy of neutron capture events and well above that of low energy backgrounds, SNO observed a very pure single–electron–event neutrino signal from which were extracted the contributions of the CC reaction and ES signals to derive the solar neutrino fluxes:

$$\begin{aligned}\phi_{\mathrm{CC}} &= 1.75 \pm 0.07\,(\mathrm{stat.})^{+0.12}_{-0.11}\,(\mathrm{syst.}) \pm 0.05\,(\mathrm{theor.}) \\ \phi_{\mathrm{ES}} &= 2.39 \pm 0.34\,(\mathrm{stat.})^{+0.16}_{-0.14}\,(\mathrm{syst.})\,,\end{aligned}$$

in units of $10^6\,\mathrm{cm}^{-2}\,\mathrm{s}^{-1}$. Under the assumption that neutrinos do not change flavour between their production in the Sun and detection at Earth, both signals should be a measure of purely ν_e interactions and as such the respective flux of each should agree. By comparing the CC ^{8}B neutrino flux with the more statistically significant ES flux measured by Super-Kamiokande [14],

$$\phi_{\mathrm{ES}} = 2.32 \pm 0.03\,(\mathrm{stat.})^{+0.08}_{-0.07}\,(\mathrm{syst.}) \times 10^6\,\mathrm{cm}^{-2}\,\mathrm{s}^{-1},$$

the non-ν_e flavour solar neutrino flux was inferred to be

$$\phi_{\mu\tau} = 3.69 \pm 1.13 \times 10^6\,\mathrm{cm}^{-2}\,\mathrm{s}^{-1}.$$

This demonstrates a violation of the no neutrino flavour change hypothesis by more than three standard deviations. Assuming no distortion of the energy spectrum of electron neutrinos, the total flux of ^{8}B solar neutrinos was determined to be

$$\phi_{\nu_x} = 5.44 \pm 0.99 \times 10^6\,\mathrm{cm}^{-2}\,\mathrm{s}^{-1};$$

in complete agreement with the solar model predictions of Bahcall et al. [12].

Lowering the energy threshold to 5 MeV, SNO was able to make a direct measurement of the total active flux of solar neutrinos via the NC reaction. Together with

updated ϕ_{CC} and ϕ_{ES}, ϕ_{NC} was reported by Ahmad et al. [15] to be

$$\begin{aligned}\phi_{\mathrm{CC}} &= 1.76^{+0.06}_{-0.05}\,(\mathrm{stat.})^{+0.09}_{-0.09}\,(\mathrm{syst.})\\ \phi_{\mathrm{ES}} &= 2.39^{+0.24}_{-0.23}\,(\mathrm{stat.})^{+0.12}_{-0.12}\,(\mathrm{syst.})\\ \phi_{\mathrm{NC}} &= 5.09^{+0.44}_{-0.43}\,(\mathrm{stat.})^{+0.46}_{-0.43}\,(\mathrm{syst.})\,,\end{aligned}$$

in units of $10^6\,\mathrm{cm}^{-2}\,\mathrm{s}^{-1}$. The flux of non-$\nu_e$ flavour solar neutrino flux was determined to be

$$\phi_{\mu\tau} = 3.41^{+0.45}_{-0.45}\,(\mathrm{stat.})^{+0.48}_{-0.45}\,(\mathrm{syst.}) \times 10^6\,\mathrm{cm}^{-2}\,\mathrm{s}^{-1},$$

This result indicated a violation of the hypothesis of no neutrino flavour change by more than 5.3 standard deviations.

The significant deviation from zero of the non-ν_e flavour content of the solar neutrino flux is strong evidence that neutrino flavour change is occurring en route from their creation in the Sun and verifies the neutrino flux predicted by solar model calculations.

1.2 Phase II: The salt phase

In the second phase of SNO, the salt phase, 2 tonnes of NaCl was dissolved in the D_2O. Neutrons, including those that are the signal of a NC reaction, were much more likely to be captured by ^{35}Cl than the deuterium. Neutron capture by ^{35}Cl produces an excited state of ^{36}Cl. The energy released when a ^{36}Cl nucleus relaxes to its ground state is up to 8.58 MeV [16] via multiple γ-rays. The increased energy released by neutron capture on ^{35}Cl shifts the energy of NC events farther above the low energy backgrounds. More importantly, the distribution of triggered photomultiplier tubes (PMTs) from the release of the multiple γ-rays is much more isotropic than the pattern for single electron events from the CC reaction. This provides discrimination between the single electron CC (and ES) events and NC events.

As described by Mikheyev and Smirnov [17], building on the work of Wolfenstein [18], if neutrinos change their flavour via the oscillation of massive neutrinos, then there is an additional interaction that can occur between electron neutrinos and the

dense concentration of electrons in the Sun. This interaction is energy dependent and can distort the energy spectrum of electron neutrinos at the earth. With the addition of salt, the increased isotropy of triggered PMTs from multiple γ-rays helps to differentiate between CC and NC events independent of their energy distributions making it possible to make a measurement of the electron neutrino energy spectrum via the CC reaction. The distribution was found to be consistent with an undistorted ^{8}B spectrum. The following fluxes were derived from the salt phase data in Ahmed et al. [19]:

$$\begin{aligned}
\phi_{\mathrm{CC}} &= 1.68^{+0.06}_{-0.06}\,(\mathrm{stat.})^{+0.08}_{-0.09}\,(\mathrm{syst.}) \\
\phi_{\mathrm{ES}} &= 2.35^{+0.22}_{-0.22}\,(\mathrm{stat.})^{+0.15}_{-0.15}\,(\mathrm{syst.}) \\
\phi_{\mathrm{NC}} &= 4.94^{+0.21}_{-0.21}\,(\mathrm{stat.})^{+0.38}_{-0.34}\,(\mathrm{syst.})\,,
\end{aligned}$$

in units of $10^6\,\mathrm{cm}^{-2}\,\mathrm{s}^{-1}$. An undistorted ^{8}B spectrum was assumed when extrapolating the CC and ES fluxes down to the lowest neutrino energies.

By extracting the number of CC events in each of 16 energy bins up to 14 MeV, SNO was also able to make a measurement of the CC energy distribution. Shown in figure 1.2 is the extracted number of CC events with statistical error bars. Also shown are the contributions of the dominant systematic uncertainties as the bands around the undistorted CC shape predicted by assuming a ^{8}B neutrino spectrum for the incident ν_e. The dominant systematic uncertainties are those associated with the energy reconstruction and those associated with the parametrization of the hit PMT isotropy: β_{14} (see [20] for a detailed discussion of β_{14}). As stated above, no spectral distortion as a result of solar neutrino flavour transformation was observed.

Given that no spectral distortions were observed, a measure of the solar ν_e survival probability was given as

$$\frac{\phi_{\mathrm{CC}}}{\phi_{\mathrm{NC}}} = 0.340 \pm 0.023\,(\mathrm{stat.})^{+0.029}_{-0.031}\,(\mathrm{syst.})\,.$$

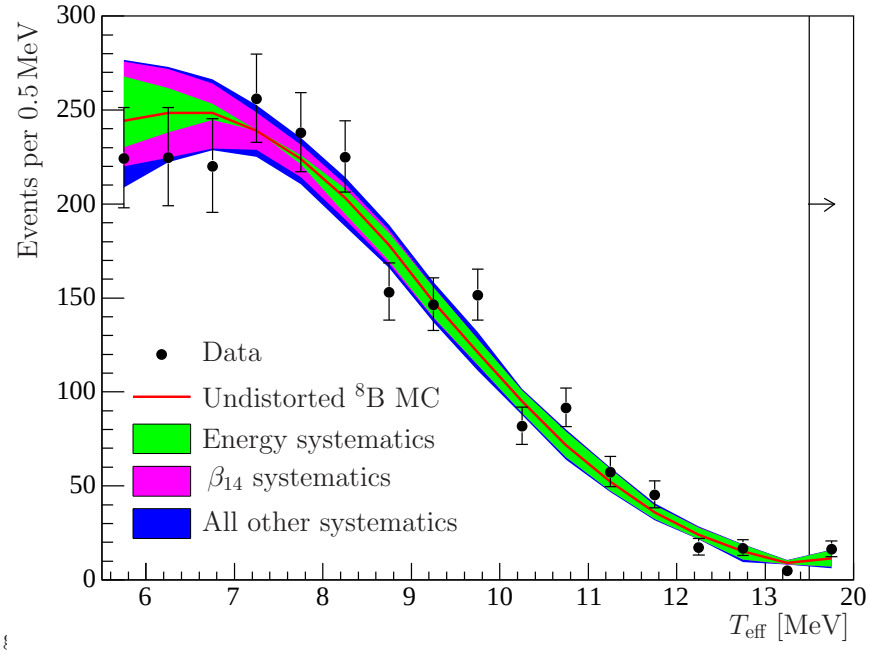

Figure 1.2: The distribution of CC event energy as extracted from the salt phase data. Also shown is the CC energy shape predicted to arise from an undistorted ^{8}B ν_e spectrum. The CC event energy is strongly correlated with that of the incident ν_e. Taken from Aharmim et al. [21].

1.3 Phase III: The NCD Phase

For the third and final phase of SNO, the neutral-current detector (NCD) phase, SNO deployed 40 strings of proportional counters (the NCDs) within the D_2O. The NC neutrons then captured primarily on ^{3}He 36 of the counters[3]. The NCDs provide an opportunity to break the correlation between the measured flux of CC and NC neutrinos since they are primarily observed in two distinct detectors. The purest CC spectral measurement, with the least NC "background", is also expected from the PMT data. The first results from the NCD phase of SNO were published in [1]. The fluxes extracted from the combination of the PMT and NCD data were

$$\begin{aligned}
\phi_{\mathrm{CC}} &= 1.67^{+0.05}_{-0.04}\,(\mathrm{stat.})^{+0.07}_{-0.08}\,(\mathrm{syst.}) \\
\phi_{\mathrm{ES}} &= 1.77^{+0.24}_{-0.21}\,(\mathrm{stat.})^{+0.09}_{-0.10}\,(\mathrm{syst.}) \\
\phi_{\mathrm{NC}} &= 5.54^{+0.33}_{-0.31}\,(\mathrm{stat.})^{+0.36}_{-0.34}\,(\mathrm{syst.})\,,
\end{aligned}$$

in units of $10^6\,\mathrm{cm}^{-2}\,\mathrm{s}^{-1}$.

1.4 Neutrino mixing

In the standard model of particle physics, three massless flavours of neutrinos exist[4] to complement the massive charged leptons. Neutrino flavour change, that has been demonstrated not only with solar neutrinos but atmospheric [10] and reactor [23] neutrinos as well, requires that neutrinos have mass. If the neutrino mass eigenstates do not directly correspond to the flavour eigenstates, neutrino oscillation can occur. The phenomenon of neutrino oscillations does not contradict the well verified standard model interactions of the three neutrino flavours (ν_e, ν_μ, and ν_τ) via the W and Z bosons, rather they occur as a result of the neutrinos propagating in their mass eigenstates ν_1, ν_2, and ν_3 with masses m_1, m_2, and m_3. The flavour states α can be

[3]Four of the counters were filled with ^{4}He to measure alpha particle backgrounds produced by radioactivity in the counters themselves and instrumental backgrounds associated with the NCDs.

[4]Measurements of the width of the Z^0 boson [22] constrain the number of light (less than one-half the Z^0 mass) neutrinos to 2.984 ± 0.008.

related to the mass-eigenstates i via a unitary matrix U

$$|\nu_\alpha\rangle = \sum_i U^*_{\alpha i} |\nu_i\rangle \,, \tag{1.1}$$

where U is commonly know as the unitary leptonic mixing matrix or Pontecorvo-Maki-Nakagawa-Sakata (PMNS) matrix.

The mixing matrix can be parametrized

$$U = \begin{pmatrix} 1 & 0 & 0 \\ 0 & \mathrm{c}_{23} & \mathrm{s}_{23} \\ 0 & -\mathrm{s}_{23} & \mathrm{c}_{23} \end{pmatrix} \times \begin{pmatrix} \mathrm{c}_{13} & 0 & \mathrm{s}_{13} e^{i\delta} \\ 0 & 1 & 0 \\ -\mathrm{s}_{13} e^{-i\delta} & 0 & \mathrm{c}_{13} \end{pmatrix} \times \begin{pmatrix} \mathrm{c}_{12} & \mathrm{s}_{12} & 0 \\ -\mathrm{s}_{12} & \mathrm{c}_{12} & 0 \\ 0 & 0 & 1 \end{pmatrix}, \tag{1.2}$$

where $\mathrm{s}_{ij} = \sin\theta_{ij}$, $\mathrm{c}_{ij} = \cos\theta_{ij}$, and δ is a CP–violating phase.

Neutrino oscillation may be approximated, either in the solar or atmospheric regime, as mixing between two states since θ_{13} is known to be small ($\sin\theta_{13} \simeq 0.016$) [24] and $\Delta m^2_{21} \ll \Delta m^2_{32}$. For solar neutrinos the mixing reduces to

$$\begin{pmatrix} \nu_e \\ \nu_x \end{pmatrix} = \begin{pmatrix} \mathrm{c}_{12} & \mathrm{s}_{12} \\ -\mathrm{s}_{12} & \mathrm{c}_{12} \end{pmatrix} \begin{pmatrix} \nu_1 \\ \nu_2 \end{pmatrix}, \tag{1.3}$$

where ν_x is a linear combination of ν_μ and ν_τ. Incorporating the time evolution of the system leads to the electron neutrino survival probability ($P_{\nu_e \to \nu_e}$) given by

$$P_{\nu_e \to \nu_e} = 1 - \sin^2 2\theta_{12} \sin^2 \left(\frac{1.27 \Delta m^2 L}{E} \right) \to 1 - \frac{1}{2} \sin^2 2\theta_{12} \tag{1.4}$$

where $\Delta m^2_{12} = m^2_2 - m^2_1$ in eV^2, L is the distance traveled in kilometers and E is the energy of the neutrino in GeV. When ^{8}B solar neutrinos traverse the vacuum of space to the Earth, the $\sin^2\left(\frac{1.27\Delta m^2 L}{E}\right)$ averages to 1/2.

The Hamiltonian $\mathcal{H}$ of the two flavour neutrino state in vacuum may be written

$$\mathcal{H} = \frac{\Delta m^2}{4E} \begin{bmatrix} -\cos 2\theta & \sin 2\theta \\ \sin 2\theta & \cos 2\theta \end{bmatrix}. \tag{1.5}$$

However, when neutrinos pass through normal matter electron neutrinos undergo

the added interaction via the W boson. This adds an extra interaction term to the vacuum Hamiltonian such that

$$\mathcal{H} \rightarrow \mathcal{H} + \begin{bmatrix} \sqrt{2}G_{\mathrm{F}}N_{\mathrm{e}} & 0 \\ 0 & 0 \end{bmatrix}, \tag{1.6}$$

where G_{F} is the Fermi constant and N_{e} is the number density of electrons. This coupling of the interactions of neutrinos in the flavour states with the mixing of the neutrino mass-eigenstates is know as the Mikheyev Smirnov Wolfenstein (MSW) effect.

For ^{8}B neutrinos produced in the core of the Sun, $\frac{\Delta m^2}{4E} \ll \sqrt{2}G_{\mathrm{F}}N_{\mathrm{e}}$ due to the large local N_{e}. The Hamiltonian reduces to the matter term added in equation 1.6 resulting in ν_e that are produced purely in the ν_2 mass-eigenstate. For the current estimates of the solar neutrino mixing parameters, the propagation of neutrinos from the core to the surface of the Sun (where $N_{\mathrm{e}} \rightarrow 0$) is adiabatic leaving the neutrinos in a pure ν_2 state. As $\nu_2 = \nu_e \sin\theta + \nu_x \cos\theta$ the survival probability of ^{8}B solar electron neutrinos is simply

$$P_{\nu_e \rightarrow \nu_e} = \sin^2\theta \tag{1.7}$$

where $\theta = \theta_{12}$. The contribution of the MSW effect (or that of some other comparable theory) is necessary to explain the observation of solar electron neutrino survival probabilities of less than 1/2 (see equation 1.4).

1.5 Contributions of this work

Event energy reconstruction and energy calibration are essential components of the analysis of all SNO data. The uncertainty associated with energy calibration and the error in energy reconstruction dominate the uncertainty in all SNO solar neutrino flux results. This work follows the development of an energy reconstructor, which is also used as an integral part of the energy calibration, from the fundamental processes of energy deposition in the water, through to the application of an analytic optical model of the detector, to the full calibration of the detector energy scale and reconstruction of the energy of events.

Prior to this work, the energy response processor RSP was used in conjunction

with Monte Carlo calculations to calibrate the energy response of SNO and estimate event energy. Its approach to energy reconstruction was to renormalize the number of PMTs triggered during an event (N_{hit}) to what would have been observed had the event occurred at the centre of the detector, thereby removing the position dependence introduced by the varying optical response of the detector. Using an analytic model, it calculated the total optical response at both the centre of the detector and at the reconstructed event vertex as the sum of the response in each of 100 angular bins. This method assumes that the detector is uniformly instrumented with identical PMTs and that the optical response at the centre of each bin is representative of the angular extent of the bin. Although RSP was more than sufficient for previous analysis—it was sufficiently accurate and its energy resolution was much better than an energy estimate based solely on N_{hit}—these points indicated that improvements could be made. Also, as SNO transitioned from demonstrating solar neutrino flavour change to the precision measurements of neutrino oscillation greater precision and accuracy were required.

The analytic approach to the problem of energy calibration and reconstruction is both efficient and serves as an independent test of Monte Carlo calculations. In this work, an analytic model is again used; in this case however, to calculate the optical response of the detector as the sum of the response of each individual PMT. As both RSP, as described above, and the approach taken by this work employ an analytic optical model of the detector, in contrast to the Monte Carlo calculation method of the FTK energy reconstruction algorithm [25], the new energy response processor bears the same name; namely RSP. This new strategy enables the precise determination of the instrumented regions of the detector, accounts for the position of absent and malfunctioning PMTs, and implementation of the variation in efficiency from PMT to PMT[5].

A subtle correction (that can be significant) for the multi-photoelectron effect[6] is also much improved with the new RSP. An estimate of the number of photons created by an event is made by RSP which, when combined with the detector optical

[5]This information did not exist until about the time of the development of the new energy response processor.

[6]SNO PMTs have not the capability to distinguish between single and multi-photoelectron triggers. Subsequent photons are as uncounted as those that miss the PMT altogether.

response, can be used to predict the number of photons expected to hit any given PMT (almost always less than 1.0 for solar neutrino events occurring in the D_2O). Taking this to be the mean of a Poisson distribution, the probability of multiple hits can be properly accounted for.

All references to RSP in this work refer to the energy response processor developed herein unless otherwise explicitly stated. The full details of the RSP energy calibration and reconstruction are the subject of the following chapters. The contributions of these strategies and the author to the, primarily, solar neutrino results presented by SNO are briefly highlighted below.

1.5.1 Solar *hep* neutrinos and the DSNB

The first application of RSP, as developed by the author, was to the solar *hep* neutrino and diffuse supernova neutrino background (DSNB) analysis of the pure D_2O phase data [26]. The author performed the energy scale calibration of both the Monte Carlo calculations and energy reconstruction used in this analysis based on the comparison between calibration data and simulations. The applicability of the energy reconstruction was extended to over 100 MeV higher, to at least 130 MeV, than any previous SNO analysis. The performance of RSP was tested for both accuracy and precision and was compared to the original. Again, based on the comparison between calibration data and simulations, the potential error in the energy scale and energy resolution were estimated by the author. It was shown that RSP modestly, yet consistently, outperformed its predecessor in both accuracy and resolution. The details of this effort are not presented in this work but are similar to those of the pure D_2O phase analysis presented in chapter 5.

The analysis of the data consisted primarily[7] of counting the number of neutrino candidate events within separate, signal-to-background–optimized, energy windows above the endpoint energy of ^{8}B neutrinos. No *hep* or DSNB neutrinos were observed

[7] Also of considerable note is the accounting for the expected number of ^{8}B neutrino "background" leaking into the analysis window from below.

in the energy analysis windows. The limits on the fluxes that this implies are

$$\begin{aligned} \phi_{hep} &< 2.3 \times 10^4\,\mathrm{cm}^{-2}\mathrm{s}^{-1} && \text{and} \\ \phi_{\mathrm{DSNB}} &< 70\,\mathrm{cm}^{-2}\mathrm{s}^{-1} && \text{for } 22.9\,\mathrm{MeV} < E_\nu < 36.9\,\mathrm{MeV}, \end{aligned}$$

at the 90% confidence level. Both of these are substantial improvements over the previous limits published by Hosaka et al. [27] and Aglietta et al. [28].

1.5.2 The low energy threshold analysis

SNO detects solar neutrinos well below the analysis energy threshold applied to the previous analyses discussed above. The benefit of requiring that events have a higher energy limits the low energy background contamination in the data to essentially none or at least a level that is understood. The challenge in lowering the analysis energy threshold is to reduce and constrain the low energy backgrounds in order to make a meaningful measurement.

Preliminary low energy threshold analyses have been published by Kos [29] and Dunford [25]. The former analyzes the salt phase data using an energy dependent fiducial volume that restricts the volume analyzed to regions of lower background at lower energies. A combined analysis of the first two phases of SNO—the pure D_2O and salt phases—has been performed by Dunford [25]. Dunford [25] has shown that a 1% reduction in energy resolution, or in the uncertainty on energy resolution, reduces the background contamination in the signal region by up to 10%. To decrease the energy resolution beyond what is achieved by RSP, a total light[8], Monte Carlo calculation based, energy reconstruction technique named FTK was developed by Dunford [25]. Considerable effort was undertaken by Dunford [25] to improve the simulation of reflected photons in the Monte Carlo calculations to be able to include the approximately 20% more light than RSP does.

More advanced low energy threshold analyses of the combined first two phases of SNO are presented by Gann [30] and Seibert [31]. Both of these analyses are based on that of [25] and primarily use the FTK reconstructed energy of events. A further

[8]RSP considers only triggered PMTs within 10 ns of the prompt peak to reject reflected light; the optical path of which is indeterminate.

low energy threshold analysis (LETA) of the first two phases of SNO that is based on these two analyses is currently being prepared for publication.

Numerous advancements in the understanding of SNO have led to improved data analysis techniques including the two new energy reconstruction strategies, and improved detector simulations since the previous SNO results. These improvements were incorporated into the reprocessing—unpacking and reconstruction of event position, direction, and energy—of this data in preparation for LETA. The calibration of the energy scale of this reprocessed data, performed by the author, is presented in chapter 5[9]. Although FTK energy is being used for the final analysis, the RSP energy is used to verify the energy calibration and reconstruction uncertainty that will be reported. This analysis is also presented in chapter 5. The verification of FTK energy reconstruction, with the independent analytic calculation of RSP, is essential to ensure this new technique and the upgraded detector simulations are robust and accurate, since the errors related to these are expected to remain the dominant contribution to the uncertainty on any physics results.

1.5.3 The NCD phase solar neutrino analysis

The addition of 40, 10 to 12 m long and approximately 5 cm in diameter, proportional counters to the central region of the D_2O presents a significant challenge in calculating the optical response of the detector during the NCD phase. An exact function is derived in chapter 6 to calculate the shadow cast on a single PMT by an NCD; however, it is found to be too computationally intensive to be fully implemented. An average efficiency reduction, as a function of only event radial position and direction with respect to the radial position vector, due to the shadowing of the NCDs is subsequently derived from Monte Carlo calculations. While this correction still has some small bias, the overall performance of the energy calibration and reconstruction using RSP are satisfactory and are highlighted in chapter 6 and in the publication of the first NCD phase results in Aharmim et al. [1].

The energy scale calibration of the NCD phase data, as performed by the author, is presented in chapter 6. It should be noted that the author also played a major role

[9]It should also be noted that the author played a major role in acquiring the salt phase calibration data used for this analysis.

in acquiring the calibration data used in this analysis. The energy calibration and reconstruction errors used by Aharmim et al. [1] are not the work of this author. These errors are reevaluated in chapter 6 with a more refined technique exactly analogous to the errors calculated for LETA. In every case, the previous estimates used by Aharmim et al. [1] are found to be conservative and therefore validated.

1.6 Organization of thesis

Chapter 2, discusses the physical components and function of the SNO detector, especially those components relevant to its response to Čerenkov photons. Chapter 3 formulates a model of the optical response of the detector that is position, direction, and time dependent. The model is then parametrized in terms of the parameters that are determined from optical calibrations and Monte Carlo calculations. Chapter 4 applies the optical response discussed in chapter 3 to estimate the fraction of Čerenkov photons that are lost as they travel from their point of creation, which is assumed to be at the reconstructed position of an event, to the PMTs. From the number of observed photons and the fraction that are not detected, the number of initial photons can be predicted. A series of predetermined Monte Carlo calculations are then applied to reconstruct the event energy from the number of initial photons. This is the RSP energy reconstruction algorithm.

The calibration of the absolute energy scale in SNO and the errors associated with energy calibration and reconstruction are discussed in chapter 5. The actual calculation of these errors for the LETA of the pure D_2O and salt phase data are also presented. This analysis of the performance of RSP is used to verify the performance of the primary energy reconstruction technique FTK, as quoted by Seibert [31].

In chapter 6, the process of the integration of the NCD geometry into the optical response of RSP is documented[10]. The chapter also contains the energy calibration and a calculation of the energy calibration and reconstruction errors for the NCD phase. These refined estimates of the energy scale and resolution errors verify the more conservative estimates used by Aharmim et al. [1].

[10]While the geometry of the NCD phase is also available to the Monte Carlo calculation technique of FTK, it is too computationally intensive to process the data in a reasonable amount of time. RSP was therefore the only viable energy processor for the NCD phase analysis.

Chapter 7 presents the potential energy scale errors associated with calibrating electron energy (such as those scattered by solar neutrinos) with an ^{16}N γ-ray source via an intermediate Monte Carlo calculation. Given the many improvements in energy calibration that were made for LETA and also applied to the NCD analysis, this error had become the dominant energy scale uncertainty. To verify this, all of the sources of error previously known are re-evaluated. The dominant contribution to this source of error—using a simplified model to pick the wavelength of Čerenkov photons produced in the Monte Carlo calculations—is shown to be negligible. This significantly improves the estimate of the total energy scale error. In light of the significant reduction in the total error, other sources of error previously thought to be negligible are also evaluated.

The first solar neutrino analysis of the NCD phase data is reviewed in chapter 8. Although not directly the work of the author, an overview of the analysis procedure with emphasis on the energy calibration and reconstruction processes developed by the is presented author. The basic physics implications of these results on the favoured neutrino oscillation theory are also briefly discussed.

Chapter 2

The SNO detector

The Sudbury Neutrino Observatory is a one kilotonne heavy water Čerenkov detector. It is situated in a large cavity on the 6800 ft level (at an actual depth of 2092 m) of an active nickel mine located in Sudbury, Ontario, Canada. The cavity that the detector occupies, as depicted in figure 2.1, is barrel-shaped: 22 m in diameter, 34 m in height. During the data collection described in this thesis, the primary neutrino target consisted of 1000 tonnes of ultra pure D_2O contained within a 12 m diameter, spherical acrylic vessel (AV), that is on average 5.5 cm thick. Čerenkov light emitting events in the inner detector are observed by 9456 inward looking Hamamatsu R1408 photomultiplier tubes (PMTs) mounted on a 17.8 m diameter stainless steel geodesic support structure (PSUP). The D_2O region is shielded from radioactivity in the PMTs, external water shielding, and the mine rock by two regions containing H_2Oin addition to the AV. The region between the mine rock and the PSUP contains 5.7 kT of H_2O while the inner region, between the PSUP and AV, contains approximately 1.7 kT of ultra pure H_2O [32]. The top of the detector is shielded from radon in the mine air by a continuous overpressure of radon-reduced nitrogen gas in the gap between the top of the D_2O and H_2O and the deck. The entire detector is shielded from cosmic-rays by an overburden, at that depth, equivalent to approximately 6 km of water shielding. This reduces the muon flux within the PSUP to less than 70 muons per day [33].

After the completion of the third and final phase of SNO, the detector was drained of all water, the D_2O returned to Atomic Energy of Canada Limited and Ontario

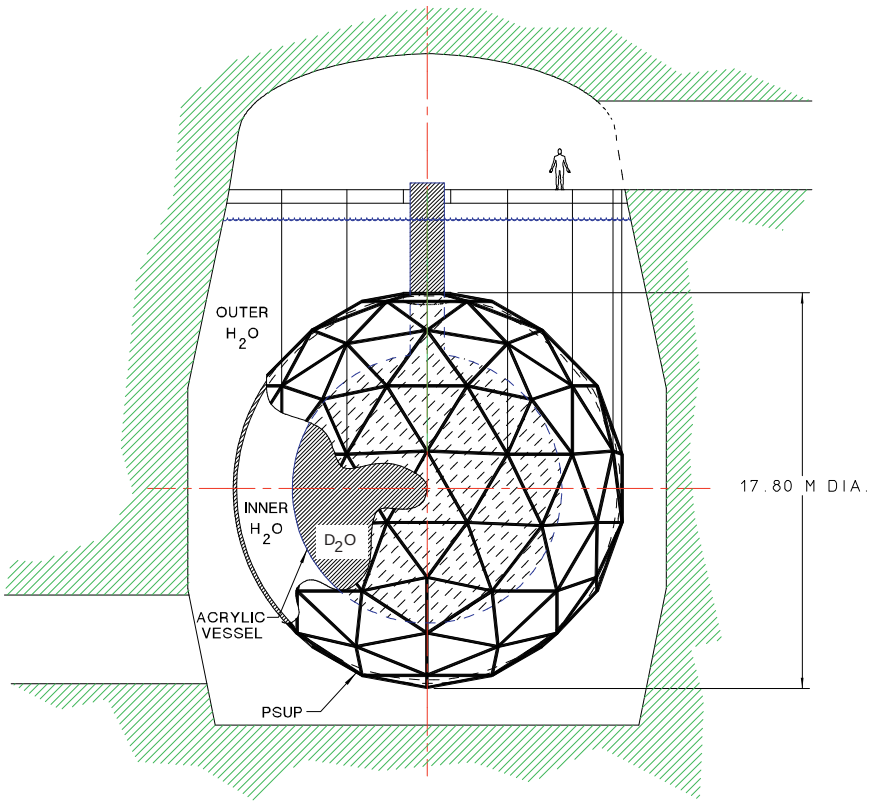

Figure 2.1: Schematic of the barrel-shaped cavity that contains the SNO detector. Also shown is the geodesic PMT support structure (PSUP) and acrylic containment vessel. The regions filled with D_2O and H_2O are as indicated. Taken from Boger et al. [34].

Power Generation. It is intended to reuse the detector by filling the acrylic vessel with liquid scintillator, to be again shielded by ultrapure H_2O. Although only sensitive to charged current and elastic scattering neutrino interactions, the greater light yield of the scintillation will significantly improve the energy resolution of the detector and suppress low energy backgrounds. In this configuration, the detector, named SNO+ [35, 36], will be able to observe lower energy *pep*, CNO, and ^{7}Be solar neutrinos, and geo [37] and reactor [38] antineutrinos. With the capability of dissolving a large mass of ^{150}Nd in the liquid scintillator, SNO+ can alternatively be sensitive to neutrinoless double β-decay [39].

The following sections highlight the detector elements that are particularly relevant to SNO energy calibration with the exception of the primary energy calibration sources that are discussed in greater detail in chapter 5. The majority of this chapter is referenced, except where explicitly noted, from a complete description of the SNO detector that can be found in Boger et al. [34].

2.1 The ultra pure D_2O

The total mass of heavy water within the acrylic vessel (AV) is 1011 ± 1 T with about 9 T residing in the chimney. The mean measured density of the heavy water in SNO, at 11.5°C and corrected for compressibility, is $1.10565 \pm 0.00010\,\mathrm{g/cm^3}$. The isotopic fraction of D_2O in the target heavy water is $99.9168 \pm 0.0021\%$ by mass or $99.9076 \pm 0.0021\%$ by number [40]. The number of target deuterons can then be calculated from the density and isotopic fraction for any arbitrary volume of the heavy water. The remaining isotopic fraction of the heavy water is dominated by HDO with very little H_2O. Even this small amount of hydrogen affects neutron transport and capture in the heavy water and must be accounted for. The isotopic fraction of the oxygen isotopes ^{17}O and ^{18}O, which enhance neutron capture and CC neutrino interactions respectively, were determined to be $0.0485 \pm 0.0005\%$ and $0.320 \pm 0.008\%$ [40]. The number of target electrons, for the ES reaction, is relatively insensitive to the isotopic fraction.

Radioactivity in the D_2O that results in the production of a γ-ray with energy greater than 2.2 MeV creates a background of photodisintegration neutrons that are

especially difficult to distinguish from NC neutrons. For this reason, photodisintegration neutrons were budgeted at no more than 10% of the expected rate of NC neutrons in the detector. The decays of ^{214}Bi and ^{208}Tl, from the decay chains of ^{238}U and ^{232}Th, involve γ-rays that can photodisintegrate deuterium. This limits the concentrations of ^{238}U and ^{232}Th in the D_2O to 4.5×10^{-14} g ^{238}U and 3.7×10^{-15} g ^{232}Th per average gram of D_2O [34]. Levels below these limits were maintained throughout the operation of SNO [1, 15, 21] with the exception of brief incursions of ^{222}Rn during breakdown of the water purification system and by intentional contamination for the purposes of calibration. The details of the water purification procedures that achieved these limits are presented in Boger et al. [34].

Decays of ^{214}Bi and ^{208}Tl, which produce copious amounts of low energy electromagnetic radiation, are referred to as the β–γ background. Although consistently low in energy, the high rate of these decays combined with the finite energy resolution of the detector cause some events to spill into the solar neutrino analysis window (as low as 5–6 MeV). The rate of the β–γ background, for a given energy resolution, sets the effective energy threshold for the experiment. This limit is currently being tested by the ongoing low energy threshold analysis (LETA).

2.2 The D_2O-acrylic containment vessel

The acrylic vessel (AV) consists primarily of an acrylic shell with an inner radius of 600.5 cm and a nominal thickness of 5.5 cm. The spherical vessel was constructed from 122 ultraviolet transmitting (UVT) acrylic panels that were bonded together in the detector cavity. Among other reasons, the UVT acrylic was selected due to its low radioactivity and the fact that its light transmission properties are similar to the sensitivity regime of the PMTs [34]. Regardless, more Čerenkov light is attenuated by the few centimeters of UVT acrylic than by either the D_2O or H_2O. A schematic of the AV showing the acrylic paneling, chimney, and machined support panels is shown in figure 2.2.

The spherical symmetry of the AV is broken most notably at the top where a 150 cm diameter chimney breaches it to permit the introduction of calibration sources

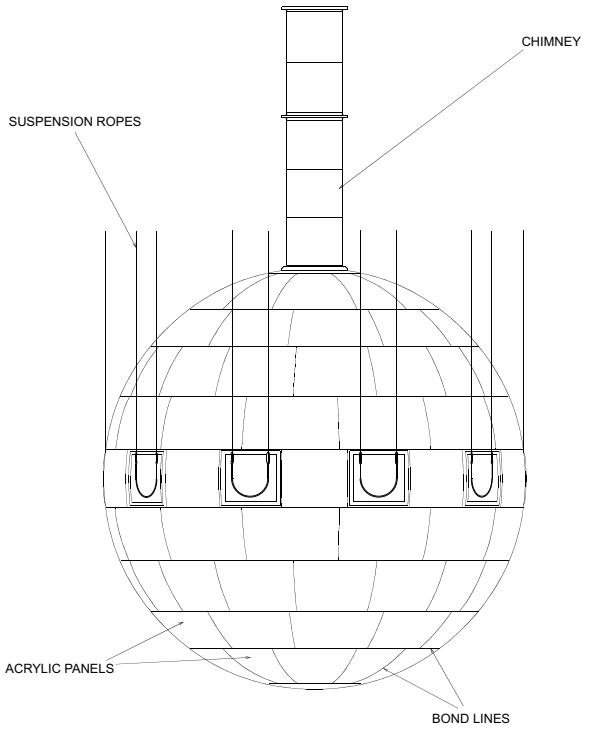

Figure 2.2: Schematic of the SNO D_2O-acrylic containment vessel. Taken from Boger et al. [34].

and, just prior to the NCD phase, the proportional counters. The chimney is cylindrical in shape, approximately 6.8 m in height and 1.5 m in diameter. Piping designed to transport the D_2O enters the spherical vessel inside the chimney. Pipes also introduce or remove D_2O for recirculation at the bottom of and at four different heights in the spherical vessel and once again in the chimney. None of these components penetrates significantly into the D_2O enclosed by the spherical vessel.

Ten acrylic panels around the equator of the spherical vessel are approximately twice as thick as the other panels. Semi-circular grooves are machined into these thicker panels to support the AV on loops of Vectran rope. The D_2O contained within the AV is denser than the surrounding H_2O requiring it to be suspended from the deck via the Vectran ropes. 96 acrylic NCD anchors are also affixed to the inner surface of the lower hemisphere of the spherical vessel. These anchors are approximately cylindrical, 3" in diameter and 2.25" in height.

The AV, although it is very large, does not constitute a significant fraction of the total mass of the detector. As such, the limits on radioactive contamination per average gram of acrylic are less stringent than those on the D_2O: 10^{-12} g of ^{238}U and ^{232}Th. However, a particularly difficult background that was rediscovered[1] during the salt phase originates on the surfaces of the acrylic vessel. (α, n) reactions, from ^{222}Rn that plated out onto the surfaces of the AV in the form of Pb deposits during construction, apparently release free neutrons into the D_2O. These neutrons can only be distinguished from NC neutrons based on their spatial distribution. Only during the salt phase are neutrons captured with a high enough efficiency to localize the neutrons to the vicinity of the AV.

2.3 The H_2O shielding and PSUP

The inner H_2O shielding fills the region between the AV and the PMTs and associated support structure (PSUP); it occupies the volume between roughly 606 cm to approximately 840 cm radially from the centre of the detector. Also present in this region are the 24.4 mm diameter Vectran AV support ropes and D_2O piping that access the

[1] This background was a concern when SNO was proposed but misplaced in the intervening period [41].

AV. The outer H_2O shielding, which cannot be kept as clean, is separated from the PMTs and inner H_2O shielding by a 99.99% leak-tight plastic barrier that also serves as a light shield from β–γ events exterior to the PSUP. Approximately 85% of the inner surface of the PSUP is dedicated to Čerenkov light collection (including the PMTs and associated infrastructure).

The radioactivity in the H_2O is as important to minimize as that in the D_2O. γ-rays from the decays of ^{238}U and ^{232}Th can produce photodisintegration neutrons in the D_2O; albeit with lower probability than those internal to the D_2O. Although low in energy, ^{214}Bi and ^{208}Tl β–γ decays in the H_2O do not suffer from the attenuation of the AV if they illuminate the PMTs directly. Given the high rate of these decays, position mis-reconstruction sometimes places them in the D_2O region; constituting a significant background at low energy.

2.4 SNO photomultiplier tubes

There are 9456 inward looking photomultiplier tubes (PMTs) mounted on the inside of the PMT support structure; 18 were removed for testing prior to the pure D_2O phase. A further 91 PMTs are mounted on the outside of the PSUP to act as vetoes for external events that produce light in the inner detector; mainly consisting of muons. Four (eight in the NCD phase) PMTs are also mounted in the top of the neck, the region inside the AV chimney, to veto events generated by light from the water pipes.

The inward looking PMTs provide only 31% coverage of the D_2O region. 27 cm diameter light concentrators, made up of 18 reflector strips or petals each, increases the coverage to 59%. This is reduced to 54% after accounting for the efficiency of the light concentrators as reflectors [34]. The concentrators substantially increase the light collection of the PMTs with no increase in PMT noise. Having only a 100° acceptance, they also decrease sensitivity to light from radioactive backgrounds external to the D_2O region[2]. Schematics of the Hamamatsu model R1408 PMT with the elements forming the water tight seal and, separately, the hexagonal mounting bracket are shown in figure 2.3.

[2]For a complete description of the reflector assembly design see Doucas et al. [42].

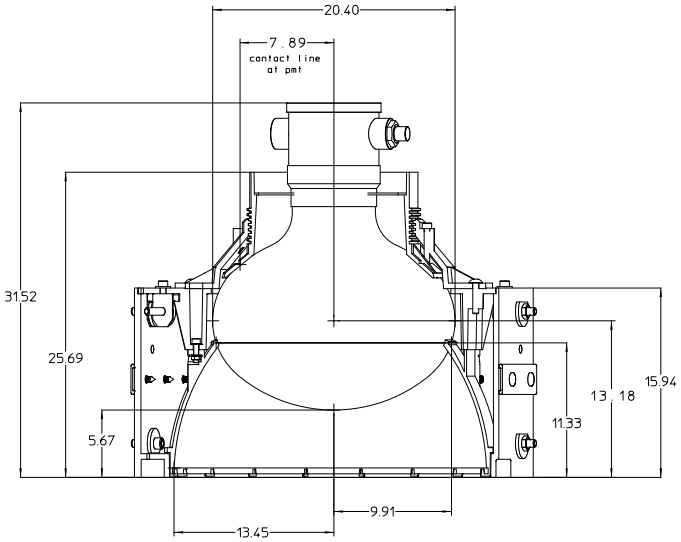

(a) A PMT in the hexagonal mounting bracket. The curved surface attached to the face of the PMT holds the 18 reflector petals that make up the reflector assembly.

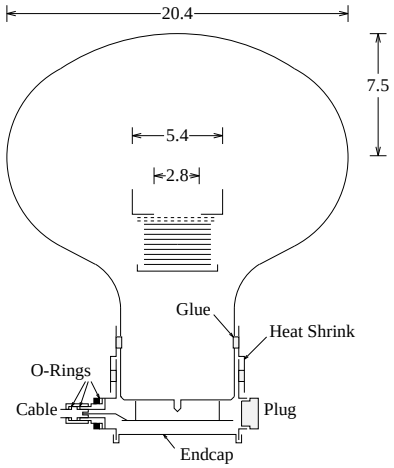

(b) The nine dynodes are shown as horizontal lines below the focusing grid (dashed lines).

Figure 2.3: Schematics of the Hamamatsu model R1408 PMT. The dimensions are all in centimeters. Both figures taken from [34].

Photons passing through the front surface of the PMT glass encounter a bialkali photocathode deposited on its inner surface. The photon can liberate an electron from the photocathode via the photoelectric effect. The electron, in the evacuated envelope, is drifted to the anode where it is focused onto the dynode stack. The nine stages of dynodes (see figure 2.3b) amplify the signal by a factor of 10^7 for the standard operating voltages from 1700 to 2100 V. The high voltage and signal are both transmitted via a 32 m long cable to electronics and power supplies located on the deck above the detector.

The charge distribution for single photoelectrons (*pe*) liberated in the R1408 PMT is shown in figure 2.4. The broad spectrum makes it difficult to associate observed charge with the number of detected *pe*. Fortunately, ^{8}B neutrinos rarely produce multiple *pe* in a single PMT. The total transit time from the cathode to the anode of the PMT is about 30 ns with an RMS of about 1.5 ns [43]. The very good timing resolution allows event position reconstruction to be accurately performed based entirely on PMT timing.

The noise rate in the PMTs is dominated by thermal electron emission in the

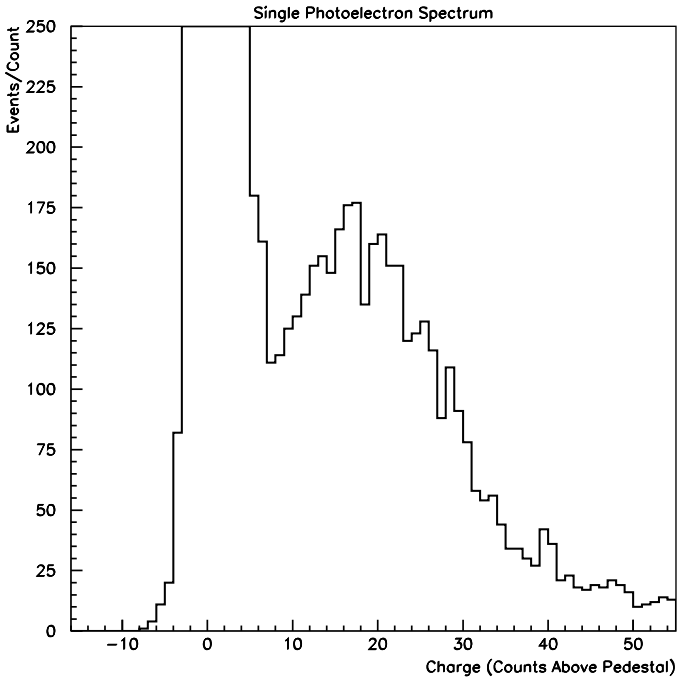

Figure 2.4: The single photoelectron charge spectrum of an R1408 PMT. Taken from Boger et al. [34].

photocathode and dynode stack. This effect is minimized by cooling the entire detector to about 11.5°C; which is still high enough so as not to freeze the D_2O. The average noise rate in the PMTs at this temperature is about 500 Hz. The Earth's magnetic field reduces the average efficiency of the PMTs in SNO by distorting their internal electromagnetic field. At the SNO detector the magnetic field is measured to be about 55 μT approximately 15° from vertical. According to Boger et al. [34], this would result in an average reduction in PMT efficiency of 18%. Compensating for the vertical component of the magnetic field with 14 horizontal field coils embedded in the surrounding rock reduces this loss to about 2.5% with a residual magnetic field of 19 μT. The overall performance of the PMTs including their wavelength sensitivity and light collecting efficiency are presented in detail in chapter 4.

Although each component of the PMT assembly was chosen to minimize radioactivity, the PMTs are the most contaminated components in the inner detector. The dominant contribution to this radioactivity is in the glass envelope. Special low radioactive borosilicate glass (Schott type 8246) was produced for SNO in a special low radioactivity furnace and was mouth-blown to form the PMT envelope. In total each PMT contains less than 100 μg of ^{238}U and ^{232}Th combined. This is 14 times below specifications [34].

2.5 SNO proportional counters

An array of 40 strings of proportional counters were deployed in the central region of the D_2O after the removal of the salt from the salt phase. The physical parameters of the proportional counters, referred to as neutral current detectors (NCDs), are listed in table 2.1. A top down view of the NCD string layout in the D_2O is shown in figure 2.5. The strings of NCDs vary in length from the outermost at 9 m to 11 m nearest the centre of the detector.

Of the 40 strings of NCDs, 36 contain ^{3}He, four contain ^{4}He. The 36 that contain ^{3}He are used to observe NC neutrons. The four strings of NCDs containing ^{4}He, that are not sensitive to neutrons but are still referred to as NCDs, provide a control sample of the non-neutron backgrounds in the primary array. ^{3}He was selected as the active counter gas due to its high neutron capture cross section and its use in

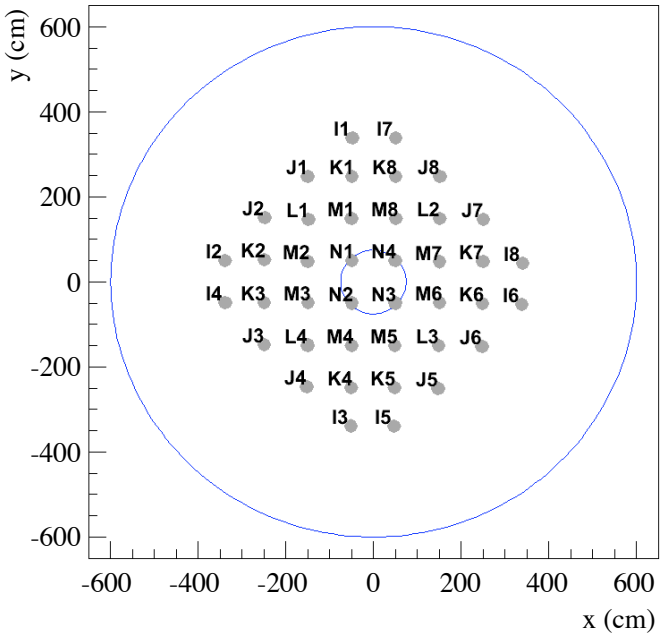

Figure 2.5: A top-down view of the layout of the NCD strings. The label letters denote strings of the same length, becoming shorter farther from the centre. The strings I2, I3, I6, and I7 contain ^{4}He rather than ^{3}He. The outer circle, which is 12 m in diameter, represents the maximum extent of the AV. The inner circle, 1.5 m in diameter, represents the chimney of the AV through which the NCDs were deployed. The circular NCD markers are not drawn to scale. Taken from Amsbaugh et al. [44].

Physical property	Value
outer diameter	5.08 cm
wall thickness	305–533 μm
lengths	200, 227, 250, 272, 300 cm
anode wire diameter	50 μm
gas pressure	2.50 ± 0.01 atm
gas mixture (by pressure)	85:15 He:CF_4
weight	525 g/m

Table 2.1: Some physical parameters of the NCDs. Adapted from Amsbaugh et al. [44].

detecting neutrons being well-established [44]. Neutron capture on ^{3}He proceeds via

$$^3\mathrm{He} + \mathrm{n} \rightarrow \mathrm{p} +^3 \mathrm{H} + 764\,\mathrm{keV}, \tag{2.1}$$

where the proton and triton are produced nearly back-to-back. This requires the proton to acquire 573 keV, the triton the remaining 191 keV. This pair then ionize gas along their respective trajectories. The electrons that are produced are drifted towards the central anode wire ionizing more gas; creating an avalanche effect. The electrons striking the anode produce the signal in the anode. The anode was connected to the electronics and power supplies on the deck above the detector via a coaxial cable less than 0.890 cm in diameter.

If both the proton and triton are completely stopped in the gas, 764 keV of energy is deposited in the detector. When either the proton or triton strike the wall of the counter, some of their energy does not get deposited in the gas. Events that occur close to the counter wall can have either[3] the proton or triton strike the wall, thus depositing in the gas a range of energies down to 191 keV. The energy lost is mitigated by the addition of the CF_4 to the gas by shortening the particle tracks and therefore minimizing the probability of encountering the wall. However, it is limited by the anode voltage required to drift the electrons at the higher gas pressures. The CF_4 was also required to provide quenching and sufficient gas pressure to keep the counter tube from collapsing under the pressure of the water.

Once again, the decay chains of ^{238}U and ^{232}Th present in the counters is be problematic due the γ-rays greater than 2.2 MeV that they produce. To mitigate these the NCD bodies were constructed from ultra-pure chemical-vapour-deposited nickel that reduced the natural ^{238}U and ^{232}Th concentrations by six orders of magnitude [44]. This resulted in a total ^{238}U and ^{232}Th content in the NCD array of less than a few micrograms; equivalent to about 1% of the NC neutron detection rate. The low energy β–γs from the decays of ^{214}Bi and ^{208}Tl require a relatively high analysis energy threshold in the analysis of the PMT data taken during the NCD phase. However, the measurement of these decays with the PMT data was used to extrapolate the number of photodisintegration neutrons that would have been produced by their parent decay

[3]It is highly unlikely that both particles strike the counter wall therefore the lowest deposited energy comes when all of the energy of the more energetic particle is lost.

chains.

α-particles from the decay chains of ^{238}U and ^{232}Th also present a background to neutrons in the NCDs although the primary α-particle background stems from the decay of ^{210}Po, introduced as a daughter product of ^{222}Rn decay in the air during detector fabrication. In total 16 ± 1 α-particles per day were detected by the NCD array, five times the expected NC neutron rate [44]. However, due to the distinctive shape of the neutron energy distribution, the NC signal can be extracted from the α-particle background with better than 5% fit uncertainty.

2.6 Detector response calibration

A series of detector calibrations are required in order to make accurate measurements of the interesting physical properties related to each triggered event[4]: position, direction, and energy. These calibrations include built-in electronic calibrations, optical calibrations, radioactive source calibrations, and Monte Carlo calculations. The driving purpose behind all the calibrations is to tune a global model of the detector, usually in the form of a Monte Carlo simulation, that can be used to predict the detector response to all relevant physical processes; providing a model against which to test neutrino data.

2.6.1 Electronics calibration

Figure 2.6 depicts the time evolution of a PMT pulse significant enough to have fired the associated discriminator. Simultaneously the voltage begins to ramp in a time to amplitude converter and the signal from the PMT is integrated to yield the total charge Q. If no global trigger is issued within about 400 ns, which would have signaled the information from all triggered PMTs to be assigned to an event and written to tape, the channel is reset. Otherwise, the charge and timing information are stored in capacitors. There are 16 sets of capacitors designated to store the information from each PMT to be able to handle very high rates of data. As in the figure, T and Q are read by separate analog to digital converts (ADCs) from the capacitors. The output

[4]For a complete description of the SNO trigger system see Klein et al. [45].

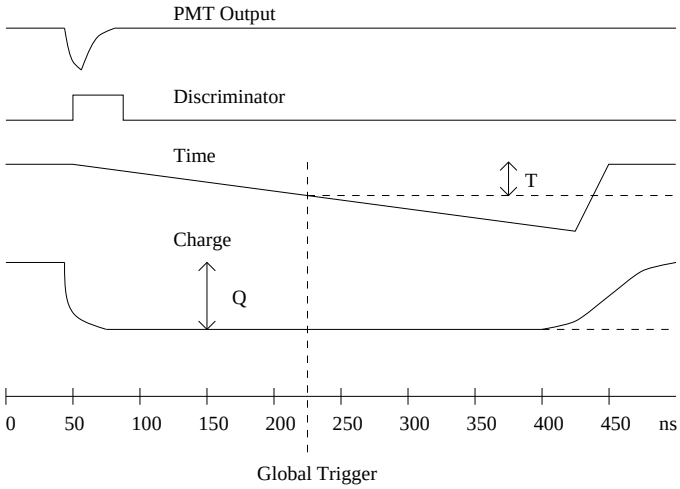

Figure 2.6: The approximately 400 ns single PMT timing cycle. Time refers to the time to amplitude converter, T the time the PMT triggered relative to a global trigger, and Q the total integrated charge from the PMT signal.

of the ADCs is the raw charge and timing information from the PMT channel that is ultimately recorded.

Three calibrations are performed to normalize the performance of each channel: a pedestal calibration, required to determine the number of ADC counts that correspond to zero charge; a charge slope calibration, required to determine the rate of increase in ADC counts as a function of input charge; and a time slope calibration, required to determine the number of ADC counts that correspond to a given time offset between the discriminator firing and a global trigger. All PMT channels are designed to be artificially triggered by a test pedestal pulse. Charge can also be applied artificially to the pulsed channel and by varying the pulse length the charge input can also be varied. For the pedestal calibration each channel is pulsed with zero charge and a global trigger is issued to collect the ADC outputs. The charge slopes are determined by injecting increasingly more charge into each channel, each time issuing a global trigger and collecting the ADC outputs. The slope is determined from the whole series of artificially triggered events. The time slopes are determined in a similar fashion by varying the time the global trigger is issued rather than the input charge. Despite the name, the time slopes are not entirely linear. The pedestal values of the timing outputs are determined via optical calibrations. In this way

the timing through the physical PMT and PMT channel can be determined directly. PMT channels with calibration constants lying outside of the norms are flagged and ignored for most SNO analysis and specifically when performing event reconstruction. The complete description of these rejection criteria can be found in Biller et al. [46].

2.6.2 Optical calibration

The primary source of the SNO optical calibrations derives from the pulsed laser diffuser ball or laserball. A schematic of the laserball and its connection to the laser system is shown in figure 2.7. 0.6 ns-337 nm pulses are generated by the nitrogen laser at a rate of up to 45 Hz. The laser light can also be used to pump one of four dyes to produce pulses of different wavelengths. These are necessary to span the sensitivity range of the PMTs. The laser light is piped via optical fibers from the detector deck, where the laser resides, to a 10 cm diffuser ball which produces a somewhat isotropic burst of light in the detector. The full documentation on the laserball calibration source can be found in Ford [47] and Moffat [48] while a good review of SNO optical calibrations is given in Moffat et al. [49].

Relative PMT timing

The relative PMT timing offsets, effectively the timing pedestals, are determined from extended laserball calibrations taken with the diffuser ball positioned at the centre of the detector. The time spectrum of each calibration is measured and parametrized. For each event the timing offset for a given PMT is determined from the measured time, at a given pulse height, corrected for the laserball timing offset, for the same pulse height. Both of these are also corrected for photon time-of-flight from the event or laserball positions respectively.

In order to achieve the required timing resolution the laser pulse is also used to issue a special global trigger via a beam splitter and a photodiode. The standard global trigger is tied to a 50 MHz clock such that it can only occur on 20 ns intervals whereas the timing resolution of the individual PMTs can be as low as 1.5–1.7 ns. A more detailed description of the determination of the timing offsets can be found in Skensved [50].

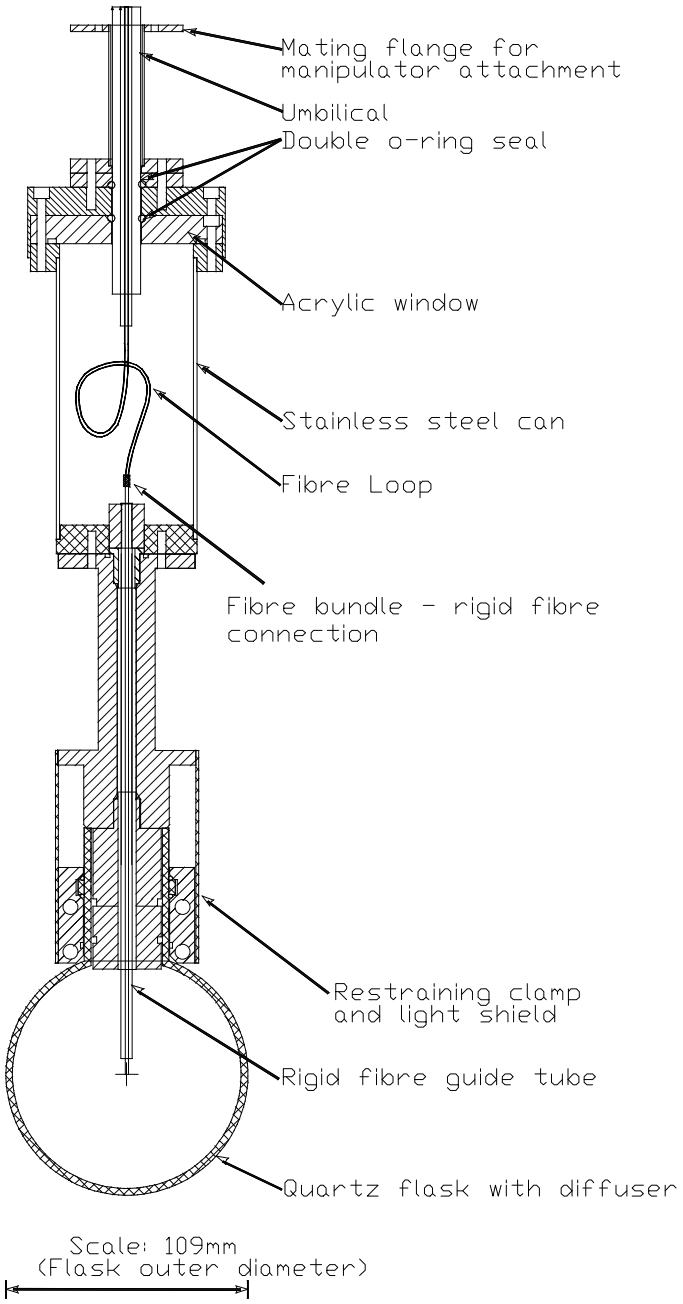

Figure 2.7: Schematic of the optical calibration source: the laserball.

The calibration source manipulator system

The response of SNO is very much position dependent. The manipulator system was developed in order to deploy calibration sources throughout the interior of the acrylic vessel. A schematic of the calibration–source manipulator system is shown in figure 2.8 with the laserball attached to the manipulator carriage. The position of the carriage in a plane is completely determined by three 1/16" Vectran ropes. All three ropes extend down from neck of the detector; the control systems being located above the deck. The central rope terminates at the top of the manipulator carriage while the side ropes feed through pulleys mounted on opposite sides of the carriage and terminate on the inner surface of the acrylic vessel as in figure 2.8. A second pair of Vectran side ropes also exist that can manipulate the carriage in an orthogonal plane. A clean, waterproof cable, called an umbilical [48], also extends from the deck above the detector to the manipulator carriage. The umbilical is a 1/2" silicone tube that can transport power, fibre-optics, and gas capillary tubes to the source and trigger signals back up to the detector electronics.

An air and light–tight glove box is mounted on the deck directly above the detector neck that permits manual manipulation of the sources such as installing and swapping the Vectran side ropes. Air and light tight flanges on the glove box also enable the extraction of the calibration sources to undergo maintenance and exchange. The control motors, rope and umbilical spools, and source chamber above the glove box flanges are purged with nitrogen gas to maintain the radon free barrier above the top of the detector, below the detector deck.

Optical model parameter extraction

In order to extract the optical parameters of the detector media and the PMTs, an optical model containing these elements is fit to laserball calibration data. In the original optical model proposed by Moffat [48], the intensity N_{ij} observed for the i^{th} run, in the j^{th} PMT, is parametrized

$$N_{ij} = N_i \Omega_{ij} R_{ij} T_{ij} L_{ij} \epsilon_j \mathrm{e}^{-(d_{\mathrm{D_2O}}\alpha_{\mathrm{D_2O}} + d_{\mathrm{acrylic}}\alpha_{\mathrm{acrylic}} + d_{\mathrm{H_2O}}\alpha_{\mathrm{H_2O}})}, \tag{2.2}$$

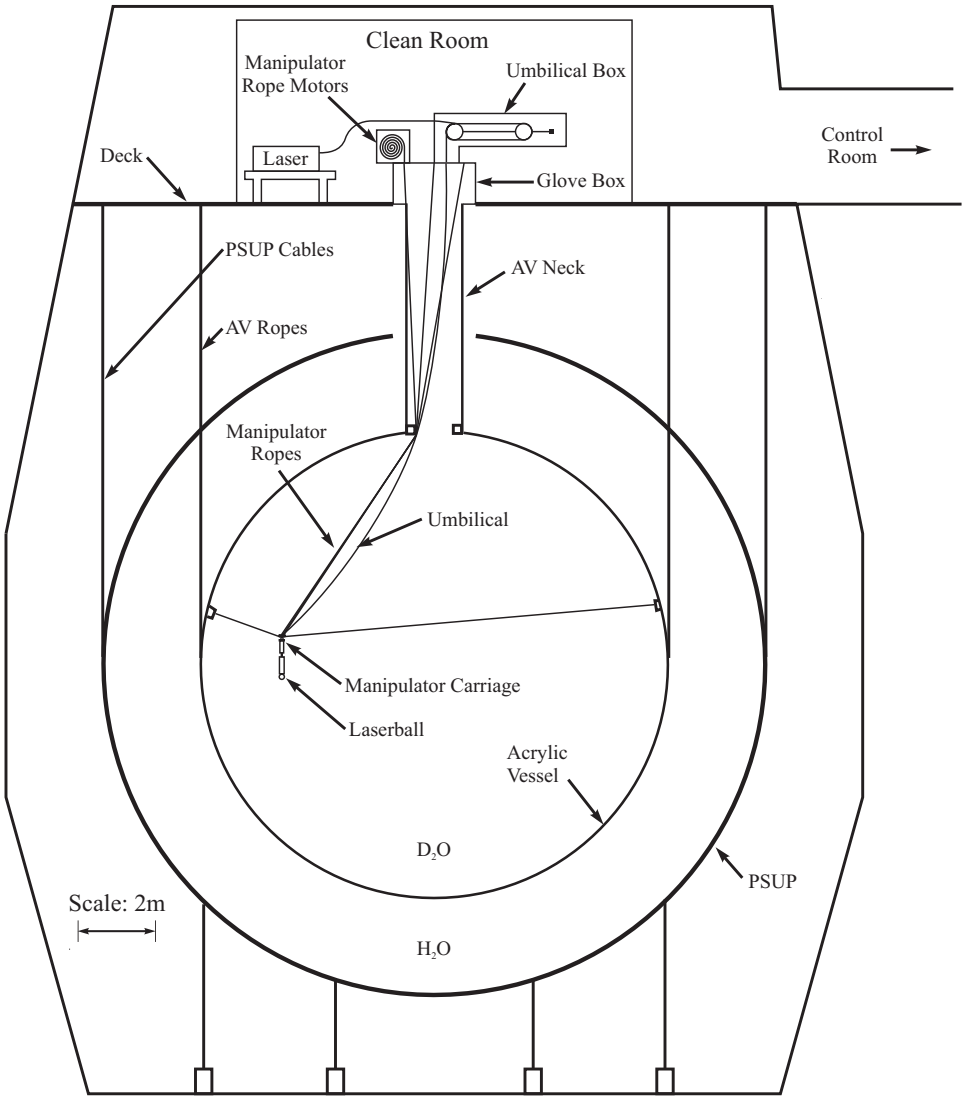

Figure 2.8: The calibration source position manipulator system shown in the laserball configuration.

where

N_i is the intensity normalization for the i^{th} run,
Ω_{ij} is the solid angle of the j^{th} PMT from the position of the i^{th} run,
R_{ij} is the PMT and reflector assembly angular response beyond that of Ω_{ij},
T_{ij} is the joint Fresnel transmission coefficient for the D_2O-acrylic and acrylic-H_2O interfaces,
L_{ij} is the intensity profile of the laser,
ϵ_j is the efficiency of the j^{th} PMT coupled with its electronics channel gain and threshold,
d_{x} is the optical path through the medium x, and
α_{x} is the inverse attenuation coefficient of the medium x.

The parameters L_{ij} and the reconstructed position of the laserball, which is also a fit parameter that is not explicitly in equation 2.2, are specific to the laserball calibration while the remaining parameters are inherent to the detector and applicable to all physics processes occurring therein. To break the many correlations between the parameters, such as the D_2O and H_2O attenuation, laserball calibrations are required to be done throughout the D_2O. To update the parameters as they change with time, such as the quality of the reflector petals surrounding the PMTs, the calibrations and optical model fit are done periodically and at the beginning and end of each phase of operation. The detector specific parameters extracted from this optical model are detailed in chapter 3 as they relate to the detector energy response.

The method of Moffat [48] normalizes the model and calibration responses (the occupancies N_{ij} of each) to the centre of the detector. This removes the individual PMT efficiencies ϵ_j that account for up to about 9000 free parameters out of a total of about 9500. A χ^2 fit between the model and calibration occupancy ratios is performed to determine the best fit model parameters. An enhanced understanding of the detector has made the effects of the PMT efficiencies significant in the detector simulation and energy calibration. The work of Simard [51] has shown that the model fit including the relative PMT efficiencies ($\epsilon_j/\bar{\epsilon}$) can be performed with enough calibration data to yield the relative PMT efficiencies as well as the other model parameters.

Radioactive source	Event type	Additional notes
^{16}N	6.13 MeV γ-ray	primary Čerenkov event calibration
^{8}Li	β-particle	isospin mirror of ^{8}B β^{+}-decay
pT	19.8 MeV γ-ray	accelerator produced
^{252}Cf	fission neutrons	primary neutron calibration
^{241}AmBe	(α, n)	
^{238}U	β–γs	
^{232}Th	β–γs	
^{222}Rn	β–γs	distributed in the D_2O or inner H_2O
^{24}Na	β–γs and pd neutrons	primarily as distributed in the D_2O

Table 2.2: The primary radioactive sources used to calibrate the response of SNO.

2.6.3 Radioactive calibration sources

A list of the radioactive sources used to calibrate SNO is presented in table 2.2. The ^{16}N, ^{8}Li, and pT sources are discussed in chapter 5 as they pertain to SNO energy calibration. The ^{222}Rn and ^{24}Na distributed sources are injected into the water in solution at various points and mixed throughout with the water circulation system. The remaining radioactive sources are encapsulated in acrylic so as not to contaminate the water. The acrylic capsules can be positioned throughout the D_2O, and below the calibration guide tubes in the H_2O, by the manipulator system, to which they are easily attached.

The ^{238}U, ^{232}Th, and ^{222}Rn sources are used to calibrate low energy β–γ events. ^{222}Rn is in the decay chain of ^{238}U therefore these calibrations differ only in their disbursement within the detector[5]. The ^{241}AmBe and ^{24}Na sources were primarily used to calibrate the response of the NCD array to neutrons. The ^{241}AmBe was required due to its high neutron production rate while the homogeneity of the ^{24}Na source was a good approximation of the expected NC neutron distribution within the D_2O.

[5]The ^{238}U, with a half-life of 4.5×10^{9} yr, decay makes a very stable encapsulated source of radiation but presents obvious difficulties when dissolved in the D_2O.

2.7 Summary

The energy response of the SNO detector, basically the number of hit PMTs or $N_{\rm hit}$, varies from point to point even within the acrylic vessel. It is essential to understand the physical and optical properties of the detector optical media and efficiency of the PMTs in order to estimate the energy of an event based primarily on $N_{\rm hit}$. To correct for the spatial variation in $N_{\rm hit}$, the optical response of the detector must be determined. The optical response of the detector to Čerenkov events is calculable from an optical model similar to that derived from equation 2.2 but with key differences; the most important being the introduction of the characteristic Čerenkov angular distribution in place of the laserball intensity profile. A further complication to the optical response of Čerenkov events is that the origin of the photons is not known with the accuracy of the laserball position. This precludes the rejection of PMTs obscured by complicated optical geometry as is done when fitting the optical model to laserball data. The response of the detector to Čerenkov events and their supplemental energy reconstruction are the focus of the following chapters.

Chapter 3

SNO energy response

SNO was designed to observe neutrinos in the ^{8}B solar neutrino energy range as presented in figure 1.1. The expected neutrino signals in D_2O are electrons up to the energy of the incident neutrino and γ-rays, emitted after neutron capture, of up to almost 9 MeV. SNO also observes high energy cosmic ray muons and atmospheric neutrinos. However, the energy deposition at these energies has a different morphology than their lower energy counterparts. SNO actually observes Čerenkov radiation from high energy electrons, either directly produced by neutrino interaction or those scattered by γ-rays. The Čerenkov photons can be attenuated, scattered, and reflected as they traverse the detector optical media before being adsorbed either by a PMT, potentially triggering a signal, or the dark space between the PMTs.

3.1 Čerenkov radiation

The first classical theory describing the physical process behind Čerenkov radiation [52] was by Frank and Tamm [53]. They considered the electromagnetic field associated with a charged particle as it travels through a medium with a constant velocity. Atomic electrons along the particle track are expected to be slightly displaced by the passage of the field, inducing temporary, local polarization. The electrons must be farther from the track than atomic dimensions or the charged particle would experience energy loss due to ionization or excitation. Other processes such as these are occurring in tandem with the emission of Čerenkov radiation and must not be ignored

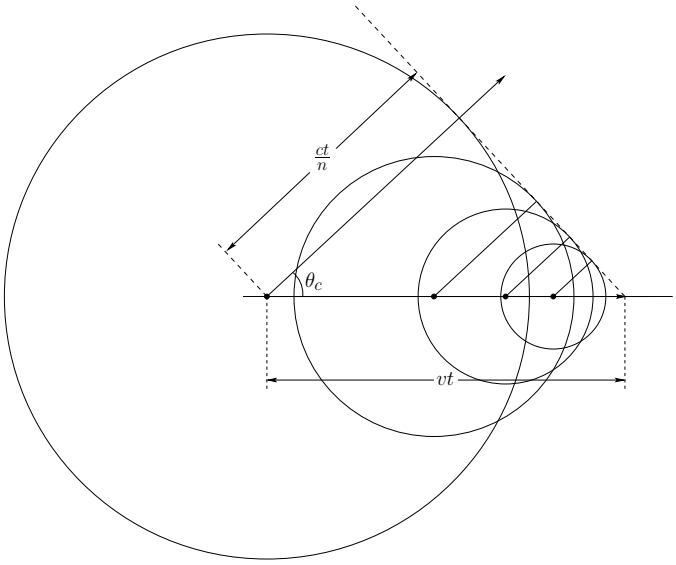

Figure 3.1: Diagram of Čerenkov radiation emitted by a charged particle traveling at a velocity v that is greater than the phase velocity of the electromagnetic field (c/n). Shown is the coherent addition of spherical wavelets from points of emission along the particle track. The relation giving the emission angle of the electromagnetic radiation (θ_c) is apparent from the geometry.

when considering the total energy loss of the charged particle.

Under most circumstances the atomic electrons simply return to their unperturbed position after the passing of the charged particle, emitting no radiation due to total destructive interference. If, however, the particle is traveling faster than the phase velocity of the electromagnetic field in the medium, some of the induced polarization can persist, appearing to be a freely oscillating dipole. The dipole produces electromagnetic radiation, which adds coherently with that emitted farther down the charged particle track. Frank and Tamm [53] derive the following expression for the angle of emission θ_c:

$$\cos\theta_c = \frac{1}{\beta n}, \tag{3.1}$$

where β is the relativistic velocity and n is the index of refraction in the medium. The derivation of this formalism is apparent from the geometry of the situation as depicted in figure 3.1.

Of particular interest is the derivation of the energy loss, $\frac{dE}{dx}$, of the charged

particle given by

$$\frac{\mathrm{d}E}{\mathrm{d}x} = \left(\frac{e}{c}\right)^2 \int\limits_{\beta n>1} \left[1 - \frac{1}{(\beta n)^2}\right] \omega \mathrm{d}\omega, \tag{3.2}$$

where the integral is done over the emitted photon frequency ω between the limits defined by the condition for Čerenkov emission:

$$\beta n(\omega) > 1.0 \tag{3.3}$$

The Čerenkov yield Y is the number of Čerenkov photons produced by the decelerating charged particle as a function of wavelength λ. The yield of a charged particle with initial kinetic energy T, which can be deduced from equation 3.2, is

$$Y(\lambda; T) = \frac{\mathrm{d}N}{\mathrm{d}\lambda} = \frac{2\pi\alpha}{\lambda^2} \int \left[1 - \frac{1}{(\beta n)^2}\right] \mathrm{d}x, \tag{3.4}$$

where α is the fine structure constant and the integral is done over the track length of the charged particle. As the charged particle decelerates its velocity eventually falls below that necessary to satisfy the Čerenkov condition (equation 3.3). This provides the upper limit to the integrand in equation 3.4.

According to Jelley [54], the energy emitted by a minimum ionizing particle as Čerenkov radiation amounts to less than 1% of that lost due to ionization. Therefore, total amount of radiation depends primarily on other more dominant mechanisms for energy loss that determine the distance over which the particle will travel. Although these tend to be more statistical processes, the average track length, and total yield, are strongly correlated with the initial velocity of the particle, specified by β in equation 3.4. The initial β is directly proportional to the initial kinetic energy of the charged particle, T. Thus Y is a function of T, although not explicitly so[1]. The average track length of a Čerenkov electron in D_2O is roughly linearly proportional to T. This implies that the Čerenkov yield of an electron in D_2O is also roughly linearly

[1] If the energy loss of the particle was a continuous function of x then the yield could be expressed explicitly as a function of T. In that case

$$\beta(x) = \beta(0) - \int_0^x \left|\frac{\partial\beta}{\partial x'}\right| \mathrm{d}x'$$

where $\beta(0)$ is directly proportional to the initial energy of the particle T, and $\frac{\partial\beta}{\partial x'}$ is proportional to $v(x')\frac{\partial E}{\partial x'}$, the product of the particle velocity and the total energy loss of the particle.

proportional to T.

3.2 An optical model of the SNO detector

If the SNO detector consisted of perfectly transmitting optical media, then the number of Čerenkov photons N_i, that would be expected to strike the i^{th} PMT, for an electron of initial kinetic energy T, can be written

$$N_i = \frac{1}{4\pi} \int \mathrm{d}\lambda\, Y(\lambda; T) \int_{S_i} D(\hat{u} \cdot \hat{p}_i'; T)\, \mathrm{d}\Omega, \tag{3.5}$$

where Y is the Čerenkov yield introduced in equation 3.4 and D is the probability of a Čerenkov photon being emitted in a direction $\hat{p}_i'$ relative to the initial electron direction $\hat{u}$. The integral over solid angle Ω is performed over the surface S_i of the i^{th} PMT. The direction $\hat{p}_i'$ is the direction in which a photon must be emitted to impact a point on S_i. This differs from the direct path $\hat{p}_i$ owing to refraction along the photon optical path.

The Čerenkov angular distribution D is shown for 8 MeV electrons in figure 3.2. If not for electron multiple scattering, D would be almost[2] a delta function at the characteristic Čerenkov angle (equation 3.1).

When the effects of the three primary optical media (D_2O, acrylic, and H_2O) are introduced, equation 3.5 becomes

$$\begin{aligned} N_i = \int \mathrm{d}\lambda\, Y(\lambda; T) \int_{S_i} & F(\lambda, \vec{r}, \vec{p}_i) \\ & \times \exp\big[-d_{\mathrm{D_2O}}(\lambda, \vec{r}, \vec{p}_i)\, \alpha_{\mathrm{D_2O}}(\lambda) \\ & \quad - d_{\text{acrylic}}(\lambda, \vec{r}, \vec{p}_i)\, \alpha_{\text{acrylic}}(\lambda) \\ & \quad - d_{\mathrm{H_2O}}(\lambda, \vec{r}, \vec{p}_i)\, \alpha_{\mathrm{H_2O}}(\lambda) \big] \\ & \times D(\hat{u} \cdot \hat{p}_i'; T)\, \mathrm{d}\Omega, \end{aligned} \tag{3.6}$$

where F is the joint probability of transmission through both surfaces of the acrylic

[2]There would still be a distribution of angles over which Čerenkov photons would be emitted since the characteristic Čerenkov angle varies with the emitted photon wavelength and as the fast electron decelerates.

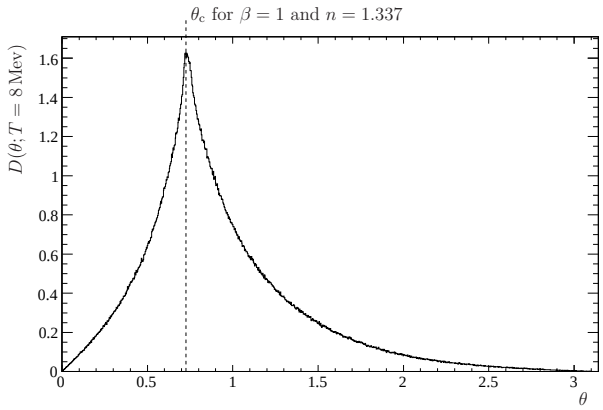

Figure 3.2: 8 MeV electron Čerenkov angular distribution in D_2O; the angle at which Čerenkov photons are emitted relative to the initial direction of the electron. The peak of the distribution is the characteristic Čerenkov angle.

vessel, d_{x} is the distance traveled through the medium x, having an inverse attenuation length α_{x}, $\vec{r}$ is the position of the electron, and $\vec{p}_i$ is a point on S_i (the surface of the i^{th} PMT). $\vec{r}$ and $\vec{p}_i$, which both originate at the centre of the detector, specify a unique optical path. Therefore, the initial direction of a photon, $\hat{p}'_i$, can be derived from $\vec{r}$ and $\vec{p}_i$, which are explicitly related to the elements of $\mathrm{d}\Omega$[3]. At this point, the electron is assumed to have emitted the Čerenkov photons from within the acrylic vessel and the complication of considering scattered or reflected light has been ignored.

Introducing the likelihood that a photon striking the PMT will trigger it, including the efficiency of the electronics channel to register the signal, equation 3.6 becomes

$$\begin{aligned} N_i = \int \mathrm{d}\lambda\, Y(\lambda;T) \int_{S_i} \epsilon_i(\lambda,\vec{r},\vec{p}_i,\hat{n}_i)\; F(\lambda,\vec{r},\vec{p}_i) \\ \times \exp\big[-d_{\mathrm{D_2O}}\,(\lambda,\vec{r},\vec{p}_i)\,\alpha_{\mathrm{D_2O}}\,(\lambda) \\ - d_{\mathrm{acrylic}}\,(\lambda,\vec{r},\vec{p}_i)\,\alpha_{\mathrm{acrylic}}\,(\lambda) \\ - d_{\mathrm{H_2O}}\,(\lambda,\vec{r},\vec{p}_i)\,\alpha_{\mathrm{H_2O}}\,(\lambda)\big] \\ \times D(\hat{u}\cdot\hat{p}'_i;T)\,\mathrm{d}\Omega, \end{aligned} \tag{3.7}$$

[3]In principle, $\hat{p}'_i$ also depends on λ since the optical path of a photon depends on the refractive indices of the detector media

where the normal vector of the front face of the PMT is $\hat{n}_i$[4], and ϵ_i is the joint PMT and associated electronics channel efficiency. In this context, ϵ_i incorporates the transmittance of the glass envelope, the wavelength sensitivity and efficiency of the photocathode, the efficiency of collecting the photoelectron, the probability of triggering the discriminator, through to the efficiency of the electronics channel readout. All of these properties vary from PMT to PMT.

The total number of PMTs expected to trigger ($N_{\rm hit}$), is then

$$N_{\rm hit} = \sum_{i=1}^{N_{\rm PMTs}} N_i \, M(N_i) \tag{3.8}$$

where the function M has been introduced to account for multiple photoelectrons, from multiple photon-photocathode interactions, in the same PMT appearing to be a single trigger. Multi-photoelectron triggered PMTs are not distinguishable from singularly triggered channels due to a lack of sufficient charge resolution in the SNO PMTs. The function M is the subject of section 4.3

One further complication neglected by this model is the effect of coherent Rayleigh scattering of Čerenkov photons. While these photons remain as likely to trigger a PMT as those that have not been scattered, the alteration of their optical path through the detector media and incidence upon a potentially different PMT is not accounted for. In practice, the majority of these photons that are scattered at large angles are rejected from analysis by utilizing only those having prompt arrival times.

3.3 A tractable optical model of the SNO detector

When measuring the optical properties of the detector it is not tractable to characterize, individually, the interaction of photons with many different wavelengths, at all incidence angles, over the entire surface of every PMT and reflector assembly. The PMTs are instead approximated by flat disks the size of the reflector housing, facing in the direction of the PMT normal at the known coordinates of the PMT. Under

[4]In principle, ϵ should also slightly sensitive to the PMT orientation about $\hat{n}$ since the PMT dynode stack is not azimuthally symmetric.

this assumption the optical model presented in equation 3.7 reduces to

$$\begin{aligned} N_i = \int \mathrm{d}\lambda\, Y(\lambda;T)\; \epsilon_i(\lambda,\vec{r},\vec{p}_i,\hat{n}_i)\, F(\vec{r},\vec{p}_i) \\ \times \exp\big[-d_{\mathrm{D_2O}}\,(\vec{r},\vec{p}_i)\,\alpha_{\mathrm{D_2O}}\,(\lambda) \\ - d_{\mathrm{acrylic}}\,(\vec{r},\vec{p}_i)\,\alpha_{\mathrm{acrylic}}\,(\lambda) \\ - d_{\mathrm{H_2O}}\,(\vec{r},\vec{p}_i)\,\alpha_{\mathrm{H_2O}}\,(\lambda)\big] \\ \times D(\hat{u}\cdot\hat{p}_i';T)\,\Omega_i\,(\vec{r},\vec{p}_i,\hat{n}_i)\,, \end{aligned} \tag{3.9}$$

where $\vec{r}$ is the reconstructed vertex, $\vec{p}_i$ is the position of the i^{th} PMT, and the integral over the PMT and reflector petal surfaces is replaced by the total solid angle of the PMT and reflector assembly Ω. Also note that the wavelength dependence of the optical path (and by association that of F), specified by the vectors $\vec{r}$ and $\vec{p}_i$, is replaced by the optical path of an average photon[5]. As in previous discussions, $\hat{p}_i'$ refers to the direction a photon would have to be emitted in, from $\vec{r}$, to strike the i^{th} PMT at $\vec{p}_i$.

The optical path of the average photon is readily calculable using wavelength averaged indices of refraction for the detector optical media. The averaged indices of refraction for the three primary optical media are presented in table 3.1. The optical path directly yields the path lengths through each medium: $d_{\mathrm{D_2O}}$, d_{acrylic}, and $d_{\mathrm{H_2O}}$. The joint probability for transmission through both interfaces of the acrylic vessel F, can be readily calculated from the Fresnel transmission coefficients. The PMT solid angle Ω, can also be determined from the optical path and the detector geometry. A Monte Carlo calculation of the Čerenkov angular distribution D is shown in figure 3.2. The measurement of the optical path lengths—$d_{\mathrm{D_2O}}$, d_{acrylic}, and $d_{\mathrm{H_2O}}$—and the PMT efficiency ϵ_i are discussed in the following sections.

3.4 PMT efficiency

The overall PMT and associated electronics channel efficiency (ϵ) was introduced in equation 3.7. It is effectively the probability that a photon, having impacted the

[5]The average photon wavelength is determined by a convolution of the PMT wavelength response with an approximation of the Čerenkov spectrum ($\frac{1}{\lambda^2}$).

Medium	Average index of refraction
D_2O	1.337
Acrylic	1.5
H_2O	1.342

Table 3.1: Indices of refraction of the primary detector media that have been averaged over a convolution of the PMT photocathode wavelength response and an approximation of the Čerenkov spectrum ($\frac{1}{\lambda^2}$).

surface of a PMT, will register as a triggered PMT in the electronics channel readout. In the simpler model described by equation 3.9, this efficiency is averaged over photons striking both the PMT and reflector assembly. Decomposing ϵ into the factors that can be determined from calibration data and Monte Carlo calculations yields

$$\epsilon_i\left(\lambda, \cos\theta_n\right) = \epsilon_\circ \cdot \epsilon'(\lambda, \cos\theta_n) \cdot E_i^{\text{optical}}(\lambda)\, E_i^{\text{electronic}}, \tag{3.10}$$

where $\epsilon_\circ$ is a free parameter representing the average PMT collection efficiency, ϵ' is the response of a typical PMT as a function of incidence angle (θ_n)[6] and wavelength (λ), and E_i^{optical} and $E_i^{\text{electronic}}$ are the relative optical and relative electronics channel efficiencies. ϵ' is further factored into $\epsilon' = \epsilon^{\text{qe}}(\lambda)E(\lambda, \cos\theta_n)$, where ϵ^{qe} is the absolute quantum efficiency of the typical PMT at normal incidence and E is the angular dependence, which is wavelength dependent. E is effectively normalized to ϵ^{qe} at normal incidence. ϵ^{qe} is also measured as a function of wavelength but with much finer resolution. In summary, $\epsilon_\circ$ and ϵ^{qe} are measured absolute efficiency factors of the typical PMT, E is the relative response of a typical PMT as a function of incidence angle, and E^{optical} and $E^{\text{electronic}}$ are the relative responses of each individual PMT and PMT electronics channel respectively.

[6] In equation 3.7 ϵ is expressed as a function of $\vec{r}$, $\vec{p}_i$, and $\hat{n}_i$, all of which are required to specify θ_n.

3.4.1 PMT relative efficiencies

The relative PMT optical efficiency E^{optical} is determined by dividing the relative channel efficiency $E^{\text{electronic}}$ out of the overall relative efficiency of each PMT E^{relative}. E^{relative} is extracted from an optical model fit to laserball calibration data. E^{relative} is, as defined by this measurement, the efficiency of registering a trigger in a PMT channel relative to the average efficiency of all PMTs that produce a viable measurement[7]. For a central laserball calibration, E^{relative} is simply

$$E_i^{\text{relative}} = \frac{n_i}{\overline{n}},$$

where n_i is the number of times the i^{th} PMT is triggered and $\overline{n}$ is the average occupancy (trigger rate) of all PMTs during the run. Unfortunately the laser diffuser ball does not emit light completely isotropically. In order to distinguish laserball anisotropies from variations in E^{relative}, optical calibrations are done at many positions throughout the D_2O. This necessitates the fit of the entire optical model to the calibration data as described in subsection 2.6.2.

The distribution of E^{relative} as measured at 420 nm during the pure D_2O phase is shown in figure 3.3. The PMT relative efficiencies are measured at six different wavelengths but were found to be generally consistent with one another. Measured as such, $E^{\text{relative}}{=}E^{\text{optical}}E^{\text{electronic}}$ for the laserball calibrations. The extraction of these fundamental optical model parameters from E^{relative} is the focus of the following sections.

PMT electronics channel relative efficiencies

The relative efficiency for each PMT channel $E^{\text{electronic}}$ is calculated for each run according to the procedure outlined by Klein [55]. $E^{\text{electronic}}$ accounts for the PMT electronics channel to channel variations from charge collection in the PMT through to the electronics readout. To calculate $E^{\text{electronic}}$ a gain–scaled average PMT charge spectrum is integrated above the threshold recorded for each PMT before every run.

[7] Direct light from the laserball can be obscured from the PMTs by complicated detector geometry. These PMTs and those for which the optical model fit returns a non-physical efficiency are assigned the average efficiency as measured by all other PMTs.

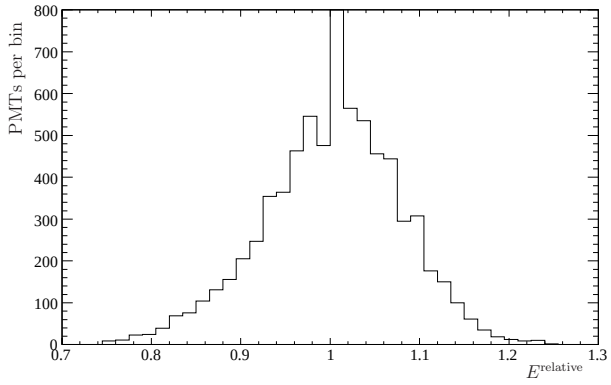

Figure 3.3: The relative PMT efficiency as determined from 420 nm laserball calibrations taken during the pure D_2O phase. The extraneous peak at unity arises from PMTs for which a measurement could not be made. Such PMTs are assigned the average relative efficiency–unity by definition.

The individual PMT gains are extracted from PMT charge spectra collected during the long central laserball calibrations used to determine the relative timing of each PMT. The charge spectra, an example of which is shown in figure 2.4, are approximated by scaling an average SNO PMT charge spectrum by the calibrated gain of each PMT. The distribution of relative channel efficiencies for a run during the pure D_2O phase is displayed in figure 3.4.

PMT relative optical efficiencies

The relative PMT optical efficiency E^{optical} is calculated for each PMT for each run by dividing out the relative PMT channel efficiency from the overall relative PMT efficiency E^{relative}. E^{optical} accounts for PMT to PMT variations in the average optical properties of the PMT and reflector assemblies and also includes the variation in ϵ^{qe} and $\epsilon_{\circ}$. E^{optical} is calculated for the i^{th} PMT for each run via

$$E_i^{\text{optical}} = \frac{E_i^{\text{relative}}}{E_{i_\circ}^{\text{electronic}}}, \tag{3.11}$$

where $E_{i_\circ}^{\text{electronic}}$ refers to $E_i^{\text{electronic}}$ as calculated for the laserball calibrations that specify E^{relative}, not that of the current run. The relative PMT optical efficiencies are

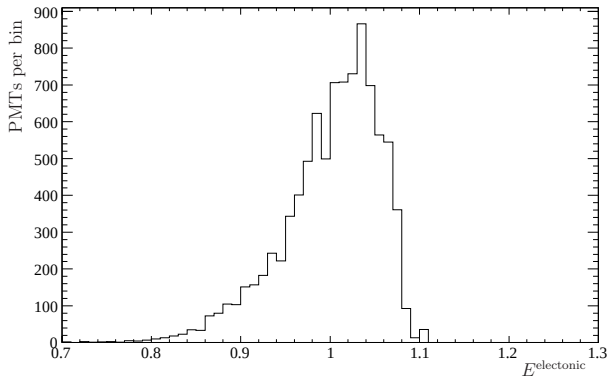

Figure 3.4: Relative PMT channel efficiencies ($E^{\text{electronic}}$) as calculated for a pure D_2O phase neutrino run.

plotted in figure 3.5 for the same run as figure 3.4.

3.4.2 PMT angular response and quantum efficiency

ϵ' can further be decomposed into

$$\epsilon'(\lambda, \cos\theta_n) = \epsilon^{\text{qe}}(\lambda) E(\cos\theta_n; \lambda),$$

where ϵ^{qe} is the absolute quantum efficiency of the PMTs at normal incidence and E is the response as a function of incidence angle. The relative PMT angular response E is determined from a combination of laserball calibration data taken at various wavelengths and Monte Carlo calculations. The absolute quantum efficiency of the PMTs ϵ^{qe} is determined from bench top measurements made at many wavelengths. The overall measured PMT angular response ϵ' consists of an interpolation of E, normalized to ϵ^{qe} at normal incidence.

PMT angular response

The average response of the PMTs as a function of incidence angle $E$is extracted from the optical model fit to laserball calibration data. It is extracted as a relative measurement. E is normalized to the response at normal incidence. For the calibration data, the incidence angle is the angle between the PMT normal and the optical

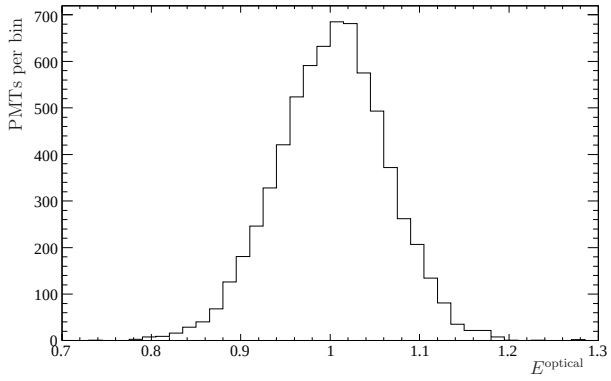

Figure 3.5: Relative PMT optical efficiency E^{optical} of a pure D_2O phase neutrino run. The efficiency is calculated by dividing the PMT relative efficiency E^{relative} by the relative channel efficiencies calculated for the calibration runs that produced E^{relative}. None of the PMTs assigned the default average relative efficiency (see figure 3.3) are included in this distribution.

path from the laser diffuser ball position to the centre of the PMT. The measurement is therefore not only an average over PMTs with similar incidence angles, but also over the surface of the PMT and PMT reflector assembly. Laserball calibration data taken within the D_2O cannot provide a measurement of E beyond about 45° owing to the geometry of the detector. A Monte Carlo calculation that is tuned to match E below is used to estimate the response above about 40°. This is adequate since precise calibration of E at these incidence angles is not required; E falls of very quickly. The PMT angular response extracted from a laserball calibration during the salt phase is presented in figure 3.6. Above 38° E is determined by Monte Carlo calculation.

The detailed optical calibration of the salt phase shows a variation in E as a function of time. The variation between two laserball calibrations performed during the salt phase is shown in figure 3.7. The change is attributed to the degradation of the reflector pedals surrounding the PMTs which caused sections of them, especially at the base near the contact with the PMT, to become less reflective. Only one detailed optical scan was performed during the pure D_2O phase so it is unclear when the reflector petal degradation began. A preliminary laserball calibration, when compared to the one detailed calibration, indicates that the angular response did change over the course of the pure D_2O phase as well [56]. However, no significant change in the

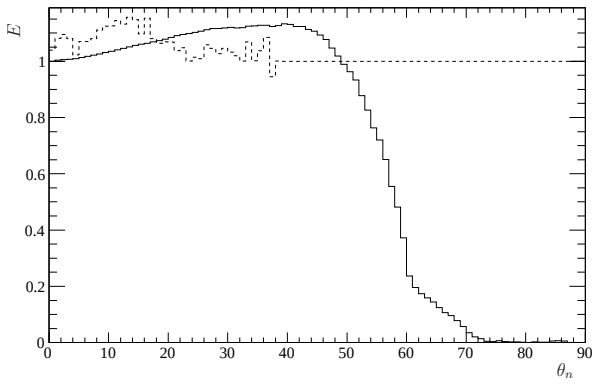

Figure 3.6: The PMT angular response as extracted from 420 nm laserball calibrations and the ratio of Monte Carlo calculations to the measurement (dashed line). The deviation from 1.0 in the ratio is scaled up by a factor of 10. The response above 38° is determined from the Monte Carlo calculations.

optical response is observed during the NCD phase.

PMT quantum efficiency

The PMT quantum efficiency ϵ^{qe} is presented in figure figure 3.8. The quantum efficiency was measured as the probability of a photon, of wavelength λ, liberating an electron from the PMT photocathode into the vacuum envelope of the PMT [57, 58]. The photoelectric current incident on the dynode stack was compared to the estimated radiation incident on photocathode by [57]. The experiment was setup such that the charge from all photoelectrons ejected from the photocathode was collected; the PMT collection efficiency was made essentially 1.0 by the wiring the PMT to act as a diode.

3.4.3 PMT global collection efficiency ($\epsilon_{\circ}$)

In equation 3.10, $\epsilon_{\circ}$ represents the PMT collection efficiency: the efficiency for photoelectrons, once liberated from the photocathode, to trigger the PMT. In practice however, $\epsilon_{\circ}$ also absorbs the residual normalization offsets of ϵ', E^{optical}, and $E^{\text{electronic}}$. The precise value of the PMT collection efficiency is difficult to determine because it requires a well calibrated source that provides a single photon counting rate in the PMTs. Estimates of the single photoelectron collection efficiency, made by [57] who

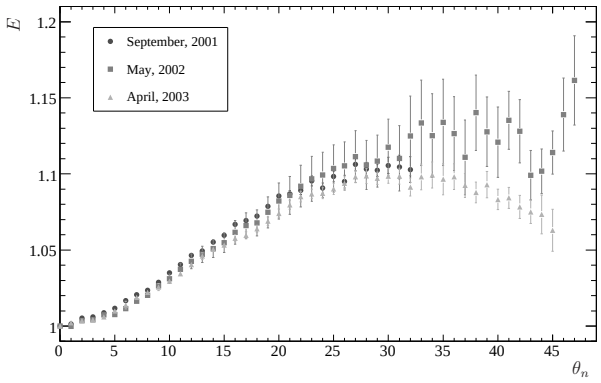

Figure 3.7: PMT angular response E as extracted from two 386 nm laserball calibrations taken during the salt phase (May 2002 and April 2003). The September 2001 calibration occurred during the pure D_2O phase.

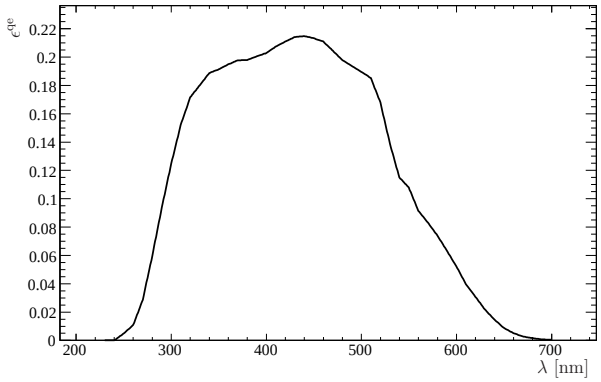

Figure 3.8: PMT quantum efficiency ϵ^{qe} defined as the probability of a photon liberating an electron from the photocathode, as measured by Boardman [57].

compared a Čerenkov light source to detailed Monte Carlo calculations, ranged from 0.55 to 0.60. Due to the proximity of the source to the test PMT and the anisotropy of Čerenkov emission, multiple photon coincidences are likely to have resulted in a low estimate of the collection efficiency [58].

The most precise and relevant measure of the collection efficiency is made with the PMTs in their final configuration, installed in the SNO detector. This is accomplished by tuning the PMT collection efficiency in a full simulation of the detector to match calibration data, including all of the other measured optical parameters and contributions to the overall PMT efficiency. The details of this calibration are discussed in section 5.3 but basically consist of comparing the mean number of triggered PMTs for a source of known energy, namely ^{16}N, to that predicted by the full detector simulation.

$\epsilon_{\circ}$ is known to vary between SNO operational phases due to changes in PMT operating voltages and improvements in the accuracy of both the measurements of the other efficiency factors and in the detector simulation. The measurement of $\epsilon_{\circ}$ for the pure D_2O, salt, and NCD phases are presented in subsections 5.6.2, 5.8.2 and 6.3.2.

3.5 Optical attenuation

Čerenkov photons are attenuated/absorbed when traversing the detector optical media, which includes the D_2O, acrylic, and H_2O. The attenuation length in D_2O and the combined attenuation length through acrylic and H_2O are extracted from the optical model fit to laserball calibrations performed throughout the D_2O. Only a combined attenuation through the acrylic, which makes up the acrylic vessel, and the H_2O can be determined from calibrations done solely within the D_2O. The acrylic attenuation is much larger than the H_2O attenuation and is assumed to be constant. The attenuation of acrylic has been measured externally (according to Moffat [48]) by the method described in Zwinkels et al. [59]. The H_2O attenuation is determined by removing the acrylic contribution from the combined attenuation. It is necessary to periodically measure the attenuation lengths as they change with the composition of the water. Two measurements of the inverse attenuation lengths, both α_{D_2O} and

α_{H_2O}, measured during the salt phase are compared to those measured during the pure D_2O phase (September 2001) in figure 3.9. Also shown is the acrylic inverse attenuations α_{acrylic} interpolated from the external measurements.

The D_2O and H_2O attenuations may be compared to those presented in figure 3.10, which were measured by Sullivan [60], Tam and Patel [61], Boivin et al. [62], Pope and Fry [63] and Sogandares and Fry [64]. Note that the vertical scale of figure 3.10a is 16 times that of figure 3.9a.

3.6 Rayleigh scattering

The Rayleigh scattering of Čerenkov photons does not necessarily prevent their detection in SNO. Rayleigh scattering increases the path length of photons to the PMTs and thus the associated transit time. Only when a timing window is applied, such as for energy reconstruction, to remove late reflected light do some Rayleigh scattered photons get rejected. It is necessary to estimate the Rayleigh scattered photons before determining their effect on energy reconstruction (see subsection 4.2.7). The standard analysis timing window is discussed in appendix A.

Coherent Rayleigh scattering was first formalized by Lord Rayleigh [65] but only for diffuse gases. It was not until Einstein's treatment in [66] that a theory relevant at liquid densities was made available. According to Einstein [66], the probability of Rayleigh scattering per unit length is

$$\frac{\mathrm{d}\sigma}{\mathrm{d}x} = \frac{8\pi^3}{27}\frac{1}{\lambda^4} k_{\mathrm{B}} T \beta_{\mathrm{T}} \left(n-1\right)^2 \left(n+2\right)^2 , \tag{3.12}$$

where k_{B} is the Boltzmann constant, and T is the temperature (11°C on average in SNO), β_{T} is the isothermal compressibility, and n is the index of refraction of the optical medium.

Two other modes of scattering considered by Moffat [48] with respect to the optics of SNO are: Mie scattering and scattering from particulate matter in the D_2O. The effects of Mie scattering are not expected to be observable as it is mainly forward peaked. Specular scattering off of contaminants in the D_2O however, scatters photons uniformly in all directions. This is not distinguishable from Rayleigh scattering in

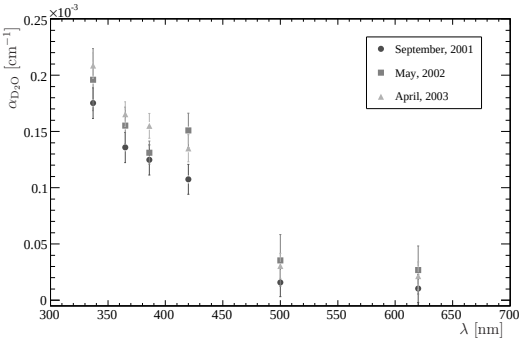

(a) D_2O.

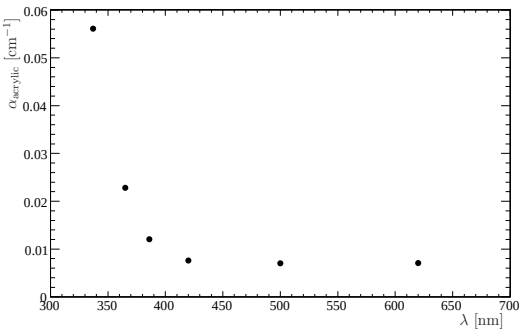

(b) Acrylic.

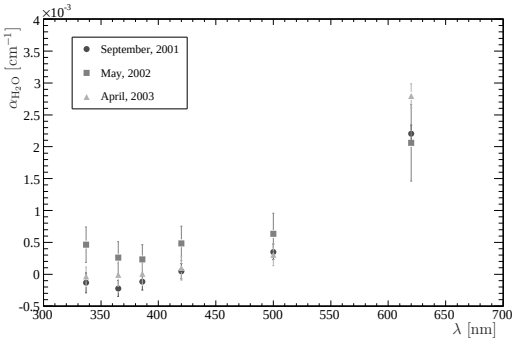

(c) H_2O.

Figure 3.9: The inverse attenuation lengths for photons in the D_2O and H_2O as extracted from the fit of an optical model to laserball calibration data taken at 337, 365, 386, 420, 500, and 620 nm. The inverse attenuation lengths through acrylic are measured externally [48]. The SNO detector was in its initial pure D_2O phase in September 2001 while the other two measurements were taken a year apart during the salt phase.

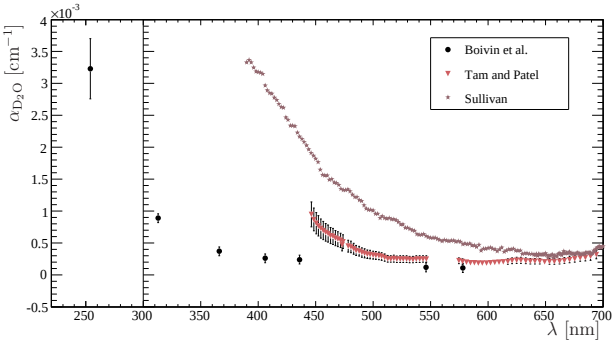

(a) D_2O.

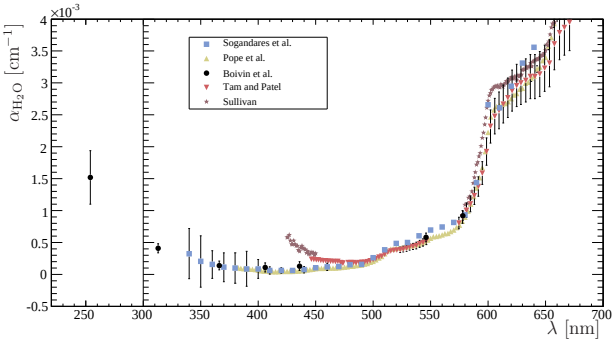

(b) H_2O.

Figure 3.10: The inverse attenuation lengths for photons in the D_2O and H_2O as measured by Sullivan [60], Tam and Patel [61], Boivin et al. [62], Pope and Fry [63] and Sogandares and Fry [64]. The measurements made by Boivin et al. [62] were conducted as proof of principle for SNO.

SNO. Therefore, a determination of the effective, scaled, Rayleigh scattering in SNO is required.

3.6.1 The measurement of effective Rayleigh scattering

The effective Rayleigh scattering length in the D_2O was measured during the salt phase[8]. A collimating mask was fitted to the diffuser ball of the optical calibration source [67]. The mask projects a beam of light only onto PMTs near the bottom of SNO. Measuring the light observed by PMTs as a function of the angle from the beam, at several wavelengths and various positions throughout the detector, a scale factor for the theoretical Rayleigh scattering length of 1.289 was defined [67] such that equation 3.12 becomes

$$\frac{\mathrm{d}\sigma}{\mathrm{d}x} = 1.289\frac{8\pi^3}{27}\frac{1}{\lambda^4}k_{\mathrm{B}}T\beta_{\mathrm{T}}\left(n-1\right)^2\left(n+2\right)^2. \tag{3.13}$$

Although it was not directly measured in either the pure D_2O or NCD phases, a scale factor of 1.0 is found to be consistent with observations made with the standard optical and energy calibration sources.

3.7 Summary

The fundamental measure of energy in SNO is the number of Čerenkov photons generated by electrons. What SNO actually observes is the number of PMTs triggered (N_{hit}) by some fraction of these photons. In order to reconstruct the energy of a Čerenkov light emitting electron, N_{hit} must be extrapolated back through the detector media using an optical model to estimate the initial number of photons. In order to make use of the optical model, the parameters must first be determined.

Many of the optical parameters depend on the path that photons take to the PMTs. The optical path is determined from the event position $\vec{r}$, the position of a given PMT $\vec{p}$, and the geometry of the detector. The determination of the optical path also yields the initial direction of a photon $\hat{p}$ that ensures it will hit the PMT, the incidence angles on the D_2O-acrylic and acrylic-H_2O interfaces, and the incidence

[8]The calibration device was not completely developed until the salt phase.

angle of impact on the PMT. Then, from the optical paths to each PMT, the distance traveled by photons through each medium (d), the Fresnel coefficients for transmission through the AV (used to calculate F), and the solid angle (Ω) of the PMTs can be determined. The determination of these parameters for use in energy reconstruction is detailed in the following chapter.

The Čerenkov angular distribution (D) and the Rayleigh scattering rejection probability (P) are determined from Monte Carlo calculations. The measurement of the attenuation lengths (α) and PMT efficiencies (ϵ) are determined from an optical model fit to laserball calibration data, with the exception of the global collection efficiency ($\epsilon_{\circ}$). The calibration of $\epsilon_{\circ}$ using the ^{16}N source is discussed in chapter 5.

The optical model presented in this chapter includes the primary photon interactions within SNO. It does not incorporate the complicated optics of acrylic vessel support ropes, D_2O plumbing, the chimney acrylic[9], or late light from reflections or Rayleigh scattering. The contribution of these detector components are expected to be small and the fraction of photons passing through the chimney are small for the average event. These have been selectively disregarded as they are also not considered in the reconstruction and calibration of event energy presented in the following chapters.

[9]The acrylic in the chimney not only complicates the geometry of photon optical paths but also transmission. The acrylic that makes up the chimney was specially selected to prevent piping of light down into the inner sensitive region of the detector.

Chapter 4

SNO event energy reconstruction

The event energy reconstruction algorithm RSP was originally developed by Boulay [68]. The original RSP corrects the number of PMTs triggered, within a 10 ns prompt time window (see appendix A), to that which would be observed had the event occurred at the centre of the detector. The prompt, noise–corrected number of triggered PMTs (N_{eff}) is corrected to the number expected had the event occurred at the centre of the detector (N_{cor}) via

$$N_{\text{cor}} = N_{\text{eff}} \frac{R^{\text{centre}}}{R} \cdot \frac{N_{\text{PMTs}}}{N_{\text{working}}}, \tag{4.1}$$

where R is the optical response of the detector, N_{PMTs} is the total number of PMTs, and N_{working} is the number of PMTs working at the time the event occurred (determined on a run-by-run basis). Detailed detector simulations of monoenergetic electrons are used to create a map from N_{cor} to an effective electron energy: T_{eff}.

Given the reconstructed position and direction of an event, RSP is able to calculate R analytically. The original RSP divides approximately 70% of the detector, optimized around the event direction to include most of the Čerenkov light cone[1], into 100 angular bins as seen from the event position. It assumes that the detector is uniformly instrumented with identical PMTs and calculates R for a PMT at the centre of each angular bin. The original RSP is thus unable to account for local

[1]To be specific, the original RSP includes the range of 0.2–2.0 rad from the event direction (see figure 3.2).

variations in the detector energy response such as PMT to PMT efficiency variations or the location of disabled or malfunctioning PMTs.

A new energy response processor, hereafter referred to as RSP while the RSP discussed above will be referred to as the "original RSP" was developed by the author to include a more precise optical model that accounts for more of the elements presented in equation 3.9. Again the energy reconstruction is based on $N_{\rm eff}$ and the reconstructed position and direction of an event. As opposed to the optical response calculated by the original RSP, the new RSP optical response includes not only the number of triggered PMTs but the response characteristics of each PMT individually. This is achieved by calculating the optical response of every PMT rather than for a number of angular regions. This also enables a more accurate determination of the multi-photoelectron correction.

The most basic experimental measure of event energy in SNO is the number of PMTs triggered by an event: $N_{\rm hit}$. The fundamental measure of event energy in SNO is the number[2] of Čerenkov photons produced by electrons. The energy reconstruction discussed in the following sections attempts to determine the number of photons N_γ produced by an electron that results in a prediction of the number of triggered PMTs equal to that observed ($N_{\rm eff}$). An estimate of the event energy $T_{\rm eff}$ can then be derived from a one-to-one relationship between electron kinetic energy $T_{\rm e}$ and mean N_γ via the energy calibration function $\mathcal{F}_E : N_\gamma \rightarrow T_{\rm e}$[3].

4.1 The new RSP algorithm

For the initial estimate of event energy $T_{\rm eff}$, an initial estimate of N_γ can be calculated via the energy calibration function:

$$\mathcal{F}_E : N_\gamma \rightarrow T_{\rm e} \qquad \text{or more precisely} \qquad \mathcal{F}_E^{-1} : T_{\rm e} \rightarrow N_\gamma. \tag{4.2}$$

[2]The spectrum of Čerenkov radiation is not energy dependent other than near the Čerenkov threshold.

[3]$\mathcal{F}_E$ is derived for events in which only a single electron, of energy $T_{\rm e}$, produces Čerenkov light in the detector. The energy of an event that follows from $\mathcal{F}_E$ is therefore referred to as $T_{\rm eff}$ since it is the effective energy of the event assuming that all of the light results from the track of a single electron.

These N_γ photons are assumed to have an inverse square spectral distribution as a function of wavelength. This is what would be expected from equation 3.4 for a constant index of refraction. The number of photons (always less than 1.0) expected to trigger the i^{th} PMT N_i is calculated

$$N_i = N_\gamma \frac{\sum_\lambda R_i\left(\lambda, \vec{r}, \hat{u}\right) \frac{1}{\lambda^2}}{\sum_\lambda \frac{1}{\lambda^2}}, \tag{4.3}$$

where R_i is the response of the i^{th} PMT to a photon of wavelength λ. The sum over λ is done in 10 nm steps from 220 to 710 nm, the wavelength range over which the detector is sensitive. This may be compared to equation 3.9. In this case, an average index of refraction is used rather than the true wavelength dependent one. This enables the Čerenkov yield to be replaced by a constant normalization (N_γ) weighted by an approximate Čerenkov spectral dependence.

The total number of PMT hits predicted by RSP is then

$$N_{\text{predicted}} = \sum_i^{N_{\text{working}}} N_i M\left(N_i\right), \tag{4.4}$$

where M_i is a correction function that accounts for the possibility of multiple photons counting as a single trigger and the sum is over all functioning and properly calibrated PMTs (N_{working})[4]. This predicted number of direct[5] photons calculated is then compared to the number of prompt, noise-corrected, triggered PMTs that were observed (N_{eff}), be they in the data or a full detector simulation. N_{eff} is calculated

$$N_{\text{eff}} = N_{\text{win}} - N_{\text{dark}},$$

where N_{win} is the number of promptly triggered PMTs and

$$N_{\text{dark}} = R_{\text{noise}} \cdot 20\,\text{ns} \cdot N_{\text{working}}.$$

[4]A PMT is considered working by RSP if it is on (has high voltage applied and triggers enabled), has valid time, gain, and electronics calibration constants, and passes a number of offline data quality tests. See McCauley [69] and Huang et al. [70] for a robust listing.

[5]Neither RSP nor N_{win} (N_{win} by definition) consider reflected photons.

R_{noise} is the noise rate per PMT as estimated from the pulsed global trigger.

The initial estimate of the number of photons N_γ is then modified

$$N_\gamma \rightarrow \frac{N_{\text{eff}}}{N_{\text{predicted}}} N_\gamma, \tag{4.5}$$

and the process is iterated until agreement is reached between $N_{\text{predicted}}$ and N_{eff}.

From the final estimate of N_γ, T_{eff} is determined via $\mathcal{F}_E$. N_γ is stored along with T_{eff} for use in energy calibration before $\mathcal{F}_E$ has been precisely determined. The derivation of the energy calibration function from detailed Monte Carlo simulations is discussed in section 4.5.

4.2 The RSP optical response

The optical response R of a given PMT is calculated based on the optical model presented in equation 3.9. In this case however, the integration of the Čerenkov yield appears elsewhere (in equation 4.3) as discussed in the previous section. RSP calculates R for the i^{th} PMT

$$\begin{aligned} R_i(\lambda, \vec{r}, \hat{u}, \vec{p}_i, \hat{n}; T) = \epsilon_i(\lambda, \vec{r}, \vec{p}_i, \hat{n})\ \Omega_i\left(\vec{r}, \vec{p}_i, \hat{n}\right)\ D(\hat{u}, \vec{r}, \vec{p}_i; T) \\ \times F(\vec{r}, \vec{p}_i) \exp\left(\sum_{m=1}^{3} -d_m\left(\vec{r}, \vec{p}_i\right) \alpha_m\left(\lambda\right)\right) \end{aligned} \tag{4.6}$$

where, as is detailed for equation 3.9, λ is photon wavelength, $\vec{r}$ and $\hat{u}$ are the event position (with respect to the centre of the detector) and direction vectors, and $\vec{p}_i$ and $\hat{n}_i$ are the position and normal vectors of the PMT, the media $m = (D_2O,\ \text{acrylic},\ H_2O)$,

- ϵ is the PMT efficiency as defined in section 3.4,
- Ω is the fraction of solid angle that the collection area of the PMT subtends as described in subsection 4.2.6,
- D is the Čerenkov angular distribution function presented in subsection 4.2.5,
- F is the joint probability of transmission through the acrylic vessel discussed in subsection 4.2.4,

d are the average photon path lengths through each medium as calculated in the following section, and

α are the inverse attenuation coefficients described in section 3.5.

The value of T is determined from $\mathcal{F}_E$, with the corresponding value of N_γ, via equation 4.3.

The photon optical path is defined as the path a photon takes from its point of creation at $\vec{r}$ through the acrylic vessel to the centre of the PMT located at $\vec{p}$. The derivation of the optical path in the following section yields the initial direction $\hat{p}'$ and angle of incidence on the inner surface of the acrylic vessel θ_{i_1}. The optical path and the normal vector of the PMT $\hat{n}$ yield the angle of incidence on the PMT θ_n. With these definitions the following simplifications may be made:

$$\begin{aligned}
\epsilon(\lambda, \vec{r}, \vec{p}, \hat{n}) &\rightarrow \epsilon(\lambda, \cos\theta_n); \\
F(\vec{r}, \vec{p}) &\rightarrow F(\cos\theta_{i_1}); \\
D(\hat{u}, \vec{r}, \vec{p}; T) &\rightarrow D(\hat{u}\cdot\hat{p}'; T); \text{ and} \\
\Omega_i(\vec{r}, \vec{p}, \hat{n}) &\rightarrow \Omega_i(\vec{r}, \hat{p}', \cos\theta_n).
\end{aligned}$$

4.2.1 The average photon optical path

The optical path from the point of photon creation to a given PMT is required in order to calculate the distances d_x through the detector optical media, the initial direction $\hat{p}'$ of the photon, the angle of incidence upon the D_2O-acrylic interface θ_{i_1}, and the incidence angle on the PMT θ_n. Assuming a spherically symmetric acrylic vessel, the optical path a photon has to travel from its creation at $\vec{r}$ to intersect a PMT, with position and orientation given by $\vec{p}$ and $\hat{n}$, is completely determined by $\vec{r}$ and $\vec{p}$ and the radius and thickness of the acrylic vessel[6]. However, even knowing the originating and final positions of a photon, ascertaining its exact path to a PMT requires an iteration about the initial photon direction $\hat{p}'$.

The optical path of a photon is schematically shown in figure 4.1 as the dashed lines. The photon is assumed to have been created at the reconstructed event vertex:

[6]In principle the path of the photon also depends on the average direction of the electron in so much as it dictates the polarization of the photon.

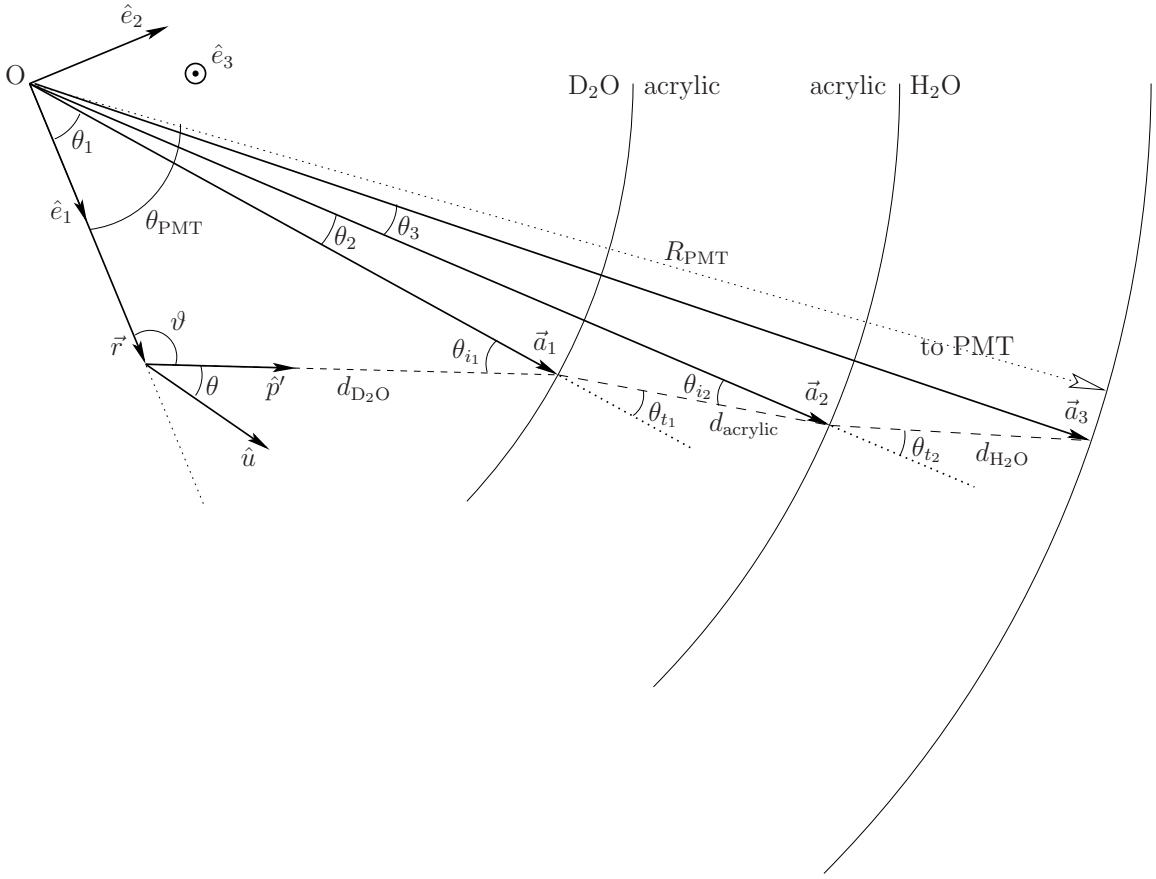

Figure 4.1: A schematic of the optical path of a photon, the dashed line, from a reconstructed event vertex at $\vec{r}$, to the PMT array. The reconstructed event direction is shown as the vector $\hat{u}$, although it need not be in the plane of the figure. The derivation of each parameter appears in the text. Note also that $\vec{p}$, as it appears in the text, is the vector from the origin (O) to the PMT.

$\vec{r}$. The reconstructed event direction is also indicated in the figure by $\hat{u}$. For the first iteration, the direction of the photon $\hat{p}'$ is chosen to be the direction of the PMT from $\vec{r}$: $\vec{p} - \vec{r}$. The photon travels to an intersection with the acrylic vessel at $\vec{a}_1$. From there it traverses the acrylic to $\vec{a}_2$, striking the PMT array at $\vec{a}_3$. However, as shown in figure 4.1, $\vec{a}_3$ does not initially correspond to the position of the PMT. Therefore, the initial direction of the photon is adjusted accordingly.

The Numerical Recipes [71] routine *rtsafe*[7] is used to determine the root of

$$f(\vartheta) = \theta_{\mathrm{PMT}} - \theta_1(\vartheta) - \theta_2(\vartheta) - \theta_3(\vartheta), \tag{4.7}$$

where $\vartheta = \pi - \arccos(\hat{p}' \cdot \hat{r})$. The direction $\hat{p}'$ that corresponds to $f = 0$ is the direction that the photon has to travel to strike the PMT: when $\vec{a}_3$ terminates at the desired PMT. A more convenient form of equation 4.7 that is actually implemented in the RSP optical response is

$$f'(\vartheta) = \cos\theta_{\mathrm{PMT}} - \cos\theta_1(\vartheta) - \cos\theta_2(\vartheta) - \cos\theta_3(\vartheta). \tag{4.8}$$

The root of the f' is necessarily the same as that of f for $\vartheta \in [0, \pi]$.

The value of $\cos\theta_{\mathrm{PMT}}$ is calculated

$$\cos\theta_{\mathrm{PMT}} = \hat{p} \cdot \hat{r}, \tag{4.9}$$

where $\vec{p}$ [8] is the vector from the event vertex $\vec{r}$ to the PMT. The functions θ_1, θ_2, and θ_3 are derived below. The derivatives of the functions—θ_1, θ_2, and θ_3—are also required by the Newton-Raphson root finding method but follow directly from these functions.

In the following derivations, the magnitudes of the vectors $\vec{a}_1$, $\vec{a}_2$, and $\vec{a}_3$ are the inner radius of the acrylic vessel, the outer radius of the acrylic vessel, and the radial coordinate of the PMT (R_{AV}, $R_{\mathrm{H_2O}}$, and R_{PMT} in the figure). The coordinate system $\hat{e}_i$ is chosen such that the origin and the event and PMT positions are all constrained

[7] The Numerical Recipes [71] routine *rtsafe* determines the root of a function using a combination of the Newton-Raphson and bisection methods; the latter when the former encounters a local extremum.

[8] Typically, $\hat{v} = \vec{v}/|\vec{v}|$.

to the $\hat{e}_1$-$\hat{e}_2$ plane: the plane of figure 4.1.

Determination of $\cos\theta_1$

From figure 4.1, the law of cosines yields the relation for $\cos\theta_1$:

$$d^2_{\mathrm{D_2O}} = R^2_{\mathrm{AV}} + r^2 - 2R_{\mathrm{AV}} r\cos\theta_1.$$

From the same triangle, the law of cosines also yields

$$R^2_{\mathrm{AV}} = r^2 + d^2_{\mathrm{D_2O}} + 2r d_{\mathrm{D_2O}}(\hat{p}\cdot\hat{r}),$$

which can be solved for $d_{\mathrm{D_2O}}$. $\cos\theta_1$ is then found to be

$$\cos\theta_1 = \frac{r}{R_{\mathrm{AV}}}\sin^2\vartheta + \cos\vartheta\sqrt{1-\left(\frac{r}{R_{\mathrm{AV}}}\right)^2\sin^2\vartheta}, \tag{4.10}$$

where again, $\vartheta = \pi - \arccos(\hat{p}'\cdot\hat{r})$.

Determination of $\cos\theta_2$

Again from figure 4.1, the law of cosines yields

$$d^2_{\mathrm{acrylic}} = R^2_{\mathrm{H_2O}} + R^2_{\mathrm{AV}} - 2R_{\mathrm{H_2O}} R_{\mathrm{AV}}\cos\theta_2.$$

From the same triangle, the law of cosines also yields

$$R^2_{\mathrm{H_2O}} = R^2_{\mathrm{AV}} + d^2_{\mathrm{acrylic}} + 2R_{\mathrm{AV}} d_{\mathrm{acrylic}}\cos\theta_{t_1},$$

which can be solved for d_{acrylic}. With the D_2O and H_2O indices of refraction $n_{\mathrm{D_2O}}$ and n_{acrylic} the application of Snell's law at the D_2O-acrylic interface yields

$$n_{\mathrm{D_2O}}\sin\theta_{i_1} = n_{\mathrm{acrylic}}\sin\theta_{t_1}, \tag{4.11}$$

relating θ_{t_1} to θ_{i_1}. Finally, from the law of sines

$$\left(\frac{\sin\theta_{i_1}}{r}\right)^2 = \left(\frac{\sin\vartheta}{R_{\mathrm{AV}}}\right)^2 \tag{4.12}$$

which relates θ_{i_1} to ϑ, $\cos\theta_2$ is found to be

$$\begin{aligned}\cos\theta_2 = &\left(\frac{n_{\mathrm{D_2O}}}{n_{\mathrm{acrylic}}}\right)^2 \frac{r^2}{R_{\mathrm{AV}}R_{\mathrm{H_2O}}}\sin^2\vartheta \\ &+ \sqrt{1-\left(\frac{n_{\mathrm{D_2O}}}{n_{\mathrm{acrylic}}}\frac{r}{R_{\mathrm{AV}}}\sin\vartheta\right)^2}\sqrt{1-\left(\frac{n_{\mathrm{D_2O}}}{n_{\mathrm{acrylic}}}\frac{r}{R_{\mathrm{H_2O}}}\sin\vartheta\right)^2}.\end{aligned} \tag{4.13}$$

Determination of $\cos\theta_3$

Again from figure 4.1, the law of cosines yields:

$$d^2_{\mathrm{H_2O}} = R^2_{\mathrm{PMT}} + R^2_{\mathrm{H_2O}} - 2R_{\mathrm{PMT}}R_{\mathrm{H_2O}}\cos\theta_3.$$

From the same triangle, the law of cosines also yields

$$R^2_{\mathrm{PMT}} = R^2_{\mathrm{H_2O}} + d^2_{\mathrm{H_2O}} + 2R_{\mathrm{H_2O}}d_{\mathrm{H_2O}}\cos\theta_{t_2};$$

which can be solved for $d_{\mathrm{H_2O}}$. With the acrylic and H_2O indices of refraction n_{acrylic} and $n_{\mathrm{H_2O}}$ Snell's law evaluated at the acrylic-H_2O interface yields

$$n_{\mathrm{acrylic}}\sin\theta_{i_2} = n_{\mathrm{H_2O}}\sin\theta_{t_2} \tag{4.14}$$

relating θ_{t_2} to θ_{i_2}. From the law of sines

$$\left(\frac{\sin\theta_{i_2}}{R_{\mathrm{AV}}}\right)^2 = \left[\frac{\sin\left(\pi-\theta_{t_1}\right)}{R_{\mathrm{H_2O}}}\right]^2 \tag{4.15}$$

relates θ_{i_2} to θ_{t_1}. With equations 4.11 and 4.12, θ_{i_2} can be related to ϑ as above. Then $\cos\theta_3$ is found to be

$$\cos\theta_3 = \left(\frac{n_{D_2O}}{n_{H_2O}}\right)^2 \frac{r^2}{R_{AV}R_{PMT}}\sin^2\vartheta + \sqrt{1-\left(\frac{n_{D_2O}}{n_{H_2O}}\frac{r}{R_{AV}}\sin\vartheta\right)^2}\sqrt{1-\left(\frac{n_{D_2O}}{n_{H_2O}}\frac{r}{R_{PMT}}\sin\vartheta\right)^2}. \tag{4.16}$$

4.2.2 Average optical path lengths

Finding the root of equation 4.8 yields the direction $\hat{p}'$ that a photon must be emitted to hit the centre of the PMT. The incidence angles on each of the dielectric boundaries, θ_{i_1} and θ_{i_2} are found from

$$\cos\theta_{i_1} = \hat{p}' \cdot \hat{a}_1 \tag{4.17}$$

and

$$\cos\theta_{i_2} = \frac{(\vec{a}_2 - \vec{a}_1)\cdot\hat{a}_2}{|\vec{a}_2 - \vec{a}_1|.} \tag{4.18}$$

From figure 4.1, the vector from the origin O to the inner surface of the acrylic vessel is

$$\vec{a}_1 = R_{AV}(\cos\theta_1\hat{e}_1 + \sin\theta_1\hat{e}_2). \tag{4.19}$$

Then the distance the photon travels through D_2O is

$$d_{D_2O} = |\vec{a}_1 - \vec{r}\,|. \tag{4.20}$$

The vector from the origin to the outer surface of the acrylic vessel is

$$\vec{a}_2 = R_{H_2O}(\cos\theta_2\hat{e}_1 + \sin\theta_2\hat{e}_2). \tag{4.21}$$

The distance the photon travels through acrylic is then

$$d_{\text{acrylic}} = |\vec{a}_2 - \vec{a}_1\,|. \tag{4.22}$$

The vector from the origin to the PMT is

$$\vec{a}_3 = R_{\rm PMT}(\cos\theta_3\hat{e}_1 + \sin\theta_3\hat{e}_2) = \vec{p}. \tag{4.23}$$

The distance the photon travels through H_2O is

$$d_{\rm H_2O} = |\vec{a}_3 - \vec{a}_2\,| = |\vec{p} - \vec{a}_2, |. \tag{4.24}$$

4.2.3 Optical path-PMT incidence angle

The direction that each PMT faces is not precisely the centre of the detector (O in figure 4.1). Arrays of 7 to 21 PMTs are mounted perpendicularly on flat panels that attach to the PSUP. The array panels are installed to face the centre of the detector O. Therefore, the normal vectors ($\hat{n}$) of the PMTs are the normal vectors of the panels to within the degree to which the PMTs face perpendicular to the plane of the panel array on which they are mounted. Figure 4.2 highlights the average optical path-PMT incidence angle (θ_n) using the same labels as figure 4.1. The PMT normal is indicated by the vector $\hat{n}$. θ_n is calculated from

$$\cos\theta_n = \frac{(\vec{a}_3 - \vec{a}_2)\cdot\hat{n}}{|\vec{a}_3 - \vec{a}_2\,|}, \tag{4.25}$$

where the derivations of the vectors appear in the previous section.

4.2.4 The transmission probability

The joint probability of a photon being transmitted through both interfaces of the acrylic vessel is calculated from the Fresnel coefficients [72]. The transmission coefficient $t_\parallel$ for a photon with its electric field parallel to the plane of incidence is given by

$$t_\parallel = \frac{2n_i\cos\theta_i}{n_i\cos\theta_t + n_t\cos\theta_i}, \tag{4.26}$$

where the subscripts on n_i and n_t denote the incident and transmitting media, and on θ_i and θ_t the incidence and transmitted angle of the photon from the normal of the interface. The transmission coefficient $t_\perp$ for a photon with its electric field

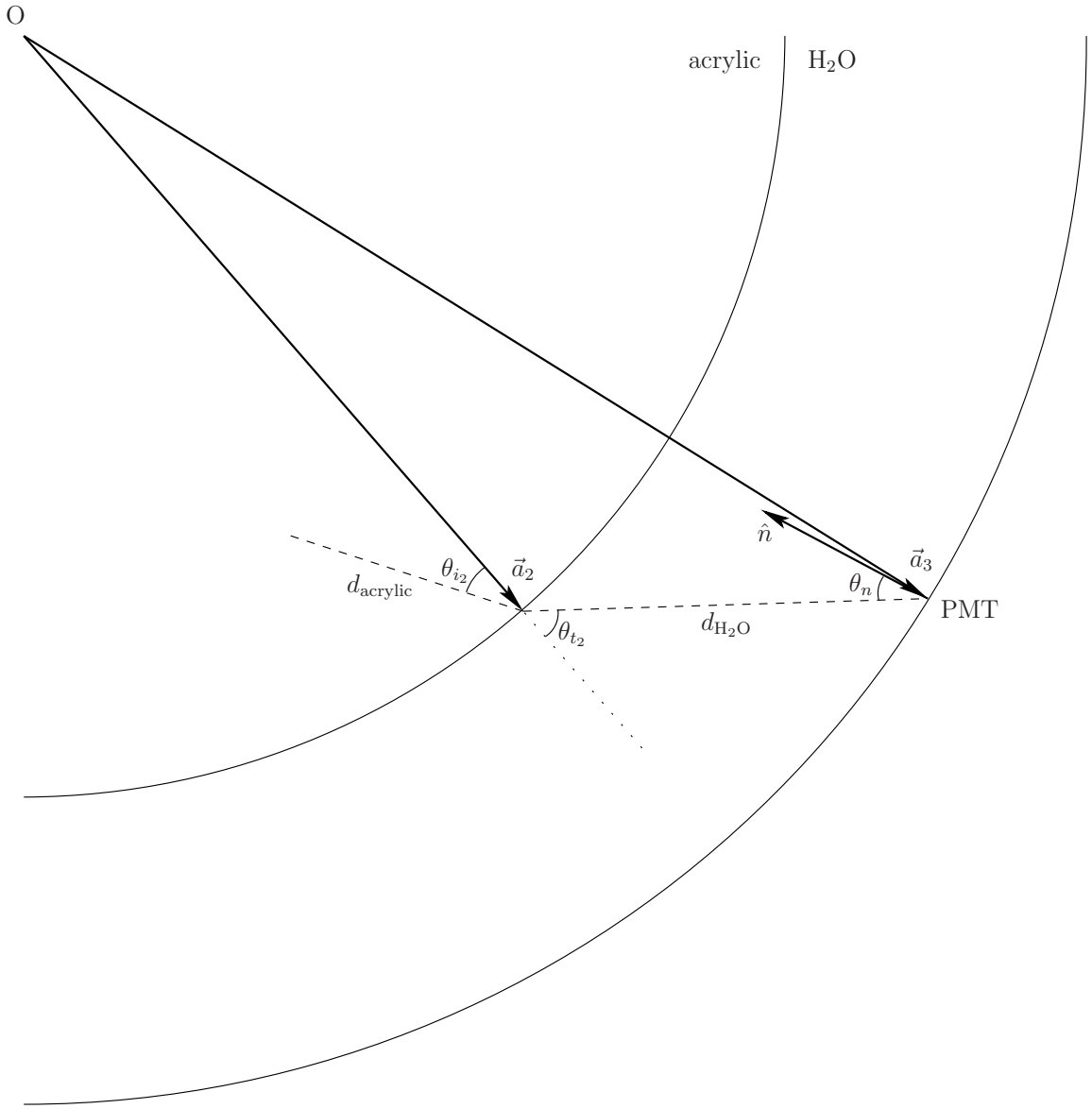

Figure 4.2: The optical path (dashed line) of an average photon from the acrylic vessel to a PMT. A subset of figure 4.1 highlighting the optical path-PMT incidence angle: θ_n.

perpendicular to the plane of incidence is given by

$$t_\perp = \frac{2n_i \cos\theta_i}{n_i \cos\theta_i + n_t \cos\theta_t}. \tag{4.27}$$

As a photon is likely neither to have its electric field completely parallel nor completely perpendicular to the plane of incidence, the transmission coefficients have to be modified such that

$$\begin{aligned} t_\parallel &\rightarrow t_\parallel \cos\phi \qquad \text{and} \\ t_\perp &\rightarrow t_\perp \sin\phi, \end{aligned}$$

where ϕ is the angle between the plane of incidence and the plane containing the electric field. The sign of the angle ϕ, or of the transmission coefficients, is irrelevant since the transmission probability or transmittance F is given by

$$F_{\parallel/\perp} = \frac{n_t \cos\theta_t}{n_i \cos\theta_i} t^2_{\parallel/\perp}, \tag{4.28}$$

where the subscript $\parallel$ / $\perp$ denotes either the parallel or perpendicular case.

Then from figure 4.1, the probability of transmission through the D_2O-acrylic interface is

$$F_1(\theta_{i_1}, \phi) = \left(\frac{n_{\text{acrylic}}}{n_{D_2O}} \frac{\cos\theta_{t_1}}{\cos\theta_{i_1}} \right) \left(t^2_{\parallel_1} \cos^2\phi + t^2_{\perp_1} \sin^2\phi \right), \tag{4.29}$$

where the subscripts 1 on F, $t_\parallel$, and $t_\perp$ indicate that they are all for the first intersection of the optical path with a dielectric boundary, and the angle ϕ is given by

$$\cos\phi = (\hat{u} \times \hat{p}') \cdot \hat{e}_3. \tag{4.30}$$

$\hat{u} \times \hat{p}'$ is the normal to the plane containing the electric field of the photon[9] and $\hat{e}_3$ is the normal to the plane of incidence: the plane of figure 4.1.

Using the parallel and perpendicular components of the photon electric field that are transmitted through the first interface of the acrylic vessel from equation 4.28

[9] Čerenkov light is polarized in the plane containing the trajectory of the electron and the direction of observation.

and equation 4.29, the combined transmission probability through both interfaces is

$$F(\theta_{i_1}, \phi) = \left(\frac{n_{\mathrm{H_2O}}}{n_{\mathrm{D_2O}}} \frac{\cos\theta_{t_1}}{\cos\theta_{i_1}} \frac{\cos\theta_{t_2}}{\cos\theta_{i_2}} \right) \left(t_{\parallel_1}^2 t_{\parallel_2}^2 \cos^2\phi + t_{\perp_1}^2 t_{\perp_2}^2 \sin^2\phi \right), \tag{4.31}$$

where $t_{\parallel_{1/2}}$ and $t_{\perp_{1/2}}$ are calculated via equations 4.26 and 4.27 and 1/2 refers to either the D_2O-acrylic or the acrylic-D_2O interface respectively. Of all the incidence and transmission angles in equation 4.31, only θ_{i_1} appears as an argument of F as the others can all be reduced to functions of θ_{i_1} and the indices of refraction.

One major caveat to the preceding argument is that the electron trajectory at the instant of photon emission is not known. Only the average electron trajectory could be determined even if the angular resolution and vertex reconstruction were perfect. In other words, the reconstructed event direction $\hat{u}$ is not the direction that the electron is traveling when it emits each photon; it is at best the average direction.

4.2.5 The Čerenkov angular distribution function

The Čerenkov angular probability density function D specifies the likelihood of a photon being emitted at an angle θ from the average trajectory of an electron. The RSP optical model requires the probability of a photon being emitted in the direction of a PMT $\hat{p}'$, from the event position $\vec{r}$. With $\hat{p}'$ having been determined from the calculation of the optical path (subsection 4.2.1), the angle θ required by D is calculated

$$\cos\theta = \hat{p}' \cdot \hat{u}, \tag{4.32}$$

where $\hat{u}$ is the reconstructed event direction.

The distribution of photons about the event direction depends on the multiple scattering of the electron and therefore has to be determined via Monte Carlo calculation. Figure 3.2 is an example of the distribution of photons emitted by 8 MeV electrons. A parametric distribution based on similar Monte Carlo calculations is given by

$$D(\theta) = \begin{cases} \frac{1}{2\pi} t_1 \theta^2 & \text{for } 0 < \theta < \theta_c \text{ and} \\ \frac{1}{2\pi} t_2 \exp(t_3 \theta) & \text{for } \theta_c < \theta < \pi, \end{cases} \tag{4.33}$$

where θ_c is the characteristic Čerenkov angle in D_2O. The parameter t_1 is fixed at

$$t_1 = t_2 \frac{\exp(t_3\theta_c)}{\theta_c}$$

to ensure the function is continuous at θ_c. The dependence of t_3 on the electron energy T_e has been determined by Ford [47] to be

$$t_3 = -2.04 - 0.034 T_e.$$

The remaining parameter, t_2, is fixed by normalizing the distribution over the possible range of angles (0 to π) such that

$$t_2 = \exp(-t_3\theta_c)\left[\frac{2\theta_c \sin\theta_c + \left(2 - {\theta_c}^2\right)\cos\theta_c - 2}{{\theta_c}^2} + \frac{e^{t_3(\pi-\theta_c)} + \cos\theta_c - t_3\sin\theta_c}{{t_3}^2 + 1}\right]^{-1}.$$

4.2.6 The PMT photon detection area

The photon detection area, which includes the PMT and reflector assembly, is considered by the RSP optical model to be a flat disk with radius equal to that of the reflector assembly housing. This is consistent with the optical model used to determine the model parameters in subsection 2.6.2. The flat disk approximation subtends an elliptical area when viewed from any given event position $\vec{r}$. This may or may not be apparent from the situation as depicted in figure 4.3.

To determine the solid angle subtended, the optical paths to both ends of the semi-major and semi-minor axes of the elliptical area are calculated exactly as is done for the optical path in figure 4.1. These paths are labeled by their vector to the inner surface of the acrylic vessel ($\vec{a}_1^{12}$, $\vec{a}_1^{3}$, $\vec{a}_1^{6}$, and $\vec{a}_1^{9}$ where the numerical superscripts refer to the points on a clock face) in figure 4.2. The coordinate system indicated by $\hat{e}_1$, $\hat{e}_2$, and $\hat{e}_3$ is defined such that $\hat{e}_3$ is directed along the PMT normal $\hat{n}$ and $\hat{e}_2 = \hat{e}_3 \times \hat{v}$, where $\vec{v} = \vec{a}_2 - \vec{a}_3$ from figure 4.1. The semi-major axis of the ellipse is directed along $\hat{e}_1$ while the semi-minor axis of the ellipse is directed along $\hat{e}_2$. The terminal coordinates of the ellipse axes are obtained by adding to the PMT coordinates ($\vec{p}$) a vector of length 13.69 cm, the radius of the reflector assembly, in the appropriate direction. The solid angle of the PMT is calculated as the solid angle of the ellipse

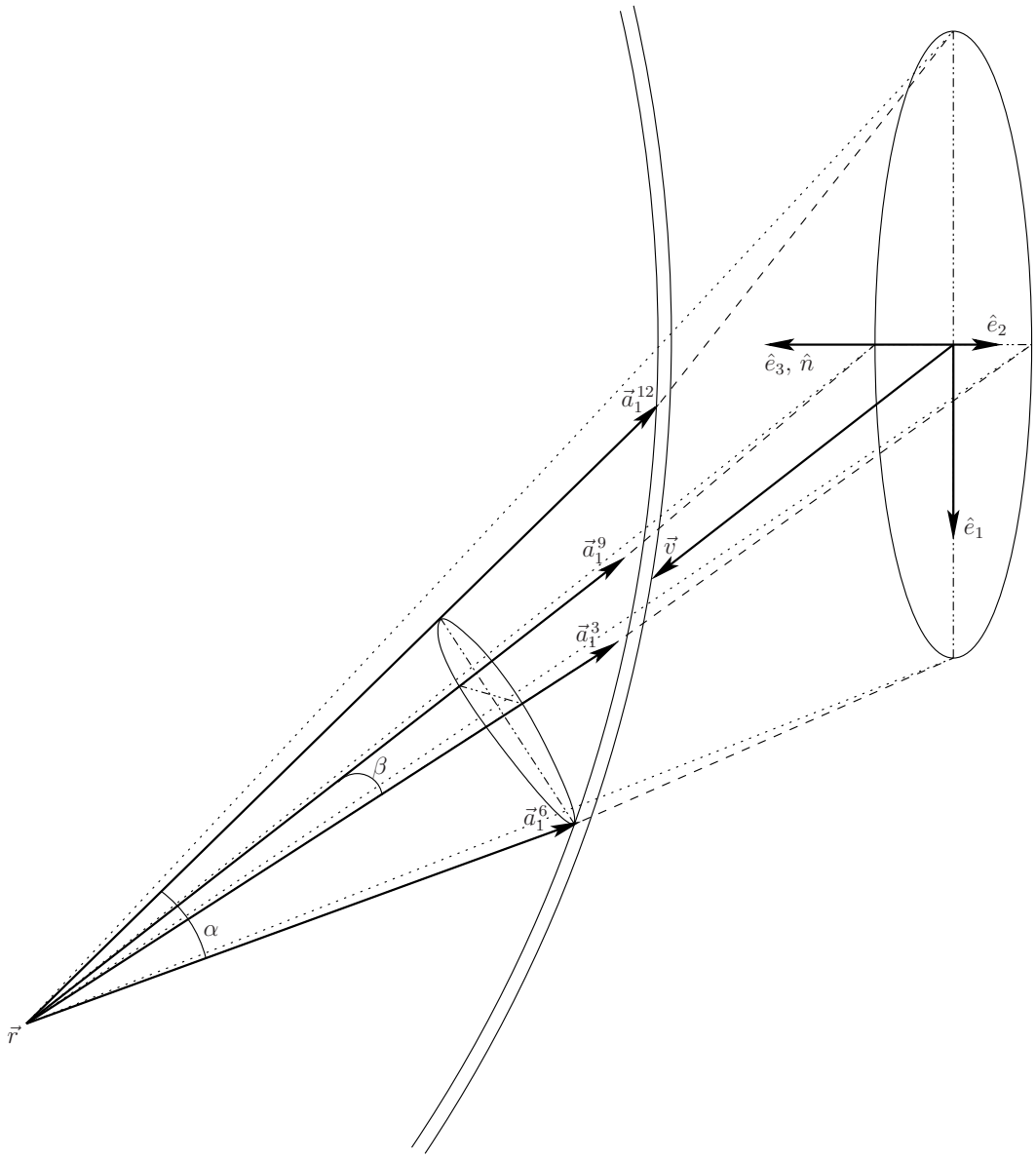

Figure 4.3: The solid angle of the photon detection area as seen from the event position $\vec{r}$ inside the acrylic vessel. The acrylic vessel is shown as the concentric arcs. The $\vec{a}_1$ vectors and the dashed lines represent optical paths. The coordinate system is set up such that $\hat{e}_2 = \hat{e}_3 \times \hat{v}$ where $\vec{v} = \vec{a}_2 - \vec{a}_3$, both of which are from figure 4.1. The vectors $\vec{a}_1^3$ and $\vec{a}_1^9$ do not appear to extend to the acrylic vessel only because they terminate above and below the plane of the figure. See equation 4.34 for the calculation of the solid angle defined by α and β.

defined by the four points of intersection with the acrylic vessel. Specifically,

$$\Omega = \pi \sin\alpha \sin\beta, \tag{4.34}$$

where $\alpha = \arccos(\hat{a}_1^{12} \cdot \hat{a}_1^{6})$ and $\beta = \arccos(\hat{a}_1^{3} \cdot \hat{a}_1^{9})$ are the angles subtended by the axis of the ellipse when projected onto the inner surface of the acrylic vessel and as depicted in figure 4.3.

4.2.7 The effective attenuation of Rayleigh scattering

Prior to this work, the estimate of the number of photons Rayleigh scattered out of the prompt timing window employed effective[10] Rayleigh attenuation lengths: β_{D_2O} and β_{H_2O}. Photons traveling a given distance in either the D_2O or H_2O were subject to the attenuation lengths presented in figure 4.4. These attenuation lengths are calculated by integrating the time distribution of laserball calibration data in a region of late light expected to be dominated by Rayleigh scattering, as described by Moffat [48]. This treatment adds the effective Rayleigh attenuation directly to the standard optical attenuation in equation 3.9 such that

$$\exp\left[-d_x \alpha_x\right] \rightarrow \exp\left[-d_x \left(\alpha_x + \beta_x\right)\right],$$

where x is either D_2O or H_2O. The Rayleigh scattering in the acrylic vessel can be considered to be negligible due to the generally short path length d_{acrylic}. However, some difference in Rayleigh scattering out of the prompt time window is expected from different positions within the detector. This original method does not take into account the varying probability of prompt detection for equivalent path lengths but different geometries.

In order to model this effect, the probability of Raleigh scattering out of the prompt time window was investigated using a Monte Carlo calculation. In this simulation of electrons producing Čerenkov radiation, the initial position of the photon and timing distribution of triggered PMTs is known. Having also recorded whether or not each photon Rayleigh scattered, the probability of photons Rayleigh scattering

[10] Effective in that they are not actually an attenuation lengths, not, as above, that they includes a correction for specular scattering from particulate contamination in the water.

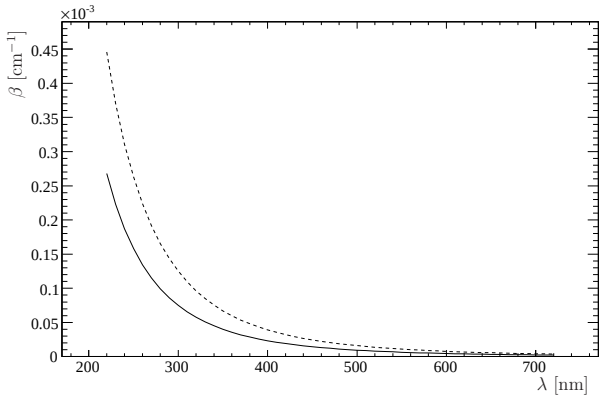

Figure 4.4: H_2O (dashed line) and D_2O (solid line) effective Rayleigh attenuation lengths.

out of the prompt time window was determined. This probability is required to be further reduced by the probability that the photons might have been late regardless of whether or not they were Rayleigh scattered as late photons are accounted for elsewhere such as in the transmission/reflection probability at the acrylic vessel interfaces. With this treatment of light lost due to Rayleigh scattering, equation 4.35 becomes

$$\begin{aligned} R_i(\lambda, \vec{r}, \hat{u}, \vec{p}_i, \hat{n}; T) = \epsilon_i(\lambda, \vec{r}, \vec{p}_i, \hat{n})\ \Omega_i\left(\vec{r}, \vec{p}_i, \hat{n}\right)\ D(\hat{u}, \vec{r}, \vec{p}_i; T) \\ \times F(\vec{r}, \vec{p}_i) \exp\left(\sum_{m=1}^{3} -d_m\left(\vec{r}, \vec{p}_i\right) \alpha_m\left(\lambda\right)\right) \\ \times \left(1 - \Big\{1 - \exp\big[-d_{D_2O}\left(\vec{r}, \vec{p}_i\right) \beta_{D_2O}\left(\lambda\right) \right. \\ \left. -d_{H_2O}\left(\vec{r}, \vec{p}_i\right) \beta_{H_2O}\left(\lambda\right)\big]\Big\} P\left(\vec{r}, \vec{p}_i\right)\right) \end{aligned} \tag{4.35}$$

where in this case the β's are the probability per unit length of Rayleigh scattering presented in equation 3.12 (or equation 3.13 for the salt phase) and P is the probability of the Rayleigh scattered photon being late/falling outside the analysis time window.

The probability P of a non-prompt detection of a Rayleigh scattered photon is presented in figure 4.5. The probability that the photon would have been late regardless of whether or not it had been Rayleigh scattered has been subtracted from

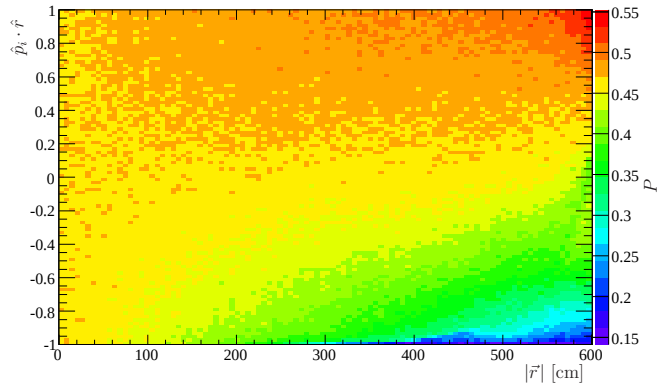

Figure 4.5: Probability P that a Rayleigh scattered photon will not be detected within the prompt time window as a function of its initial position $\vec{r}$ and direction $\hat{p}'_i$. The probability presented has been further reduced by the probability that the photon would have been late regardless of whether or not it was scattered.

figure 4.5. P is calculated assuming a spherically symmetric detector in that it averages over photons initiating from the same radius $|\vec{r}|$ that travel in the same direction (given $\arccos(\hat{p}'_i \cdot \hat{r})$) with respect to the radial position vector. This is, for example, a good approximation when estimating the time residual (appendix A). This treatment extends the accuracy of the previous one, as discussed above, by including what is expected to be the dominant remaining correction; it still does not account for where along the photon path the Rayleigh scattering occurs. This second order improvement in the estimate produces negligible improvement in energy reconstruction. However, the more detailed calculation is adopted as it is in principle more accurate.

4.3 The multi-photoelectron correction

The number of photons N_i predicted to hit the i^{th} PMT has to be further reduced by a correction for the possibility of the PMT being hit by multiple photons, the function M in equation 4.4. In this case only a single trigger is recorded. The multi-photoelectron correction, first derived by Ford [47], assumes that the number of Čerenkov photons produced in the direction of a PMT is Poisson distributed. Then the probability M of multiple photons ejecting multiple photoelectrons into the a PMT

is given by

$$M(\mu) = \frac{1 - e^{\mu}}{\mu}, \tag{4.36}$$

where μ is the number of photons expected to hit the PMT, or N_i from equation 4.6. For scale, N_i always less than 1.0 for electrons scattered by ^{8}B neutrinos in the D_2O.

It is pointed out by Dunford [25] that the number of photons produced in a given direction also depends on the deviation from the characteristic Čerenkov light emission angle (figure 3.2). Using equation 4.36, as the RSP optical model does, is equivalent to assuming a flat Čerenkov angular distribution. This is admittedly not an good approximation. The detailed calculation could potentially improve the performance of RSP if implemented.

4.4 Summary of the RSP detector response

The wavelength weighted contribution of the media attenuations, Rayleigh scattering, and PMT angular response are illustrated in figure 4.6. The PMT angular response, which includes the PMT quantum efficiency, clearly dominates. The acrylic attenuation is larger than the other attenuations everywhere. Note that this figure also demonstrates why the acrylic and H_2O attenuations are indistinguishable for positions within the acrylic vessel.

The solid angle RSP calculates for an individual PMT is shown in figure 4.7. Also shown is the total solid angle of all PMTs for events from a pure D_2O phase run. Events near the centre of the detector see roughly a 60% coverage with about 3% (absolute) variation at higher radii.

The solid angle and event direction (Čerenkov angular distribution weighted) weighted average PMT optical and electronics efficiencies for a pure D_2O phase run are shown in figure 4.8. The raw averages would be identical for each event during the same run. In the figures, events having a lower weighted average efficiency are likely to have occurred nearer to, or in the direction of, a less efficient region of the detector.

The total optical response of an individual PMT as calculated by RSP is shown in figure 4.9. The solid angle and event direction weighted total optical response for events from a pure D_2O phase run are also shown. The crest in the response at mid

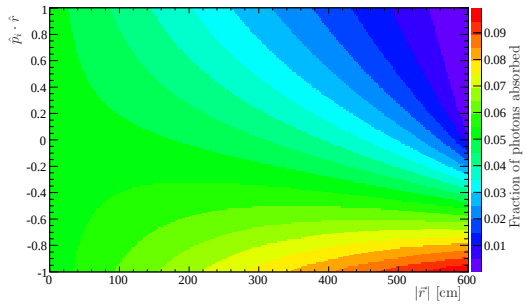

(a) D_2O attenuation.

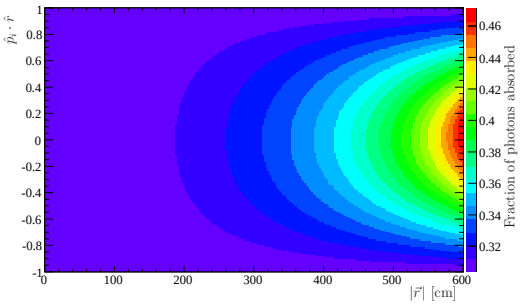

(b) Acrylic attenuation.

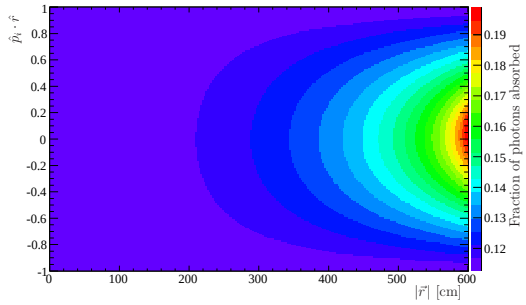

(c) H_2O attenuation.

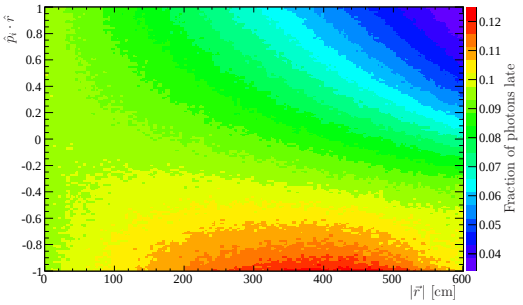

(d) Rayleigh scattering.

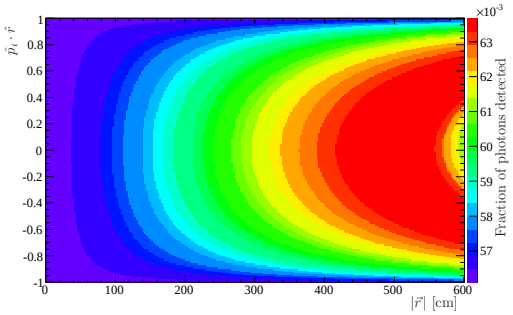

(e) PMT angular response.

Figure 4.6: Wavelength weighted response of an individual PMT as calculated by RSP.

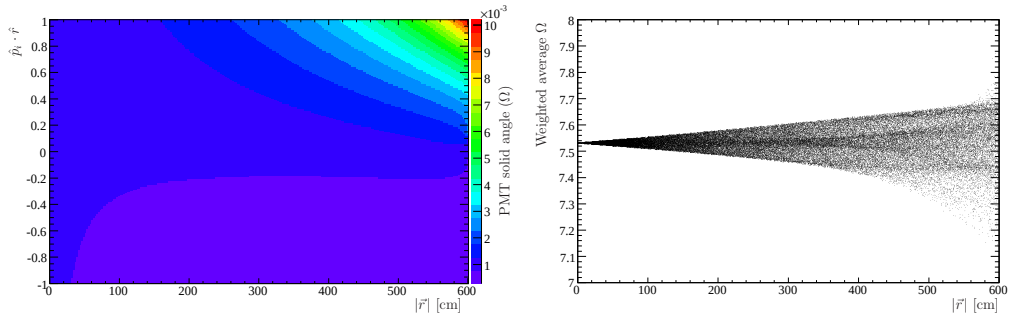

(a) Solid angle of an individual PMT.

(b) Total detector solid angle: the sum of that of each PMT.

Figure 4.7: Solid angle of an individual PMT as calculated by RSP and the total solid angle for events from a pure D_2O phase run..

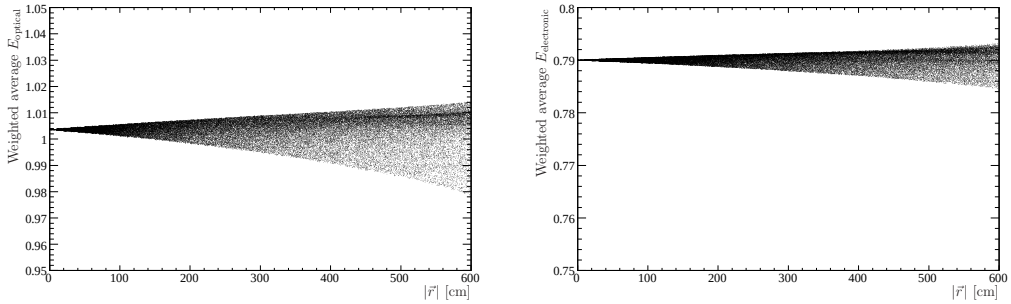

(a) PMT optical efficiency.

(b) PMT electronics efficiency.

Figure 4.8: The PMT solid angle and event direction weighted average PMT efficiency for events from a pure D_2O phase run.

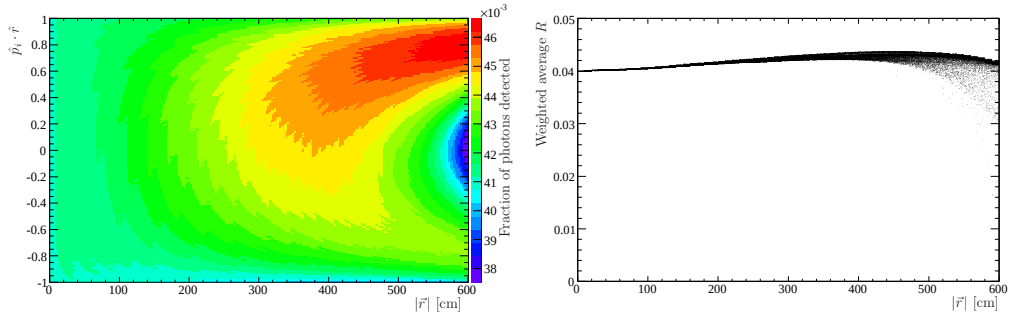

(a) Total response of an individual PMT. (b) Average response of all PMTs.

Figure 4.9: The response of an individual PMT as calculated by RSP and the solid angle and event direction weighted average response for events from a pure D_2O phase run.

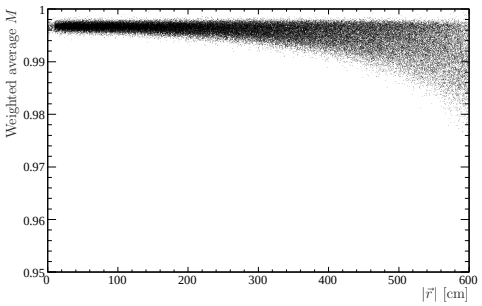

Figure 4.10: The solid angle and event direction weighted multi-photoelectron correction calculated by RSP for events from a pure D_2O phase run.

to high radii is due to the average PMT angular response peaking in that region. The weighted average multi-photoelectron correction (MPE) calculated by RSP is shown in figure 4.10. The MPE effect is roughly 1–2% primarily at higher radii.

4.5 The energy calibration function

The energy calibration function,

$$\mathcal{F}_E : N_{\text{ckv}} \rightarrow T_{\text{e}}, \tag{4.37}$$

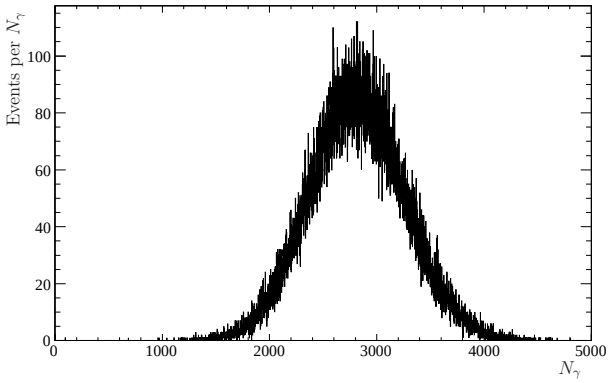

Figure 4.11: The RSP number N_γ of initial photons predicted from simulated 8 MeV electrons.

is a one-to-one function required by RSP to map the estimate of the initial number of photons N_γ to electron energy (T_e). In order to determine $\mathcal{F}_E$, detailed simulations of monoenergetic electrons are performed. The RSP energy reconstruction algorithm (section 4.1) is used to estimate the initial number of photons N_γ for each simulated event. The initial estimate of N_γ (equation 4.2) is in this case made independent of $\mathcal{F}_E$, since it is as yet unknown, and the energy dependence of the optical response uses the energy at which electrons were simulated. The N_γ distribution of 8 MeV electrons is shown in figure 4.11. The mean of this distribution, approximately 2800, is mapped to $T_\mathrm{e} = 8\,\mathrm{MeV}$ T_e in $\mathcal{F}_E$.

The full $\mathcal{F}_E$ function is determined from a series of full SNO detector simulations including all the electron energies listed in table 4.1. The mean of the N_γ distribution for each electron energy is determined via the procedure outlined in appendix B. $\mathcal{F}_E$ then consists of an interpolation of a table made up of these mean N_γ and their corresponding electron energies T_e.

The derivation of $\mathcal{F}_E$ requires the full, absolutely–normalized, RSP optical response and a complete detector model to simulate electron events. Therefore, the PMT collection efficiency $\epsilon_\circ$ must first be determined by comparing the full detector simulation to calibration data. The calibration of $\epsilon_\circ$ is discussed in the following chapter.

Electron energy [MeV]				
2	11	20	40	80
3	12	22	45	90
4	13	24	50	100
5	14	26	55	110
6	15	28	60	120
7	16	30	65	130
8	17	32	70	
9	18	34	75	
10	19	36		
		38		

Table 4.1: Electron energies (T_{e}) included in the energy calibration function $\mathcal{F}_E$.

Chapter 5

SNO Energy calibration

An ideal optical model of the SNO detector is presented in chapter 3. This model is simplified in order to incorporate the optical parameters measured via optical and electronic calibrations and Monte Carlo calculations. The application of these parameters by RSP to determine the energy response of the detector is presented in chapter 4. RSP reconstructs event energy from the reconstructed position and direction of an event and the position and timing of the triggered PMTs associated with that event. The final component of the optical models to be evaluated is the PMT collection efficiency $\epsilon_{\circ}$. This parameter is determined by tuning the energy scale in a full detector simulation, in which $\epsilon_{\circ}$ is the last remaining free parameter, to match that observed during ^{16}N calibrations.

A time dependence to the energy scale of the calibration data is observed which is generally not modeled. The time dependent correction δ_{drift} is therefore applied to $\epsilon_{\circ}$ in the simulation such that it better track the observed data. $\epsilon_{\circ}$ as applied in the RSP optical model remains constant with time. Therefore, the inverse of δ_{drift} is applied to the RSP reconstructed energy of events in both the data and the simulation to remove the expected time variation.

The determination of the energy calibration function $\mathcal{F}_E$ is done using the RSP reconstructed energy of simulated electron events. There are energy scale dependent parameters, mainly the multi-photoelectron correction, in the RSP optical model. Therefore $\mathcal{F}_E$ is somewhat dependent on the energy scale of the simulation—the

determination of $\epsilon_\circ$. The energy calibration function $\mathcal{F}_E$ is therefore calculated subsequent to the determination of $\epsilon_\circ$ and any potential δ_{drift}.

The primary energy calibration of SNO using the ^{16}N γ-rays is described in this chapter. The ^{8}Li and pT sources, and Michel electrons from muon decay are also discussed as they provide tests of the energy reconstruction at event energies above those of the ^{16}N source γ-rays[1]. The determination of the pure D_2O and salt phase energy scale $\epsilon_\circ$, the energy response drift δ_{drift}, and the associated energy calibration functions $\mathcal{F}_E$ are presented. The potential sources of systematic error associated with the energy scale and resolution will also be discussed in this chapter followed by a detailed evaluation of those directly derived from the comparison between ^{16}N calibrations to a full detector simulation.

5.1 Energy calibration sources

The energy response of the SNO detector is calibrated using an isotropic optical source, γ-rays, β-particles, and, to some extent, neutrons. The ^{16}N γ-ray source is used as the primary energy calibration for SNO. The ^{8}Li β–particle source is used to verify the ^{16}N calibration with electrons directly and over a broader energy range. The proton-tritium (pT) source and Michel electrons from muon decay are used verify the ^{16}N calibration above the energy range of the ^{8}B spectrum. The analyses of the pT source data, Michel electrons and ^{8}Li calibrations are discussed by Klein et al. [75] with regard to the energy non-linearity in the low energy threshold analysis (LETA) of the pure D_2O and salt phase data. The discussions in this work will focus on the analysis of ^{16}N calibration data, however, a discussion of the other energy calibration sources is also presented for completeness.

5.1.1 The ^{16}N source

The main branches for ^{16}N β-decay to ^{16}O are depicted in figure 5.1. Most ^{16}N decays result in a single 6.13 MeV γ-ray. About 5% of decays are to the 7.12 MeV level of

[1]The fission neutron source ^{252}Cf [29] and the distributed ^{222}Rn low energy γ-ray [73] and ^{24}Na neutron [74] calibrations are also used to test the stability and uniformity of the energy reconstruction.

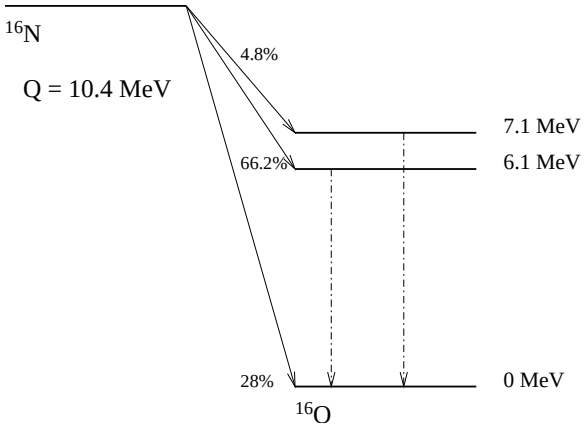

Figure 5.1: The three most probable branches of ^{16}N β-decay as presented by Dragowsky et al. [76]. The energies available for γ-rays are listed on the right while the branching ratios are listed on the left.

^{16}O, which primarily emits a single γ-ray. Almost 1% of ^{16}N decays produce multiple γ-rays, the majority of these include one of either the 6.13 or 7.12 MeV γ-rays. 28% of ^{16}N decays are to the ground state in which a β-particle is produced with no γ-ray emission.

Figure 5.2 is schematic of the source showing the decay chamber and PMT. ^{16}N is piped into the source chamber through a silicone umbilical line. The production of the ^{16}N is done approximately 20 m from the SNO detector where a DT generator activates ^{16}O via fast neutrons bombarding CO_2 gas. The inner chamber of the ^{16}N source, which is cylindrical with a radius of 4.78 cm and a height of 15.21 cm, is surrounded by a 3 mm thick plastic scintillator. The scintillator is viewed by a PMT, also mounted within the source. The triggering of the source PMT is used to verify that the ^{16}N decay, and subsequent γ-ray emission, occur at the desired source position: within the source decay chamber.

The ^{16}N source is used to determine the absolute energy scale of the detector; in other words, to calculate the global PMT collection efficiency $\epsilon_\circ$ (see subsection 3.4.3). The ^{16}N source is also used to measure the systematic error associated with the energy calibration and reconstruction. The source is deployed extensively throughout the D_2O and in selected locations in the H_2O; between the PSUP and the acrylic vessel. The assessment of energy scale and resolution errors using the ^{16}N source is discussed

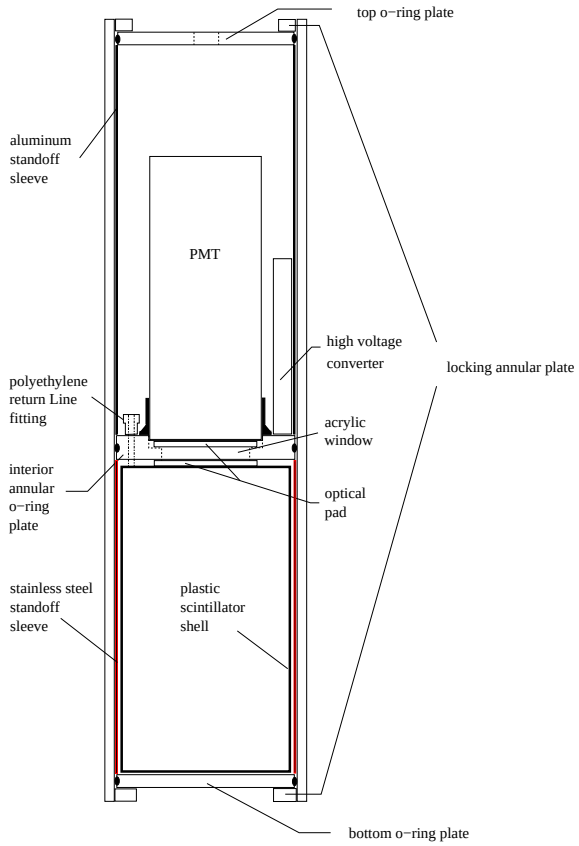

Figure 5.2: A schematic of the ^{16}N source showing the source chamber and its relation to the source PMT as taken from Dragowsky et al. [76].

in section 5.5.

It is essential that the mean energy deposited in the detector by the ^{16}N source be well known in order to use it to calibrate the energy scale. The 10.4 MeV endpoint β-particle, although it likely triggers the source PMT, rarely initiates a global event trigger. If the β-particle manages to reach the D_2O and trigger an event (or an event is triggered for some other reason such as background noise), a spurious ^{16}N event is recorded. These events are easily rejected by standard SNO data cleaning cuts. However, attenuation of the γ-rays and β-particle bremsstrahlung emission in the source materials need to be considered when determining the mean γ-ray energy of events tagged by the source PMT. It is conservatively estimated by Dragowsky et al. [76] that the total energy scale uncertainty associated with the ^{16}N calibration is less than 0.5%. However, this does not completely take into account an observation made by Lay [77] that the spectrum of Čerenkov photons generated in the simulation is only an approximation. This introduces another source of uncertainty of up to 0.5%. A complete discussion of the uncertainties associated with the ^{16}N source calibration is presented in chapter 7.

5.1.2 The ^{8}Li source

The ^{8}Li decay scheme is presented in figure 5.3. ^{8}Li β-decays with an endpoint energy of 12.96 MeV. The energy spectrum of the β-particles is very similar to that of the ^{8}B β^+-decay also depicted in figure 5.3. Both decays result in the same excited state of ^{8}Be at 3040 keV, which immediately decays to two α-particles.

Figure 5.4 is a schematic of the ^{8}Li source. ^{8}Li is piped into the decay chamber within a flow of helium gas (along with some N_2). The decay chamber of the source consists of the interior of a hollow stainless steel sphere with a radius of about 6 cm. The stainless steel shell is as thin as possible (less than 1 mm) to allow the β-particles to escape with minimal energy loss while still being able to resist collapse at a depth of over 18 m of water. A decrease in β-particle energy of about 1 MeV [78] is expected in an average transit of the shell thickness.

A PMT is mounted within the source to observe the scintillation of the ^{8}Be α-particles in helium. The spherical decay chamber provides a symmetric/isotropic source of β-particles and maximizes the efficiency for scintillation light to trigger the

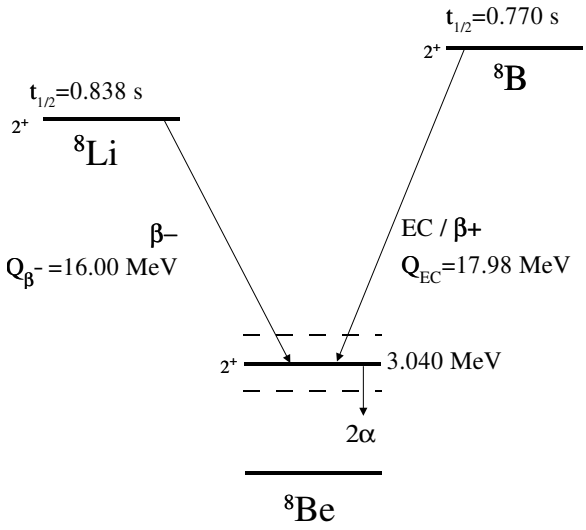

Figure 5.3: ^{8}Li decay scheme from Tagg et al. [78]. Also shown is the ^{8}B β^+-decay which has a similar spectrum to that of ^{8}Li β^--decay. Both isotopes decay to the 3040 keV excited state of ^{8}Be which promptly decays to two α-particles.

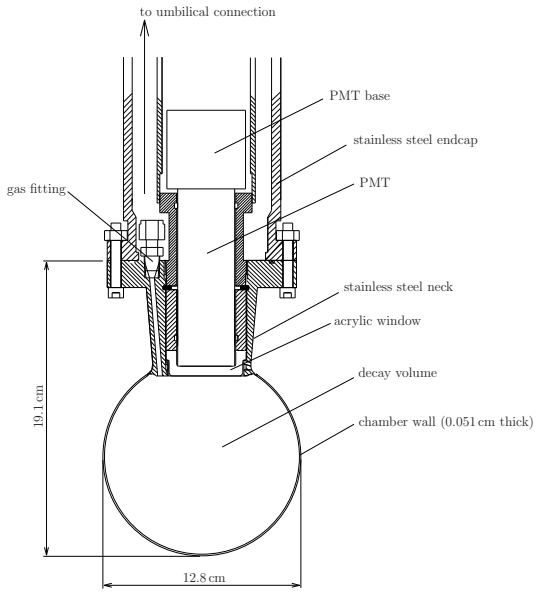

Figure 5.4: Schematic of ^{8}Li source. ^{8}Li decays within the decay volume are tagged when the PMT is triggered by the scintillation light of α-particles. Taken from Tagg et al. [78].

source PMT. A significant number of ^{16}N decays are also found to be occurring in the source chamber. Fortunately the probability of the β-particles interacting with the acrylic window (see figure 5.4) and triggering the source PMT is low. Those ^{16}N events that do trigger the source PMT are distinguished from ^{8}Li events based on the integrated charge and rise time of the PMT signal; both of which are smaller for the β-decay. It is conservatively estimated by Tagg et al. [78] that ^{16}N contamination events in ^{8}Li calibration data make up less than 1% of tagged events.

^{8}Li calibrations are used to verify the energy calibration and reconstruction systematic errors measured with ^{16}N calibrations. ^{8}Li calibrations provide a direct measure of the detector response to Čerenkov electrons, as opposed to the multiple electrons generally scattered by γ-rays. ^{8}Li calibrations also provided a measure of the energy response above the ^{16}N γ-ray energy with a spectrum very similar to that of solar ν_e (to be precise ^{8}B neutrinos since the spectrum of solar neutrinos may be distorted). However, as is indicated in the previous section, the ^{16}N source provides the primary energy calibration of SNO. The uncertainties associated with the ^{8}Li calibration, especially the sensitivity of the electron energy to the thickness of the chamber wall, and its low rate which results in low statistics, limit the significance of its energy calibration to a crosscheck of those done via the ^{16}N source.

5.1.3 The pT source

The pT source is designed to produce 19.8 MeV γ-rays via the reaction $^{3}\mathrm{H}(p,\gamma)^{4}\mathrm{He}$. This reaction is achieved by bombarding a tritium target with a DC proton beam. The energy of the pT source γ-rays lies above the endpoint for solar neutrinos; complementing the lower energy calibrations. ^{4}He also has no bound excited state therefore the reaction produces only the 19.8 MeV γ-ray, which makes it ideal for energy calibration.

The pT source is the first self-contained, compact, and portable source of high energy (greater than 10 MeV) γ-rays [79]. A schematic of the pT source is shown in figure 5.5. From left to right in the figure, the source consists of a gas-discharge line, an ion acceleration line, and a target interaction chamber. The ion beam consists primarily of protons, however, deuterons are also present at the level of 1.5×10^{-4}.

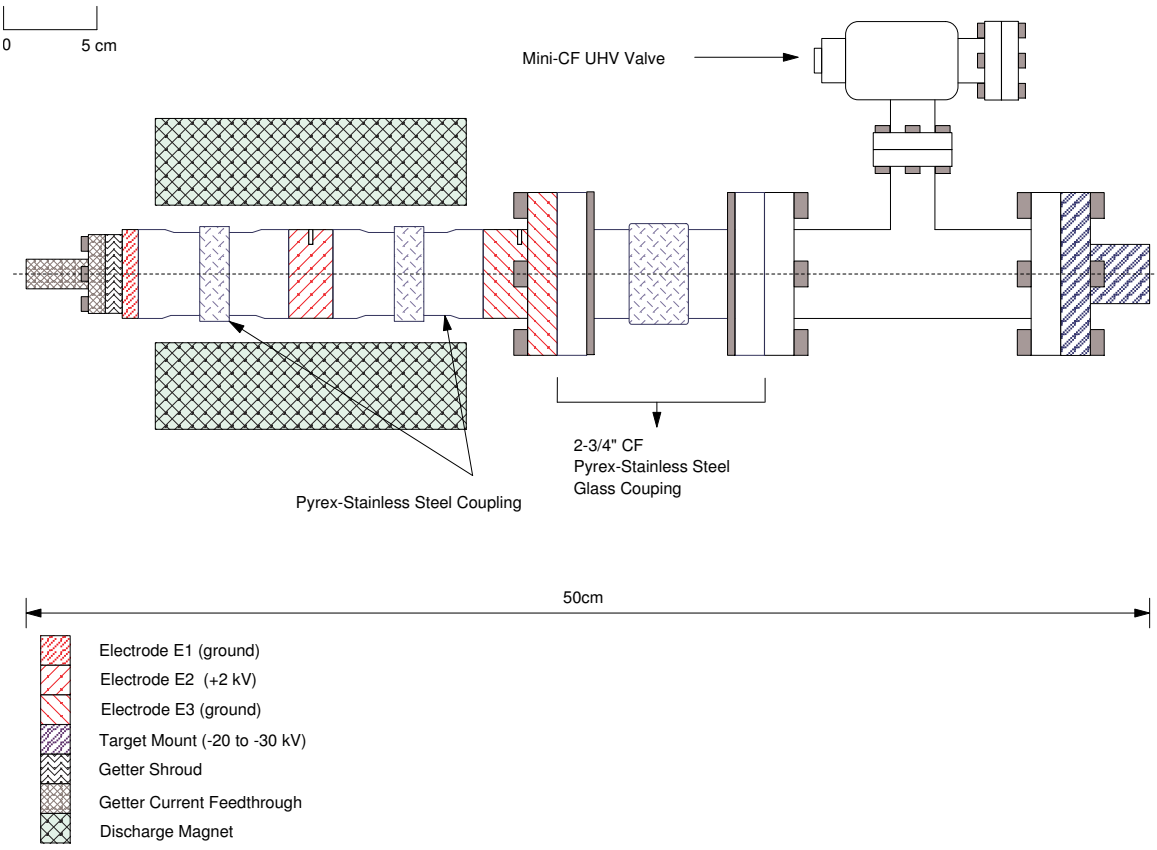

Figure 5.5: pT source schematic. Taken from Poon et al. [79].

The target is constructed by the deposition of evaporated scandium onto a molybdenum substrate. Tritium gas, desorbed from uranium tritide, is then sorbed onto the scandium. The target also contains deuterium at the level of 1.2×10^{-3}.

Tritium in the ion beam, produced by beam-target exchange, results in ^{3}H–^{3}H interactions that generate copious amounts of neutrons. The interactions $^2\mathrm{H}(t,n)^4\mathrm{He}$ and $^3\mathrm{H}(d,n)^4\mathrm{He}$ involving the deuterium contamination in the beam and target also results in the production of high energy neutrons. The reaction $^3\mathrm{H}(p,\gamma)^4\mathrm{He}$, although potentially a further source of background, requires a much higher energy to proceed than the source is operated at. In total, the neutron rate from the pT source, after reduction from source material absorption and scattering, is approximately $2500\,\mathrm{s}^{-1}$. This may be compared to the rate of 19.8 MeV γ-rays which is measured to be about $0.6\,\mathrm{s}^{-1}$.

The source was only deployed for a single series of measurements near the end of the pure D_2O phase. The source was operated with an approximately 30 keV beam of protons incident on roughly 4 Ci tritium source. The 19.8 MeV γ-rays were clearly observed above the 6.25 MeV γ-rays emitted by neutron capture in the D_2O. Unfortunately the pT source, unlike the ^{16}N and ^{8}Li sources, does not provide a tag for the 19.8 MeV γ-ray. Only analysis cuts can be employed to distinguish them from the neutrons and umbilical light (HV discharges). The primary analysis cuts include requiring the event to reconstruct within 150 cm from and be directed outward from the source position; neutrons tend to travel farther and emit γ-rays isotropically subsequent to their capture. Development of these selection criteria is hampered by the accuracy of the source simulations. The $^3\mathrm{H}(p,\gamma)$ interaction emits γ-rays with an angular dependence. Coupled with the complicated source geometry and the ultra-high vacuum materials used, the angular distribution of the source is difficult to model. Additionally the pT source was only deployed at three positions along the central axis of the detector due to operational and time constraints.

In the end, the high energy calibration of the SNO detector energy response relies mostly on Michel electrons tagged subsequent to muon decays. Although low in number, such electrons are homogeneously distributed within the detector volume and span an energy range up to about 50 MeV with a well known energy spectrum. Also, as muon events are collected during all data taking, the Michel electrons do

not suffer from position or time dependent systematic errors when relating them to neutrino data.

The pT source was not deployed during the salt phase due to what would have been an over whelming neutron capture rate. The pT source was also not deployed during the NCD phase due to the complicated nature of the source and the evolution of alternative calibrations such as the Michel electrons.

5.2 SNO Monte Carlo simulation

The SNO Monte Carlo and analysis package, SNOMAN, provides a robust platform for the simulation and analysis of SNO data. On the analysis side, SNOMAN reconstructs the position and direction of events after unpacking the data. SNOMAN also contains the energy reconstruction routines including both versions of RSP which are generally run after position reconstruction. SNOMAN Monte Carlo simulations include detailed models of all of the detector components (including calibration sources), photon detection by the PMTs, and even a model of the electronics response–from the triggering of individual PMTs through to the SNO global event trigger. All of the relevant physics interactions are available to be simulated by SNOMAN including those of neutrinos, radioactive backgrounds, and calibration sources. The propagation of neutrons and hadrons is handled via the MCNP [80] and FLUKA [81] packages while electron and γ-rays are accurately tracked by the EGS4 processor [82]. In particular, the propagation of electrons contains all of the relevant energy loss mechanisms such that SNOMAN can accurately simulate equation 3.4 (albeit with an average index of refraction). SNOMAN also incorporates the parameters measured via the optical and electronic calibrations of SNO. SNOMAN consists of as complete and accurate a simulation of the fully operational SNO detector as possible; it is continually upgraded as graduate student and computer processing resources permit. The last remaining parameter to be set in SNOMAN is always the PMT global collection efficiency $\epsilon_{\circ}$.

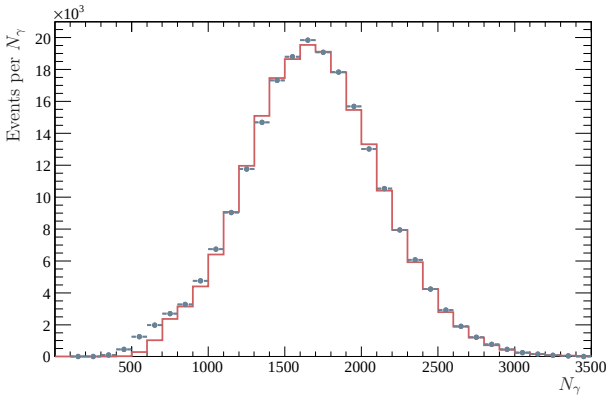

Figure 5.6: A comparison of the N_γ distributions of a ^{16}N calibration (data points) and its simulation (histogram). By the method of appendix B, the peaks of the distributions are found to disagree by only 0.01%. The disagreement at low energy is a result of the ground state β-particle of the ^{16}N decay not being simulated.

5.3 Setting the energy scale/Determining the PMT collection efficiency

As discussed in the previous section, the PMT collection efficiency ($\epsilon_\circ$) is required to complete the SNOMAN detector model. To calibrate $\epsilon_\circ$, SNOMAN is used to generate simulations of a series of central ^{16}N calibrations, corresponding to high statistics calibrations of the detector, with $\epsilon_\circ$ set to the benchtop measurement made by Boardman [57] or that of a previous iteration of this process (somewhere in the range 0.5–0.7). RSP is used (see section 4.1) to estimate the number of initial photons N_γ for each event, both in the data (N_γ^{data}) and in the simulations (N_γ^{MC}). The initial estimate of $\epsilon_\circ$ is then tuned such that

$$\epsilon_\circ \longrightarrow \epsilon_\circ \frac{N_\gamma^{\text{data}}}{N_\gamma^{\text{MC}}}.$$

A comparison of the N_γ distributions from a salt phase ^{16}N calibration and its simulation are shown in figure 5.6. The means of the two distributions, with $\epsilon_\circ$ in the simulation already having been calibrated, disagree by only 0.01%.

One subtlety of this argument is that the energy of these events cannot be accurately reconstructed until the energy calibration function ($\mathcal{F}_E$) is determined,;which of course requires $\epsilon_\circ$ to be known. This problem arises as a result of $\epsilon_\circ$ serving a dual purpose: to tune the energy scale of the detector simulation to match that observed for detector calibrations, and as the PMT collection efficiency in the RSP optical response. The only point at which event energy is required by RSP when estimating N_γ is in the determination of the Čerenkov angular dependence D, which is a factor in the RSP optical response (section 4.2). The energy dependence of D is small[2] and strictly only applicable to single electron events[3], which is generally not the case for ^{16}N γ-rays. For these two reasons, an approximate event energy, anywhere within the ^{8}B energy spectrum for example, is sufficient for RSP to estimate N_γ independent of an accurate knowledge of $\mathcal{F}_E$. The degree to which this is not the case adds directly to the measured energy scale error.

This subtlety advocates for the use of the much more straight forward comparison of mean $N_{\rm hit}$ to determine $\epsilon_\circ$. However, $N_{\rm hit}$ is highly dependent on the position and direction of an event. Even central ^{16}N calibration events are distributed over a large volume and are not isotropically emitted from the source. If the simulation does not reproduce these distributions correctly, a discrepancy between the mean $N_{\rm hit}$ of the calibrations and simulations will manifest, independent of $\epsilon_\circ$. Using N_γ, which varies much less with event position and direction, is less sensitive to these effects. The degree to which this is not the case adds directly to the measured energy scale error as discussed in section 7.2.

Due to a few remaining simplifying assumptions and inaccuracies in SNOMAN, and due to the continuous improvements made in the modeling of the detector, the measured value of $\epsilon_\circ$ changes from time to time and always from phase to phase. This requires the re-evaluation of $\epsilon_\circ$ to re-sync the energy scale of the simulation to that of calibration data. The re-evaluation of $\epsilon_\circ$ for the pure D_2O and salt phases is presented in the following sections. The evaluation of $\epsilon_\circ$ for the NCD phase is presented in the following chapter. A slow decline in the energy scale of the detector

[2]The dependence of reconstructed event energy on the exact shape of the Čerenkov angular distribution is weak. The energy dependence is included primarily for completeness.

[3]The angular distribution of photons emitted by multiple electrons can readily be simulated. However, as with the energy dependence of the single electron angular distribution, the overall effect on the energy reconstruction would be completely negligible.

is observed over extended periods of detector operation (months to years). The tuning of the detector simulation energy scale to match the time dependence observed in the detector calibrations is dealt with in the following section.

5.4 Energy scale drift correction

During the first attempt to determine $\epsilon_\circ$, for the first analysis of the pure D_2O phase (circa 2001), the energy scale of the detector was observed to be decreasing with time. Specifically, the difference between the mean $N_{\rm cor}$, defined in equation 4.1, was systematically decreasing as a function of time. A time dependent scale function ($\delta_{\rm drift}$) was fit to the mean $N_{\rm cor}$ of central ^{16}N calibrations. It was then applied to $\epsilon_\circ$ in SNOMAN to tracked the change observed in the ^{16}N calibrations. This was done by modifying $\epsilon_\circ$ such that

$$\epsilon_\circ \rightarrow \delta_{\rm drift}(t)\epsilon_\circ, \tag{5.1}$$

where t is time, usually in days. The result was that SNOMAN simulations tracked the energy scale of the calibrations.

At the time, the exact cause of the energy scale drift was not known. During the salt phase, detailed optical calibrations revealed that the PMT angular response (E) was changing. While the NCDs were being installed (after the salt phase) the PMTs and their reflector assemblies were visually inspected. The reflector petals surrounding the PMTs showed signs of degradation. This is now thought to be the source of the change in E and the decrease in PMT light collection modeled by $\delta_{\rm drift}$. Note that although the change in E was measured, it is not a measure of absolute efficiency: it is relative to normal incidence which is fixed to the PMT quantum efficiency $\epsilon^{\rm qe}$. The only measurement of the absolute efficiency of the PMTs that can address the reflector degradation is the measurement of $\epsilon_\circ$. To precisely account for this change in the state of the detector, the change in the reflectivity of the reflector petals would have to be measured external to the detector and properly modeled.

In this work, $\delta_{\rm drift}$ is determined by fitting a function, generally a series of first order polynomials, to the mean N_γ of high statistics central ^{16}N calibrations as a function of time. Multiple calibrations done during a short period of time are excluded so as not to bias the fit of $\delta_{\rm drift}$ to the value at those particular time. $\delta_{\rm drift}$ is then normalized

at an arbitrary time generally near the middle of the phase in question. This δ_{drift} is applied to $\epsilon_\circ$ as in equation 5.1. Including this in SNOMAN simulations generated to determine the final value of $\epsilon_\circ$ in the previous section thereby ensures the proper normalization of $\delta_{\text{drift}}\epsilon_\circ$. This is the procedure followed for the LETA re-calibration of the pure D_2O phase and for the NCD phase. The peculiarities of the δ_{drift} calibration in the salt phase will be discussed as it is performed in subsection 5.8.1.

Rather than applying δ_{drift} to the PMT collection efficiency $\epsilon_\circ$ in the RSP optical response, the effective energy (T_{eff}) is calculated exactly as indicated in chapter 4. The reconstructed T_{eff} is then corrected by δ_{drift} such that

$$T_{\text{eff}} \rightarrow T_{\text{eff}}/\delta_{\text{drift}}(t). \tag{5.2}$$

This is an acceptable approximation given that $\mathcal{F}_E$ is linear for small variations (on the order of a few percent) and that $|1 - \delta_{\text{drift}}|$ is generally less than 0.01%.

5.5 SNO systematic errors in general

SNOMAN simulations are used to characterize physics events within the SNO detector, especially where direct calibration is not possible. This includes Čerenkov electrons that are the signal of neutrino interactions. As was described in chapter 1, events induced by the three neutrino signals and backgrounds cannot be distinguished from one another on an event-by-event basis. A statistical signal extraction is performed to derive the separate neutrino fluxes based on the observed properties of the events: reconstructed event position, direction, energy, and hit PMT pattern and direction with respect to the centre of the detector. SNOMAN simulations are almost always responsible for the generation of probability distribution functions (PDFs) of each of these observables for each signal and background. The observables collected during calibrations performed at specific times, in specific locations, with specific types of interactions are compared to predictions made by SNOMAN simulations. SNOMAN essentially interpolates and extrapolates, via Monte Carlo calculations, the measured detector response across the entire detector, energy range of interest, and interaction types to provide a complete model of the observed data.

If the SNOMAN model of the detector or its modeling of physical processes is

flawed, the comparison of its simulations to calibrations provide a measure of these effects on the event observables. Discrepancies between the simulations and calibrations are due to either error in the model inputs or error in the model itself. Errors in the input parameters, that are not correlated with any other model parameters, are easily propagated through the simulation to examine the potential error in the observables. However, this would be a difficult proposition for correlated parameters such as those of the optical model. Instead, the effects of the optical parameters are directly tested by the comparison of the simulations to calibration data. In the case of the error in the detector energy scale and resolution, this is done primarily with ^{16}N calibrations. The error in the observables, once determined, can then be applied to the simulated events that make up the signal PDFs and propagated through the signal extraction to determine their effect on the final results.

The energy response of SNO to events of a specific energy is well described by a Gaussian function. The energy response is therefore parametrized by an energy scale, represented by the mean of the Gaussian distribution, and an energy resolution, represented by the Gaussian width. The SNOMAN simulated reconstructed energy PDFs can in principle be analytically derived by convolving the detector energy response with the fundamental energy spectrum of a particular signal. The systematic uncertainties associated with the energy reconstruction are therefore broken down into those that affect the energy scale and those that affect the energy resolution.

5.5.1 Energy scale error

Error in the mean reconstructed energy, or the energy scale, resulting from the uncertainty in the measurement of PMT and PMT electronics channel status are comprised of:

PMT status

PMTs with high voltage or electronic triggers disabled are recorded for each run. Malfunctioning PMTs are diagnosed via analysis of electronics and timing calibrations and of the data itself. Malfunctioning or offline PMTs not properly diagnosed contribute directly to energy scale error. If a PMT that is not counting photons is considered working when the total optical response is calculated, then on average,

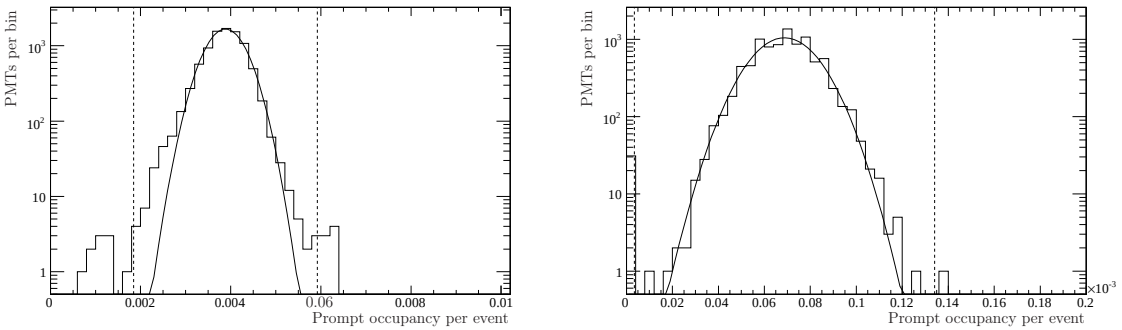

(a) A pure D_2O phase ^{16}N calibration. (b) A long pure D_2O phase neutrino run.

Figure 5.7: The prompt occupancy distribution of all PMTs considered working by RSP. The dashed lines indicate the 5σ range around the mean of the fitted Gaussian.

that response will be one too large in the number of working PMTs. This roughly translates to a 0.01% error in the energy scale per misdiagnosis. Functional channels mistakenly tagged as faulty do not result in energy scale error as they are neither considered during the RSP optical response calculation nor when totaling the number of triggered PMTs N_{hit}.

The PMT prompt occupancy rate, the rate at which a PMT triggers, within 10 ns of the prompt-peak per event, is shown in figure 5.7a for all the PMTs presumed to be working during a central ^{16}N calibration. No PMTs are seen to have a zero occupancy rate. However, to be conservative, the number of PMTs lying more than 5σ from the mean, as determined from a Gaussian fit to the prompt occupancy distribution, are presumed to be not optimally functioning. These PMTs lie beyond the range defined by the dashed lines in figure 5.7a. A conservative estimate of the energy scale uncertainty introduced by these PMTs is determined by averaging the fraction of working PMTs falling outside of the 5σ range for all of the central ^{16}N runs taken during each phase.

As a cross-check of the ^{16}N calibration, the PMT prompt occupancy distributions of production data is also examined. The prompt occupancy distribution for the PMTs during one such pure D_2O phase run is shown in figure 5.7b. Because of the much lower PMT trigger rate, a 5σ range around the peak often includes zero occupancy channels. Only runs containing more than about 6000 events passing data

cleaning cuts are observed to have PMT prompt occupancy distributions with means 3σ above zero occupancy. To be conservative, the PMTs falling in the first, potentially zero occupancy bin, are also included in the number of suspect PMTs counted for each run. The average of the number of suspect PMTs determined from runs with greater than 6000 events is then compared to the more precise determination made using the ^{16}N calibration source data.

PMT gain and threshold

The gains of the PMTs are measured periodically with the laserball while PMT thresholds are recorded at the beginning of every run. Both of these vary with time. These variations can lead to three sources of energy scale error: imprecise modeling in the simulation, variations that are not tracked, and variations that are artificial.

The modeling of the PMT charge spectrum and discriminators is not perfect. Therefore it is not expected that the observed variations are accurately tracked by the simulation. Variations in threshold, beyond those tracked from run to run, and in gain, between the laserball measurements, are likely, but they are obviously not simulated. Additionally, a global offset may exist between high rate ^{16}N calibrations and data that is not modeled in the simulation. There is likely error in the laserball gain calibration as well that results in spurious variations in time.

These effects are to some extent tested by comparing ^{16}N calibrations to simulations. Also, any energy scale errors that average to zero over the livetime of the data do not contribute to the total energy scale error. A preliminary assessment of these uncertainties was performed by the author for the *hep* neutrino analysis of the pure D_2O phase which is discussed in chapter 1, but before any PMT gain and threshold variations were modeled by the simulation. The energy scale uncertainty induced by PMT gain and threshold variations for the LETA analysis of the pure D_2O and salt phases (and incidentally a very complete review of the issues involved in making these measurements) appear in Klein [83]. The energy scale uncertainty caused by PMT gain and threshold variations in the NCD phase, which are determined based on what was done for the *hep* analysis of the pure D_2O phase by this author, are given by Secrest [84]. Note that this analysis is rudimentary when compared to the analysis of Klein [83] but the uncertainties are safely conservative.

PMT timing calibration

The PMT trigger times, corrected for photon time-of-flight from the event vertex to the PMT, are shown in figure A.1. For analysis by RSP the PMT time residuals ($t_{\rm res}$) must be less than 10 ns from the prompt peak. Variation in the mean $t_{\rm res}$ or its resolution alters the number of triggered PMTs within the prompt analysis window. The possible energy scale error caused by this effect was initially estimated at 0.1% by Graham [85]. The $t_{\rm res}$ distribution mean and resolution variations are consistent from phase to phase therefore a value of 0.1% is adopted for all three.

The direct comparison of SNOMAN simulations to calibrations provides the most robust test of the accuracy of the simulated signal PDFs. To test the energy scale, the fractional difference F between the mean energy of ^{16}N calibrations ($T^{\rm data}$) and the mean energy of the simulations ($T^{\rm MC}$) is calculated via

$$F^{\mu} = \frac{T^{\rm data} - T^{\rm MC}}{T^{\rm data}} \tag{5.3}$$

for each ^{16}N calibration separated in time, space, or by event rate. The weighted mean average of a series or subset of ^{16}N calibrations is then used to determine the error resulting from the specific conditions associated with those runs. Generally the weighted mean is determined via the prescription outline in appendix C and applied as the energy scale uncertainty or error with an uncertainty.

The error associated with using the simulation to determine the reconstructed energy scale, specifically how the simulation can differ from the data, include:

Temporal variation

The detector energy scale is known to vary with time. A correction is applied in the form of $\delta_{\rm drift}$ as described in section 5.4. The correction is derived based only on high statistics central ^{16}N calibrations as evenly spaced in time as possible so as not to bias the determination of $\delta_{\rm drift}$ to any specific calibration period. To determine any residual time dependence, the mean energy of all nominal central ^{16}N calibrations[4]

[4]The time distribution of these calibrations differs from that used to tune $\delta_{\rm drift}$ for the simulation since many more calibration runs are included.

are compared to the simulation by calculating F^{μ} for each pair. The weighted mean of F^{μ} is the error in the energy scale at the centre of the detector. This error is generally negligible because the energy scale is tuned at the centre of the detector. The energy scale uncertainty associated with any remaining time dependence in the temporal variation of the energy scale is assessed from the error on the mean. If the reduced χ^2 of the mean is less than 1.0 the assumption that the energy scale is constant is good to within the uncertainty on the mean. If it is greater than 1.0, then the uncertainty in the mean is increased to account for the disagreement with the constant energy scale model. A procedure to weight the uncertainty on the mean by the χ^2 is reviewed in appendix C.

Spatial variation

The energy scale of SNO is known to differ from that in the simulation as a function of event position. This is apparent when comparing the mean energy of calibration sources, especially ^{16}N, to their simulation. To quantify the error this induces on the energy scale, the F^{μ} for each pair of calibration and simulation must be weighted according to the fraction of the expected signal that they are representative of. Since the neutrinos interact uniformly in within the D_2O, this amounts to volume weighting the significance of each calibration.

To accomplish this, the detector is divided into N elements, the i^{th} possessing a volume v_i. The location and size of each volume element is chosen such that they surround local groupings of ^{16}N calibrations[5]. The average fractional difference f^{μ}, between the mean energy of each calibration (T^{data}) and the mean energy of its simulation (T^{MC}) is calculated for each volume element via

$$f^{\mu} = \frac{\sum_j W_j F_j^{\mu}}{\sum_j W_j}, \tag{5.4}$$

where the sums are over all the calibrations done in the volume element, $j = 1$ to n_i, and $W_j = (1/\delta F_j^{\mu})^2$.

[5]Every attempt is made to centre the calibrations within the volume elements and to have the element boundaries centred between the groups of calibration points. This is not necessarily achievable as several calibrations are required to lie within every volume element to average statistical and temporal variations (see the previous section where these are accounted for).

As the spread in the values of F^μ within each volume element is generally more than expected based on the statistics, the RMS of the fractional differences in a given volume element is assumed to be a better estimate of the uncertainty on the mean, as is done by Seibert [31]. This amounts to an uncertainty δf^μ on f^μ given by

$$(\delta f^\mu)^2 = \frac{1}{n_i - 1} \sum_{j=1}^{n_i} \left(F_j^\mu - f^\mu\right)^2 . \tag{5.5}$$

The χ^2 is calculated between the weighted mean of the f^μ and each measurement to determine the appropriate scale factor S to apply to the errors δf^μ as detailed in appendix C. In this case S reflects the fact that the f^μ values do not sample the same distribution (assumed when calculating the standard error on a weighted mean) since the energy scale is known to vary between volume elements. Including the volume weighting, the energy scale error $\Delta\mu_T$ is determined from

$$\Delta\mu_T \pm \delta\mu_T = \frac{\sum_i w_i f_i^\mu}{\sum_i w_i} \pm \left(\textstyle\sum_i w_i\right)^{-\frac{1}{2}}, \tag{5.6}$$

where in this case, the sum is over all the volume elements and

$$w_i = \frac{N v_i}{\sum_i v_i} \left(S \delta f_i^\mu\right)^{-2} .$$

If $\Delta\mu_T$ is small, the uncertainty in the energy scale may be taken as the quadrature sum of $\Delta\mu_T$ and $\delta\mu_T$. Alternatively, $\Delta\mu_T$ may be used to correct the energy of events in the data, in which case the energy scale uncertainty is then simply $\delta\mu_T$.

Event rate dependence

The total data taking rate varies from a few hundred to thousands of Hz. The majority of these events are instrumental backgrounds that generally induce a small amount of charge in the average PMT. The ^{16}N source, as it is generally operated, produces a triggered event rate greater than 100 Hz, while the normal rate of physics events, including backgrounds from radioactivity in the detector, is on the order of only a few Hz. The increase in rate of high charge PMT triggers during the calibration can make it easier for a PMT to trigger if there is residual charge build up. A series of

low rate ^{16}N calibrations are performed during each phase, fewer in the pure D_2O phase, to test how applicable the calibrations done at high rate are to normal data taking. These low rate ^{16}N calibrations yield a triggered event rate of only about a few Hz above normal.

The comparison between the mean energy of the low rate ^{16}N calibrations and that of the simulation is calculated in the form of F^{μ}. The weighted mean of F^{μ}, calculated as in appendix C, is the energy scale error associated with any event rate dependence.

Low rate ^{16}N calibrations are also done at other positions within the detector. The limited number of non-central calibrations, coupled with the spatial variations discussed in the previous section, preclude a measurement of the event rate effect other than at the centre of the detector. However, examination of these runs shows no significant deviation from the trends observed for the high rate ^{16}N calibrations.

The contributions of each of these errors to the total energy scale error are evaluated for the energy calibration of each phase. They are generally evaluated independently due to the changes in the detector configuration from phase to phase. The analysis of the pure D_2O and salt phase energy scale errors is presented later in this chapter. The analysis of the NCD phase energy scale error is presented in the following chapter.

5.5.2 Energy resolution error

There is no single parameter that describes energy resolution in the way that $\epsilon_{\circ}$ is representative of the energy scale. It is consistently observed that SNOMAN simulations underestimate the energy resolution of the detector. The source of this discrepancy could be in some simplification of the detector geometry in the simulation or that some randomizing effects are either overlooked or underestimated. It is unlikely that the input model parameter errors can contribute significantly to these effects, rather they are likely due to errors in the model itself.

Again, as in the case of the energy scale error measurement, SNOMAN simulations are directly compared to ^{16}N calibrations. To test the energy resolution, the fractional

difference F^{σ}, between the energy resolution of ^{16}N calibrations (σ^{data}) and the energy resolution of the simulations (σ^{MC}) is calculated

$$F^{\sigma} = \frac{\sigma^{\mathrm{data}} - \sigma^{\mathrm{MC}}}{\sigma^{\mathrm{data}}}, \tag{5.7}$$

for each ^{16}N calibration run. The dominant contributions to energy resolution errors include:

Temporal variation

The energy resolution can potentially vary with time as is observed of the energy scale. To quantify any time dependence, the energy resolution of all nominal central ^{16}N calibrations are compared to SNOMAN simulations by calculating F^{σ} for each pair. The weighted mean of these F^{σ} is the error in the energy resolution at the centre of the detector. This error is consistently greater than zero; the simulation underestimates the energy resolution of the detector. The energy resolution uncertainty associated with any potential time dependence in the temporal variation of the energy resolution is assessed from the error on the mean. If the χ^2 of the weighted mean is poor, indicating poor agreement with the hypothesis that the energy resolution error is constant in time, the uncertainty on the mean is increased as per the schema described in appendix C. The χ^2 weighted–weighted mean uncertainty is taken as the uncertainty in the energy resolution due to any potential time dependence in the energy scale error.

Spatial variation

The energy resolution can potentially vary with position as is observed of the energy scale. To quantify the potential error this induces on the energy resolution, the fractional differences F^{σ}, between ^{16}N calibrations and simulations, must be weighted according to the fraction of the expected signal that they are representative of. Since the neutrinos interact uniformly in within the D_2O this amounts to volume weighting the significance of each calibration.

To accomplish this, the detector is divided into the same N elements as is done for the energy scale spatial variation error determination. The average fractional

difference f^σ is calculated from equations 5.4 and 5.5 with F^μ obviously replaced with F^σ.

The χ^2 for the weighted mean of all f^σ is then calculated to determine the appropriate scale factor S to apply to the errors δf^σ as detailed in appendix C. Including the volume weighting, the energy resolution error $\Delta\sigma_T$ due to spatial variation is calculated:

$$\Delta\sigma_T \pm \delta\sigma_T = \frac{\sum_i w_i f_i^\sigma}{\sum_i w_i} \pm \left(\sum_i w_i\right)^{-\frac{1}{2}}, \tag{5.8}$$

where the sum is over all the volume elements and

$$w_i = \frac{N v_i}{\sum_i v_i} \left(1/\delta f_i^\sigma\right)^2 .$$

The energy resolution uncertainty determined by the ^{16}N calibrations is directly applicable only to γ-ray events such as the signal of the NC reaction. The energy resolution of the ^{16}N calibration includes a contribution due to the energy distribution of Compton scattered electrons, due to the various energies of γ-rays and the statistical nature of Compton scattering. This has been estimated at 0.61 MeV by Dunford [86] via Monte Carlo calculations. The ^{16}N energy resolution must be corrected for this (in quadrature difference) to determine the single electron equivalent energy resolution of the γ-ray calibration.

The energy resolution error is therefore the result of error in the simulation of Compton scattering and error in the energy resolution of the individual electrons. To be conservative, the latter is assumed to be responsible for all of the energy resolution error measured using the ^{16}N calibrations. Then, the absolute value of the ^{16}N energy resolution error $\Delta\sigma_{^{16}\mathrm{N}}$ should be applied to the equivalent energy resolution σ_e for a single electron of equivalent energy (to the ^{16}N mean energy). This net effect is a fractional energy resolution error for single electrons of

$$\Delta\sigma_\mathrm{e} = \frac{\left[(1+\Delta\sigma_{^{16}\mathrm{N}})\sigma_{^{16}\mathrm{N}}\right]^2 + \sigma_\mathrm{e}^2}{\sigma_\mathrm{e}^2}.$$

Given that the electron equivalent energy resolution error is parametrized as a function of that measured with the ^{16}N calibrations, only $\Delta\sigma_{^{16}\mathrm{N}}$ is specified throughout

the remainder of this work.

The contributions of these errors to the total energy resolution error are evaluated for the energy calibration of each phase. Like the energy scale errors, they are generally evaluated independently due to the changes in the detector configuration from phase to phase. The analysis of the pure D_2O and salt phase energy scale errors is presented later in this chapter. The analysis of the NCD phase energy scale error is presented in the following chapter.

5.6 LETA pure D_2O phase energy response

To complete the SNOMAN simulation of the detector and to be able to determine the energy response of the detector using RSP, the energy scale of the detector, which is parametrized by the PMT collection efficiency $\epsilon_\circ$, is determined by comparing the energy response of the simulation to that of ^{16}N calibrations. A time dependence to the detector energy scale is noted and applied to $\epsilon_\circ$ in order to better model the detector. With these in hand, the energy calibration function ($\mathcal{F}_E$) is determined from simulated electrons. The performance of the RSP energy reconstruction as a whole is also evaluated with these simulated electrons.

5.6.1 Energy scale drift

The mean number of initial photons N_γ is plotted in figure 5.8 for selected ^{16}N calibrations performed during the pure D_2O phase. The data points represent the mean N_γ as estimated by RSP for only high statistics central ^{16}N calibrations. N_γ should be constant for all times and positions to within the accuracy of the RSP optical response. From the data it is clear that there is a time dependent response not accounted for by RSP.

As is described in section 5.4, a parametrization of this energy scale drift (δ_{drift}) is required to tune the time variation of $\epsilon_\circ$ in the SNOMAN simulation. The function shown in figure 5.8 is the pure D_2O phase δ_{drift}, which is defined by

$$\delta_{\text{drift}}(t) = \begin{cases} m_1 t + b & \text{for } t \leq t_\circ \text{ and} \\ m_2 t + b' & \text{for } t > t_\circ, \end{cases} \tag{5.9}$$

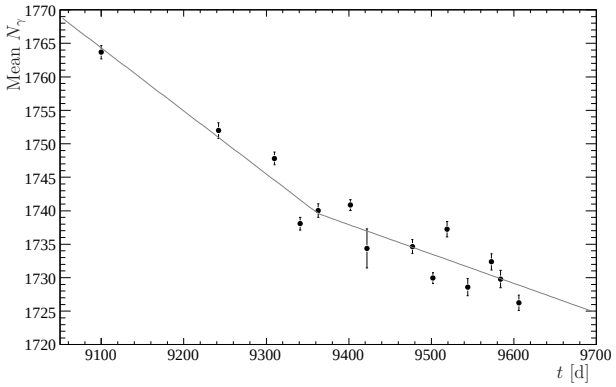

Figure 5.8: The mean N_γ of selected central ^{16}N calibrations performed during the pure D_2O phase.

Parameter	Fit result
$t_\circ$	9363
b	1.50674
m_1	-5.41216×10^{-5}
m_2	-2.52443×10^{-5}

Table 5.1: The parameters extracted from a fit of the function defined by equation 5.9 to the mean response of ^{16}N calibrations presented in figure 5.8. The function parameters have been scaled such that the equation 5.9 is normalized at $t_\circ$.

where b' is fixed by requiring the function to be continuous at $t_\circ$. This condition is satisfied for

$$b' = m_1 t_\circ + b - m_2 t_\circ. \tag{5.10}$$

The parameters b, m_1, m_2, and $t_\circ$ are determined by a χ^2 fit of δ_{drift} to the ^{16}N calibrations as shown in figure 5.8. The parameters extracted from the fit are presented in table 5.1 after normalizing the function at $t_\circ$.

The energy response drift observed in the pure D_2O phase data, equation 5.9 with the parameters listed in table 5.1, is implemented in SNOMAN by applying it as a time dependent correction to the PMT collection efficiency $\epsilon_\circ$ as per equation 5.1. It is also used to correct the RSP reconstructed energy T_{eff} as per equation 5.2.

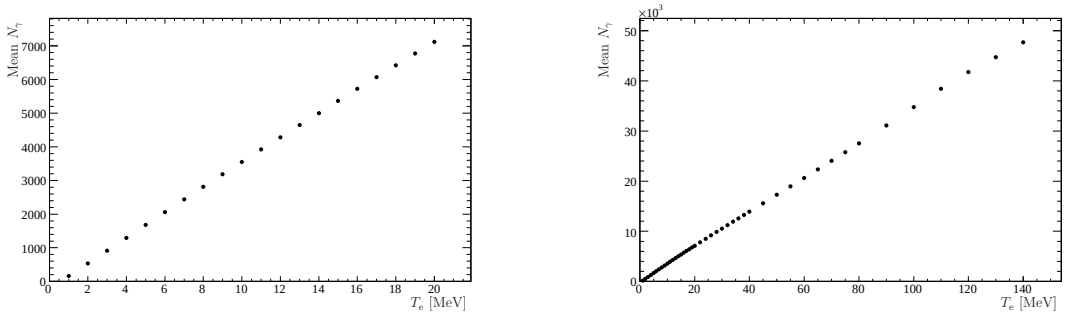

(a) Electrons with energies from 1 to 20 MeV. (b) Electrons with energies from 1 to 140 MeV.

Figure 5.9: The pure D_2O phase energy calibration function $\mathcal{F}_E$.

5.6.2 PMT collection efficiency

The PMT collection efficiency ($\epsilon_\circ$) is tuned for the LETA pure D_2O phase analysis following the procedure outlined in section 5.3 using the comparison between all central ^{16}N calibrations and SNOMAN simulations. Initially, $\epsilon_\circ$ was set to 0.54225[6] in the simulation. The difference between the ^{16}N calibration mean N_γ and that of the simulation implied that $\epsilon_\circ$ should be 0.674770. The large increase in $\epsilon_\circ$, from that of the previous analysis, was due to significant improvements made in the simulation—most notably in the PMT angular response. $\epsilon_\circ$ is therefore set to 0.674770 for all pure D_2O phase SNOMAN simulations and in the RSP optical response for the energy reconstruction of all pure D_2O phase events, be they simulated or in the data.

5.6.3 Energy calibration function

The energy calibration function ($\mathcal{F}_E$) is derived from the number of initial photons N_γ, as estimated by RSP, produced by electron events simulated by SNOMAN. A series of homogeneously distributed electrons, with the energies appearing in table 4.1, were generated. For each electron energy, a Gaussian function is fit to the N_γ distribution as described in appendix B. The mean of the Gaussian function is plotted as a function of electron energy T_e in figure 5.9. For the pure D_2O phase, $\mathcal{F}_E$ consists of a linear interpolation of the points in figure 5.9.

[6] 0.54225 is the value of $\epsilon_\circ$ determined by the author for the *hep* analysis of the pure D_2O phase.

5.6.4 Electron energy response

Homogeneously distributed electron simulations provide an interesting test of the energy reconstruction because they are equivalent to the signal expected from the charged current and elastic scattering neutrino interactions. To test the accuracy and resolution of the RSP energy reconstruction, the simulated electrons in the previous section were reprocessed with $\mathcal{F}_E$ as shown in figure 5.9. The mean RSP reconstructed energies (T_{eff}) of the electrons, simulated with energies from 2 to 10 MeV, are plotted in figure 5.10a as a function of reduced radius. A bias is noted in the reconstructed energy; T_{eff} decreases with increasing radial position.

The radial bias is believed to be a result of an approximation made by RSP in determining the PMT solid angle (Ω in equation 4.35). For the LETA pure D_2O and salt phase reprocessing, Ω is calculated as

$$\Omega_i = \cos\theta_n \frac{589\,\text{cm}^2}{|d|^2}, \tag{5.11}$$

where θ_n is the angle of incidence from the PMT normal, $589\,\text{cm}^2$ is approximately[7] the normal incidence cross-sectional area of the PMT reflector assembly, and d is the sum of the optical path lengths through the D_2O, acrylic, and H_2O. With the more detailed calculation of Ω presented in subsection 4.2.6, no radial dependence to the energy scale is observed. This is the case for the energy reconstruction of NCD phase events, which is to be described in the following chapter.

Given that the source of the bias in the pure D_2O and salt phases is well understood, a correction based on the energy response of the simulated electrons is deemed appropriate. Figure 5.11 is the ratio of the mean reconstructed energy T_{eff} to electron energy T_{e}. This correction function consists of an interpolation of the complete set of data, for electrons with energies from 2 to 130 MeV, represented by the subset shown in figure 5.10a. No radial bias is apparent in figure 5.10b which is derived from the events used to create figure 5.10a but with the radially dependent energy correction presented in figure 5.11.

[7]This value is inherited from the original version of RSP. The actual normal incidence cross-sectional area of the PMT reflector assembly—with a radius of 13.45 cm—is $568\,\text{cm}^2$.

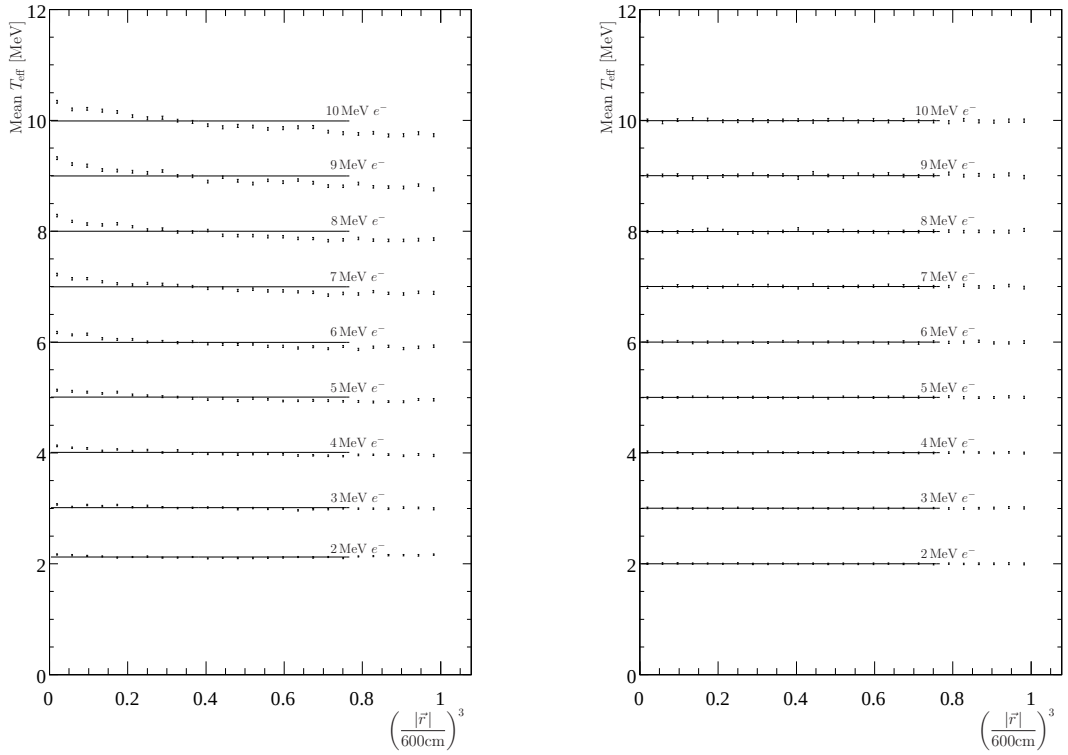

(a) Before applying a radially dependent correction.

(b) After applying the correction function represented by figure 5.11.

Figure 5.10: The mean reconstructed energy of electrons as a function of radial position for the pure D_2O phase. The electrons within the radius of the acrylic vessel (reduced radius of 1.0) are divided into 20 radial bins. The mean energy (each point) is the result of fitting a Gaussian to the energy distribution of electrons within each radial bin.

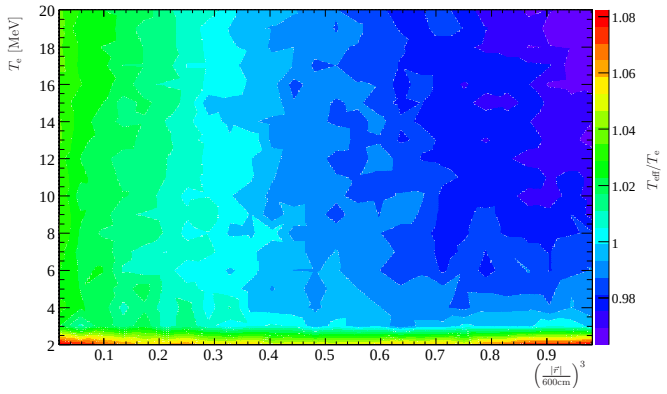

Figure 5.11: The ratio of mean reconstructed energy T_{eff} to the electron energy T_{e} at which the electrons were simulated by SNOMAN. The mean T_{eff} are the same as those presented in figure 5.10a. The RSP T_{eff} of all pure D_2O phase events, both those that are simulated and those that appear in the data, should be divided by the value of this function.

Figure 5.12 shows the deviation of the mean T_{eff} from T_{e}. The mean T_{eff} is determined from the weighted average of the data points shown in figure 5.10b. The weighted means are also shown in figure 5.10b as the fits to the data points. Only the data points within the fiducial volume, defined by a maximum radius of 550 cm (a reduced radius of 0.77), are used in the average.

The energy resolution σ_T that is determined from these SNOMAN simulated electrons is presented in figure 5.13. The energy resolution function shown fit to the data is

$$\sigma_T = -0.185 + 0.413\sqrt{T_{\text{e}}} + 0.0254\,T_{\text{e}}. \tag{5.12}$$

This may be compared to the dashed line in figure 5.13 that indicates the energy resolution measured for the first analysis of the pure D_2O phase data published in Aharmim et al. [32].

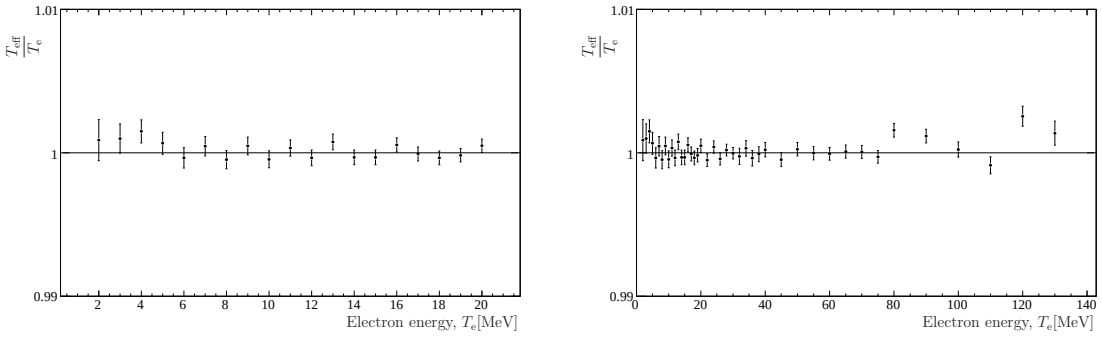

(a) Electrons with energies from 2 to 20 MeV. (b) Electrons with energies from 2 to 130 MeV.

Figure 5.12: Fractional deviation of the mean reconstructed energy ($T_{\rm eff}$) from the electron energy ($T_{\rm e}$) for the pure D_2O phase. The mean at each electron energy is also shown as fit to the data points in figure 5.10b.

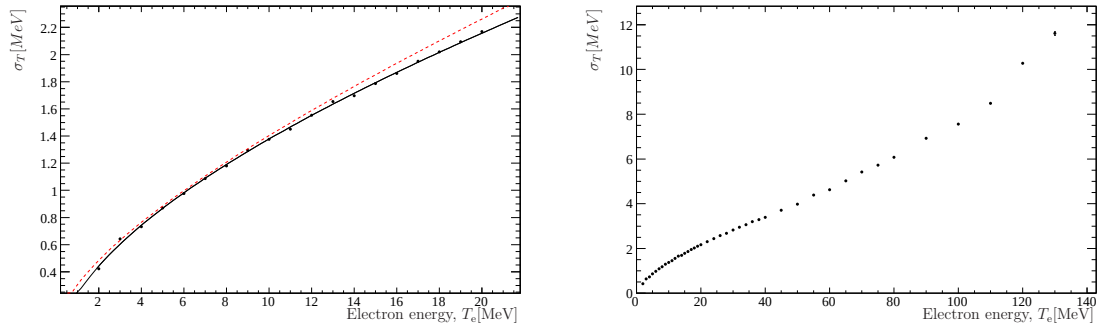

(a) Electrons with energies from 2 to 20 MeV. (b) Electrons with energies from 2 to 130 MeV.

Figure 5.13: Energy resolution σ_T of SNOMAN simulated electrons as a function of the electron energy $T_{\rm e}$. The dashed line is the energy resolution of the original RSP as published in Aharmim et al. [32].

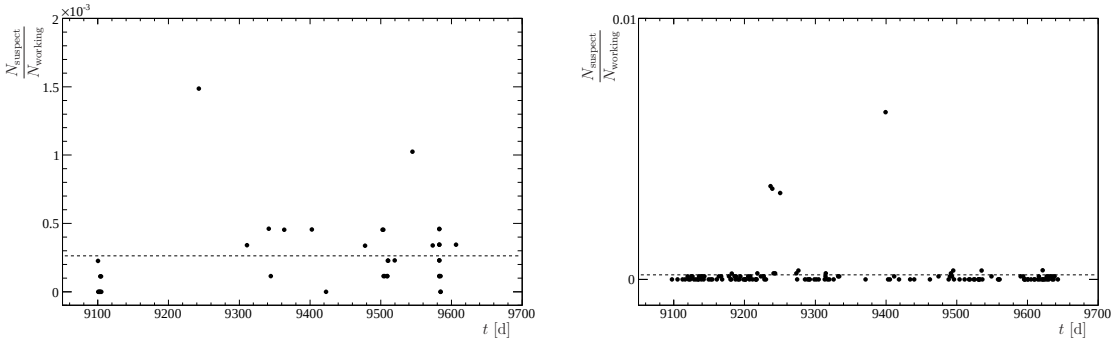

(a) Low rate central ^{16}N calibrations. (b) Long neutrino runs.

Figure 5.14: The fraction of PMTs considered in good working order that have suspect occupancy rates during pure D_2O phase. The means of the data points are 0.026% and 0.015% respectively.

5.7 LETA pure D_2O phase energy reconstruction error

Contributions to the RSP energy reconstruction error for the LETA of the pure D_2O phase are presented. The potential errors detailed in section 5.5, including those from other sources, are summarized in section 5.10.

5.7.1 PMT status

The fraction of working PMTs with occupancy rates, per event, more than 5σ from the mean is plotted in figures 5.14a and 5.14b for pure D_2O phase central ^{16}N calibrations and data runs respectively. The mean value for the ^{16}N calibrations is 0.026%.

As a cross-check of the ^{16}N calibration, the mean fraction of PMTs that are suspect but considered working by RSP are shown in figure 5.14b for high statistics neutrino runs. The mean value from figure 5.14b is 0.015%, which is consistent with that observed for the more precise determination made using ^{16}N calibrations. Therefore, the greater of the two uncertainties—0.026%—is adopted as the contribution to the pure D_2O phase energy reconstruction error.

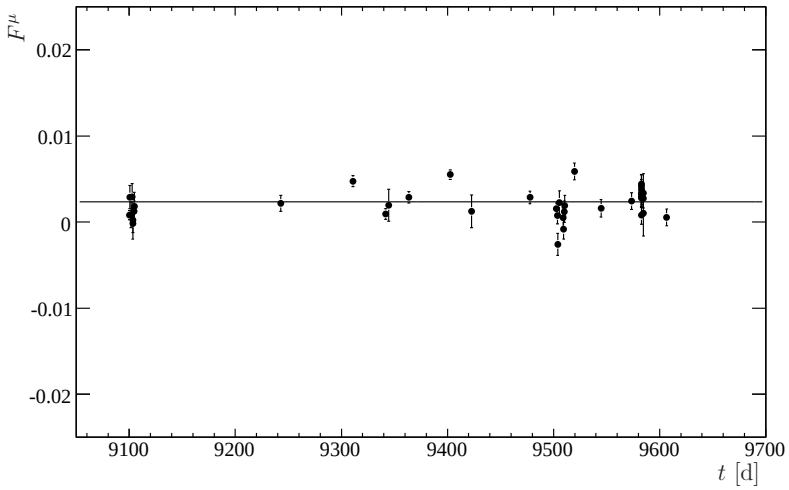

Figure 5.15: The fractional difference F^{μ} between the mean energy of central ^{16}N calibration data, taken during the pure D_2O phase, and the simulation as a function of time. The mean of the data points is $-0.237 \pm 0.016\%$.

5.7.2 Energy scale temporal variation

The fractional difference F^{μ} between the mean energy of central ^{16}N calibrations and simulations for the pure D_2O phase are shown in figure 5.15. A mean error of $0.237 \pm 0.016\%$ is observed. However, the χ^2 per degree of freedom is 128.4/38. The uncertainty on the mean is increased to account for this (see appendix C) such that the mean becomes $0.237 \pm 0.029\%$. The overall error is accounted for, with its proper weight, in the determination of the spatial variation error. The contribution to the uncertainty in the energy scale error is 0.029%.

It is worth commenting on the fact that the mean is not zero. The energy scale is tuned, via the comparison of ^{16}N calibrations to the simulations, at the centre of the detector. An offset at the centre of the detector implies that the energy scale is set. via $\epsilon_{\circ}$, incorrectly; an inaccurate value of $\epsilon_{\circ}$ is used in the simulation. The source of the offset has been traced to an empirical correction that is used to improve agreement between the ratio of prompt to total number of triggered PMTs in the calibrations and the simulation by a factor of 0.996. The correction alters the mean N_{eff} in the simulation. The correction was not in place when $\epsilon_{\circ}$ was tuned leading to

Radial bin range (cm)	Polar angle bin edges
0–150	0, π
150–375	0, 1.17, 1.96, π
375–550	0, 0.38, 1.17, 1.96, 2.75, π
550–600	0, 0.38, 1.17, 1.96, 2.75, π

Table 5.2: Spatial binning of the pure D_2O phase ^{16}N calibrations based on the distribution of calibrations done within the D_2O. The outermost radial bin is lies outside the fiducial volume.

the slightly incorrect energy scale determination.

5.7.3 Energy scale spatial variation

The spatial distribution of ^{16}N calibrations during the pure D_2O phase leads to the volume partitioning of the detector listed in table 5.2. This volume binning is also depicted in figure 5.16 where only about half of each of the outer bins is shown for illustrative purposes. Several volume bins are combined to increase the number of calibrations in these regions. The volume bounded by radii of 375 and 550 cm and angles 0.38 to 1.17 contains no ^{16}N calibrations during the pure D_2O phase. The outer most radial bins are not considered during this analysis as they are external to the fiducial volume.

Figure 5.17 shows the distribution of F^{μ} for each of the pure D_2O phase ^{16}N calibrations as a function of the source radial position. The colours of the points indicate in which volume element, as in figure 5.16, the data resides. The mean, with RMS error, of each group of like-coloured points is plotted in figure 5.18. The coloured bands indicate the fraction of the total fiducial volume each point represents. The energy scale error $\Delta\mu_T$, calculated as per the prescription detailed in subsection 5.5.1, is shown as the solid line with dashed error band on figure 5.18. $\Delta\mu_T$ is determined to be $0.304 \pm 0.169\%$.

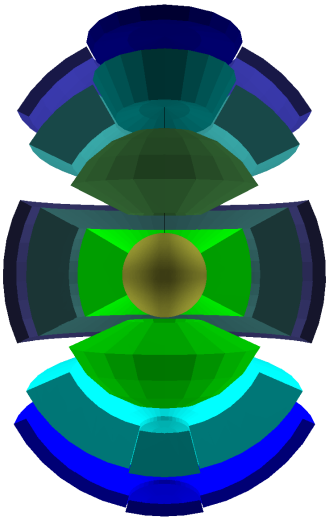

Figure 5.16: Exploded cross-sectional depiction of the spatial binning listed in table 5.2. The polar angle coordinate is the angle from a vertical line with its origin at the centre of the solid inner sphere.

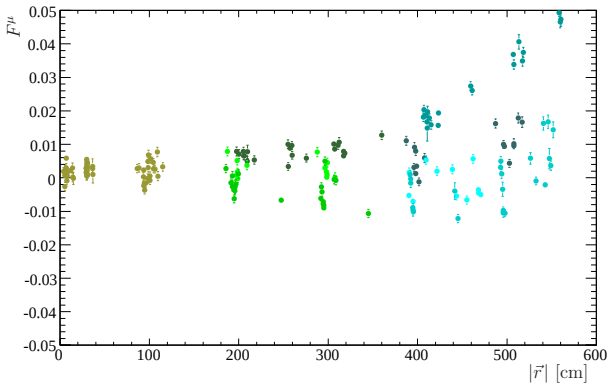

Figure 5.17: The fractional difference F^μ between the mean energy of pure D_2O phase ^{16}N calibrations and simulations as a function of source radius. The colours of the points correspond to the volume element colours in figure 5.16.

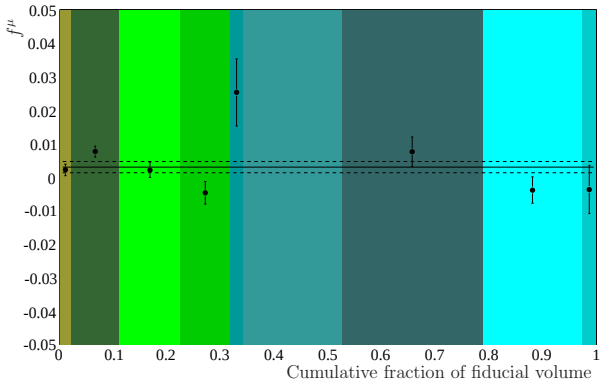

Figure 5.18: The mean f^μ of the like coloured points in figure 5.17 with RMS error bars. The colours of the bands correspond to the volume element colours in figure 5.16. There is no data point in the sixth colour band as no ^{16}N calibrations are performed in that volume element. The solid line with dashed error band illustrates the volume weighted mean of the data points is $\Delta\mu_T = 0.304 \pm 0.169\%$.

5.7.4 Event rate dependence

The fractional difference F^μ, between the mean energy of low rate central ^{16}N calibrations and the simulation in the pure D_2O phase, is plotted in figure 5.19. An energy scale error of $-0.083 \pm 0.199\%$ is observed.

5.7.5 Energy resolution temporal variation

The fractional difference F^σ, between the energy resolution of central ^{16}N calibrations and that of the simulation, in the pure D_2O phase are shown in figure 5.20. A mean error of $1.610 \pm 0.119\%$ is observed. The overall error is large but is accounted for, with the proper weighting, in the determination of the spatial variation error. The contribution to the uncertainty in the energy resolution error is 0.119%.

5.7.6 Energy resolution spatial variation

The same spatial binning that is used for the determination of the energy scale error associated with spatial variations (subsection 5.7.3) is appropriate to use in this case. Figure 5.21 shows the distribution of F^σ for each of the pure D_2O phase ^{16}N calibra-

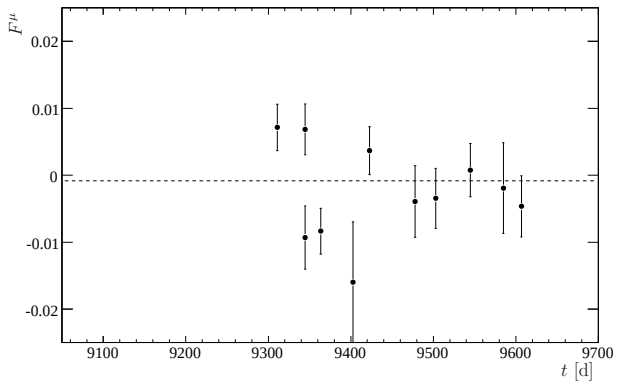

Figure 5.19: The fractional difference (F^{μ}) between the mean energy of low rate ^{16}N calibrations and the simulation is plotted as a function of time during the pure D_2O phase. A mean offset of $-0.083 \pm 0.199\%$ is observed.

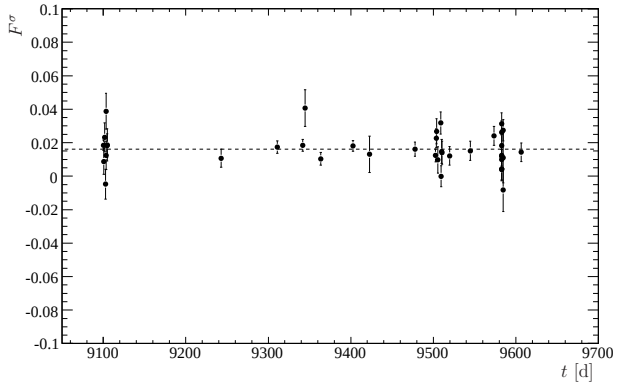

Figure 5.20: The fractional difference F^{σ} between the energy resolution of ^{16}N calibrations and that of the simulation in the pure D_2O phase. The mean of the data points is $1.610 \pm 0.119\%$.

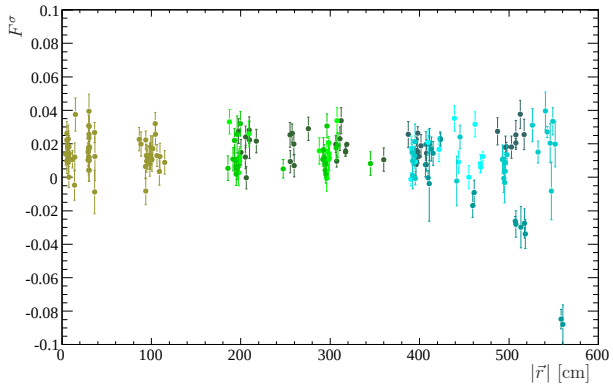

Figure 5.21: Fractional difference F^σ between the energy resolution of pure D_2O phase ^{16}N calibrations and that of the simulation. The colors of the points correspond to the volume element colors in figure 5.16.

tions as a function of the source radial position. The colours of the points indicate in which volume element, as in figure 5.16, the data resides. The mean, with RMS error, of each group of like-coloured points is plotted in figure 5.22. The coloured bands represent the fraction of the total fiducial volume each point represents. $\Delta\sigma_T$, calculated as per the prescription detailed in subsection 5.5.1, is shown as the solid line with dashed error band on figure 5.22. The energy resolution error $\Delta\sigma_T$ due to the spatial variation in the difference between ^{16}N calibrations and the simulation is $1.528 \pm 0.238\%$.

5.8 LETA salt phase energy response

In the salt phase, the time dependence of the detector energy response is well modeled; the energy scale is constant in time. An incidental time dependence to the energy scale of the simulation is easily accounted for. The PMT collection efficiency $\epsilon_\circ$ and the energy calibration function $\mathcal{F}_E$ are determined analogously to those in the pure D_2O phase.

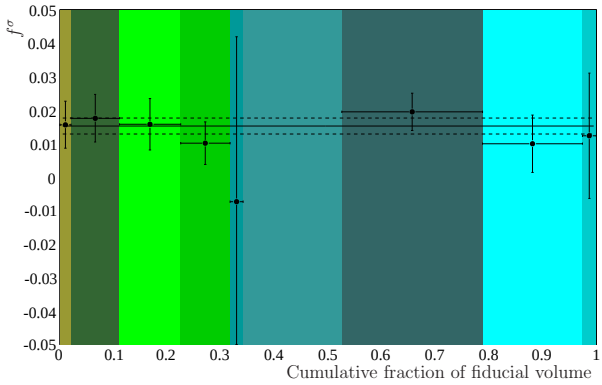

Figure 5.22: The mean f^σ of the like coloured points in figure 5.21 with RMS error bars. The colours of the bands correspond to the volume element colours in figure 5.16. There is no data point in the sixth colour band as no ^{16}N calibrations were performed in that volume element. The solid line with dashed error band illustrates the volume weighted mean of the data points $\Delta\sigma_T = 1.528 \pm 0.238\%$.

5.8.1 Energy response drift

The mean number of initial photons N_γ is plotted in figure 5.23 for selected ^{16}N calibrations (grey points) performed during the salt phase. The N_γ of each event is estimated with RSP; the mean of the N_γ distribution of each calibration is the mean of a Gaussian function fit to it according to the method described in appendix B. Also shown in figure 5.24 are the mean N_γ of the corresponding simulations. The two disagree by 4–5% because the PMT collection efficiency $\epsilon_\circ$ has yet to be tuned in the simulation.

In contrast to the pure D_2O phase, the energy scale of the detector is constant in time during the salt phase. However, this is obviously not the case for the simulation. This indicates that there is a time dependence in the simulation that is not observed in the data; this is the opposite of the case in the pure D_2O phase and, as will be shown, the NCD phase. Due to the detailed optical calibration performed during the salt phase, the time dependent changes in the water attenuations[8] and PMT

[8]The time dependence of the attenuations is specific to the salt phase. Manganese contamination in the water, introduced from MnO_x water assays, continually built up over the course of the phase. The Mn is removed during the pure D_2O and NCD phases by a process that would have removed the salt from the salt phase.

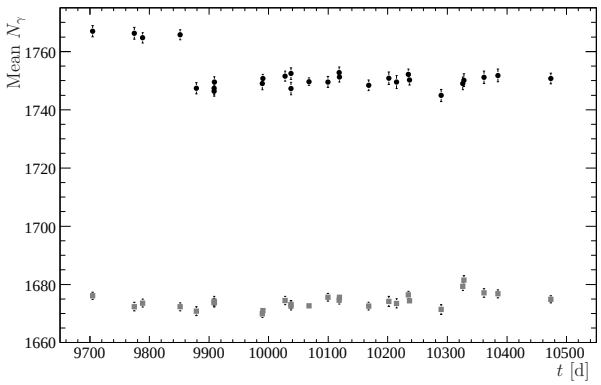

Figure 5.23: The mean N_γ. The black points are the mean N_γ of the corresponding simulations. The large offset is a result of the fact that the energy scale of the simulation had yet to be tuned.

angular response are measured with enough confidence to incorporate both into the the simulation and the RSP optical model. The implementation of the PMT angular response in the simulation and RSP differs. RSP uses the angular response determined from laserball calibrations directly; it approximates the PMT response in exactly the same way. The simulation tracks photons through a full three dimensional simulation of the PMTs. It is tuned such that its integrated response matches that observed by the laserball. This tuning [30] is done for three time periods corresponding to the three major optical calibrations which is obvious from the two steps seen at 9879 d and 10350 d in figure 5.24 (the ratio of the response of the data to the simulation is normalized to 1.0 in the central region). The normalization of the 3–D PMT model angular response varies between these time periods. However, as is discussed in section 3.4, the angular response E is relative; the absolute efficiency is specified by the PMT collection efficiency $\epsilon_\circ$. Hence, a time dependence to $\epsilon_\circ$ in the simulation is required to properly normalize the overall PMT efficiency.

The energy scale drift δ_{drift}, of the simulation in this case, combined with any residual scale drift in the ^{16}N calibrations is the function shown fit to the data points

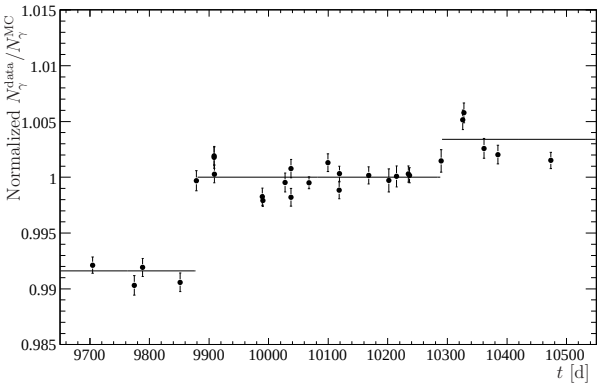

Figure 5.24: The ratio of the mean N_γ of ^{16}N calibrations to that of the simulation. The three piece function shown fit to the data points is $\delta_{\rm drift}$ for the salt phase.

in figure 5.24. The function is given by

$$\delta_{\rm drift}(t) = \begin{cases} 0.9916 & \text{for } t < 9879\,\text{d}, \\ 1.0000 & \text{for } 9879\,\text{d} \leq t \leq 10290\,\text{d}, \text{ and} \\ 1.0034 & \text{for } t > 10290\,\text{d}. \end{cases} \tag{5.13}$$

Applying this function to $\epsilon_\circ$ in the simulation, as specified by equation 5.1, ensures that any time dependence in the ^{16}N calibrations is tracked by the simulation. However, no correction is made to the RSP reconstructed energy of events during the salt phase as the RSP estimated energy scale, indicated by the mean N_γ of the ^{16}N calibrations in figure 5.23, is not observed to vary with time.

5.8.2 PMT collection efficiency

The PMT collection efficiency ($\epsilon_\circ$) is tuned for the LETA processing of the salt phase data following the procedure outlined in section 5.3 using the data presented in figure 5.23 together with all other, nominal, central ^{16}N calibrations. $\epsilon_\circ$ was initially set to 0.674770, the value determined for the pure D_2O phase, when generating the simulations shown in figure 5.23. The difference between the ^{16}N calibration mean N_γ and that of the simulation, as evident in figure 5.23, implies that $\epsilon_\circ$ should be 0.6454 for the salt phase. $\epsilon_\circ$ is therefore set to 0.6454 for all of the LETA salt phase

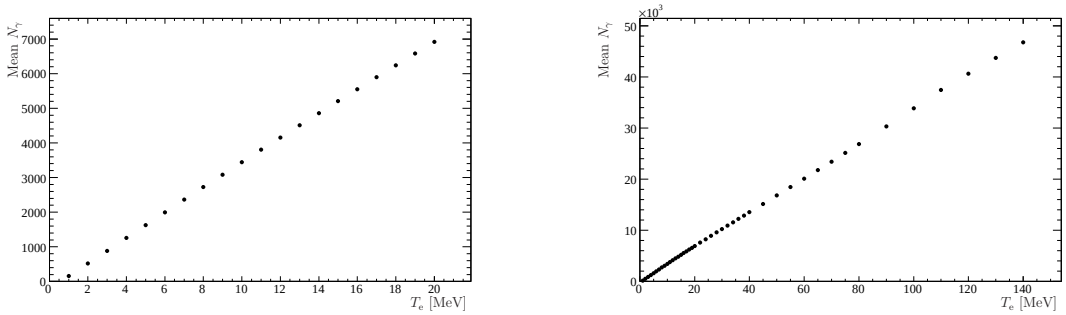

(a) Electrons with energies from 1 to 20 MeV. (b) Electrons with energies from 1 to 140 MeV.

Figure 5.25: The salt phase energy calibration function $\mathcal{F}_E$.

SNOMAN simulations and in RSP for the energy reconstruction of all salt phase events, be they simulated or in the data.

5.8.3 Energy calibration function

The principles and method behind the derivation of the energy calibration function ($\mathcal{F}_E$) are the subject of section 4.5. To calibrate $\mathcal{F}_E$ that is specific to the salt phase detector conditions a series of homogeneously distributed monoenergetic electrons are simulated. The energies at which these electrons are simulated appear in table 4.1. For each electron energy, a Gaussian function is fit to the distribution of N_γ as estimated by RSP. The mean of the Gaussian function is plotted as a function of the energy of the simulated electrons T_e in figure 5.25. For the salt phase, $\mathcal{F}_E$ consists of a linear interpolation of the points in figure 5.25.

5.8.4 Electron energy response

To test the accuracy and resolution of the RSP energy reconstruction, the simulated electrons used in the previous section were reprocessed with $\mathcal{F}_E$ as shown in figure 5.25. The mean RSP reconstructed energies (T_eff) of the electrons, simulated with energies from 2 to 130 MeV, are plotted in figure 5.26a as a function of reduced radius. A bias is noted in the reconstructed energy T_eff; T_eff decreases with increasing radius.

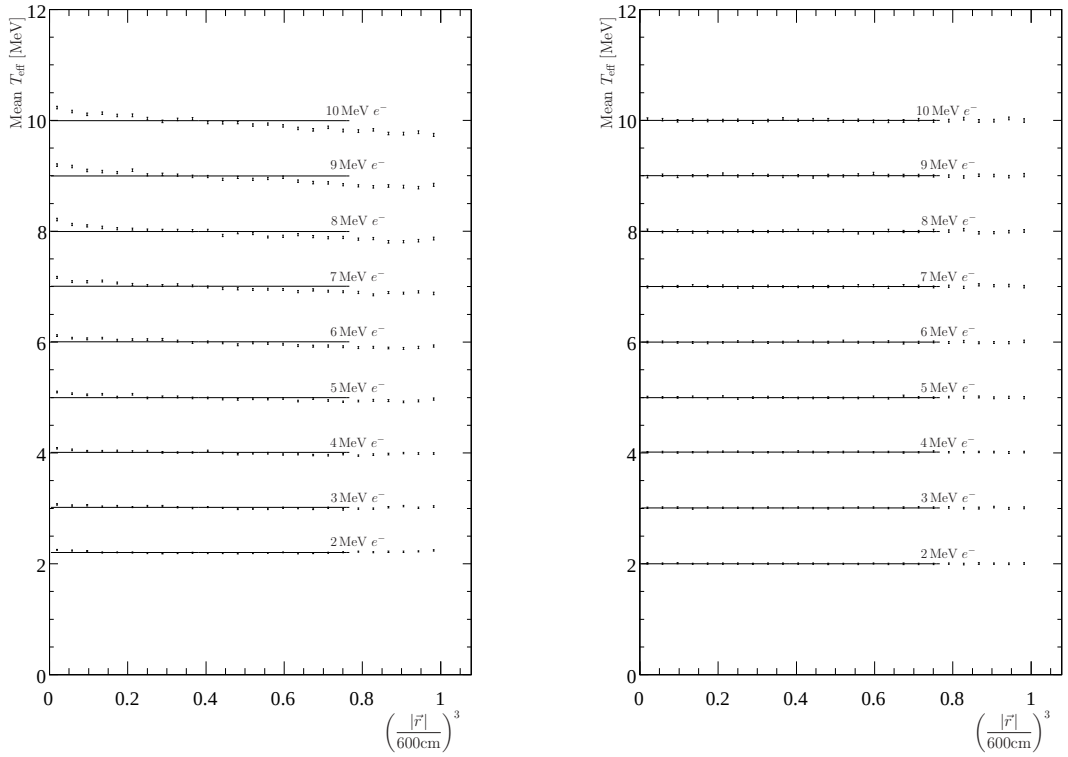

(a) Before applying a radially dependent correction.

(b) After applying the correction function represented by figure 5.27.

Figure 5.26: The mean reconstructed energy of electrons as a function of radial position for the salt phase. The electrons within the radius of the acrylic vessel (reduced radius of 1.0) are divided into 20 radial bins. The mean energy (each point) is the result of fitting a Gaussian function to the energy distribution of electrons within each radial bin.

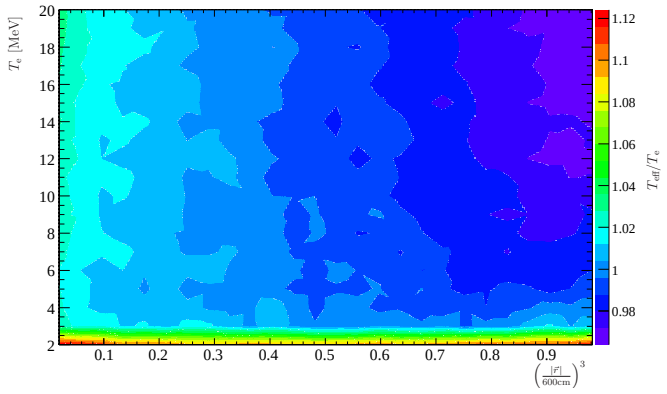

Figure 5.27: The ratio of mean reconstructed energy T_{eff} to the electron energy T_{e} at which the electrons were simulated by SNOMAN. The mean T_{eff} are the same as those presented in figure 5.26a. The RSP T_{eff} of salt phase events, both those that are simulated and those that appear in the data, should be divided by the value of this function.

The source of this bias and the justification for a simulation based correction is presented in subsection 5.6.4. Figure 5.27 is the ratio of the mean reconstructed energy T_{eff} to the energy at which the electrons were simulated T_{e}. This correction function consists of an interpolation of the complete set of data, for electrons with energies from 2 to 130 MeV, represented by the subset shown in figure 5.26a. No radial bias is apparent in figure 5.26b which is derived from the events used to create figure 5.26a but with the additional radius dependent energy correction presented in figure 5.27 applied to the data.

Figure 5.28 shows the deviation of the mean reconstructed energy T_{eff} from the electron energy T_{e}. The mean T_{eff} is determined from the weighted mean of the data points shown in figure 5.26b. The weighted means are also shown in figure 5.26b as the fits to the data points. Only the data points within the fiducial volume, defined by a maximum reconstructed radius of 550 cm (a reduced radius of 0.77), are used in the average.

The energy resolution σ_T that is determined from these SNOMAN simulated electrons is presented in figure 5.29. The energy resolution function shown fit to the data is

$$\sigma_T = -0.142 + 0.399\sqrt{T_{\text{e}}} + 0.0300\,T_{\text{e}}. \tag{5.14}$$

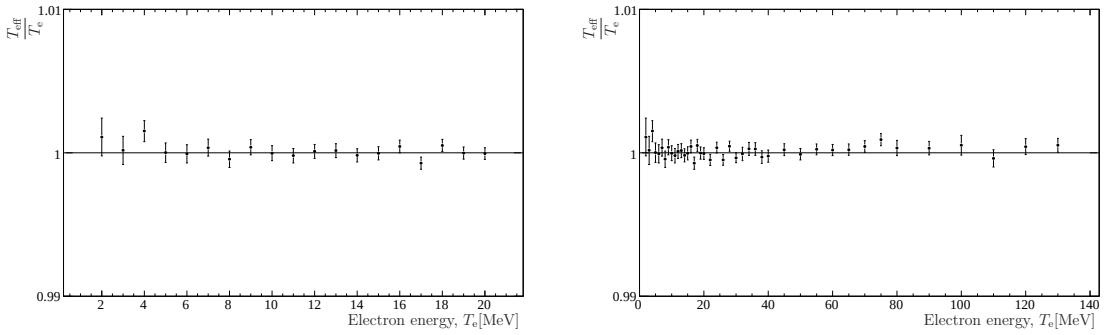

(a) Electrons with energies from 2 to 20 MeV. (b) Electrons with energies from 2 to 130 MeV.

Figure 5.28: Fractional deviation of the mean reconstructed energy $T_{\rm eff}$ from electron energy $T_{\rm e}$ for the salt phase. The mean at each electron energy is also shown as fit to the data points in figure 5.26b.

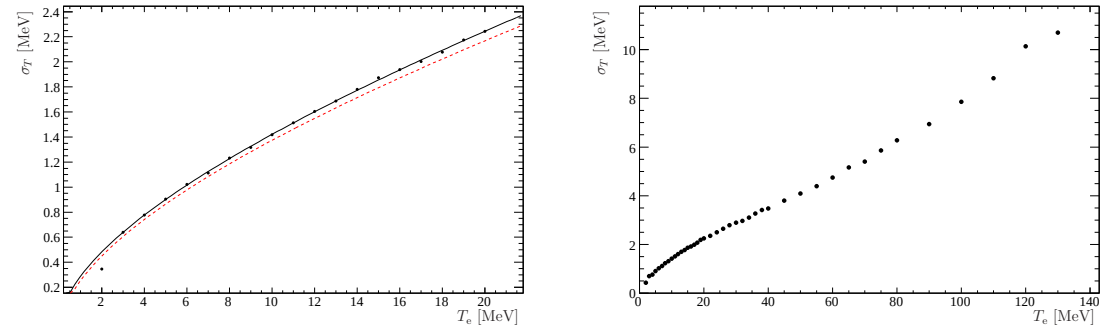

(a) Electrons with energies from 2 to 20 MeV. (b) Electrons with energies from 2 to 130 MeV.

Figure 5.29: Energy resolution σ_T of SNOMAN simulated electrons as a function of the electron energy $T_{\rm e}$. The dashed line is the energy resolution function measured for the pure D_2O phase (equation 5.12) for comparison.

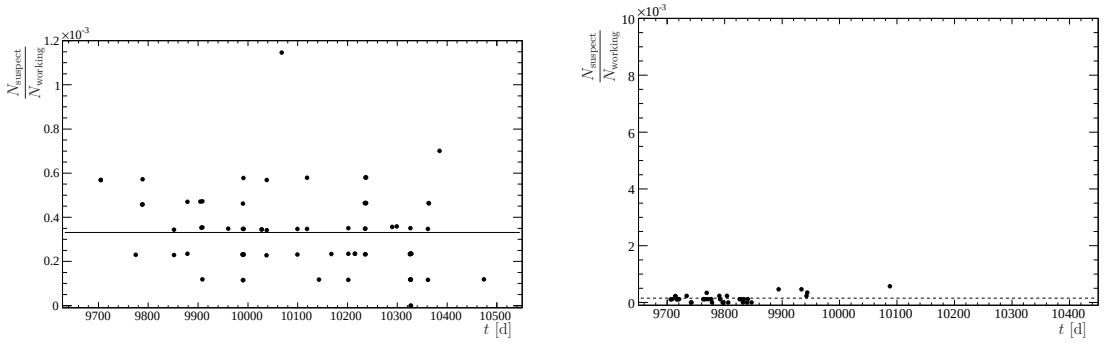

(a) Central ^{16}N calibrations. (b) Long neutrino runs.

Figure 5.30: The fraction of PMTs considered in good working order that have suspect occupancy rates during salt phase. The means of the data points are 0.033% and 0.015% respectively.

This may be compared to the dashed line in figure 5.29 that indicates the energy resolution function determined for the LETA pure D_2O phase: equation 5.12.

5.9 LETA salt phase energy reconstruction error

Contributions to the RSP energy reconstruction error for the LETA of the salt phase are presented. The potential errors detailed in section 5.5, including those from other sources, are summarized in section 5.10.

5.9.1 PMT status

The fraction of working PMTs with occupancy rates, per event, more than 5σ from the mean is plotted in figures 5.30a and 5.30b. The mean value for the ^{16}N calibrations is 0.015%.

As a cross-check the mean fraction of suspect PMTs considered working during high statistics neutrino runs[9] is plotted in figure 5.30b. This reduces the total number of available runs considerably and eliminates all runs in the later half of the salt phase. This is a result of shorter more frequent runs in the salt phase. The mean of the data

[9]Highs statistics in this case refers to runs with more than 3000 events with at least 19 N_{hit}. A further cut removes runs with a mean PMT occupancy rate less than 3σ from zero.

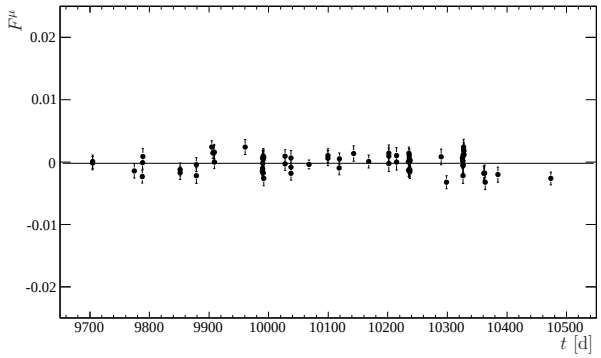

Figure 5.31: The fractional difference F^μ between the mean energy of central ^{16}N calibration data, taken during the salt phase, and the simulation as a function of time. The mean of the data points is $-0.019 \pm 0.013\%$.

points in figure 5.30b is 0.015%, which is consistent with that observed for the more precise determination made using ^{16}N calibrations. Therefore, the greater of the two uncertainties—0.033%—is adopted as the contribution to the salt phase energy reconstruction error.

5.9.2 Energy scale temporal variation

The fractional difference F^μ between the mean energy of central ^{16}N calibrations and simulations for the salt phase are shown in figure 5.31. A mean error of $-0.019 \pm 0.013\%$ is observed. However, the χ^2 per degree of freedom is 118.2.4/76. The uncertainty on the mean is increased to account for this (see appendix C) such that the mean becomes $-0.019 \pm 0.016\%$. The overall error is accounted for, with its proper weight, in the determination of the spatial variation error. The contribution to the uncertainty in the energy scale error is 0.019%.

5.9.3 Energy scale spatial variation

The spatial distribution of ^{16}N calibrations during the salt phase leads to the volume partitioning of the detector listed in table 5.3. This volume binning is also depicted in figure 5.32 where only about half of each of the outer bins is shown for illustrative purposes. Unlike the pure D_2O phase binning, only the central bins are combined into

Radial bin range (cm)	Polar angle bin edges
0–150	0, π
150–375	0, 0.375, 1.165, 1.955, 2.745, π
375–550	0, 0.375, 1.165, 1.955, 2.745, π
550–600	0, 0.375, 1.165, 1.955, 2.745, π

Table 5.3: Spatial binning of the salt phase ^{16}N calibrations based on the distribution of calibrations done within the D_2O. The outermost radial bin lies outside the fiducial volume.

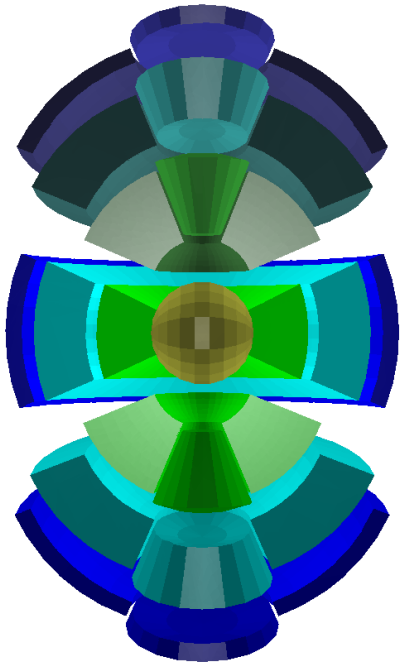

Figure 5.32: Exploded cross-sectional depiction of the spatial binning listed in table 5.3. The polar angle coordinate is the angle from a vertical line with its origin at the centre of the solid inner sphere.

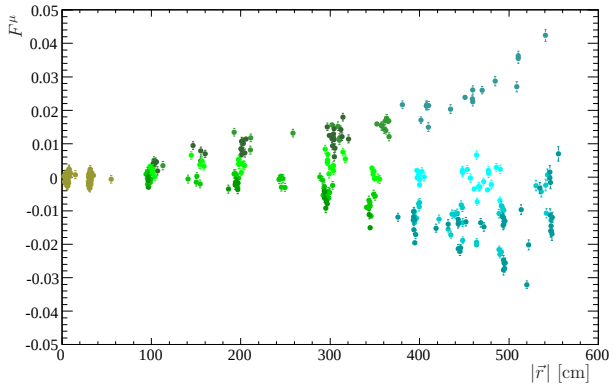

Figure 5.33: The fractional difference F^μ between the mean energy of the salt phase ^{16}N calibrations and that of the simulation as a function of source radius. The colours of the points correspond to the volume element colours in figure 5.32.

a single sphere. The volume bounded by radii of 375 and 550 cm and angles 0.375 to 1.165 contains no ^{16}N calibrations during the salt phase. The outer most radial bins are not considered by this analysis as they are external to the fiducial volume.

Figure 5.33 shows the distribution of F^μ for each of the salt phase ^{16}N calibrations as a function of the source radial position. The colours of the points indicate in which volume element, as in figure 5.32, the data resides. The mean, with RMS error, of each group of like-coloured points is plotted in figure 5.34. The coloured bands indicate the fraction of the total fiducial volume each point represents. As per the prescription detailed in subsection 5.5.1, the energy scale error $\Delta\mu_T$, shown as the solid line with dashed error band on figure 5.34, is determined to be $-0.067 \pm 0.255\%$.

5.9.4 Event rate dependence

The fractional difference F^μ between the mean energy of low rate central ^{16}N calibrations and the simulation is plotted in figure 5.35. An energy scale error of $-0.322 \pm 0.101\%$ is observed.

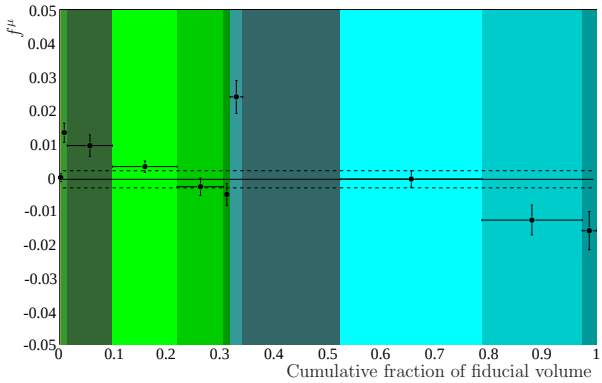

Figure 5.34: The mean f^μ of the like coloured points in figure 5.33 with RMS error bars. The colours of the bands correspond to the volume element colours in figure 5.32. There is no data point in the eighth colour band as no ^{16}N calibrations are performed in that volume element. The solid line with dashed error band illustrates the volume weighted mean of the data points $\Delta\mu_T = -0.067 + / - 0.255\%$.

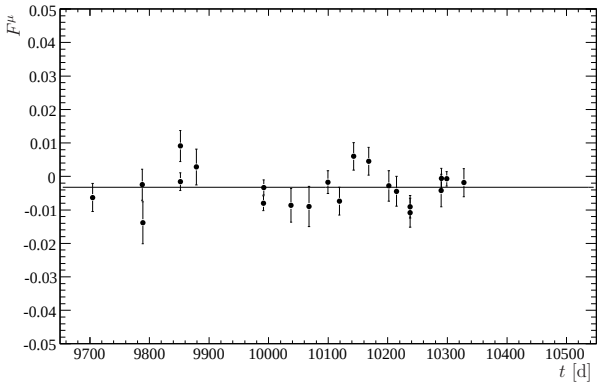

Figure 5.35: The fractional difference F^μ between the mean energy of low rate ^{16}N calibrations and the simulation during the salt phase. A mean offset of $-0.322 \pm 0.101\%$ is observed.

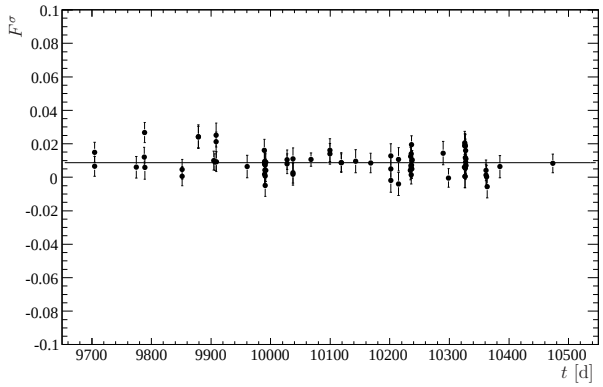

Figure 5.36: The fractional difference (F^σ) between the energy resolution of ^{16}N calibrations and that of the simulation in the salt phase. The mean of the data points is $0.875 \pm 0.193\%$.

5.9.5 Energy resolution temporal variation

The fractional difference F^σ, between the energy resolution of central ^{16}N calibrations and that of the simulation, shown in figure 5.36 for the salt phase.A mean error of $0.875 \pm 0.193\%$ is observed. The overall error is large but is accounted for, with the proper weighting, in the determination of the spatial variation error. The contribution to uncertainty in the energy resolution error is 0.193%.

5.9.6 Energy resolution spatial variation

The same spatial binning that is used for the determination of the energy scale error associated with spatial variations (subsection 5.9.3) is appropriate to use in this case. Figure 5.37 shows distribution of F^σ for each of the salt phase ^{16}N calibrations as a function of the source radial position. The colours of the points indicate in which volume element, as in figure 5.32, the data resides. The mean, with RMS error, of each group of like-coloured points is plotted in figure 5.38. The coloured bands represent the fraction of the total fiducial volume each point represents. $\Delta\sigma_T$, calculated as per the prescription detailed in subsection 5.5.1, is shown as the solid line with dashed error band on figure 5.38. The energy resolution error $\Delta\sigma_T$ due to spatial variation in the difference between ^{16}N calibrations and the simulation is $0.598 \pm 0.195\%$.

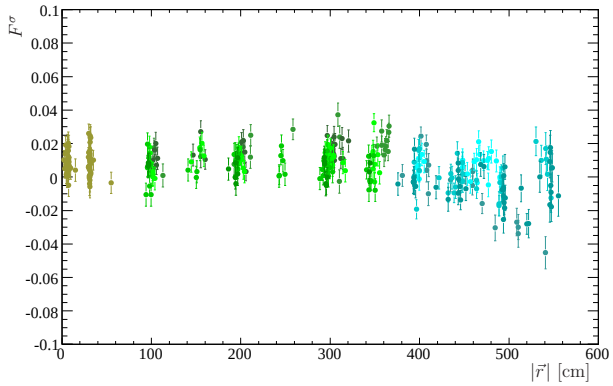

Figure 5.37: Fractional difference F^σ between the energy resolution of salt phase ^{16}N calibrations and that of the simulation. The colors of the points correspond to the volume element colors in figure 5.32.

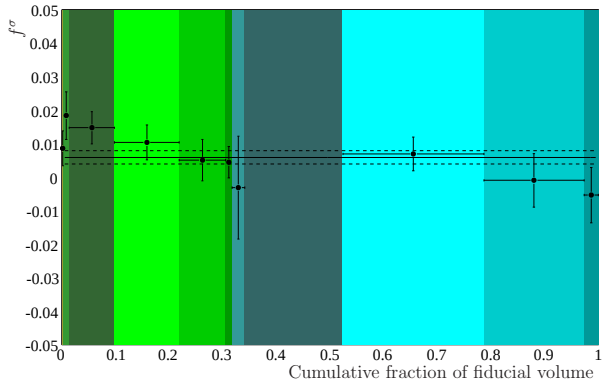

Figure 5.38: The mean f^σ of the like coloured points in figure 5.37 with RMS error bars. The colours of the bands correspond to the volume element colours in figure 5.32. There is no data point in the eighth colour band as no ^{16}N calibrations are performed in that volume element. The solid line with dashed error band illustrates the volume weighted mean of the data points $\Delta\sigma_T = 0.598 \pm 0.195\%$.

Source of error	LETA RSP errors: Pure D_2O	Salt	LETA FTK errors: Pure D_2O	Salt
PMT status	$\pm 0.026\%$	$\pm 0.033\%$	$\pm 0.01\%$	$\pm 0.01\%$
PMT threshold, gain	$^{+0.16\%}_{-0.32\%}$	$^{+0.11\%}_{-0.07\%}$	$^{+0.18\%}_{-0.31\%}$	$^{+0.13\%}_{-0.07\%}$
Timing	$\pm 0.1\%$	$\pm 0.1\%$	0	0
Temporal variation	$0.237 \pm 0.029\%$	$-0.019 \pm 0.016\%$	0	0
Spatial variation	$0.304 \pm 0.169\%$	$-0.067 \pm 0.255\%$	$\pm 0.18\%$	$\pm 0.31\%$
Event rate	$-0.083 \pm 0.199\%$	$-0.322 \pm 0.101\%$	$\pm 0.30\%$	$\pm 0.05\%$
^{16}N source	$\pm 0.41\%$	$\pm 0.41\%$	$\pm 0.41\%$	$\pm 0.41\%$
Total	$-0.016^{+0.532\%}_{-0.592\%}$	$-0.370^{+0.516\%}_{-0.509\%}$	$^{+0.568\%}_{-0.622\%}$	$^{+0.533\%}_{-0.521\%}$

Table 5.4: Summary of LETA RSP and FTK energy scale errors. FTK applies a spatially dependent correction to make the energy of ^{16}N calibrations match that of the data. The FTK values are taken from Klein et al. [75]. The combined PMT threshold and gain uncertainties are taken from Klein [83]. The timing uncertainty (applicable only to RSP) is taken from Graham [87]. The remaining errors are derived in this work. A discussion of these results appears in the text.

5.10 Summary of LETA RSP energy reconstruction errors

RSP–reconstructed energy is serving as a cross-check of FTK–reconstructed energy for LETA. Although each is based on a somewhat different philosophy, both energy estimates are based on the number of triggered PMTs (FTK considering also a large fraction of late, reflected–photon, triggered PMTs). A summary of the LETA RSP energy scale error on the energy scale and the FTK energy scale uncertainty are presented in table 5.4.

The spatial variation error is a measure of the energy scale error averaged over time and the fiducial volume using high rate ^{16}N calibrations. This must be corrected to account for the difference in the energy scale between high rate calibrations and neutrino data. The rate effect is only measured at the centre of the detector due to time constraints. The difference between the high and low rate calibrations is the difference between the temporal variation error (measured at the centre of the detector with high rate ^{16}N calibrations) and the event rate error (measured at the

centre of the detector with low rate ^{16}N calibrations). For the pure D_2O phase this is: $0.237\% - -0.083\% = 0.320\%$. The total energy scale error is the difference between the average high rate energy scale error corrected for the difference between the high and low rate ^{16}N energy calibrations: $0.304\% - 0.320\% = 0.016\%$. The uncertainties on all three direct comparisons of the simulation to the ^{16}N calibrations are added in quadrature, along with the other energy scale uncertainties listed in table 5.4, to obtain the total energy scale error with some uncertainty. The total energy scale error for the salt phase RSP reconstructed energy is derived analogously to that of the pure D_2O phase.

In general, the energy scale errors estimated for LETA are in good agreement. Brief discussions of the individual contributions to the total energy scale error follow.

- LETA is currently using an estimate of the PMT status energy scale uncertainty derived by the author for the pure D_2O phase solar *hep* neutrino analysis [26]. Although the more recent estimates present in this work are slightly larger, none of the measurements contribute considerably to the total energy scale error.

- The PMT threshold and gain energy scale uncertainties are derived in great detail by Klein [83] for both RSP and FTK.

- FTK imposes a very loose PMT timing cut when reconstructing energy such that very few PMT triggers are rejected from analysis. Therefore, only RSP, with a prompt PMT timing window of ± 10 ns, is assigned an uncertainty due to the variability in the PMT timing. The uncertainty is derived by Graham [87].

- FTK performs a position and direction dependent correction to reconstructed energy that makes ^{16}N calibrations more similar to the simulation. This effectively eliminates any energy scale error as a function of time and position. The energy scale spatial variation uncertainty listed for FTK in table 5.4 includes the residual energy scale error. In the RSP case, the energy scale error listed is the correction that should be applied to the reconstructed energy of events in the data to match the simulation.

- The ^{16}N source uncertainty is derived in chapter 7.

	LETA RSP errors:	
Source of error	Pure D_2O	Salt
Temporal variation	$1.610 \pm 0.119\%$	$0.875 \pm 0.193\%$
Spatial variation	$1.528 \pm 0.238\%$	$0.598 \pm 0.195\%$
Total	1.528%	$\pm 0.266\%$

Table 5.5: Summary of LETA RSP energy resolution errors. A discussion of these results appears in the text.

As with the energy scale, the spatial variation error is a measure of the energy resolution error averaged over time and the fiducial volume using high rate ^{16}N calibrations. The comparisons used to derive the temporal variation error are a constituent of the spatial variation error and, therefore, are added to the total. The uncertainty on the temporal variation is a measure of the temporal stability of the energy resolution and is therefore added in quadrature with the spatial variation error uncertainty to obtain the totals listed in table 5.5. In both cases the simulation has a narrower energy resolution than the calibrations. The energy resolution error analysis for FTK is considerably more complex than the one presented in this work [75]. It is not directly comparable to the energy resolution quoted in table 5.5.

Chapter 6

NCD phase energy reconstruction

The NCDs affect the response of the PMTs to Čerenkov events in two appreciable ways: photons are either scattered/reflected or absorbed upon contact with an NCD. RSP considers only promptly triggered PMTs in an attempt to reduce systematic error associated with tracking the paths scattered photons take. Continuing with this philosophy, it is reasonable for RSP to consider all photons incident upon an NCD to be lost when evaluating the response of the detector. Photons that scatter may not necessarily be late which could contribute to increased systematic error for the NCD phase.

6.1 NCD–PMT shadowing probability

To first order, if an NCD lies between an event position and a given PMT, the response of that PMT to prompt light should be negligible. This assumes that the interaction is point like, the likelihood is small that scattered/reflected photons arrive within the prompt analysis window, and, least plausibly, that the fit position is perfectly accurate. SNO vertex reconstruction resolution is worse than 15 cm. Not accounting for vertex resolution can lead to a significant underestimate in the response of PMTs to events near an NCD. An initial approach taken was to simulate NCD-PMT shadowing, from which an analytic approximation to the amount of shadowing is derived. This function is required to explicitly depend on the position of the reconstructed event, the position of the NCD, and the position of a PMT.

To simulate the shadowing of a single PMT by a single NCD, a simple Monte Carlo calculation was performed. Photons were generated with a three dimensional Gaussian distribution. The mean μ of the distribution corresponds to a mock event position while the width σ was set to the vertex reconstruction resolution. The photons were propagated directly to a random point on the surface of a flat faced PMT. A top down view of the simplest geometry is shown in figure 6.1a. The event vertex is shown at the centre of the detector while both the centres of the NCD and the PMT, indicated by the dashed and dotted lines respectively, lie along the x-axis of the detector.

The distribution of initial and final photon positions, in the absence of NCD-PMT shadowing, is parametrized by their y-coordinates from figure 6.1b (or any case as it turns out) in figure 6.2a. This distribution is exactly described by the function

$$f\left(y_{\mathrm{i}}, y_{\mathrm{f}}\right) = \frac{2}{\pi b}\sqrt{1-\left(\frac{y_{\mathrm{f}}-a}{b}\right)^2} \times \frac{1}{\sqrt{2\pi}\sigma} e^{-\frac{(y_{\mathrm{i}}-\mu)^2}{2\sigma^2}}, \tag{6.1}$$

where

y_{i} is the initial y-coordinate of the photon,
y_{f} is final y-coordinate of the photon on the face of the PMT,
μ is the y-coordinate of the event,
σ is the event vertex reconstruction resolution,
a is the y-coordinate of the PMT, and
$b \equiv r_{\mathrm{PMT}} \dfrac{x_{\mathrm{PMT}}}{\sqrt{x_{\mathrm{PMT}}^2 + y_{\mathrm{PMT}}^2}}$

which is the projection of r_{PMT} onto the y-axis. In the definition of b, r_{PMT} is the radius of the PMT concentrator assembly, and x and y_{PMT} are the coordinates of the PMT. This function, with normalization fixed to the number of photons in figure 6.2a, is shown in figure 6.2b.

The photons whose path to the PMT face carry them within the radius of the NCD, from the x and y-coordinates of the centre of the NCD, have been removed from figure 6.1b. The y-coordinate limits on the PMT face, y_{f}, that bound these

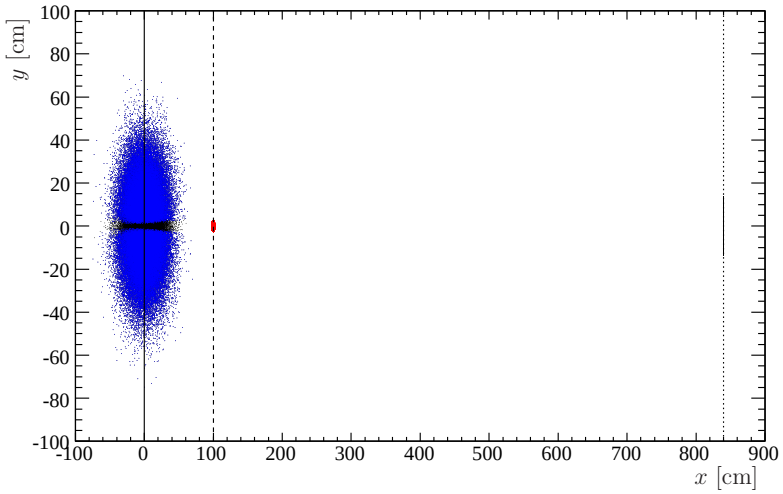

(a) The initial x and y-coordinates of photons distributed about a reconstructed event position (left), the space that an NCD occupies (centre), and the flat face of a PMT (right). The black photons are obscured by the NCD while the blue ones are not.

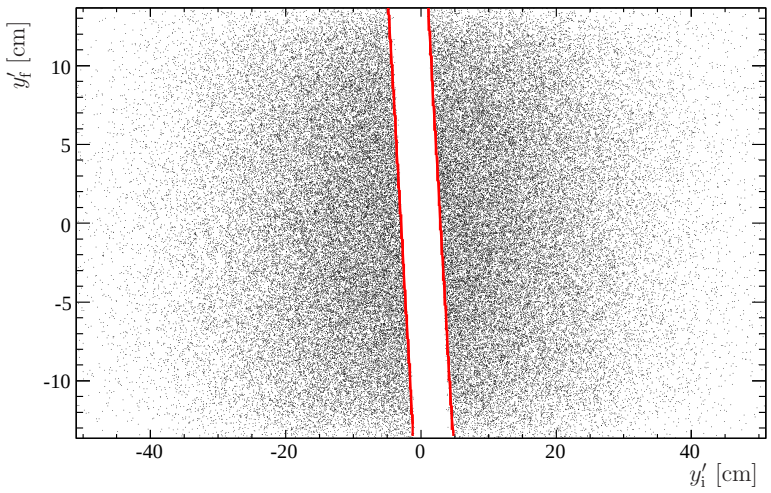

(b) The initial and final y-coordinates—the prime designation indicates that the distribution has been shifted to be centred on the origin—of photons traveling from the reconstructed event position to the face of a PMT as displayed in the figure above. The photons that intersect the NCD have been removed.

Figure 6.1: Monte Carlo calculation of NCD-PMT shadowing: simplest NCD-PMT shadow.

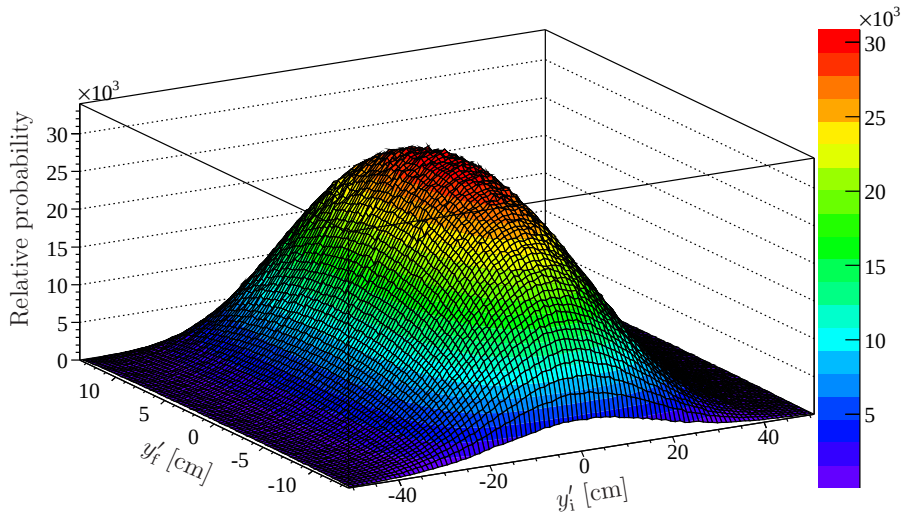

(a) Monte Carlo calculation.

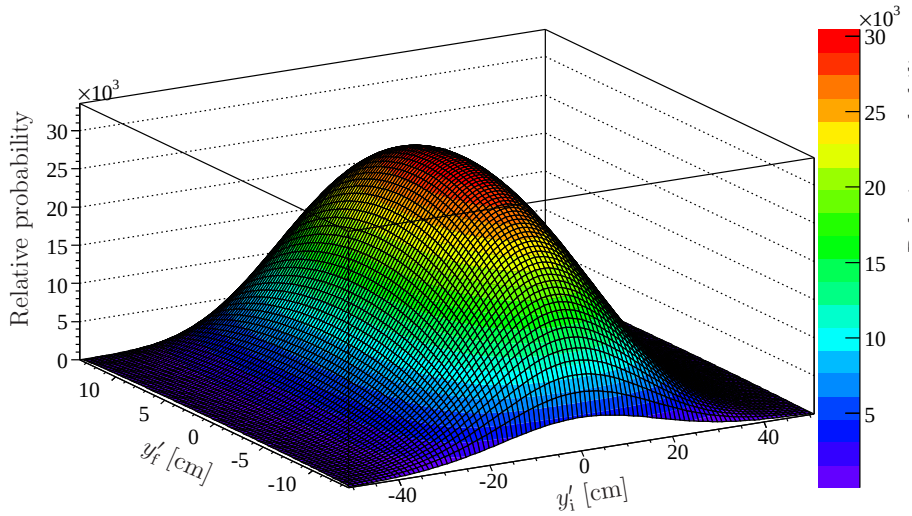

(b) Fit function.

Figure 6.2: The position of photon impacts on the face of a PMT relative to where they were generated, which was about the reconstructed event position.

photons are given by

$$y_{\mathrm{f}} = \frac{\alpha - 1}{\alpha} y_{\mathrm{i}} + \frac{y_{\mathrm{NCD}} \pm R_{\mathrm{NCD}}}{\alpha} \tag{6.2}$$

where

$$\alpha \equiv \frac{x_{\mathrm{NCD}} - x_{\mathrm{i}}}{x_{\mathrm{PMT}} - x_{\mathrm{i}}},$$

x_{i}	is the x-coordinate of the initial position of the photon
x and y_{NCD}	are the x and y-coordinates of the NCD,
r_{NCD}	is the radius of the NCD (averaging 2.576 cm), and
x_{PMT}	is the x-coordinate of the PMT.

If the initial photon positions are projected onto the y-axis, then x_{i} is equivalent to the x-coordinate of the reconstructed event vertex. In this approximation the limits are as indicated in figure 6.1b by the two red lines.

For use in the following derivation, the boundaries of the NCD-PMT shadow can alternatively be expressed as

$$y_{\mathrm{i}}^{\pm} = \frac{\alpha y_{\mathrm{f}} - y_{\mathrm{NCD}} \pm R_{\mathrm{NCD}}}{\alpha - 1}. \tag{6.3}$$

The reduction in efficiency of the PMT due to the NCD shadow, according to equations 6.1 and 6.3, is then

$$\begin{aligned}
\epsilon_{\mathrm{shadow}} &= \int_{-b}^{b} \mathrm{d}y_{\mathrm{f}} \left(\int_{-\infty}^{y_{\mathrm{i}}^{-}(y_{\mathrm{f}})} f\left(y_{\mathrm{i}}, y_{\mathrm{f}}\right) \mathrm{d}y_{\mathrm{i}} + \int_{y_{\mathrm{i}}^{+}(y_{\mathrm{f}})}^{\infty} f\left(y_{\mathrm{i}}, y_{\mathrm{f}}\right) \mathrm{d}y_{\mathrm{i}} \right) \\
&= 1 - \int_{-b}^{b} \mathrm{d}y_{\mathrm{f}} \int_{y_{\mathrm{i}}^{-}}^{y_{\mathrm{i}}^{+}} f\left(y_{\mathrm{i}}, y_{\mathrm{f}}\right) \mathrm{d}y_{\mathrm{i}} \\
&= 1 - \int_{-b}^{b} \mathrm{d}y_{\mathrm{f}} \, \frac{2}{\pi b} \sqrt{1 - \left(\frac{y_{\mathrm{f}} - a}{b}\right)^2} \left[\mathrm{erf}\left(\frac{y_{\mathrm{i}}^{+} - \mu}{\sqrt{2}\sigma}\right) - \mathrm{erf}\left(\frac{y_{\mathrm{i}}^{-} - \mu}{\sqrt{2}\sigma}\right) \right] /2.
\end{aligned} \tag{6.4}$$

Any arrangement of reconstructed event vertex, NCD, and PMT positions can be transformed such that the event vertex lie at the origin and rotated such that the NCD lie along the x-axis. Then the NCD-PMT shadowing $\epsilon_{\mathrm{shadow}}$ can be calculated via equation 6.4. The only caveat to this entire procedure is that the calculation of b becomes more complicated when the reconstructed vertex is not at the centre of the

detector.

For a slightly more complicated situation such as in figure 6.3a, where the shadowed photons are no longer contained within a slice perpendicular to the y-axis, the approximation that projects the initial photon positions onto the y-axis begins to break down. Figure 6.3b shows the distribution of photons that strike the PMT in figure 6.3a. The NCD-PMT shadowing limits (the red lines in figure 6.3b) do approximate the region of missing photons yet some photons in that region are not shadowed. In this case ϵ_{shadow} is an overestimate of the NCD-PMT shadow.

If the NCD lies within the extent of the initial photon distribution, as in figure 6.4b, some photons between the bounds defined by equation 6.2 are not shadowed as they originate between the NCD and the PMT. To account for this a correction factor is applied to ϵ_{shadow} such that

$$(1 - \epsilon_{\text{shadow}}) \rightarrow (1 - \epsilon_{\text{shadow}}) \left[1 + \text{erf}\left(\frac{\beta}{\sqrt{2}\sigma}\right)\right] /2, \tag{6.5}$$

where

$$\beta \equiv \frac{x_{\text{NCD}}}{\sqrt{1+\gamma^2}} \qquad \text{and}$$
$$\gamma \equiv \frac{y_{\text{PMT}}}{x_{\text{PMT}} - x_{\text{NCD}}}.$$

This correction is the integral of a normalized Gaussian distribution from $-\infty$ to the position of the NCD along the line of sight from the NCD to the PMT.

A comparison between ϵ_{shadow} derived via the numerical integration of the analytic function and the ratio of photons in the simulation that actually struck the PMT are compared in table 6.1 for each of the cases discussed above as well as several other "worst case" scenarios.

Up to this point this model does not take into account shadowing induced by the NCD electronics cables or the fact that the NCDs are of finite length, although the latter would be only a simple extension. Even at this level of complexity however, the large number of numerical integrations required to reconstruct the energy of each event (up to approximately 8500 PMTs by 40 NCD strings) demands excessive processing time. While the accuracy of this method for calculating the optical shadowing

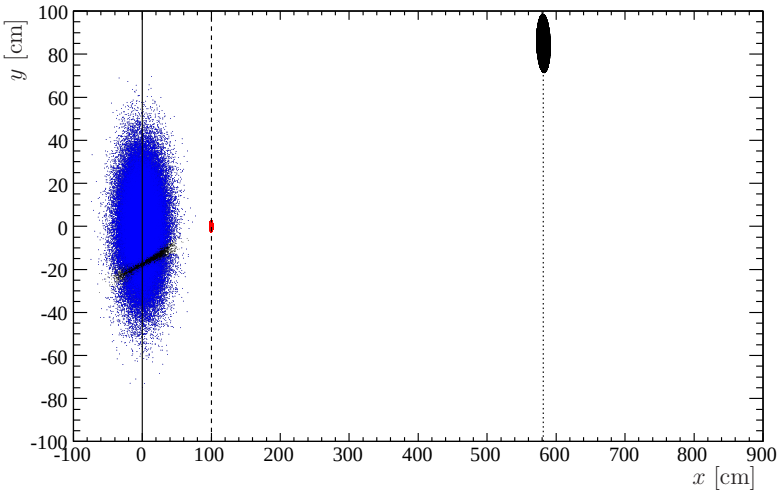

(a) The initial x and y-coordinates of photons distributed about a reconstructed event position (left), the space that an NCD occupies (centre), and the flat face of a PMT (right). The black photons are obscured by the NCD while the blue ones are not.

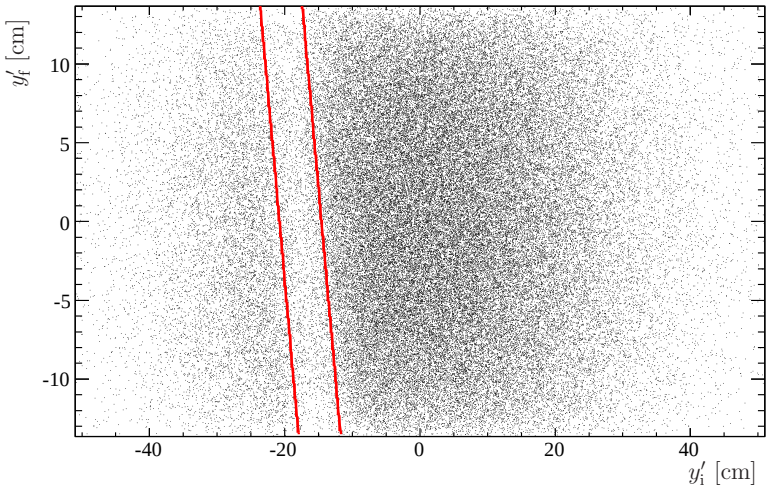

(b) The initial and final y-coordinates—the prime designation indicates that the distribution has been shifted to be centred on the origin—of photons traveling from the reconstructed event position to the face of a PMT as displayed in the figure above. The photons that intersect the NCD have been removed.

Figure 6.3: Monte Carlo calculation of NCD-PMT shadowing: off-axis PMT.

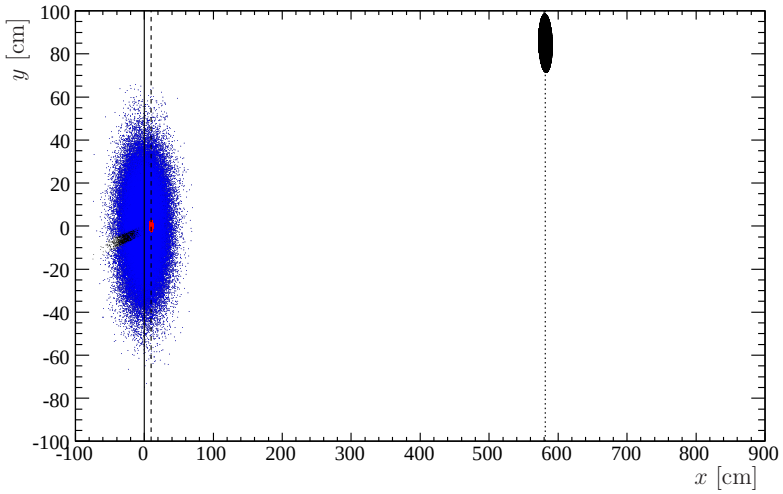

(a) The initial x and y-coordinates of photons distributed about a reconstructed event position (left), the space that an NCD occupies (centre), and the flat face of a PMT (right). The black photons are obscured by the NCD while the blue ones are not.

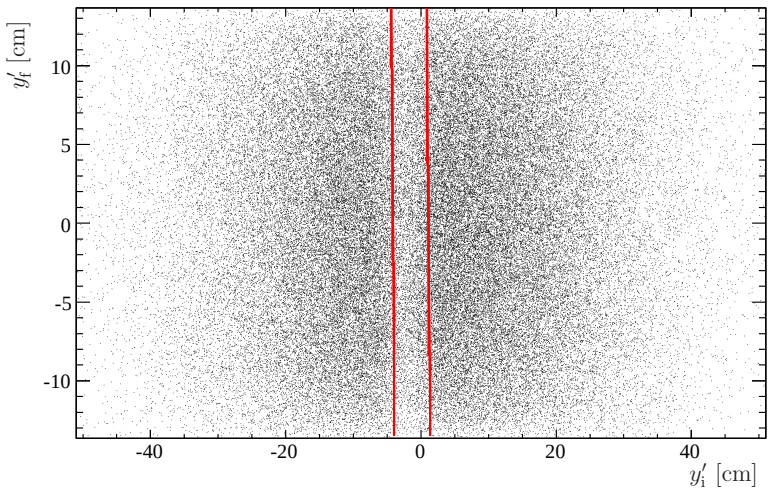

(b) The initial and final y-coordinates—the prime designation indicates that the distribution has been shifted to be centred on the origin—of photons traveling from the reconstructed event position to the face of a PMT as displayed in the figure above. The photons that intersect the NCD have been removed.

Figure 6.4: Monte Carlo calculation of NCD-PMT shadowing: off axis PMT with the NCD near the event vertex.

Figure	x_{NCD} [cm]	x_{PMT} [cm]	y_{PMT} [cm]	z_{PMT} [cm]	Percent difference
Figure 6.1a	100	840	0	0	-0.02
Figure 6.3a	100	582	85	600	0.15
–	100	182	0	820	-7.8
–	10	840	0	0	-2.2
Figure 6.4a	10	582	85	600	-1.8
–	10	182	0	820	-2.2

Table 6.1: The percentage difference between $\epsilon_{\mathrm{shadow}}$ calculated via equation 6.4 and that derived from Monte Carlo calculations for various scenarios. The reconstructed vertex is in all cases the centre of the detector while the NCD is also fixed on the x-axis since the scenario can always be translated and rotated to this configuration.

of the PMTs by the NCDs is more than acceptable, a less computationally intensive treatment is required.

6.2 NCD shadowing correction table

The alternative to the direct, event-by-event NCD-by-NCD PMT-by-PMT calculation discussed in the previous section is to tabulate a correction to the efficiency of a PMT as a function of event position and direction. To be precise this correction would have to consist of one three–dimensional table, to describe all reconstructed event positions, for each PMT. Even for very coarse granularity, such a table would consist of at least 10^8 entries.

To further simplify the problem, the detector can be considered to be spherically symmetric. This is obviously less true of the NCD phase than previous phases, however, it is anticipated that the broad position reconstruction resolution also smears out the asymmetries of NCD-PMT shadowing. With this simplification, an average correction can be tabulated as a function of event radial position ($|\vec{r}|$) and direction with respect to the radial position vector, or $\hat{v} \cdot \hat{r}$. Given an event position and the direction to a given PMT, the average efficiency reduction of the PMT can then be assessed.

A simplified[1] SNOMAN Monte Carlo simulation of photons distributed throughout the detector is used to model the situation. In this case, $\epsilon_{\text{shadow}}(\vec{r}, \hat{v}\cdot\hat{r})$ is calculated as the fraction of photons that do not interact with an NCD (or an NCD electronics cable) relative to the total number of photons simulated. The fraction of photons that interact with the NCDs $1 - \epsilon_{\text{shadow}}$ is shown in figure 6.5a. Figure 6.5b shows, for the same simulation, the fraction of photons that interact with the NCD electronics cables. The shadowing of the NCD cables is not included in the final energy reconstruction as the variation within the D_2O is small.

The NCD-PMT shadow efficiency correction (ϵ_{shadow}), is implemented in the RSP optical response as a multiplicative correction factor to the PMT efficiency ϵ such that

$$\epsilon \longrightarrow \epsilon\ \epsilon_{\text{shadow}}(|\vec{r}|, \hat{p}\cdot\hat{r}), \tag{6.6}$$

where $\hat{p}$ is the direction from the reconstructed event vertex $\vec{r}$ to the position of any given PMT and ϵ_{shadow} is the difference between 1.0 and the values tabulated in figure 6.5a.

6.3 NCD phase energy response

Considerably more ^{16}N calibrations were performed during the NCD phase than during the previous phases: over 1300 production calibrations and about 300 during NCD commissioning. The very intensive calibration regime, including optical calibrations, enables the accurate determination of the detector energy and optical parameters even with the NCDs casting complicated shadows on the PMTs. In the following sections the energy scale drift δ_{drift} and PMT collection efficiency $\epsilon_{\circ}$ are determined from central ^{16}N calibrations. An energy calibration function ($\mathcal{F}_E$) for the NCD phase is determined from electron simulations upon which the performance of the RSP energy reconstruction is also evaluated.

[1]The attenuation and scattering of photons in the simulation was suppressed in order to observe purely the geometrical obstructions.

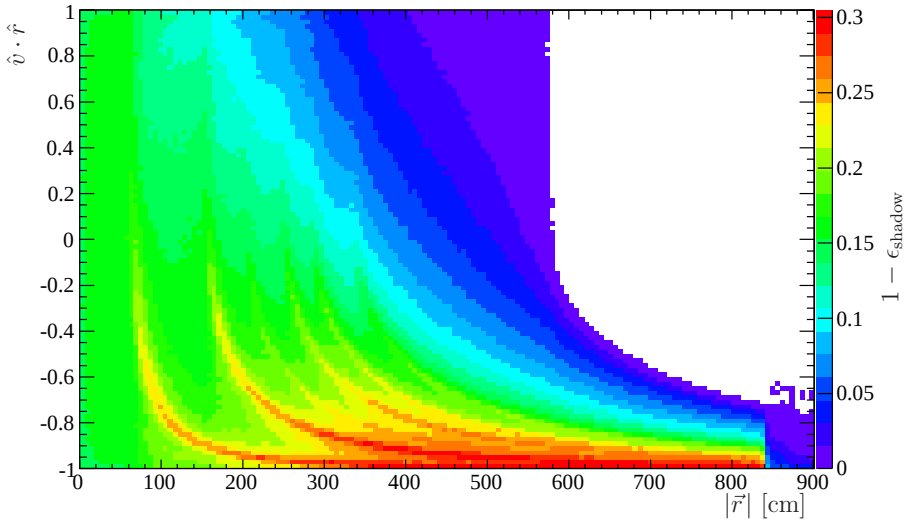

(a) The fraction of photons that encounter an NCD.

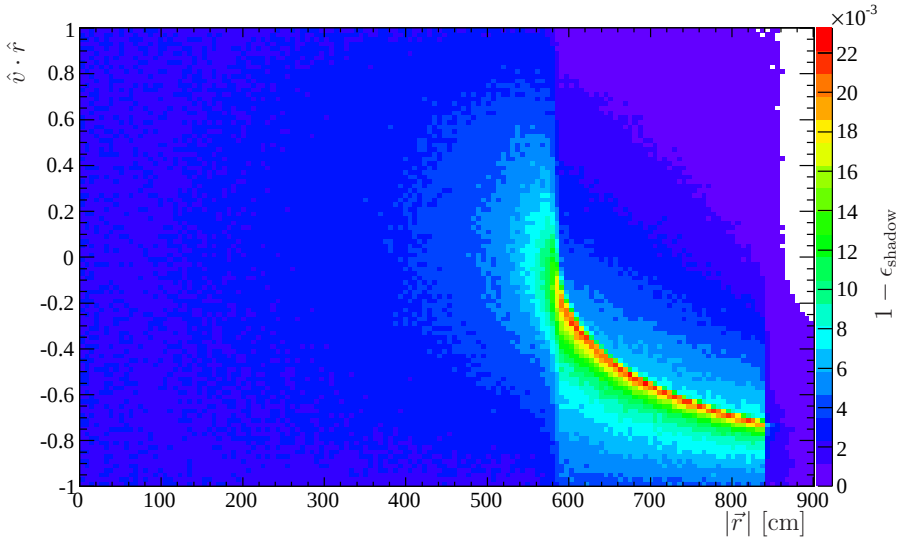

(b) The fraction of photons that encounter an NCD electronics cable.

Figure 6.5: The fraction of photons that interact with either an NCD or NCD electronics cable as a function of initial radial position $|\vec{r}|$ and direction with respect to the radial vector $\hat{v} \cdot \hat{r}$ ($\hat{v}$ being the direction vector). The NCD-PMT shadowing correction ϵ_{shadow} consists of the values in this table.

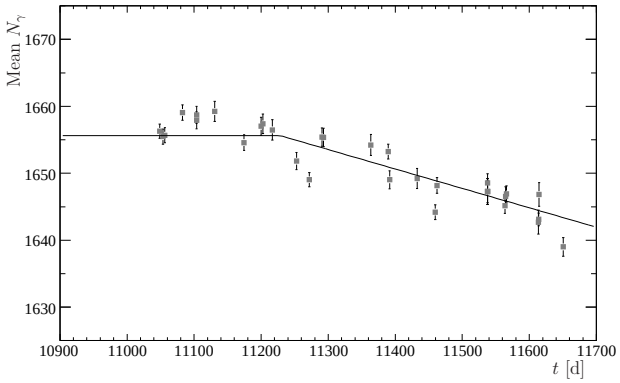

Figure 6.6: The mean N_γ of selected central ^{16}N calibrations performed during the NCD phase.

6.3.1 Energy scale drift

The mean number of initial photons N_γ is plotted in figure 6.6 for ^{16}N calibrations performed during the NCD phase. The data points represent the mean N_γ as estimated by RSP only for high statistics central ^{16}N calibrations. For like events, N_γ should be constant for all times and positions to within the accuracy of the RSP optical response. From the data it is clear that there is a time dependent response not accounted for by RSP.

The energy response drift δ_{drift} during the NCD phase is given by the same piecewise function used during the pure D_2O phase: equation 5.9. During the NCD phase, however, the energy scale is initially constant. The energy drift parameters derived by fitting equation 5.9 to the data in figure 6.6 are presented in table 6.2.

δ_{drift} is implemented in the energy reconstruction as a correction to the output reconstructed energy, T_{eff}, such that

$$T_{\text{eff}} \rightarrow \frac{T_{\text{eff}}}{\delta_{\text{drift}}}. \tag{6.7}$$

The energy response drift observed in the pure D_2O phase data, equation 5.9 with the parameters listed in table 5.1, is implemented in SNOMAN by applying it as a time dependent correction to the PMT collection efficiency $\epsilon_\circ$ as per equation 5.1. It is also used to correct the RSP reconstructed energy T_{eff} as per equation 5.2.

Parameter	Fit result
$t_\circ$	11228
b	1.0
m_1	0.0
m_2	-1.751×10^{-5}

Table 6.2: The parameters extracted from a fit of the function defined by equation 5.9 to the mean response of ^{16}N calibrations presented in figure 6.6. The function parameters have been scaled such that the equation 5.9 is normalized during the initial constant portion of the phase.

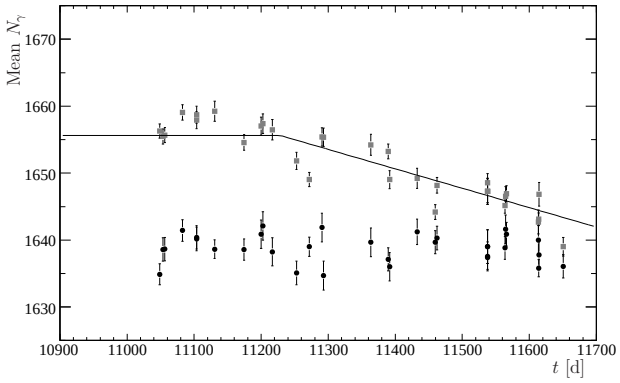

Figure 6.7: The mean N_γ as a function of time during the NCD phase for both ^{16}N calibrations and the SNOMAN simulation, prior to the application of δ_{drift} and the tuning $\epsilon_\circ$.

6.3.2 PMT collection efficiency

The PMT collection efficiency ($\epsilon_\circ$) is tuned for the processing of the NCD phase data following the procedure outlined in section 5.3. The mean energy scale of high statistics central ^{16}N calibrations are shown as the grey points in figure 6.7. The mean energy scale of the corresponding SNOMAN simulation, with $\delta_{\text{drift}}(t) = 1$, is shown as the black points. $\epsilon_\circ$ is set to 0.6454 (the value determined for the LETA processing of the salt phase data) in this simulation. After applying δ_{drift} as presented in the previous section to the energy scale of the simulation—simply scaling the data points in section 5.3 rather than re-running the simulation—the difference between the ^{16}N

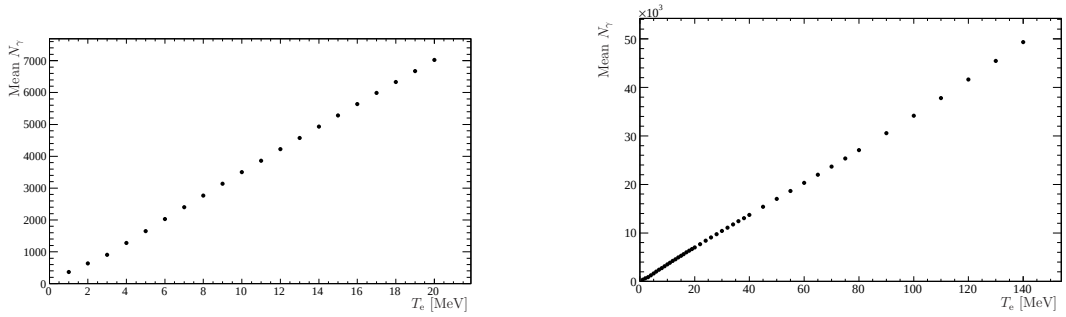

(a) Electrons with energies from 1 to 20 MeV. (b) Electrons with energies from 1 to 140 MeV.

Figure 6.8: The NCD phase energy calibration function $\mathcal{F}_E$.

calibrations and simulation imply that the value of $\epsilon_\circ$ for the NCD phase is 0.6528.

6.3.3 Energy calibration function

The energy calibration function $\mathcal{F}_E$ was derived from RSP reconstructed N_γ of SNOMAN Monte Carlo simulated events. A series of homogeneously distributed electrons, with energies appearing in table 4.1, were generated. For each electron energy, a Gaussian function is fit to the reconstructed N_γ distribution as described in appendix B. The mean of the Gaussian function is plotted in figure 6.8 as a function of the electron energy T_e. For the NCD phase, $\mathcal{F}_E$ consists of a linear interpolation of the points in figure 6.8.

6.3.4 Electron energy response

To test the accuracy and resolution of the RSP energy reconstruction, the simulated electrons used in the previous section were reprocessed with $\mathcal{F}_E$ as shown in figure 6.8. The mean RSP reconstructed energies T_eff of the electrons, simulated with energies from 2 to 130 MeV, are plotted in figure 6.9 as a function of reduced radius. Also shown in figure 6.9a is the response of the original RSP that contains no correction for the effects of the NCDs. The radial bias observed in the energy scale of the pure D_2O and salt phase LETA processing is no longer observed owing to the improvements made in the calculation of the PMT solid angle for the NCD phase analysis (see

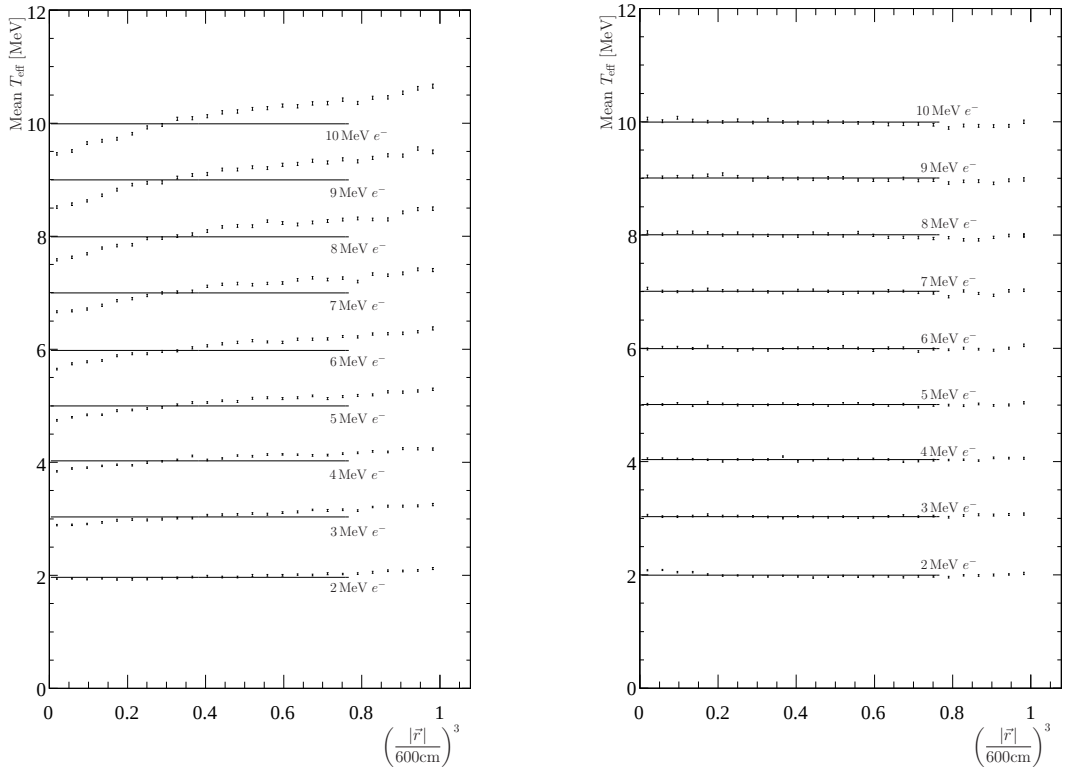

(a) NCD phase radial dependence of the original RSP reconstructed energy.

(b) NCD phase radial dependence of the nominal RSP reconstructed energy.

Figure 6.9: The mean reconstructed energy of electrons as a function of radial position. The electrons within the radius of the acrylic vessel (reduced radius of 1.0) are divided into 26 radial bins. The mean energy (each point) is the result of fitting a Gaussian function to the energy distribution of electrons within each radial bin.

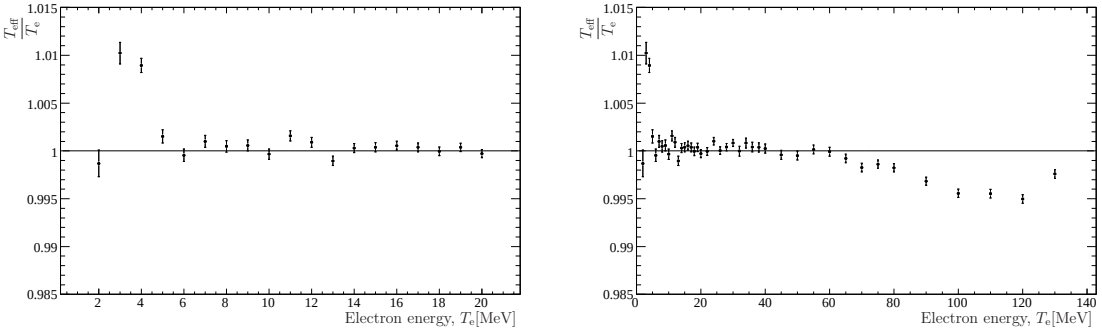

(a) Electrons with energies from 2 to 20 MeV. (b) Electrons with energies from 2 to 130 MeV.

Figure 6.10: Fractional deviation of the mean reconstructed energy from electron energy for the NCD phase. The mean at each electron energy is also shown as fit to the data points in figure 6.9.

subsection 4.2.6).

Figure 6.10 shows the deviation of the mean reconstructed energy $T_{\rm eff}$ from the electron energy $T_{\rm e}$. The mean $T_{\rm eff}$ is determined from the weighted mean of the points shown in figure 6.9. The weighted means are also shown in figure 6.9 as the fits to the data points. Only the data within the fiducial volume, defined by a maximum reconstructed radius of 550 cm (a reduced radius of 0.77), are used in the the average. The deviations from 1.0 in figure 6.10 below 5 MeV are considered acceptable given the higher energy threshold—6 MeV— set for the analysis of the NCD phase data.

The energy resolution σ_T that is determined from these SNOMAN simulated electrons is presented in figure 6.11. The energy resolution function shown fit to the data is

$$\sigma_T = -0.275 + 0.483\sqrt{T_{\rm e}} + 0.0267\,T_{\rm e}. \tag{6.8}$$

This may be compared to the dashed line in figure 5.13 that indicates the energy resolution function determined for the LETA pure D_2O phase: equation 5.12.

6.4 NCD phase energy reconstruction error

Contributions to the RSP energy reconstruction error for the NCD phase are presented here. The potential errors discussed in section 5.5, including those from other sources,

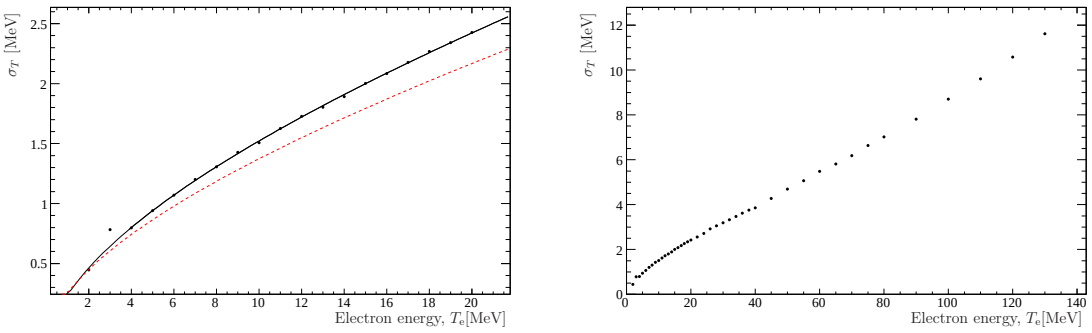

(a) Electrons with energies from 2 to 20 MeV. (b) Electrons with energies from 2 to 130 MeV.

Figure 6.11: Electron energy resolution σ_T of SNOMAN simulated electrons as a function of electron energy T_e. The solid line equation 6.8 while the dashed line is the energy resolution function of the LETA pure D_2O phase (equation 5.12).

are summarized and combined in subsection 8.3.3. In that section a comparison is made with the error used in the analysis presented by Aharmim et al. [1].

6.4.1 PMT status

The fraction of working PMTs with occupancy rates, per event, more than 5σ from the mean is plotted in figures 6.12a and 6.12b for NCD phase low rate central ^{16}N calibrations and data runs respectively. The mean value for the ^{16}N calibrations is less than 0.01%.

As a cross-check the mean fraction of suspect PMTs considered working during neutrino runs with more than 3000 events and a mean PMT occupancy rate more than 2.5σ from zero, is plotted in figure 6.12b. This considerably limits the number of available runs. This is a result of shorter more frequent runs in the NCD phase. The mean of the data points in figure 6.12b is 0.031%, which is consistent with that observed for the more precise determination made using ^{16}N calibrations. Therefore, the greater of the two uncertainties—0.031%—is adopted as the contribution to the NCD phase energy reconstruction error.

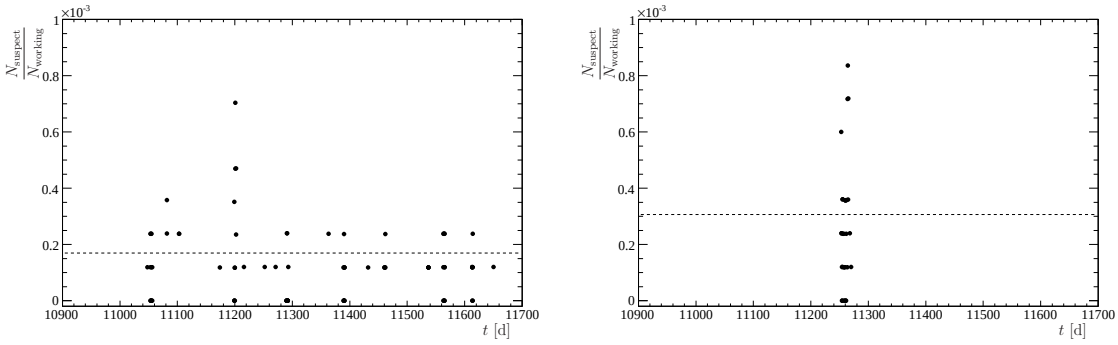

(a) Low rate central ^{16}N calibrations.

(b) Long neutrino runs.

Figure 6.12: The fraction of PMTs considered in good working order that have suspect occupancy rates during NCD phase. The means of the data points are 0.017 and 0.031% respectively.

6.4.2 Energy scale temporal variation

The fractional difference F^{μ} between the mean energy of central ^{16}N calibrations and simulations for the NCD phase are shown in figure 6.13. A mean error of $-0.052 \pm 0.013\%$ is observed. However, the χ^2 per degree of freedom is 161.6/82. The uncertainty on the mean is increased to account for this (see appendix C) such that the mean becomes $-0.052 \pm 0.018\%$. The overall error is accounted for, with its proper weight, in the determination of the spatial variation error. The contribution to the uncertainty in the energy scale error is 0.018%.

6.4.3 Energy scale spatial variation

The spatial distribution of ^{16}N calibrations during the NCD phase leads to the same volume partitioning of the detector as used for the salt phase. The volume elements are listed in table 5.3 and graphically displayed in figure 5.32. The volume bounded by radii of 375 and 550 cm and angles 0.375 to 1.165 contains no ^{16}N calibrations during the NCD phase. The outer most radial bins are not considered during this analysis as they lie beyond the fiducial volume.

Figure 6.14 shows distribution of F^{μ} for each of the NCD phase ^{16}N calibrations as a function of the source radial position. The colours of the points indicate in which

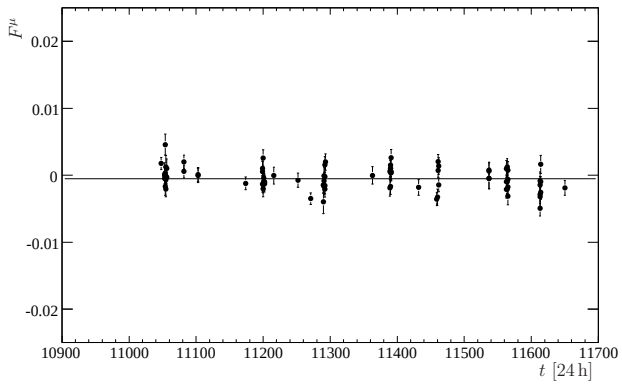

Figure 6.13: The fractional difference F^μ between the mean energy of central ^{16}N calibration data, taken during the NCD phase, and the simulation as a function of time. The mean of the data points is $-0.052 \pm 0.013\%$.

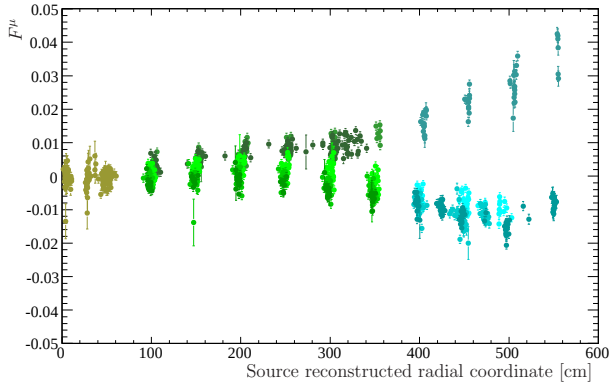

Figure 6.14: The fractional difference F^μ between the mean energy of NCD phase ^{16}N calibrations and the simulation as a function of source radius. The colours of the points correspond to the volume element colours in figure 5.32.

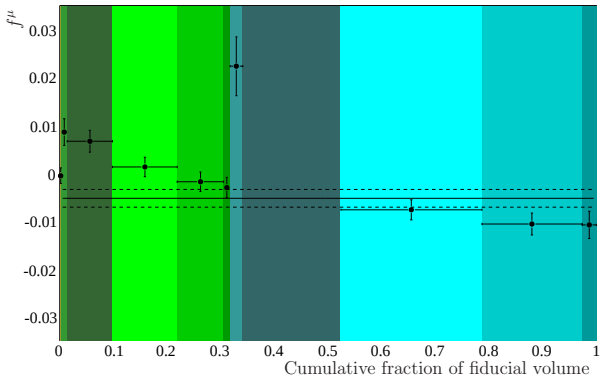

Figure 6.15: The mean f^μ of the like coloured points in figure 6.14 with RMS error bars. The colours of the bands correspond to the volume element colours in figure 5.32. There is no data point in the eighth colour band as no ^{16}N calibrations are performed in that volume element. The solid line with dashed error bands illustrates the volume weighted mean of the data points $\delta\mu_T = -0.524 \pm 0.187\%$.

volume element, as in figure 5.32, the data resides. The mean, with RMS error, of each group of like-coloured points is plotted in figure 6.15. The coloured bands indicate the fraction of the total fiducial volume each point represents. As per the prescription detailed in subsection 5.5.1, the energy scale error $\delta\mu_T$, shown as the solid line with dashed error band on figure 6.15, is determined to be $-0.524 \pm 0.187\%$.

6.4.4 Event rate dependence

The fractional difference F^μ between the mean energy of low rate central ^{16}N calibrations and the simulation in the NCD phase is plotted in figure 6.16. An energy scale error of $0.013 \pm 0.057\%$ is observed.

6.4.5 Energy resolution temporal variation

The fractional difference F^σ between the energy resolution of central ^{16}N calibrations and that of the simulation in the NCD phase are shown in figure 6.17. A mean error of $1.313 \pm 0.084\%$ is observed. The overall error is large but is accounted for, with the proper weighting, in the determination of the spatial variation error. The contribution to the uncertainty in the energy resolution error is 0.084%.

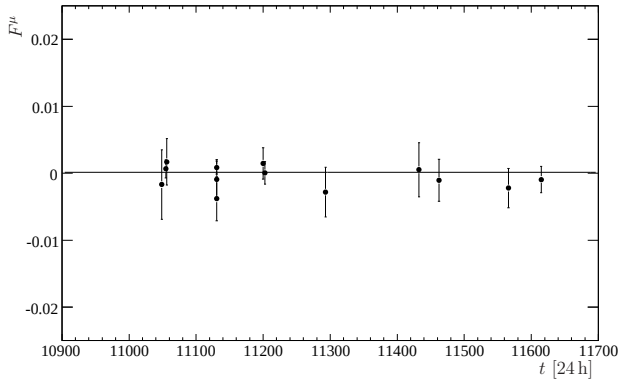

Figure 6.16: The fractional difference (F^{μ}) between the mean energy of low rate ^{16}N calibrations and the simulation during the NCD phase. A mean offset of $0.013 \pm 0.057\%$ is observed.

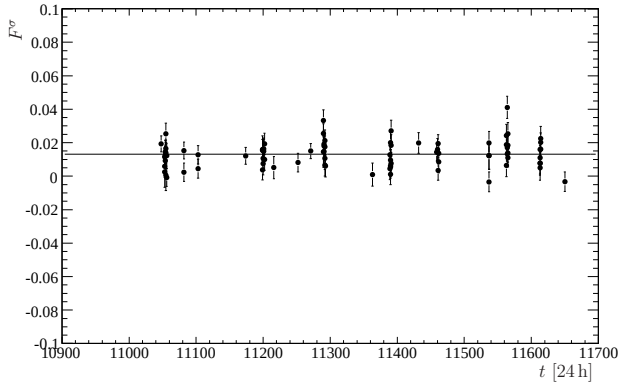

Figure 6.17: The fractional difference F^{σ} between the energy resolution of ^{16}N calibrations and that of the simulation in the NCD phase. The mean of the data points is $1.313 \pm 0.084\%$.

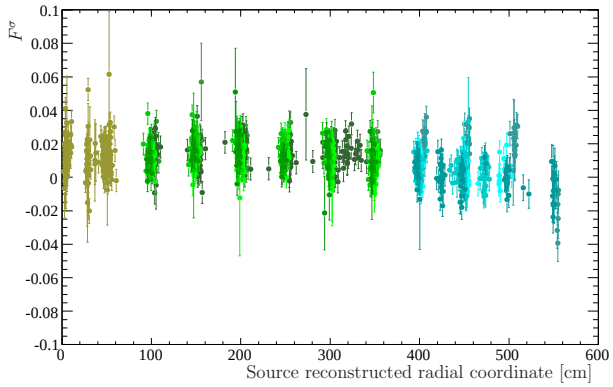

Figure 6.18: The fractional difference F^σ between the energy resolution of NCD phase ^{16}N calibration data and that of the simulation as a function of source radius. The colours of the points correspond to the volume element colours in figure 5.32.

6.4.6 Energy resolution spatial variation

The same spatial binning that is used for the determination of the energy scale error associated with spatial variations (subsection 6.4.3) is appropriate to use in this case. Figure 6.19 shows distribution of F^σ for each of the NCD phase ^{16}N calibrations as a function of the source radial position. The colours of the points indicate in which volume element, as in figure 5.32, the data resides. The mean, with RMS error, of each group of like-coloured points is plotted in figure 6.19. The coloured bands represent the fraction of the total fiducial volume each point represents. $\Delta\sigma_T$, calculated as per the prescription detailed in subsection 5.5.1, is shown as the solid line with dashed error band on figure 5.22. The energy resolution error $\Delta\sigma_T = 0.662 \pm 0.187\%$.

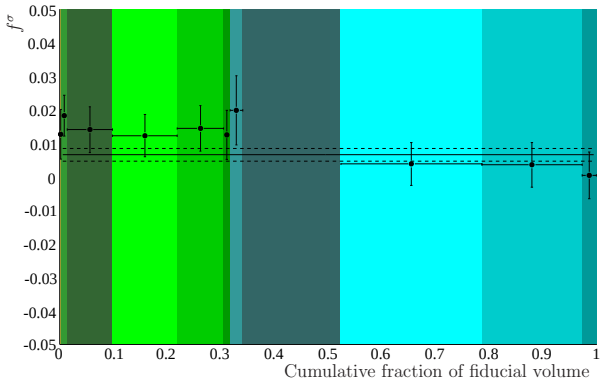

Figure 6.19: The mean fractional difference f^σ between the energy resolution of NCD phase ^{16}N calibrations and that of the simulation for each of the volume elements listed in table 5.3. The colours of the bands correspond to the volume element colours in figure 5.32. There is no data point in the eighth colour band as no ^{16}N calibrations are performed in that volume element. The solid line with dashed error bands illustrates the volume weighted mean of the data points ($\delta\sigma_T$), which is $-0.662 \pm 0.187\%$.

Chapter 7

^{16}N calibration energy scale error

The energy scale calibrated using ^{16}N calibrations (via $\epsilon_\circ$) is not necessarily the same as the energy scale that would be determined for single electron events such as those that signal neutrino interactions. Any difference in the way that the simulation deals with γ-rays in contrast to single electrons, can lead to energy scale error when calibrating $\epsilon_\circ$. This error is not specific to a particular method of energy reconstruction—$N_{\rm hit}$, the original, RSP, or FTK—rather it is inherent in the simulation. That being said, the RSP reconstructed energy is used throughout this chapter.

In this chapter, the effect of varying the simulated source geometry, the ^{16}N decay scheme, and the relevant cross section uncertainties and non-physical parameters associated with the EGS4 processor are studied. The change in energy scale induced by any possible inaccuracy in the simulated distribution of γ-rays emerging from the source is estimated by direct comparison with calibration. It was recognized by Hamer [88] that a simplification made when SNOMAN selects the energy of a Čerenkov photon could lead to an energy scale error as large as 0.5%. The implementation of a more precise calculation in the simulation yields a measurement of the error at less than 0.1%.

7.1 ^{16}N source geometry

The nominal ^{16}N source geometry used in SNOMAN simulations is shown in figure 7.1a. A more complete ^{16}N source geometry is represented by figure 7.1b.

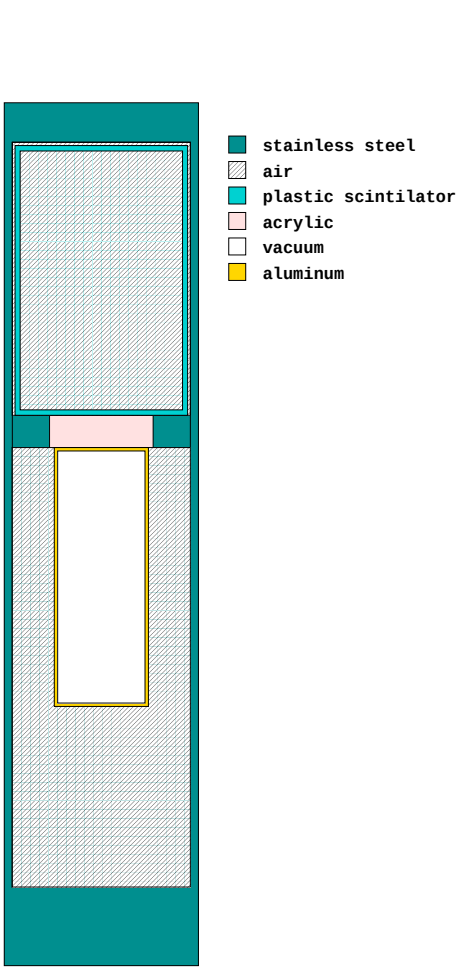

(a) Nominal ^{16}N source geometry.

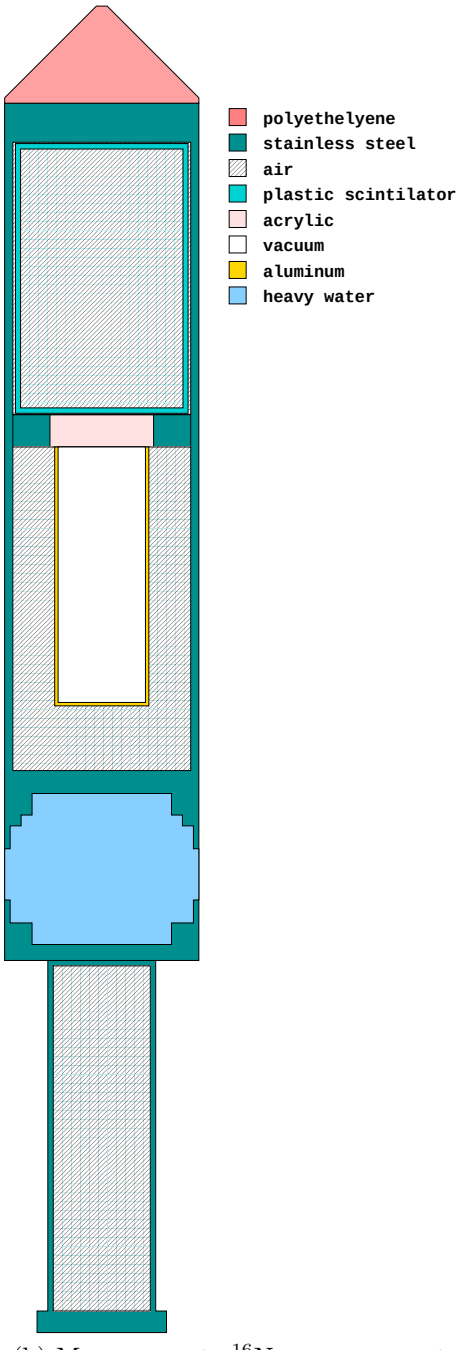

(b) More accurate ^{16}N source geometry.

Figure 7.1: Nominal and more accurate simulated ^{16}N source geometries. The outer dimensions of the source are approximately 50 cm in height by 6 cm in radius. In this depiction the sources are inverted vertically.

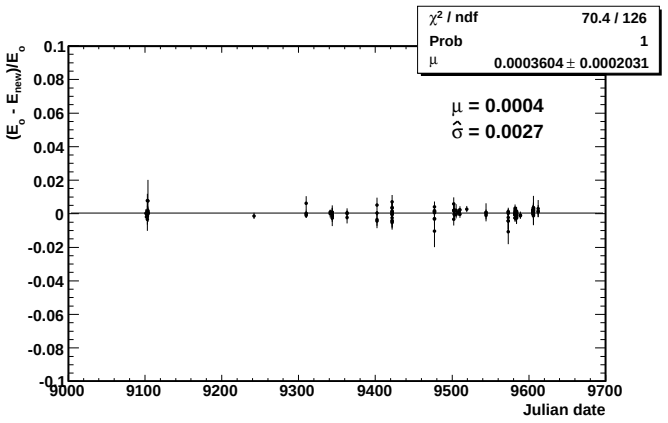

Figure 7.2: Fractional difference between the mean energy of simulated pure D_2O central ^{16}N calibrations with the two different simulated source geometries.

In the improved model, a polyethylene bumper cone is added to the bottom of the source and an attempt is made to better model the lighthouse[1] above the main source chamber. The physical lighthouse consists of stainless steel can in which eight rectangular windows are cut. The lighthouse, in the new model, is represented by a hollow cylinder of stainless steel. In the centre of the simulated lighthouse, a volume equivalent to that of the lighthouse windows is replaced with D_2O. A stainless steel weight cylinder is also added to the top of the source. The physical weight cylinder is hollow and, therefore, is filled with air in the simulation.

The difference between the energy response of the simulation with the standard source geometry and that with the updated one in figure 7.1b is plotted in figure 7.2. To ensure the accuracy of this test all of the pure D_2O phase simulations are compared to the equivalent simulations with the updated source geometry and plotted as a function of time. The weighted average energy scale error due to using the simpler source geometry in the simulation is $0.04 \pm 0.02\%$ as per figure 7.2.

[1]Light can be emitted from ^{16}N decays inside the umbilical line that traverses the lighthouse. However, the name derives from the rectangular windows with rounded corners not because it in anyway acts like a beacon of light. The windows are required for assembly and maintenance.

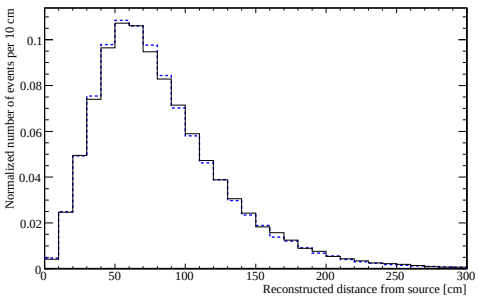

(a) Distance at which events reconstruct from the source position. Both of the histograms are normalized to the same area.

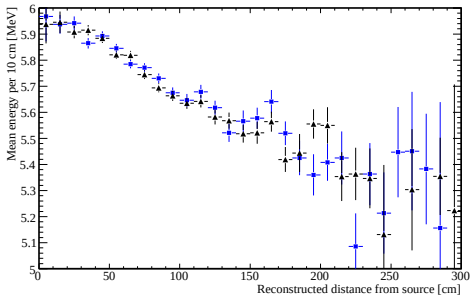

(b) Mean energy as a function of distance from the source.

Figure 7.3: The radial distribution of events from a pure D_2O phase ^{16}N calibration (blue) and that from the simulation.

7.2 Reconstructed ^{16}N γ-ray distributions

A possible source of energy scale error arises from any discrepancy between the spatial distribution of γ-rays emerging from the ^{16}N source and that emerging from the simulated one. In both the calibration data and the simulation reconstructed event energy varies with event position and direction. Therefore, variation in the radial distribution of events, event direction from the source (which is highly correlated with the direction of the γ-ray), and angular distribution of events (with respect to the direction of the γ-ray) can skew the tuning of the absolute energy scale via $\epsilon_{\circ}$. It must be noted that the energy scale errors derived from these three event distributions are likely correlated. Data selection is applied in each case to minimize these correlations.

7.2.1 Radial distribution of ^{16}N calibration events

The normalized distribution of ^{16}N events as a function of reconstructed position from the source is plotted in figure 7.3a for a pure D_2O phase calibration and simulation. The calibration events (blue dashed histogram) tend to reconstruct slightly closer to the source. The mean energy of the events in each bin of figure 7.3a are plotted in figure 7.3b–again with the calibration in blue. The difference between the mean

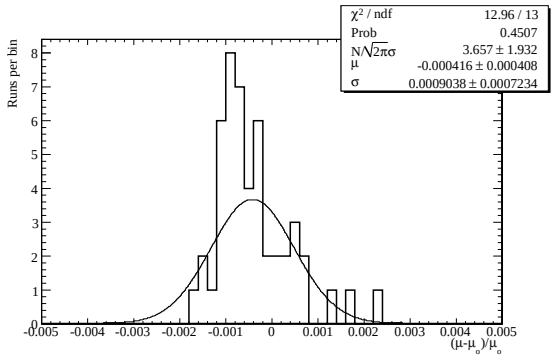

Figure 7.4: The fractional difference between the mean energy of the simulation and the mean energy predicted if the events in the simulation were distributed exactly as the calibration events. The radial (from the source position) distributions are shown in figure 7.3a while the energy dependence is shown in figure 7.3b. Each entry is derived from the simulation of a separate pure D_2O phase central ^{16}N calibration.

energy of the simulation and the mean energy predicted if the simulated ^{16}N γ-rays were distributed exactly as the calibration events, but retaining the radial profile of the mean energy from the simulation, is the energy scale error associated with the errant radial distribution. This error, derived from the comparison of each pure D_2O phase central ^{16}N calibration to the simulation, is plotted in figure 7.4. The mean of a Gaussian fit to the distribution of errors is $-0.04 \pm 0.04\%$ but with a width of 0.09%. The uncertainty on the energy scale is conservatively estimated at 0.09%.

7.2.2 Polar angle distribution of ^{16}N calibration events

The normalized distribution of ^{16}N events as a function of the vertical component of reconstructed direction is plotted in figure 7.5a for an ^{16}N calibration and the simulation. This is a better representation of the polar angle distribution of γ-rays emerging from the source than the direction from the source to the event position. Although Compton electrons tend to be collinear with this direction, the approximation breaks down due to event vertex mis-reconstruction.

In figure 7.5a, the ^{16}N calibration events (blue dashed histogram) are more likely to reconstruct in an upward direction than those of the simulation. This is a result of not only the mis-modeling of the internal components of the simulated source but also

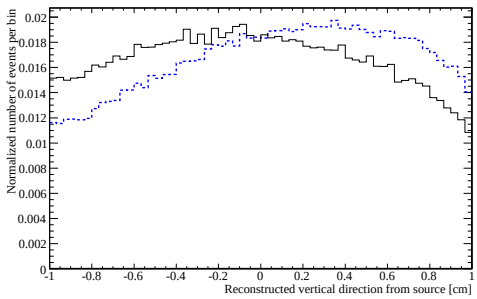

(a) Vertical component of reconstructed event direction. Both of the histograms are normalized to the same area.

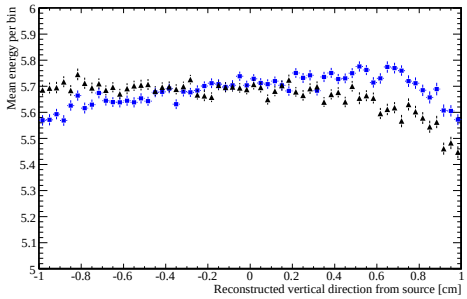

(b) Mean energy as a function of the vertical component of the reconstructed event direction.

Figure 7.5: Distribution of the vertical component of reconstructed direction for events from a pure D_2O phase ^{16}N calibration (blue) and that of the simulation.

inaccuracies in the modeling of the acrylic chimney in the simulation. Unfortunately these two effects are inseparable. However, this can only lead to a more conservative error on the energy scale by increasing the discrepancy between the ^{16}N calibration and the simulation. The mean energy of the events in each bin of figure 7.5a is plotted in figure 7.5b, again with the calibration in blue. In this case the up-down asymmetry is more likely due to the poor approximation of the chimney acrylic used in the simulation rather than the possibility of upward going γ-rays depositing less energy in the simulation than in ^{16}N calibration events. The difference between the mean energy of the simulation and the mean energy predicted if the simulated ^{16}N γ-rays were distributed exactly as the calibration events is the energy scale error associated with the errant polar angle distribution. This error, derived from the comparison of each pure D_2O phase central ^{16}N calibration to the simulation, is plotted in figure 7.6. The mean and width of a Gaussian fit to the distribution of errors are both 0.01%. The uncertainty on the energy scale is therefore take to be 0.01%.

7.2.3 Angular distribution of ^{16}N calibration events

The normalized distribution of ^{16}N events as a function of the cosine of the angle between the reconstructed direction and radial position vector, from the source position, is plotted in figure 7.7a for an ^{16}N calibration and the simulation. The calibration

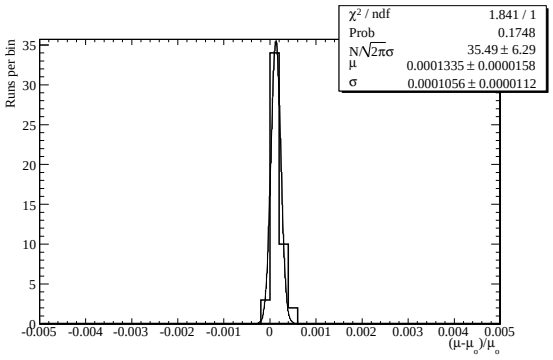

Figure 7.6: The fractional difference between the mean energy of the simulation and the mean energy predicted if the events in the simulation were distributed exactly as the calibration events. The vertical component of reconstructed event direction distributions are shown in figure 7.5a while the energy dependence is shown in figure 7.5b. Each entry in the figure derives from the simulation of a separate pure D_2O phase central ^{16}N calibration.

events (dashed blue histogram) have slightly worse angular resolution than the simulated events. The mean energy of the events in each bin of figure 7.7a is plotted in figure 7.7b, again with the calibration in blue. The difference between the mean energy of the simulation and the mean energy predicted if the simulated ^{16}N γ-rays were distributed exactly as calibration events is the energy scale error associated with the errant angular distribution. This error, derived from the comparison of each pure D_2O phase central ^{16}N calibration to the simulation, is plotted in figure 7.8. The mean and width of a Gaussian fit to the distribution of errors are 0.04% and 0.02% respectively. The uncertainty on the energy scale is therefore take to be 0.045%.

The errors measured in this section cannot distinguish between the error in the dimensions of the source and errors in γ-ray interactions in the source. However, it is their net effect that is of interest. The total energy scale error due to these effects as measured with the reconstructed position, direction, and energy of ^{16}N γ-rays is conservatively estimated to be less than 0.1%; the quadrature sum of the errors presented in this section is less than 0.1%.

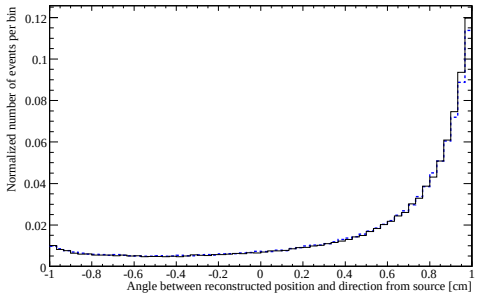

(a) Angular distribution of reconstructed events. Both of the histograms are normalized to the same area.

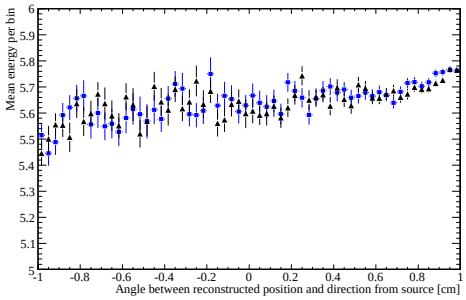

(b) Mean energy as a function of the angle between the reconstructed event direction and radial position vector.

Figure 7.7: Distribution of ^{16}N events as a function of the cosine of the angle between the reconstructed direction and radial position vector from a pure D_2O phase ^{16}N calibration (blue) and that of the simulation.

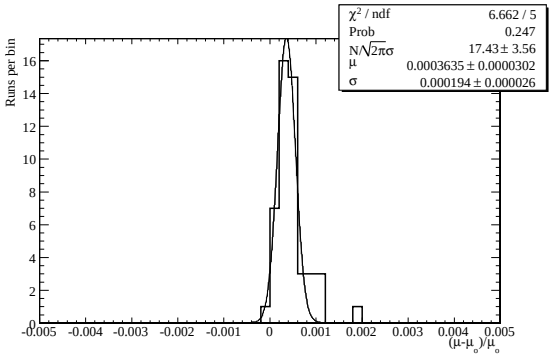

Figure 7.8: The fractional difference between the mean energy of the simulation and the mean energy predicted if the events in the simulation were distributed exactly as the calibration events. The angular distributions are shown in figure 7.7a while the energy dependence is shown in figure 7.7b. Each entry in the figure derives from the simulation of a separate pure D_2O phase central ^{16}N calibration.

β end point energy [MeV]	γ-ray energy [MeV]	Branching ratio [%]
10.4187	-	26.0
4.2883	6.1304	68.0
3.3018	7.1169	4.9
1.5468	8.8719	0.077
1.5468	6.1304	0.836
1.5468	6.9190	0.044
1.5468	7.1169	0.00153

Table 7.1: ^{16}N γ-ray branching ratios in SNOMAN simulations. The last three entries in the table are also accompanied by another γ-ray with an energy of 2.7415, 1.9529, and 1.7550 MeV respectively.

7.3 Uncertainty in the ^{16}N decay scheme

Since the Čerenkov yield of ^{16}N γ-rays (or rather that of the electrons that they scatter) directly depends on their energy, any uncertainty in their energy or branching ratios results in an offset in the calibrated energy scale via $\epsilon_\circ$. The ^{16}N γ-rays modeled in SNOMAN simulations are listed in table 7.1. The current best estimates for the ^{16}N decay from Firestone [16] are presented in table 7.2. The main branches of interest are the 6.13 and 7.12 MeV.

The uncertainty on the energy of the 6.13 MeV γ-ray energy is less than 0.1 keV. This amounts to an energy scale error of less than 0.002%. The uncertainty on the energy of the second most prolific ^{16}N γ-ray, with an energy of 7.12 MeV, is about 0.1 keV. This results in an energy scale error of less than 2×10^{-4}%. In total, the uncertainty in the energy of the γ-rays in ^{16}N decay does not result in a significant energy scale uncertainty and is therefore neglected.

The ratio between the 7.12 and 6.13 MeV γ-ray branching ratios in SNOMAN simulations is 0.0721 while that of the current best estimate is 0.0708. The dependence of the mean energy of the simulation on this ratio is shown in figure 7.9. A linear fit specifies a rate of change in energy of 0.68 MeV per unit change in the ratio of the 7.12 to 6.13 MeV branching ratios. The difference between the ratios results in an energy scale shift of -0.02%. The uncertainty in the ratio results in a 0.07% energy

β end point energy [keV]	γ-ray energies [keV]			Branching ratio	Branching ratio uncertainty
10419.1				28.0	0.4
4369.7	6048.2			0.010	0.040
4289.2	6128.63			67.82	0.60
3302.2	7115.15			4.8	0.4
3302.2	1067.5	6048.2		1.5×10^{-5}	1.5×10^{-5}
3302.2	986.93	6128.63		0.00339	0.00080
1547.2	8869.6			0.076	0.010
1547.2	2822.2	6048.2		0.13	0.04
1547.2	2741.5	6128.63		0.82	0.06
1547.2	1954.7	6915.5		0.038	0.006
1547.2	1954.7	867.7	6048.2	0.0002100	0.0000020
1547.2	1954.7	787.2	6128.63	1.5×10^{-6}	1.5×10^{-6}
1547.2	1754.9	7115.15		0.118	0.010
1547.2	1754.9	1067.5	6048.2	3.6×10^{-7}	3.3×10^{-7}
1547.2	1754.9	986.93	6128.63	8.2×10^{-5}	2.1×10^{-5}
834				0.0012	0.0005
574.6				6.5×10^{-7}	2.0×10^{-7}

Table 7.2: ^{16}N γ-ray branching ratios from [16]. The branching ratio and branching ratio uncertainty are listed as the number of γ-rays that are expected from 100 ^{16}N β decays.

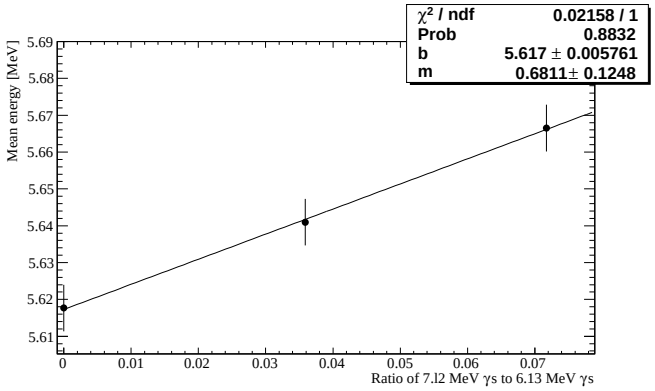

Figure 7.9: Change in the mean energy of a simulated ^{16}N calibration as a function of the ratio between the 7.12 and 6.13 MeV γ-ray branching ratios.

EGS4 parameter	Default value in SNOMAN
AE	521 keV
AP	10 keV
ECUT	660 keV
PCUT	150 keV
ESTEPE	3%

Table 7.3: The default values of the EGS4 parameters in SNOMAN simulations. Both AE and ECUT refer to total electron energy $E_e = T_e + 511\,\text{keV}$.

scale uncertainty.

7.4 EGS4 non-physical parameters

Generally EGS4 has been well tested by other fields (mainly in medical physics at energies similar to SNO). However, changes in the Čerenkov yield observed when varying the non-physical parameters in EGS4 can give rise to an error in energy scale. These non-physical parameters are listed in table 7.3 with their default value in SNOMAN simulations. The description of each and their implications for the energy scale are discussed in the following.

For electrons above 5 MeV, a 0.2% change in the Čerenkov yield is observed by Lay [77] when varying the AE parameter in EGS4 from 521 keV to 661 keV. The AE parameter is the energy below which no further electrons may be produced [82]. It serves as the boundary between where EGS4 considers energy loss to be due to discrete interactions, such as the scattering and tracking of β-rays, and where it considers energy loss to be continuous. The creation of β-rays with energy below AE is included in the calculation of continuous energy loss in EGS4. The 0.2% variation in Čerenkov yield with AE is a result of the difference between energy loss due to discrete interactions and those in the continuum as calculated by EGS4. This can be considered a threshold effect that influences the Čerenkov yield of every electron with an energy above AE equally.

A 0.8% uncertainty is observed by Lay [77] when varying ESTEPE between 1%

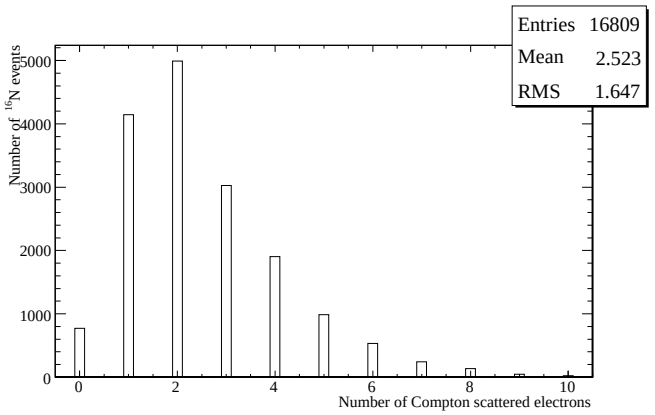

Figure 7.10: The number of Compton scattered electrons, based on SNOMAN simulations of an ^{16}N calibration, per reconstructed ^{16}N decay.

and 10%. ESTEPE is the upper limit on electron energy loss per step. Normally the step length is shorter than ESTEPE owing to discrete interactions such as the creation of δ-rays above AE. In the tests done by Lay [77] AE was set to 50 keV. Therefore, for the nominal 10 keV AE, it is expected that ESTEPE will be less influential in the calculation of the Čerenkov yield. In any case, the 0.8% uncertainty is a scaling effect rather than a threshold effect. The Čerenkov yield of all electrons is expected to be effected by the same factor: up to 0.8%.

The Čerenkov yield uncertainties observed when varying AE and ESTEPE do not necessarily translate into energy scale error. The absolute energy scale is tuned to match calibration data; any offset in the Čerenkov yield is included when tuning $\epsilon_\circ$. However, the difference between the Čerenkov yield error for γ-ray events, such as those of the ^{16}N calibration, and single electron events would remain. The uncertainty in the Čerenkov yield of a single electron is amplified by the number of electrons scattered by a γ-ray. The number of Compton scattered Čerenkov electrons per ^{16}N decay, based on SNOMAN simulations, is shown in figure 7.10. On average, 2.52 electrons are Compton scattered subsequent to ^{16}N β-decay. This may be compared to 2.46 by a 6.13 MeV [88] γ-ray.

For, on average, 2.5 electrons per ^{16}N decay, a 0.5% uncertainty is expected on the total Čerenkov yield of the ^{16}N γ-ray Compton scattered electrons due to the variations with AE (based on 0.2% per electron). This differs from the uncertainty

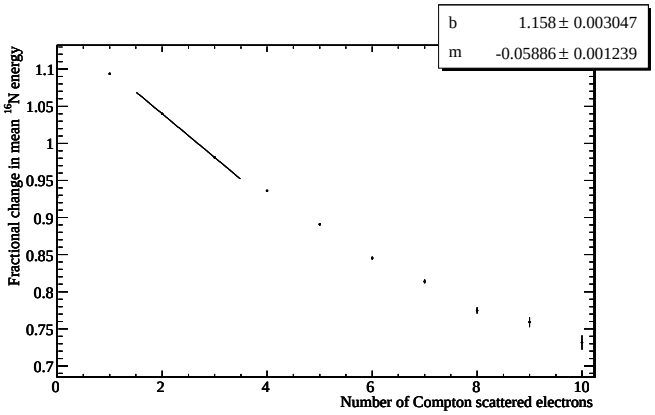

Figure 7.11: The fractional decrease in the mean Čerenkov yield of ^{16}N γ-rays, based on SNOMAN simulated ^{16}N calibrations, per Compton scattered electron.

in the single electron yield by 0.3%. Hence, the energy scale uncertainty due to the parameter AE is about 0.3%. Although varying the ESTEPE parameter can change the Čerenkov yield more so than the AE parameter [89], no difference is expected between its effect on single electrons as opposed to γ-rays. In either case the Čerenkov yield is altered by the same scale factor that would be absorbed into the PMT collection efficiency $\epsilon_\circ$ when tuning the energy scale of the simulation (see section 5.3).

7.5 EGS4 cross sections

As is introduced in the previous section, the main difference between the propagation of electrons and γ-rays lies in the multiple number of electrons produced by a γ-ray. EGS4 uses the Klein-Nishina formula [90] for the Compton scattering total and differential cross sections. Their assumption that the electron is free introduces a 0.3% uncertainty on the total cross section for energies below 300 keV [91]. It is also noted by Grodstein [91] that higher-order electrodynamic effects contribute to the cross section at about the 1% level. This may not be taken into account in EGS4. Comparing this treatment to experimental data, Storm and Israel [92] observes roughly a 3% discrepancy which is consistent with the less precise data presented by Heitler [93]. The mean energy deposited in the D_2O by γ-rays from ^{16}N decays decreased by 5.9% per electron that is Compton scattered according to figure 7.11. This may

be compared with 7.6% quoted by Hamer [88] for single 6.13 MeV γ-rays. For a 3% uncertainty on the total Compton cross section, this implies a 0.18% uncertainty in the energy scale.

Pair production by ^{16}N γ-rays also changes the energy distribution and multiplicity of electrons. The pair production cross section used in EGS4 [82] is taken from Motz et al. [94]. Further, it is corrected based on empirical data of [92], which claims an accuracy of about 5% on the measurement. It is reported by Hamer [88] that if pair production is completely removed from the simulation of 6.13 MeV γ-rays a 2% shift in the energy response is observed. This is in agreement with a 1.9% shift observed when removing pair production from the simulation of ^{16}N calibrations. For an uncertainty of 5%, this implies a 0.1% uncertainty in the energy scale.

Bremsstrahlung of either the ^{16}N β-particles in the source materials or Compton scattered electrons in the D_2O can also affect the Čerenkov yield of ^{16}N γ-rays, in the former case increasing the yield while in the later case slightly decreasing it. The Bremsstrahlung cross sections used in EGS4 are taken from Koch and Motz [95]. While they admit the cross sections may be uncertain by as much as 100% below 0.5 MeV, they conservatively estimate uncertainties at 10% for electron energies from 4 to 20 MeV. In comparison with higher energy data, they also consistently see less than 10% deviations from their theory. Removing bremsstrahlung from the simulation of ^{16}N calibrations changes the energy scale by only 0.72%, most of which is due to interactions in the source materials. For a 10% uncertainty in the bremsstrahlung cross section, the energy scale uncertainty is then, at most, 0.07% due to bremsstrahlung in the source materials.

Other interactions studied but found to contribute negligibly to energy scale error (relative to the size of those already discussed) include positron annihilation [93] and Bhabha scattering [96] after pair production, and the effects of multiple scattering (mainly Möller scattering as discussed by Messel and Crawford [96]). The effects of the positron interactions are second order compared to the effects of pair production itself, while multiple scattering is expected to affect both single electrons and electrons scattered by γ-rays in an analogous way.

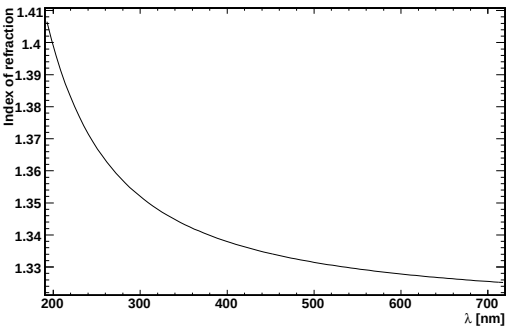

Figure 7.12: Wavelength dependent D_2O index of refraction

7.6 Čerenkov photon energy distribution

In SNOMAN, the number of Čerenkov photons created over each step of an electron track is

$$N = \delta x \frac{\alpha}{c} \int_{200\text{nm}}^{710\text{nm}} \left(1 - \frac{1}{\beta^2 n^2(\lambda)}\right) \frac{\mathrm{d}\lambda}{\lambda^2}, \tag{7.1}$$

where δx is the step length. In order to assign each generated photon a random wavelength that is representative of the parent distribution of Čerenkov light,

$$R = \frac{\displaystyle\int_{200\text{nm}}^{\lambda} \left(1 - \frac{1}{\beta^2 n^2(\lambda)}\right) \frac{\mathrm{d}\lambda}{\lambda^2}}{\displaystyle\int_{200\text{nm}}^{710\text{nm}} \left(1 - \frac{1}{\beta^2 n^2(\lambda)}\right) \frac{\mathrm{d}\lambda}{\lambda^2}}, \tag{7.2}$$

is solved for λ, where R is a random number in the interval (0,1]. The SNOMAN simulation simplifies equation 7.2 by using an average index of refraction, rather than one that is wavelength dependent. In this case, the distribution of Čerenkov light has a $1/\lambda^2$ distribution between the wavelength limits of 210 and 700 nm, as long as the condition for Čerenkov light generation is satisfied (equation 3.3).

Figure 7.13 shows the β^2 threshold for Čerenkov light generation by electrons in D_2O, for the index of refraction presented in figure 7.12. Also shown in the figure is the constant threshold in SNOMAN: the horizontal line.

The energy scale uncertainty associated with making the approximation in SNOMAN is conservatively estimated by Hamer [88] to be 0.5%. To test this, SNOMAN

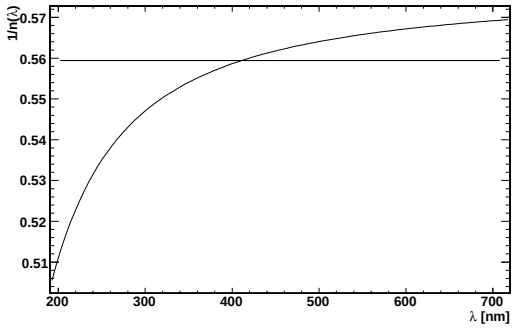

Figure 7.13: Electron Čerenkov threshold in D_2O. Both the wavelength dependent threshold and the constant threshold of the SNOMAN simulation are shown. Čerenkov light is only generated at a given wavelength above the indicated β^2 ($1/n^2$). Above a β^2 of approximately 0.57 all photon wavelengths are allowed in the region of interest to SNO.

was modified to pick the wavelength of a Čerenkov photon by interpolating a tabulated numerical solution, for λ, of equation equation 7.2. Figure 7.14 shows, for all allowed β^2 and any random number in the interval [0,1], the wavelength derived from equation 7.2 for the wavelength dependent index of refraction shown in figure 7.12. Similar tables were also constructed for acrylic and H_2O.

The difference in detector energy response between the SNOMAN simulation with the approximation and with the exact tabulated solution, is shown in figure 7.15 for the simulation of pure D_2O phase ^{16}N calibrations. 2.056% fewer photons, of the appropriate wavelength to produce hits in the PMTs, are observed. However, this is not an error in the energy scale as the simulation is tuned to match that of the ^{16}N calibrations. An error only arises if the Čerenkov yield of electrons does not change by the same amount (2.056%). Therefore, electrons of various energies were also simulated. The fractional difference in Čerenkov yield between the wavelength averaged and exact tabulated approaches was seen to exactly match the difference for the ^{16}N calibrations (2.056%). After correcting for the 2.056% offset observed in figure 7.15, the fractional difference in the Čerenkov yield of electrons is shown in figure 7.16. No energy scale error is observed. The uncertainty on the energy scale is 0.02% as indicated by the fit to the data points in figure 7.16.

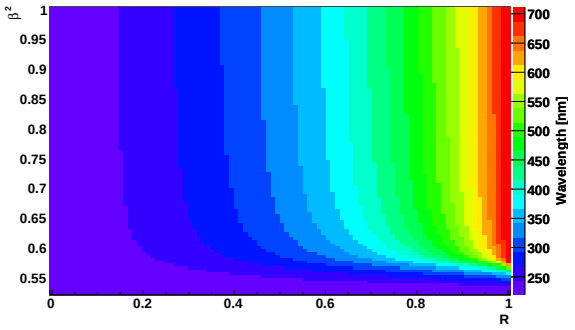

Figure 7.14: Wavelength of Čerenkov photons that satisfy equation 7.2 for the allowed β^2 and a wavelength dependent D_2O index of refraction.

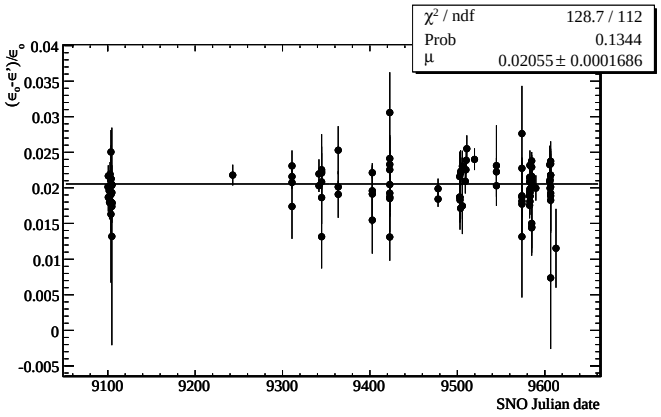

Figure 7.15: The fractional difference between the energy scale (mean N_γ) of the nominal SNOMAN simulated ^{16}N calibrations and that using the exact Čerenkov photon spectrum. Each pure D_2O phase central ^{16}N calibration is represented.

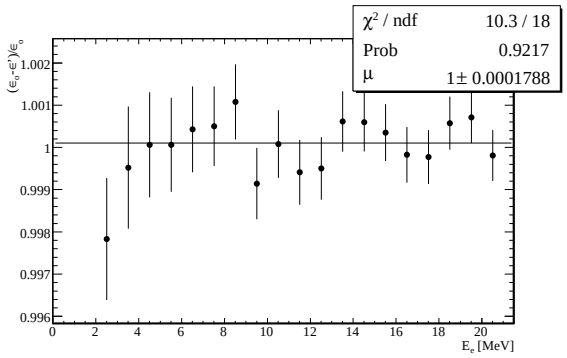

Figure 7.16: The fractional difference between the Čerenkov yield (mean N_γ) of the nominal SNOMAN simulated electrons and the simulation using the exact Čerenkov photon spectrum for various electron energies. The values have been corrected by the offset observed in figure 7.15: 2.055%.

7.7 Summary

All of the energy scale uncertainties discussed in this chapter, and one associated with the PMT noise rate, are summarized in table 7.4. The PMT noise rate uncertainty is based on measurements by Hamer [88] that show a 3% change in energy scale removing a 0.5 kHz noise rate from the simulation. For a roughly 1% uncertainty in noise rate over the duration of an ^{16}N calibration, the total energy scale uncertainty due to error in noise rate is 0.03%. The total energy scale systematic uncertainty, evaluated by adding in quadrature the individual contributions listed in table 7.4, is 0.41%.

Source of error	Energy scale uncertainty [%]
^{16}N source geometry	0.04
^{16}N decay scheme	0.08
γ-ray reconstruction	0.1
EGS4 Čerenkov yield	0.3
Compton scattering cross section	0.2
pair production cross section	0.1
bremsstrahlung cross section	0.07
Čerenkov photon energy distribution	0.02
Noise rate in PMTs	0.03
Total	0.41

Table 7.4: Summary of the contributions to the energy scale error due to the ^{16}N energy calibration. The uncertainty due to the PMT noise rate is taken from Hamer [88].

Chapter 8

NCD phase neutrino flux analysis

The goal of the neutrino flux analysis of the NCD phase is to produce a measurement of the total flux of active neutrinos from the Sun that is independent of previous measurements made using only the PMT array. The NCD array counts the neutrons that are the signal of the NC neutrino interaction in the D_2O. The data collected by the PMT array is used to derive the purest signal of the CC reaction, a measure of the ν_e flux. The largest background to the CC measurement, above 6 MeV in the PMTs, is due to NC neutrons which are efficiently suppressed through capture in the NCDs.

The solar neutrino flux analysis of the combined PMT and NCD data collected during the NCD phase of SNO is published in Aharmim et al. [1]. A summary of this data, the analysis techniques, and results from Aharmim et al. [1] is presented. Emphasis is placed on the contribution of the energy calibration of the PMT array to this analysis. The error in the energy scale and resolution that is used in the analysis of [1] is also compared to the measurements made in this work; as a verification of the analysis of Secrest [84]. This will provide valuable added perspective for future analyses wherein data from all three phases of the project will be combined to improve the overall accuracy of the results.

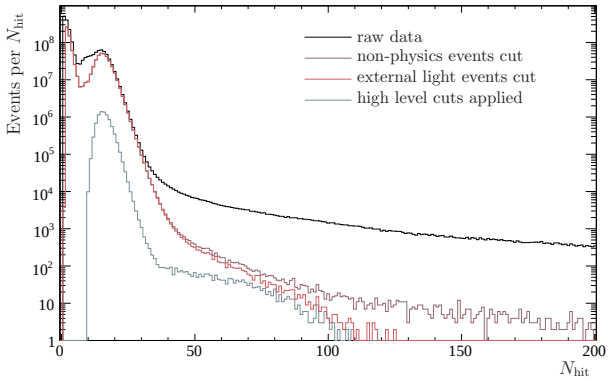

Figure 8.1: The $N_{\rm hit}$ distribution of all NCD phase PMT data. Also shown are successive data cleaning stages down to the data analyzed by Aharmim et al. [1] before application of the 6 MeV ($\gtrsim 40\,N_{\rm hit}$) energy threshold. The large reduction in the low $N_{\rm hit}$ events is primarily due to the application of a 550 cm radial cut that defines the fiducial volume.

8.1 Data set

Commissioning of the SNO detector in the NCD phase configuration was completed by the end of 2004. The detector was operated for neutrino measurement and interim calibrations from January 2005, until the end of October 2006, whereupon a final suite of calibrations, including radioactive spiking, were conducted. The data taken was subdivided into runs that were generally no more than 7 h. The data taken during a given run is considered suitable for analysis if the detector configuration was standard, both the PMTs and NCDs were properly calibrated and taking data, and no calibrations or detector maintenance activities were being performed. Numerous other checks are also performed offline to ensure data quality. The time the detector was live and recording good data amounts to 392.9 d. When corrected for dead time introduced as a result of data cleaning cuts, the live time is reduced to 385.17 ± 0.14 d [97]. The uncertainty in the livetime is the difference between the clock recorded times and that determined by counting a 5 Hz pulsed trigger. The raw $N_{\rm hit}$ spectrum of events triggering the PMT array are shown in figure 8.1 while the energy distribution of all events triggering the NCD system are shown in figure 8.2.

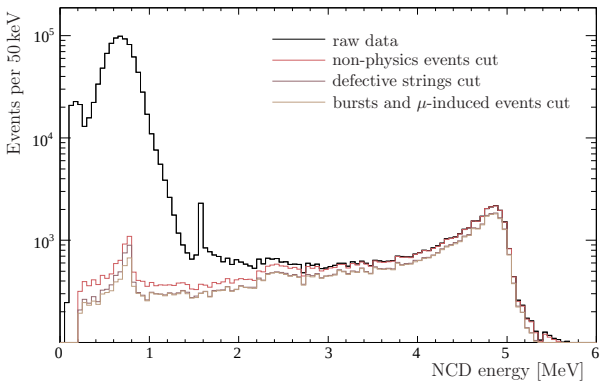

Figure 8.2: The NCD energy distribution of all NCD phase events. Also shown are successive data cleaning stages down to the data analyzed by [1], which further required events to be between 0.4 and 1.4 MeV.

8.2 Signal extraction

SNO data, as observed by the PMTs, is generally comprised of the three neutrino signals and various backgrounds. The preferred method for determining what fraction of the data each makes up is an unbinned maximum likelihood fit. During the NCD phase, an independent set of data was collected from the NCDs consisting of the NC signal and various backgrounds, some of which were in common with those observed by the PMTs. This data is incorporated into the standard SNO likelihood function $\mathcal{L}$ as

$$\mathcal{L} = \mathcal{L}_{\mathrm{PMT}} + \mathcal{L}_{\mathrm{NCD}}.$$

where the functions $\mathcal{L}_{\mathrm{PMT}}$ and $\mathcal{L}_{\mathrm{NCD}}$ are the likelihood that each set of data is the result of a particular set of parameters such as the fractions of each event type.

The construction of each likelihood function follows the same prescription. The likelihood is defined as the product of the probabilities of each event occurring given the probability density P that is based on a model parametrized by $\vec{\alpha}$. The likelihood function $\mathcal{L}_{\mathrm{XXX}}$ is therefore given by

$$\mathcal{L}_{\mathrm{XXX}} = \prod_{i=1}^{N} P(\vec{x}_i; \vec{\alpha}), \tag{8.1}$$

where[1] N is the number of events in the data.

If, as is generally the case for SNO analysis, P is a function of M distinct event types, the likelihood becomes

$$\begin{aligned}\mathcal{L}_{\mathrm{XXX}} &= \prod_{i=1}^{N}\sum_{j=1}^{M} p_j P(\vec{x}_i;\vec{\alpha}|j) \\ &= \prod_{i=1}^{N}\sum_{j=1}^{M} \alpha_j P(\vec{x}_i|j),\end{aligned}$$

where[2] p_j is the probability of the event being of type j. The model parameters, $\vec{\alpha}$, are generally taken to be the fraction of each event type in the data which are equivalent to $\vec{p}$.

By definition

$$\sum_{j=1}^{M} \alpha_j = 1,$$

therefore the number ν_j of each event type present in the data is given by

$$\nu_j = N\alpha_j.$$

If instead, the total number of events is considered to be a sampling of a Poisson distribution with mean ν, the likelihood becomes the product of the probability of observing N events and equation 8.1, or

$$\mathcal{L}_{\mathrm{XXX}} \rightarrow \frac{\nu^N e^{-\nu}}{N!}\mathcal{L}_{\mathrm{XXX}},$$

which is commonly referred to as the extended likelihood function.

At this point it is convenient to introduce the negative logarithm of the likelihood function

$$-\log \mathcal{L}_{\mathrm{XXX}} = \sum_{j=1}^{M}\nu_j - \sum_{i=1}^{N}\log\left[\sum_{j=1}^{M}\nu_j P(\vec{x}_i|j)\right], \tag{8.2}$$

[1]With respect to the notation $f(\vec{x};\vec{y})$, f is a function of the vector $\vec{x}$, or its components, yet depends on the vector components of $\vec{y}$.

[2]With respect to the notation $f(\vec{x}|\vec{y})$, f is a function of the vector $\vec{x}$, or its components, under the proposition y.

where the relations $\nu = \sum_{j=1}^{M} \nu_j$ and $\nu_j = \nu\alpha_j$ have been used and the terms not depending on any of the free parameters have been dropped. Equation 8.2 is minimized by the same parameters $\vec{\alpha}$ that maximize equation 8.1.

The PDFs P are generally[3] constructed from the observables $\vec{x}$ of simulated events. The nuisance parameters $\vec{\beta}$ are introduced to account for potential offset, scale, and resolution errors in the PDFs. These nuisance parameters are constrained by comparing simulated events to calibration data. Including n_β (on the order of three times the dimensions of P) nuisance parameters, equation 8.2 becomes

$$\begin{aligned} -\log \mathcal{L}_{\mathrm{XXX}} = & \sum_{j=1}^{n_\nu+n_\mathrm{b}} \nu_j - \sum_{i=1}^{N} \log \left[\sum_{j=1}^{n_\nu+n_\mathrm{b}} \nu_j P(\vec{x}_i; \vec{\beta}|j) \right] \\ & - \sum_{j=n_\nu+1}^{n_\nu+n_\mathrm{b}} \log P'(\nu_j|j) - \sum_{k=1}^{n_\beta} \log P''(\beta_k|k), \end{aligned} \tag{8.3}$$

where the number of event types M has been broken down into the number n_ν of neutrino signals and unconstrained backgrounds and the number n_b of constrained backgrounds. The one dimensional probability densities P' and P'' constrain the number ν_j of background events for $j > n_\nu$ and nuisance parameters $\vec{\beta}$. Generally, P' and P'' take the form of a Gaussian or an asymmetric Gaussian distribution. The P' are given a mean and width corresponding to an external estimate of the background with some measurement uncertainty. P' is potentially dependent on $\vec{\beta}$ in that the parameters can change the analysis window and therefore the number of background therein. However, this effect would be minimal above the energy threshold of 6 MeV imposed by Aharmim et al. [1]. As a prelude to discussions in the following section, it is noted that from a Bayesian perspective the unconstrained parameters are assigned uniform prior distributions while P' and P'' represent those of the constrained backgrounds and nuisance parameters.

Equation 8.3 is the underlying structure of both $\mathcal{L}_{\mathrm{PMT}}$ and $\mathcal{L}_{\mathrm{NCD}}$. However, the NC signal and several backgrounds are common to both the PMT and NCD data. The total number of unconstrained parameters is reduced and further constraints are

[3]The notable exception being the NCD neutron energy spectrum which is derived from ^{24}Na calibration data.

added to common constrained parameters when the parameters ν_j are replaced by the underlying flux or rate with which they are associated, specifically when

$$\nu_j \rightarrow f_j s_j \phi_j; \tag{8.4}$$

where f_j is the factor that converts the number of events to the flux or rate ϕ_j for the nominal P and s_j corrects f_j for any potential change in the normalization of the P when the $\vec{\beta}$ change. Although this introduces the parameters f_j into the likelihood function, they are well constrained by calibrated data.

8.3 Analysis inputs

The signals and backgrounds, with constraints where determined, in both the PMT and NCD arrays are listed in tables 8.1 and 8.2. The PDFs and associated nuisance parameters are also discussed. The complete assortment of systematic uncertainties, most of which are treated as nuisance parameters, are not listed or discussed. Rather, the error associated with the energy scale and resolution are presented in detail and compared to those derived in chapter 6.

8.3.1 Types of events: ν signals and backgrounds

The events observed by the PMT array, between 6 and 20 MeV, are classified by the event types listed in table 8.1 and discussed in this section. The neutrino flux derived from the CC, ES, and NC signals and the rate[4] of the neutron backgrounds are included as parameters in $\mathcal{L}_{\rm PMT}$. The Čerenkov backgrounds, mostly due to mis-reconstructed Compton scattered electrons, are applied as a final correction after the fluxes are determined. The isotropic acrylic vessel and other backgrounds are considered negligible compared to the approximately 1000 NC neutrons expected. The CC and ES fluxes are broken down into 13 separate parameters each[5]. The first 12 parameters represent the flux extracted from events within 0.5 MeV wide bins

[4]The rate actually determined by the analysis is the rate of background neutrons observed in the NCDs. The rate in the PMTs is fixed at a constant fraction of those observed in the NCDs.

[5]For a complete description of the validity of this procedure see Drouin [98].

between 6 and 12 MeV whilst the 13^{th} represents that from all events between 13 and 20 MeV. This differentiation is required since the energy dependence of neutrino oscillations is not constrained in the PDFs of $\mathcal{L}_{\text{PMT}}$.

The events observed by the NCD array, between 0.4 to 1.4 MeV, can be classified by the event types listed in table 8.2. All of the event types listed in table 8.2 are included as parameters in $\mathcal{L}_{\text{NCD}}$ with the exception of the other backgrounds that are considered negligible. The neutrino flux derived from the NC and the neutron background rates are treated as the same parameters, scaled by their relative detection efficiencies, in both $\mathcal{L}_{\text{PMT}}$ and $\mathcal{L}_{\text{NCD}}$. The conversion factors f (see equation 8.4) that enable this scaling were determined from SNOMAN Monte Carlo calculations and are listed in tables 8.3 and 8.4. The uncertainties on the NC conversion factors are due primarily to the uncertainty in the NC neutron detection efficiency. Given their uncertainties, both of the NC conversion factors are included as nuisance parameters in the analysis presented by Aharmim et al. [1].

8.3.2 Probability distribution functions

The analysis presented by Aharmim et al. [1] uses three-dimensional PDFs in the event observables $\vec{x} = (T_{\text{eff}}, |\vec{r}|, \cos\theta_{\odot})$ for $\mathcal{L}_{\text{PMT}}$ and one-dimensional PDFs in NCD energy for $\mathcal{L}_{\text{NCD}}$. All of the PDFs with the exception of the neutron energy spectrum in the NCDs are constructed from SNOMAN simulated events. The neutron NCD energy spectrum is taken from data collected by the NCDs while ^{24}Na, which acts as a source of photodisintegration neutrons [74], was distributed throughout the D_2O. Projections of the three-dimensional PDFs and the NCD energy PDFs of each signal and background are depicted in figure 8.3. The PDFs are scaled to represent the signal extraction fit results presented in the following section. Also shown in each figure is the data and the best-fit sum of the signal and background PDFs.

8.3.3 Nuisance parameters: energy reconstruction errors

In total 25 nuisance parameters are included in the likelihood function used by Aharmim et al. [1]: 13 associated with PMT observations and 12 associated with

Event type	External measurement [number of events]	External constraint [± number of events]
CC		
ES		
NC		
neutron backgrounds		
D_2O	8.3	0.1
AV(α,n), AV, H_2O	20.6	10.4
NCD and NCD cables	5.7	2.0
K2	9.3	1.5
K5	8.4	1.0
atmospheric and ^{16}N	24.7	4.9
total neutron background	77.0	11.9
Čerenkov backgrounds		
D_2O	0.7	0.38
AV, H_2O, PMTs	5.1	$+9.7/-2.9$
other backgrounds		
isotropic AV background	0.0	0.3
other backgrounds	0.7	0.1

Table 8.1: The three neutrino signals, neutron backgrounds, low energy Čerenkov backgrounds, and other backgrounds present in the NCD phase PMT data as analyzed by Aharmim et al. [1]. Neutrons from sources external to the D_2O are produced remotely via photodisintegration γ-rays with the exception of (α,n) decays on the inner surface of the AV. K2 and K5 are the designations of two NCD strings that exhibit regions with abnormally high levels of radioactive contamination. Other backgrounds include terrestrial $\bar{\nu}$s, reactor $\bar{\nu}$s, spontaneous fission, cosmogenics, *hep* and CNO νs, and (α, n) reactions [1]. Values taken from Jamieson [99] and Aharmim et al. [1].

Event type	External measurement [number of events]	External constraint [± number of events]
NC neutron backgrounds		
D_2O	31.0	4.8
AV(α,n), AV, H_2O	40.9	20.6
NCD and NCD cables	35.6	12.2
K2	32.8	5.2
K5	31.6	3.7
atmospheric and ^{16}N	13.6	2.7
total neutron background	185.5	25.4
α-particle background		
instrumental backgrounds		
other backgrounds	2.3	0.3

Table 8.2: The NC neutrino signal, neutron backgrounds, α-particle backgrounds, and instrumental backgrounds (the residual of data cleaning) present in the NCD phase NCD data as analyzed by Aharmim et al. [1]. Neutrons from sources external to the D_2O are produced remotely via photodisintegration γ-rays with the exception of (α,n) decays on the inner surface of the AV. K2 and K5 are the designations of two NCD strings that exhibit regions with abnormally high levels of radioactive contamination. Other backgrounds include terrestrial $\bar{\nu}$s, reactor $\bar{\nu}$s, spontaneous fission, cosmogenics, *hep* and CNO νs, and (α, n) reactions [1]. Values taken from Jamieson [99] and Aharmim et al. [1].

Neutrino signal	f [10^{-6} cm s]	δf [$\pm 10^{-6}$ cm s]
CC	1086.0	
ES	93.5	
PMT NC	46.7	0.6
NCD NC	176.7	5.9

Table 8.3: Neutrino flux to number of events conversion factors f used for the analysis presented by Aharmim et al. [1]. Values taken from Jamieson [99].

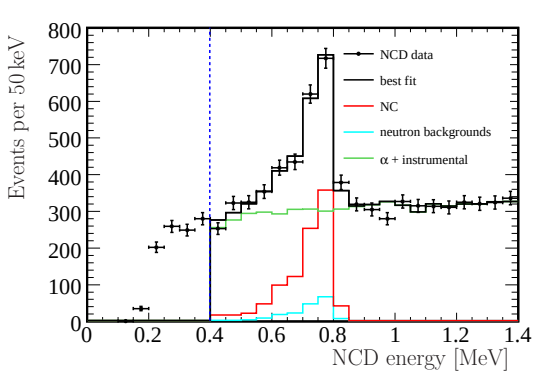

(a) NCD event energy.

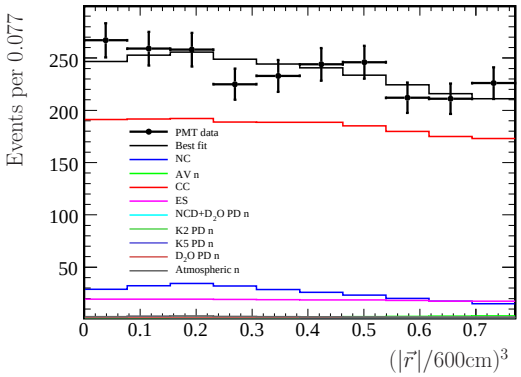

(b) Reduced radius.

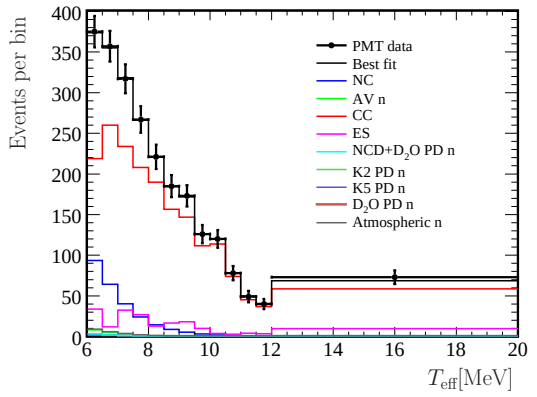

(c) PMT event energy.

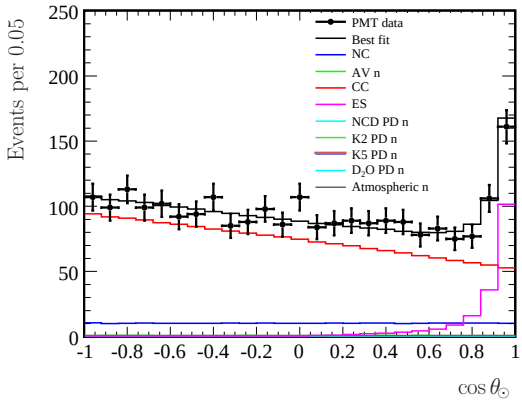

(d) Cosine of the angle between event direction and direction from the Sun.

Figure 8.3: One-dimensional projections of the three-dimensional PMT event observables PDFs and the NCD energy PDF. Shown are all the signal and background contributions to the overall data as presented in section 8.5.

Neutron background	$\mathcal{L}_{\mathrm{PMT}}\, f$	$\mathcal{L}_{\mathrm{NCD}}\, f$
D_2O PD	0.2677	1
AV(α,n), AV and H_2O PD	0.5037	1
NCD and NCD cables PD	0.1609	1
K2 PD	0.2835	1
K5 PD	0.2650	1
atmospheric νs and ^{16}N PD	1.8134	1

Table 8.4: Neutron background conversion factors f used for the analysis presented by Aharmim et al. [1]. PD refers to neutrons from the photodisintegration Deuterium. Values taken from Jamieson [99].

Source of error	Error as in Aharmim et al. [1] [%]	Error current work [%]
PMT status	$\pm\, 0.03$	$\pm\, 0.02$
PMT gain	$\pm\, 0.13$	
PMT threshold	$\pm\, 0.11$	
PMT timing calibration	$\pm\, 0.10$	
Temporal variation	0.11 ± 0.40	-0.05 ± 0.02
Spatial variation	-0.40 ± 0.25	-0.52 ± 0.19
Event rate dependence	-0.20 ± 0.07	0.01 ± 0.06
^{16}N source uncertainty	$\pm\, 0.65$	$\pm\, 0.41$
Total error	$\pm\, 1.04$	-0.46 ± 0.49

Table 8.5: The contributions to and total energy scale errors as in [1] and this work. The values in the central column are from Secrest [84].

NCD observations. Two nuisance parameters are assigned to PMT event energy: energy scale and energy resolution. The measured errors in the PMT event energy scale and resolution that are used in the analysis presented by Aharmim et al. [1], and detailed by Secrest [84], are listed in tables 8.5 and 8.6. Also shown are the values determined in chapter 6, to be used to verify those of Secrest [84].

For both the energy scale and resolution errors, the estimates used by Aharmim et al. [1] are conservative when compared to those derived in chapter 6. Although both of these analysis generally follow the same procedures and use the same ^{16}N calibrations and simulations, several improvements have been made by this work and

Source of error	Error as in Aharmim et al. [1] [%]	Error current work [%]
Temporal variation	1.40 ± 1.19	1.31 ± 0.08
Spatial variation	0.72 ± 0.32	0.66 ± 0.19
Total error	1.19 ± 1.04	0.66 ± 0.21

Table 8.6: The contributions to and total energy resolution errors as in [1] and this work. The values in the central column are from Secrest [84].

the interpretations of the total uncertainties differ. The most fundamental residual difference lies in the determination of the mean energy and energy resolution of the relevant energy distributions. The measurements made in this work employ an unbinned Gaussian fit, as described in appendix B, while the analysis of Secrest [84] histograms the data in 0.2 MeV wide bins. The primary concern when fitting binned energy is that it is ultimately derived from the integer quantity N_{hit}. Dividing the data into bins smaller than 0.5 MeV can lead to deviations from the postulated Gaussian distribution while using large bins limits the number of degrees of freedom in the fit to the distribution. Also, the unbinned approach avoids this limitation. The unbinned fit is done over a range of $\pm 1.67\sigma$[6] about the fitted mean while that of the previous work uses a range of $\pm 1.60\sigma$. The differences specific to each energy reconstruction error are discussed below.

Both analyses use approximately the same set of ^{16}N calibrations for the determination of the errors associated with spatial variation, between ^{16}N calibrations and simulation, of the energy scale. The difference between the results of the two analysis is therefore attributed primarily to the energy distribution fit discussed above.

The analysis of temporal variations between ^{16}N calibrations and the simulation differ due to the choice of ^{16}N calibrations used by each analysis. In the analysis presented in chapter 6 only high rate central ^{16}N calibration runs are used to determine the temporal variation. This is justified in that the variations introduced by non-detector-centric calibrations, or as a result of event rate effects, overwhelm any residual trends as a function of time and significantly increase the uncertainty in the measurement. In order to deal with the large variation observed when using such

[6] In both cases an iterative fit is done until both the fitted mean and Gaussian width converge.

extraneous calibration data, Secrest [84] uses the RMS of the temporal variation as a conservative estimate of the uncertainty (0.40%) rather than the uncertainty on the mean as reported in chapter 6 (0.02%).

Several differences in the calculation of the event rate energy scale error lead to a more conservative estimate by Secrest [84] compared to that measured in chapter 6. Again Secrest [84] also includes spatial variations in the measurement of event rate effects. This is of particular concern given that only a few low rate ^{16}N calibrations are done other than at the detector centre; certainly not enough to properly sample the spatial variation and therefore likely to bias the measurement. That analysis also includes a small sampling of the temporal variation in energy reconstruction error by comparing low rate to high rate ^{16}N calibrations taken during the same period rather than comparing directly to the simulation. It is noted that, while on average the temporal variation is small, the variation between ^{16}N calibrations taken during the same day can be significant (see figure 6.6).

The analysis presented in chapter 6 appropriately notes that the spatial variation, between low rate calibration data and the simulation, is consistent with that observed for the multitude of high rate calibrations. It also avoids the complications of temporal variation in the adjacent high rate calibrations, used by Secrest [84], by comparing the low rate ^{16}N calibration data reconstructed energy distribution directly to that of the simulation. This comparison is arguably more appropriate given that it is the difference between the calibration data and the simulation that is likely most similar to any potential difference between the sought after neutrino signals and their simulation. The latter comparison is used to perform the signal extraction that determines the neutrino fluxes.

The improvements in the ^{16}N source uncertainty are detailed in chapter 7. The largest improvement comes in the estimate of the 0.5% uncertainty associated with the simulation having used an average photon index of refraction to calculate the Čerenkov yield. In chapter 7, a measurement of this error is made and shown to be only 0.02%.

The proposed total error on the energy scale is determined by adding the spatial variation component and the difference between the rate dependence and temporal variation errors, the comparison between the high and low rate measurements only

being made at the centre of the detector. The temporal variation error is not specifically included in the total; rather it is properly accounted for in the spatial variation error. The uncertainty on the measurement error is determined by adding in quadrature each value listed in the right column of table 8.5 with the missing values taken from the values presented by Secrest [84] (the centre column). This differs from the procedure used to total the errors in Secrest [84] where the larger of an error and its associated uncertainty are assigned as an uncertainty. The exception is the spatial variation uncertainty which is taken as the sum of the error and its uncertainty ($—-0.40\%| + 0.25\%$) given that both are appreciable. These uncertainties are added in quadrature with the other uncertainties to determine the total energy scale uncertainty.

The proposed total error on the energy resolution is the spatial variation error alone. The temporal variation error is included in the spatial variation error. The uncertainty on the measured error is the quadrature sum of the temporal and spatial variation uncertainties. The analysis presented by Secrest [84] uses the uncertainty on the temporal variation error as the total energy resolution error. It further adds the error and uncertainty in the error ($0.72\% + 0.32\%$) due to the spatial variation to determine the uncertainty on the energy resolution error. This may have been the result of a mistake in the transcription of the results. Regardless, the uncertainty on the energy resolution used by Aharmim et al. [1], as determined by Secrest [84], remains conservative even when compared to the sum of the energy resolution error and its uncertainty as determined by this work.

8.4 Markov chain Monte Carlo parameter estimation

The standard approach to maximizing the likelihood function, or rather minimizing the negative logarithm of the likelihood function, is to use the minimization package MINUIT [100]. However, when dealing with a large number of free parameters MINUIT minimization is far from optimal. It can be the case that an attempted MINUIT minimization of the SNO likelihood function, as presented in section 8.2, would not converge in a finite time. The delay is significantly enhanced in this case

because of the time required to rebuild the likelihood PDFs each time the nuisance parameters are updated.

For the analysis presented by Aharmim et al. [1], a Markov Chain [101] Monte Carlo [102] (MCMC) utilizing the Metropolis-Hastings [103] algorithm is used for the parameter estimation. MCMC algorithms consist of a random walk through the parameter space of a model. Each step in the Markov chain, by designation, depends only on the previous state of the chain. However, these sampled steps are required to be representative of the joint posterior distribution Π, which for the analysis of the SNO data is interpreted to be $\exp(-\log\mathcal{L})$ [99]. The proper samples are generated via the transition kernel [104]. The proposed next set of parameters X_{t+1}, are derived from the current set of parameters X_t, based on a proposal distribution $\pi(X_{t+1}|X_t)$. The proposal distributions are in generally taken to be multivariate Gaussian distributions, one dimension for each model parameter, as is also the case for the analysis in Aharmim et al. [1]. The Metropolis ratio r is given by

$$\begin{aligned} r &= \frac{\Pi(X_{t+1})}{\Pi(X_t)}\frac{\pi(X_t|X_{t+1})}{\pi(X_{t+1}|X_t)} \\ &= \frac{\Pi(X_{t+1})}{\Pi(X_t)}, \end{aligned}$$

for symmetric proposal distributions. r is the ratio of the likelihood of the proposed parameters to that of the current parameters. If r is greater than 1.0 the proposed parameters are excepted; the step in the MCMC chain is taken. If it is less than 1.0, r is interpreted as the probability that the proposed parameters should be accepted. A random number generator is then used to decide if the step in the MCMC chain is taken. It can be shown [104] that samples generated with this algorithm reproduce the joint posterior distribution Π.

Two subtleties of this MCMC are an initial burn-in period and setting the widths of the proposal distributions. The initial burn-in period is required for the initial state to reach the stationary distribution, where it draws samples only from the desired posterior distribution. The widths of the proposition distributions must be calibrated to maximize the efficiency of the MCMC. If the widths are too narrow the MCMC will take longer to converge while if they are set too wide the sampled parameter space may be too sparse. Jamieson [99] proposes that a conservative burn-in period

for the NCD phase analysis is 3500 steps and that the proposition distribution widths be set to 1/3 of the prior width or expected statistical uncertainty in each parameter. This results in an acceptance of roughly 25% of all proposed steps which is the value recommended by Gregory [104].

The result of a long MCMC chain, after the initial burn-in period, will converge to the stationary posterior distribution. The posterior distribution of each free parameter, constrained or otherwise, can be projected out of the chain. The posterior distribution of a parameter extracted in this way contains all the information available in the data about the parameter including its mean, variance, and its correlations with all the other parameters in the likelihood function. It should also be noted that a reasonable estimate of the maximum likelihood can also be obtained from MCMC given that it draws many samples from the highest probability parameter space where the maximum likelihood is expect to lie.

8.5 Results

According to Jamieson [99], the neutrino fluxes reported by Aharmim et al. [1] are derived from 92 independent MCMC chains, each containing 6500 steps. After removal of the burn-in period, 276000 MCMC steps remained for parameter estimation. The result of the sum of MCMC chains, taken from Jamieson [99], are listed in table 8.7. The majority of parameters are determined from the mean value of the resulting posterior distributions. The CC and ES fluxes, however, are derived from the best-fit point corresponding to the highest likelihood step[7] in the chain. In all cases, the uncertainties on each parameter are determined from the width of an asymmetric Gaussian fit to the peak of the posterior distribution.

Assuming the ^{8}B neutrino spectrum of Winter et al. [106], the CC, ES, and NC ^{8}B neutrino fluxes (ϕ_{CC}, ϕ_{ES}, and ϕ_{NC}) derived from the NCD neutrino flux analysis

[7]The MCMC expectation values are shown by Oser [105] to have smaller errors than the best-fit values in ensemble tests. However, they also tend to have larger biases when approaching hard parameter limits, such as non-negative number of events or flux, which is the case for the individual CC and ES energy bins.

Event type	Energy range [MeV]	Results from [99]	Reproduction of [99]	This work
ϕ_{CC}	6.0–6.5	$18.96^{+2.26}_{-2.15}$	$18.90^{+2.26}_{-2.12}$	$18.83^{+2.23}_{-2.08}$
ϕ_{ES}	6.0–6.5	$33.44^{+10.61}_{-8.76}$	$34.14^{+10.92}_{-9.17}$	$33.89^{+10.91}_{-9.05}$
ϕ_{CC}	6.5–7.0	$23.66^{+2.04}_{-1.92}$	$23.60^{+2.09}_{-1.94}$	$23.61^{+2.14}_{-1.92}$
ϕ_{ES}	6.5–7.0	$10.54^{+9.15}_{-8.10}$	$10.55^{+8.86}_{-7.33}$	$10.42^{+8.84}_{-7.72}$
ϕ_{CC}	7.0–7.5	$21.17^{+1.95}_{-1.71}$	$21.23^{+1.84}_{-1.73}$	$21.28^{+1.85}_{-1.73}$
ϕ_{ES}	7.0–7.5	$33.22^{+9.31}_{-7.76}$	$34.45^{+9.51}_{-8.03}$	$34.28^{+9.57}_{-7.94}$
ϕ_{CC}	7.5–8.0	$18.88^{+1.75}_{-1.58}$	$18.97^{+1.73}_{-1.55}$	$19.08^{+1.73}_{-1.55}$
ϕ_{ES}	7.5–8.0	$28.09^{+8.41}_{-7.66}$	$27.09^{+8.77}_{-7.21}$	$26.92^{+8.92}_{-7.18}$
ϕ_{CC}	8.0–8.5	$17.17^{+1.57}_{-1.39}$	$17.07^{+1.56}_{-1.40}$	$17.15^{+1.55}_{-1.37}$
ϕ_{ES}	8.0–8.5	$12.45^{+6.72}_{-5.53}$	$12.69^{+7.23}_{-5.59}$	$12.93^{+6.98}_{-5.60}$
ϕ_{CC}	8.5–9.0	$14.25^{+1.36}_{-1.31}$	$14.17^{+1.45}_{-1.26}$	$14.26^{+1.44}_{-1.23}$
ϕ_{ES}	8.5–9.0	$16.33^{+7.29}_{-5.25}$	$16.35^{+7.18}_{-5.46}$	$16.52^{+7.29}_{-5.55}$
ϕ_{CC}	9.0–9.5	$13.30^{+1.38}_{-1.24}$	$13.27^{+1.41}_{-1.24}$	$13.41^{+1.34}_{-1.21}$
ϕ_{ES}	9.0–9.5	$17.76^{+6.95}_{-5.11}$	$18.04^{+7.24}_{-5.61}$	$17.85^{+7.29}_{-5.46}$
ϕ_{CC}	9.5–10.0	$10.00^{+1.27}_{-1.01}$	$10.00^{+1.23}_{-1.03}$	$10.18^{+1.18}_{-1.02}$
ϕ_{ES}	9.5–10.0	$9.07^{+5.78}_{-3.86}$	$9.68^{+5.42}_{-4.24}$	$9.31^{+5.60}_{-4.06}$
ϕ_{CC}	10.0–10.5	$10.28^{+1.20}_{-1.05}$	$10.20^{+1.17}_{-1.04}$	$10.42^{+1.11}_{-1.00}$
ϕ_{ES}	10.0–10.5	$0.21^{+4.83}_{-0.21}$	$0.72^{+4.66}_{-0.72}$	$0.70^{+4.71}_{-0.70}$
ϕ_{CC}	10.5–11.0	$6.62^{+1.03}_{-0.87}$	$6.54^{+1.04}_{-0.80}$	$6.73^{+0.94}_{-0.77}$
ϕ_{ES}	10.5–11.0	$1.23^{+3.33}_{-1.23}$	$0.77^{+3.47}_{-0.77}$	$0.96^{+3.47}_{-0.96}$
ϕ_{CC}	11.0–11.5	$4.05^{+0.75}_{-0.63}$	$3.95^{+0.79}_{-0.60}$	$4.09^{+0.73}_{-0.58}$
ϕ_{ES}	11.0–11.5	$3.17^{+3.24}_{-2.46}$	$3.04^{+3.49}_{-2.54}$	$3.17^{+3.41}_{-2.60}$
ϕ_{CC}	11.5–12.0	$3.30^{+0.63}_{-0.53}$	$3.23^{+0.73}_{-0.54}$	$3.38^{+0.66}_{-0.52}$
ϕ_{ES}	11.5–12.0	$2.33^{+3.05}_{-2.33}$	$2.41^{+3.04}_{-2.52}$	$2.35^{+3.16}_{-2.52}$
ϕ_{CC}	12.0–20.0	$5.30^{+1.05}_{-0.93}$	$5.12^{+1.22}_{-0.88}$	$5.51^{+0.95}_{-0.76}$
ϕ_{ES}	12.0–20.0	$9.01^{+4.80}_{-3.10}$	$9.15^{+4.73}_{-3.40}$	$9.57^{+5.15}_{-3.50}$
ϕ_{CC}	6.0–20.0	$166.94^{+8.23}_{-9.16}$	$166.25^{+9.00}_{-8.42}$	$167.92^{+8.54}_{-7.32}$
ϕ_{ES}	6.0–20.0	$176.84^{+25.46}_{-23.44}$	$179.10^{+25.46}_{-23.01}$	$178.87^{+25.13}_{-21.96}$
ϕ_{NC}	6.0–20.0	$554.31^{+48.28}_{-45.62}$	$554.94^{+49.27}_{-44.71}$	$552.41^{+48.49}_{-44.63}$
D_2O PD n	6.0–20.0	$30.9^{+4.8}_{-4.8}$	$31.1^{+4.8}_{-4.8}$	$31.0^{+4.8}_{-4.8}$
AV(α, n), AV and H_2O PD n	6.0–20.0	$41.4^{+20.0}_{-20.7}$	$41.1^{+20.1}_{-20.3}$	$41.5^{+20.1}_{-20.0}$
NCD and NCD cables PD n	6.0–20.0	$34.9^{+12.3}_{-12.0}$	$35.6^{+12.2}_{-12.2}$	$35.6^{+12.2}_{-12.2}$
K2 PD n	6.0–20.0	$32.8^{+5.0}_{-5.1}$	$32.7^{+5.1}_{-5.2}$	$32.7^{+5.2}_{-5.2}$
K5 PD n	6.0–20.0	$31.6^{+3.8}_{-3.6}$	$31.7^{+3.7}_{-3.7}$	$31.6^{+3.7}_{-3.6}$
atmospheric νs and ^{16}N PD n	6.0–20.0	$13.6^{+2.8}_{-2.7}$	$13.6^{+2.7}_{-2.7}$	$13.6^{+2.7}_{-2.7}$
α-particle background	6.0–20.0	$5555.4^{+195.6}_{-167.1}$	$5553.1^{+188.3}_{-193.6}$	$5559.1^{+200.3}_{-186.9}$
J3 type background	6.0–20.0	$346.2^{+203.7}_{-263.6}$	$366.0^{+197.9}_{-227.9}$	$353.1^{+207.9}_{-252.5}$
N4 type background	6.0–20.0	$0.0^{+330.2}_{-0.0}$	$0.0^{+345.9}_{-0.0}$	$0.0^{+410.5}_{-0.0}$

Table 8.7: NCD neutrino fluxes and backgrounds from the analysis presented by Aharmim et al. [1]. The neutron backgrounds are as measured in the NCDs. They are related to the PMT neutron backgrounds via the conversion factors in table 8.4. PD refers to photodisintegration while J3 and N4 are the designations of strings with particularly high residual instrumental background contamination. The results from Jamieson [99] are presented in Aharmim et al. [1]. The second to last column is the best fit result using the input parameters used by Jamieson [99]. The results in the last column are derived using the energy scale and resolution errors derived in this work.

are:

$$\phi_{\rm CC} = 1.67^{+0.05}_{-0.04}({\rm stat})^{+0.07}_{-0.08}({\rm syst})$$
$$\phi_{\rm ES} = 1.77^{+0.24}_{-0.21}({\rm stat})^{+0.09}_{-0.10}({\rm syst})$$
$$\phi_{\rm NC} = 5.54^{+0.33}_{-0.31}({\rm stat})^{+0.36}_{-0.34}({\rm syst}),$$

in units of $10^6\,{\rm cm}^{-2}{\rm s}^{-1}$. The ratio of the CC to NC ^{8}B neutrino fluxes derived from these results is

$$\frac{\phi_{\rm CC}}{\phi_{\rm NC}} = 0.301 \pm 0.033.$$

Verification results

The second to last column in table 8.7 represents the best attempt by the author to reproduce the results from Jamieson [99]. It is believed that remaining discrepancy is due entirely to statistical fluctuations in the sum of the MCMC chains. Several attempts to reproduce the results from Jamieson [99] converged to results with variations at least as large as the discrepancy between those quoted in table 8.7.

In an attempt to minimize these statistical variations, 146 MCMC chains were generated containing up to 30000 steps each. 1.54×10^6 steps out of a total of 2.93×10^6 were used to generate the final results. The first 10500 steps were rejected to ensure the MCMC chains had converged to a the stationary posterior distribution.

The same analysis was performed again with the total energy reconstruction errors presented in table 8.5; the energy scale was shifted by -0.46% and constrained to vary within ±0.49%, and the energy resolution was shifted by 0.66% and allowed to vary within ±0.21%. 86 MCMC chains were generated containing up to 75000 steps each. 3.25×10^6 steps out of a total of 4.19×10^6 were used to generate the final results. Again the first 10500 were rejected from each chain. The results of this analysis are presented in the last column of table 8.7. They are in good agreement with the other two results listed. The differences are small but significant between the two high statistics analysis in the last two columns of the table. The overall uncertainty in the NC does not change significantly because of the insensitivity of the measurement to the data observed by the PMTs. The ES result shows modest improvement but is limited by statistical uncertainty due to the low cross section for ES. The uncertainties

on the CC ^{8}B neutrino flux[8] improve by about 5 and 10%.

Discussion of primary results

The comparison between the ^{8}B neutrino fluxes published by Aharmim et al. [1] and those previously measured by SNO are shown in figure 8.4. The NCD phase CC ^{8}B neutrino flux is the most precise yet and in good agreement with the previous measurements. The ES ^{8}B neutrino flux is also well measured in the NCD phase however with a 2.2σ discrepancy from the most precise measurement as made by Super–Kamiokande–I [27]. The fraction of the data that is made up of ES events is almost completely determined by the prominent forward (away from the Sun) peak in the $\cos\theta_\odot$ distribution. Examining the data, no peak is observed in the $\cos\theta_\odot$ distributions of two isolated bins in energy. This suggests that the low flux is a result of a significant downward statistical fluctuation in these two energy bins. In spite of the disagreement in the ES flux, the NCD phase results are in agreement with the previous SNO results ($p = 32.8$ [107]) [1].

The NCD phase NC ^{8}B neutrino flux is in agreement with previous SNO measurements and well within the range predicted by standard solar models (SSM). The flux predicted by the SSM of Bahcall, Serenelli, and Basu [3] is indicated by the dashed band in figure 8.4c. The accuracy of the NC measurement may assist in resolving differences between solar model fluxes predicted for several presently uncertain solar parameters (see Bahcall et al. [3]).

The NCD phase NC ^{8}B neutrino flux is comparable to the measurement in the salt phase. The signal composition of the salt and NCD phases, as observed by the PMTs, is depicted in figure 8.5 and figure 8.3c, via their respective energy distributions. It is clear that the statistical significance of the NCD phase NC result does not derive from the PMT data—it is highly suppressed as compared to what it is in the salt phase. This is a clear demonstration of the independence of the NC measurement in the NCD phase despite some contribution from the PMT data.

The deficit in the CC electron neutrino flux, relative to the NC total neutrino flux, is strong, direct, evidence for neutrino flavour transformation. Accordingly, these

[8]The shift in asymmetric uncertainty on the CC ^{8}B neutrino flux between the results from Jamieson [99] and the high statistics reproduction is clearly due to the limited statistics in the former by inspection of the posterior distributions of each.

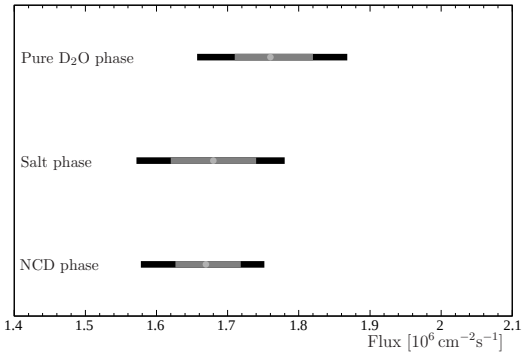

(a) CC

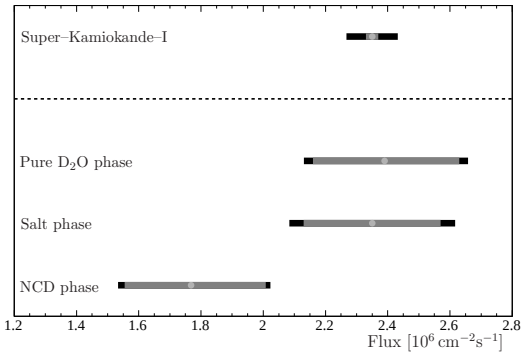

(b) ES

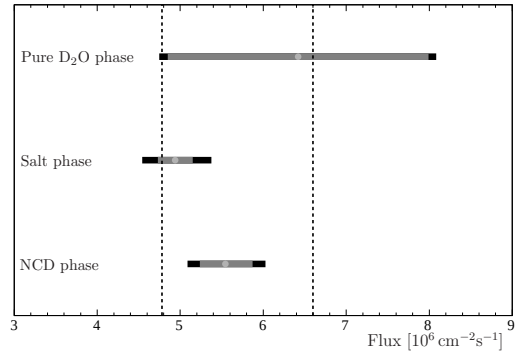

(c) NC

Figure 8.4: A comparison of the NCD phase solar ^{8}B neutrino fluxes with those previously measured by SNO. The ES flux is also compared to the current best measurement by Super–Kamiokande–I [27].

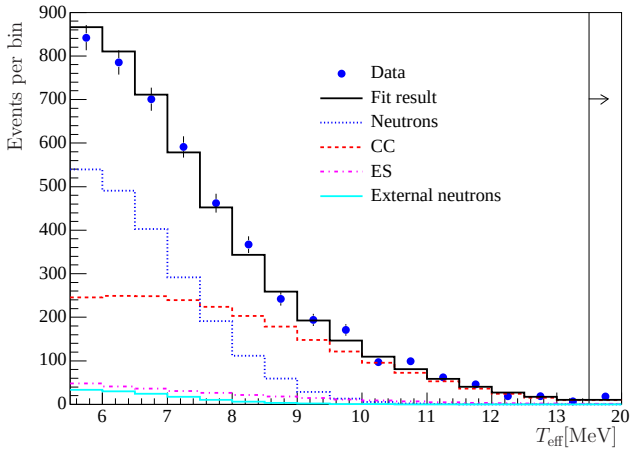

Figure 8.5: The energy distribution of the salt phase data. Shown are the relative contributions to the total that each signal and background make up. Taken from Aharmim et al. [21].

observations are applied to a model of neutrino propagation to place constraints on the neutrino oscillation parameters. Such an analysis using a two-neutrino model [108] (the two neutrinos being the ν_e and some linear combination of ν_μ and ν_τ) for solar neutrino oscillations is presented by Aharmim et al. [1]. This model is parametrized by a mixing angle θ_{sol} and the squared-mass splitting between the two mass eigenstates Δm^2_{sol}. These are equivalent to the three neutrino mixing parameters, θ_{12} and $\Delta m^2_{21} = m^2_2 - m^2_1$, in so much as $\theta_{13} \approx 0$ and $|\Delta m^2_{32}| >> m^2_{21}$. The numerical subscripts refer to the three neutrino mass eigenstates as discussed in section 1.4.

Physics interpretation of primary results

The solar neutrino oscillation model, which is described in detail by Chen et al. [109] and Chen et al. [110], accounts for the spectral and radial distribution of ν_e production in the Sun based on the solar models of Bahcall et al. [12] and Bahcall et al. [3]. The MSW[9] ν_e survival probability at the surface of the Sun is determined based on the electron number density profile provided by these solar models. Vacuum oscillations between the Sun and the Earth, the MSW survival probability, and any

[9]The MSW effect [17, 18] induces an enhancement in ν_e oscillation or, alternatively, transition from ν_1 to ν_2 in dense media such as inside the Sun. The effect is a result of the additional coherent forward scattering experienced by the ν_e via the W^- ES channel.

ν_e regeneration through the Earth are also accounted for. The cross sections of the relevant neutrino interactions with detector targets are applied to the neutrino spectra expected at the experiment. Parametrizations of detector response are applied to these expected interactions. Given the livetime of the experiment, and ideally the zenith angle[10] distribution of that livetime, a prediction is made of what the experiment should observe given the particular choice of θ and Δm^2 used in the neutrino propagation model. These predictions can then be compared to the actual observations of the experiment via a χ^2 test. The best fit parameters and allowed parameter region, defined by $\Delta\chi^2$ contours, are extracted after the neutrino propagation model calculation is tested over a wide range of the oscillation parameters.

The fit of the solar oscillation parameters to the SNO pure D_2O and salt phase day and night spectra [21, 111] and the neutrino fluxes published by Aharmim et al. [1] are shown in figure 8.6a. The best-fit oscillation parameters using only SNO measurements are $\Delta m^2_{\rm sol} = 4.57 \times 10^{-5}\,{\rm eV}^2$ and $\tan^2\theta_{\rm sol} = 0.447$. Combining the solar neutrino measurements made by SNO with those made by Super Kamiokande, the Cl and Ga experiments, and Borexino[11] yields the χ^2 limits in the left plot in figure 8.6b. Assuming CPT invariance, this data can be combined with the likelihood values from a KamLAND (reactor antineutrino oscillation experiment) oscillation analysis [23] resulting in the best-fit solar neutrino oscillation parameters $\Delta m^2_{\rm sol} = 7.94^{+0.42}_{-0.26} \times 10^{-5}\,{\rm eV}^2$ and $\theta_{\rm sol} = 33.8^{+1.4^\circ}_{-1.3^\circ}$ as shown in the right hand plot in figure 8.6b. These may be compared to[12] the salt phase results of $\Delta m^2_{\rm sol} = 8.0^{+0.4}_{-0.3} \times 10^{-5}\,{\rm eV}^2$ and $\theta_{\rm sol} = 33.9^{+1.6^\circ}_{-1.6^\circ}$ [21]. There is a strong correlation between the SNO CC to NC flux ratio and the solar mixing angle in this region of oscillation parameter space. The CC to NC ratio, and the value of $\theta_{\rm sol}$ that it implies, can help select between models of massive neutrinos such as the MSW theory or non-standard interactions. A good review of the possibilities is discussed by Smirnov [112].

[10] Zenith angle is the angle between zenith and the Sun, on which the distance traveled by neutrinos through the Earth depends.

[11] See Aharmim et al. [21] and Aharmim et al. [1] for references to the specific data used.

[12] In both cases the uncertainties on the neutrino oscillation parameters are obtained from a one–dimensional projection of the respective parameter while marginalizing the uncertainties in the other [21].

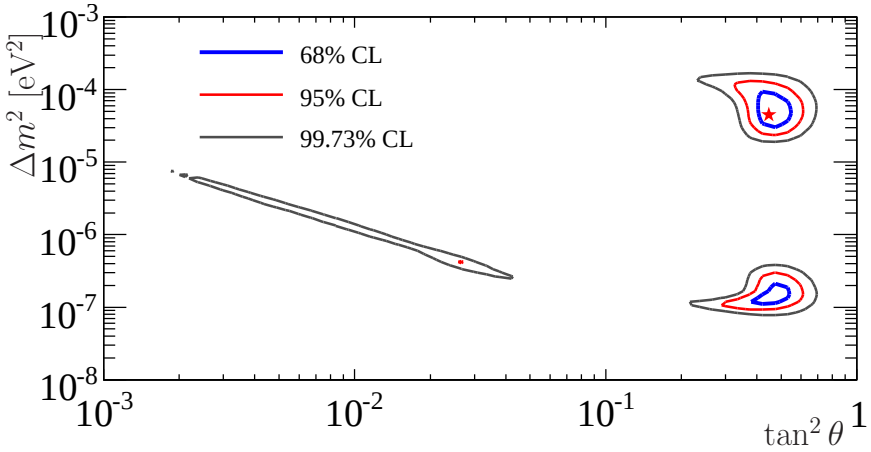

(a) D_2O and salt phase day and night spectra and NCD phase fluxes. Best fit point is $(4.57 \times 10^{-5}\,\mathrm{eV}^2, 0.447)$.

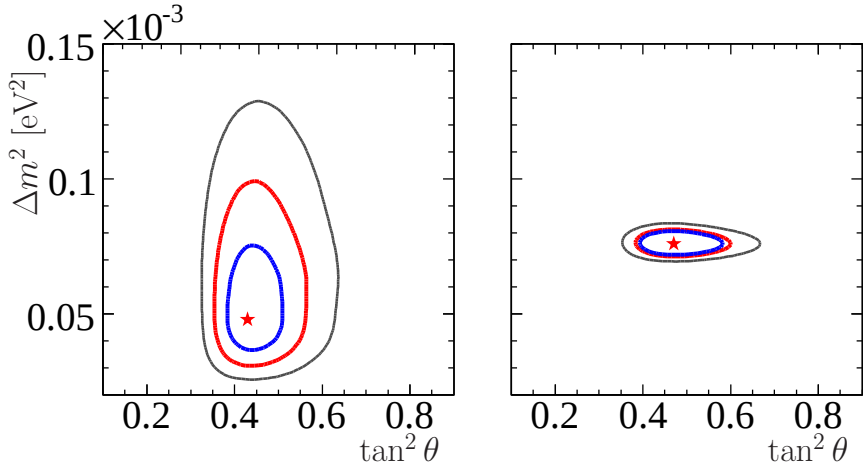

(b) On the left: The combined results of SNO, Super Kamiokande, Chlorine, Gallium, and Borexino solar neutrino experiments. On the right: the data in the left plus KamLAND reactor neutrino measurements.

Figure 8.6: Two neutrino oscillation parameter allowed regions as published by Aharmim et al. [1]. The best fit point of all available data, which is in the lower right plot, is $(7.94 \times 10^{-5}\,\mathrm{eV}^2, 0.447)$.

Chapter 9

Conclusions

The data collected during the initial pure D_2O phase of SNO has been analyzed by the SNO Collaboration to search for solar *hep* neutrinos and the diffuse supernova neutrino background (DSNB). The following limits were determined:

$$\begin{aligned} \phi_{hep} &< 2.3 \times 10^4\,\mathrm{cm}^{-2}\mathrm{s}^{-1} && \text{and} \\ \phi_{\mathrm{DSNB}} &< 70\,\mathrm{cm}^{-2}\mathrm{s}^{-1} && \text{for } 22.9\,\mathrm{MeV} < E_\nu < 36.9\,\mathrm{MeV}, \end{aligned}$$

at the 90% confidence level. Both of these limits are substantial improvements over the previous limits published by Hosaka et al. [27] and Aglietta et al. [28]. The development of the energy response processor by the author was essential to the calibration of the detector energy scale at energies beyond the ^{8}B neutrino spectrum where SNO is sensitive to these interactions.

The analysis of the third and final phase of SNO, the neutral current detector (NCD) phase, is presented by Aharmim et al. [1]. The calibration of the detector energy scale and energy response, as carried out by the author, is used extensively in all aspects of this analysis; this includes the implementation of a correction for the light lost due to the shadows cast on the PMTs by the NCD array. The solar ^{8}B

neutrino fluxes derived from that analysis are:

$$\begin{aligned}\phi_{\rm CC} &= 1.67^{+0.05}_{-0.04}({\rm stat})^{+0.07}_{-0.08}({\rm syst})\\ \phi_{\rm ES} &= 1.77^{+0.24}_{-0.21}({\rm stat})^{+0.09}_{-0.10}({\rm syst})\\ \phi_{\rm NC} &= 5.54^{+0.33}_{-0.31}({\rm stat})^{+0.36}_{-0.34}({\rm syst}),\end{aligned}$$

in units of $10^6\,{\rm cm}^{-2}{\rm s}^{-1}$.

The charged current (CC) flux is the best measured to date. The elastic scattering (ES) flux is 2.2σ lower than the best measurement by Super–Kamiokande–I [27]. All evidence indicates that the lower result is a statistical fluctuation constrained within a small energy window. Regardless, a full statistical analysis shows this result to be in agreement with previous SNO results at the level of $p = 32.8\%$ [1]. The neutral current (NC) flux—the total flux of active neutrinos from the Sun—is measured during the NCD phase independently from previous SNO analysis. It is shown to be in complete agreement with past results and with solar model calculations. In all, the results of the NCD phase are in good agreement with those of previous SNO analysis.

The resulting solar neutrino fluxes—the charged current, elastic scattering, and neutral current—are applied, in conjunction with the measurements of other solar neutrino experiments and those of the reactor antineutrino experiment KamLAND [23], to derive the neutrino oscillation parameters:

$$\begin{aligned}\Delta m^2_{21} &= 7.94^{+0.42}_{-0.26}\times 10^{-5} \qquad \text{and}\\ \theta_{12} &= 33.8^{+1.4^\circ}_{-1.3^\circ},\end{aligned}$$

based on the MSW model of solar neutrino oscillation. The current uncertainty in the measurement of θ_{12} is an improvement of over 10% from previous results [21]. The measurement of θ_{12} places constraints on possible neutrino mixing models.

The error associated with the energy calibration and reconstruction process of events observed by the PMTs during the NCD phase has been reassessed. The energy scale error, originally $\pm 1.04\%$, was reassessed at $-0.46 \pm 0.49\%$ while the energy resolution error, originally $1.19 \pm 1.04\%$, has been reassessed at $0.66 \pm 0.21\%$. The results are in agreement with the more conservative estimates used in the analysis presented by Aharmim et al. [1]. The less conservative approach to the calculation

of these errors, as presented in this work, results in a measurement of the solar ^{8}B neutrino fluxes that are in complete agreement with those presented by Aharmim et al. [1]. The measured fluxes are:

$$\begin{aligned}\phi_{\mathrm{CC}} &= 1.68^{+0.09}_{-0.07},\\ \phi_{\mathrm{ES}} &= 1.79^{+0.25}_{-0.22}, \text{ and}\\ \phi_{\mathrm{NC}} &= 5.52^{+0.48}_{-0.45},\end{aligned}$$

in units of $10^6\,\mathrm{cm}^{-2}\mathrm{s}^{-1}$. The errors on these fluxes are the combined statistical and systematic uncertainty. A modest improvement in the uncertainty on the charge current ^{8}B flux is noted. This test of the energy systematics will have implications for a future analysis looking to combine the data from all three phases of the experiment.

An analysis combining the first two phases of SNO—the pure D_2O and salt phases—down to a lower energy threshold is already in progress. The energy scale calibration of the data to be used in this analysis is presented in this work. A cross check of the energy calibration and reconstruction process errors is also presented. The errors found in this work are consistent with those being used for the primary solar neutrino analysis. It is anticipated that this low energy threshold combined analysis will produce the most precise solar ^{8}B neutrino fluxes, a measure of the charge current energy spectrum, and further constrain the neutrino oscillation parameters Δm^2_{21}, θ_{12}, and θ_{13}.

Bibliography

[1] **SNO** Collaboration, B. Aharmim *et al.*, "An independent measurement of the total active ^{8}B solar neutrino flux using an array of ^{3}He proportional counters at the Sudbury Neutrino Observatory", *Phys. Rev. Lett.* **101** (2008) 111301, 0806.0989.

[2] H. H. Chen, "Direct approach to resolve the solar-neutrino problem", *Phys. Rev. Lett.* **55** (1985) 1534–1536.

[3] J. N. Bahcall, A. M. Serenelli, and S. Basu, "New solar opacities, abundances, helioseismology, and neutrino fluxes", *Astrophys. J.* **621** (2005) L85–L88, astro-ph/0412440.

[4] B. T. Cleveland *et al.*, "Measurement of the solar electron neutrino flux with the Homestake chlorine detector", *Astrophys. J.* **496** (1998) 505–526.

[5] **SAGE** Collaboration, J. N. Abdurashitov *et al.*, "Measurement of the solar neutrino capture rate with gallium metal", *Phys. Rev.* **C60** (1999) 055801, astro-ph/9907113.

[6] **Super-Kamiokande** Collaboration, Y. Fukuda *et al.*, "Measurement of the solar neutrino energy spectrum using neutrino electron scattering", *Phys. Rev. Lett.* **82** (1999) 2430–2434, hep-ex/9812011.

[7] **GALLEX** Collaboration, W. Hampel *et al.*, "GALLEX solar neutrino observations: Results for GALLEX IV", *Phys. Lett.* **B447** (1999) 127–133.

[8] **GNO** Collaboration, M. Altmann *et al.*, "GNO solar neutrino observations: Results for GNO I", *Phys. Lett.* **B490** (2000) 16–26, hep-ex/0006034.

[9] **SAGE** Collaboration, J. N. Abdurashitov *et al.*, "Measurement of the solar neutrino capture rate with gallium metal, Part III", 0901.2200.

[10] **Super-Kamiokande** Collaboration, J. P. Cravens *et al.*, "Solar neutrino measurements in Super-Kamiokande-II", *Phys. Rev.* **D78** (2008) 032002, 0803.4312.

[11] **GNO** Collaboration, M. Altmann *et al.*, "Complete results for five years of GNO solar neutrino observations", *Phys. Lett.* **B616** (2005) 174–190, `hep-ex/0504037`.

[12] J. N. Bahcall, M. H. Pinsonneault, and S. Basu, "Solar models: Current epoch and time dependences, neutrinos, and helioseismological properties", *Astrophys. J.* **555** (2001) 990–1012, `astro-ph/0010346`.

[13] **SNO** Collaboration, Q. R. Ahmad *et al.*, "Measurement of the rate of $\nu_e + d \rightarrow p + p + e^-$ interactions produced by ^{8}B solar neutrinos at the Sudbury Neutrino Observatory", *Phys. Rev. Lett.* **87** (2001) 071301, `nucl-ex/0106015`.

[14] **Super-Kamiokande** Collaboration, S. Fukuda *et al.*, "Constraints on neutrino oscillations using 1258 days of Super-Kamiokande solar neutrino data", *Phys. Rev. Lett.* **86** (2001) 5656–5660, `hep-ex/0103033`.

[15] **SNO** Collaboration, Q. R. Ahmad *et al.*, "Direct evidence for neutrino flavor transformation from neutral-current interactions in the Sudbury Neutrino Observatory", *Phys. Rev. Lett.* **89** (2002) 011301, `nucl-ex/0204008`.

[16] R. B. Firestone, "Table of isotopes", Wiley, New York, 8$^{\text{th}}$ ed., 1999.

[17] S. P. Mikheyev and A. Y. Smirnov, "Resonance enhancement of oscillations in matter and solar neutrino spectroscopy", *Sov. J. Nucl. Phys.* **42** 913.

[18] L. Wolfenstein, "Neutrino oscillations in matter", *Phys. Rev.* **D17** (1978) 2369–2374.

[19] **SNO** Collaboration, S. N. Ahmed *et al.*, "Measurement of the total active ^{8}B solar neutrino flux at the Sudbury Neutrino Observatory with enhanced neutral current sensitivity", *Phys. Rev. Lett.* **92** (2004) 181301, `nucl-ex/0309004`.

[20] J. A. Dunmore, "The separation of CC and NC events in the Sudbury Neutrino Observatory", PhD thesis, 2004.

[21] **SNO** Collaboration, B. Aharmim *et al.*, "Electron energy spectra, fluxes, and day-night asymmetries of ^{8}B solar neutrinos from the 391-day salt phase SNO data set", *Phys. Rev.* **C72** (2005) 055502, `nucl-ex/0502021`.

[22] ALEPH, DELPHI, L3, OPAL, SLD, LEP Electroweak Working Group, SLD Electroweak Group, and SLD Heavy Flavour Group, "Precision electroweak measurements on the Z resonance", *Phys. Rept.* **427** (2006) 257, `hep-ex/0509008`.

[23] **KamLAND** Collaboration, T. Araki *et al.*, "Measurement of neutrino oscillation with KamLAND: Evidence of spectral distortion", *Phys. Rev. Lett.* **94** (2005) 081801, `hep-ex/0406035`.

[24] **Particle Data Group** Collaboration, W. M. Yao *et al.*, "Review of particle physics", *J. Phys.* **G33** (2006) 1–1232.

[25] M. Dunford, "Measurement of the ^{8}B solar neutrino energy spectrum at the Sudbury Neutrino Observatory", PhD thesis. UMI-32-46154.

[26] **SNO** Collaboration, B. Aharmim *et al.*, "A search for neutrinos from the solar *hep* reaction and the diffuse supernova neutrino background with the Sudbury Neutrino Observatory", *Astrophys. J.* **653** (2006) 1545–1551, `hep-ex/0607010`.

[27] **Super-Kamkiokande** Collaboration, J. Hosaka *et al.*, "Solar neutrino measurements in Super-Kamiokande-I", *Phys. Rev.* **D73** (2006) 112001, `hep-ex/0508053`.

[28] M. Aglietta *et al.*, "Limits on low-energy neutrino fluxes with the Mont Blanc liquid scintillator detector", *Astropart. Phys.* **1** (1992) 1–9.

[29] M. S. Kos, "Low energy solar neutrino analysis of the salt phase of the Sudbury Neutrino Observatory", PhD thesis.

[30] G. D. O. Gann, "An improved measurement of the ^{8}B solar neutrino energy spectrum at the Sudbury Neutrino Observatory", PhD thesis.

[31] S. R. Seibert, "A low energy measurement of the ^{8}B solar neutrino energy spectrum at the Sudbury Neutrino Observatory", PhD thesis, 2008.

[32] **SNO** Collaboration, B. Aharmim *et al.*, "Measurement of the ν_e and total ^{8}B solar neutrino fluxes with the Sudbury Neutrino Observatory phase I data set", *Phys. Rev.* **C75** (2007) 045502, `nucl-ex/0610020`.

[33] **SNO** Collaboration, B. Aharmim *et al.*, "Measurement of the cosmic ray and neutrino-induced muon flux at the Sudbury Neutrino Observatory", `0902.2776v1`.

[34] **SNO** Collaboration, J. Boger *et al.*, "The Sudbury Neutrino Observatory", *Nucl. Instrum. Meth.* **A449** (2000) 172–207, `nucl-ex/9910016`.

[35] M. Boulay *et al.*, "A letter expressing interest in staging an experiment at SNOLAB involving filling SNO with liquid scintillator plus double beta decay candidate isotopes", April 2004.

[36] **SNO+** Collaboration, M. C. Chen, "The SNO+ Experiment", 0810.3694.

[37] M. C. Chen, "Geo-neutrinos in SNO+", Prepared for Neutrino Sciences 2005: Neutrino Geophysics, Honolulu, Hawaii, 14-16 Dec 2005.

[38] E. Guillian, "The Sensitivity of SNO+ to Δm^2_{12} Using Reactor Anti-neutrino Data", 0809.1649.

[39] **SNO+** Collaboration, K. Zuber, "Nd double beta decay search with SNO+", *AIP Conf. Proc.* **942** (2007) 101–104.

[40] "Long D_2O paper: Target properties", SNO internal report: http://manhattan.sno.laurentian.ca/sno/ananoteb.nsf/URL/MANN-7439UR, June 2007.

[41] A. Hallin, Private communication, May 2009.

[42] G. Doucas *et al.*, "Light concentrators for the Sudbury Neutrino Observatory", *Nucl. Instrum. Meth.* **A370** (1996) 579–596.

[43] C. J. Jillings *et al.*, "The photomultiplier tube testing facility for the Sudbury Neutrino Observatory", *Nucl. Instrum. Meth.* **A373** (1996) 421–429.

[44] J. F. Amsbaugh *et al.*, "An array of low-background ^{3}He proportional counters for the Sudbury Neutrino Observatory", *Nucl. Instrum. Meth.* **A579** (2007) 1054–1080, 0705.3665.

[45] J. Klein *et al.*, "The SNO trigger system", SNO-STR-97-035, October 1997.

[46] S. Biller *et al.*, "SNO electronic calibration constants", SNO-STR-01-005, August 2001.

[47] R. J. Ford, "Calibration of SNO for the detection of ^{8}B neutrinos", PhD thesis. UMI-NQ-35959.

[48] B. Moffat, "The Optical Calibration of the Sudbury Neutrino Observatory", PhD thesis.

[49] B. A. Moffat *et al.*, "Optical calibration hardware for the Sudbury Neutrino Observatory", *Nucl. Instrum. Meth.* **A554** (2005) 255–265, nucl-ex/0507026.

[50] P. Skensved, "ECA, PCA and laserball reconstruction", SNO-STR-00-007, April 2000.

[51] O. Simard, "An enhanced measurement of the angular response of photomultiplier tubes at the Sudbury Neutrino Observatory", Master's thesis. UMI-MR00790.

[52] P. A. Cerenkov, "Visible radiation produced by electrons moving in a medium with velocities exceeding that of light", *Phys. Rev.* **52** (1937) 378–379.

[53] I. Frank and G. Tamm, "Coherent in-medium fast-electron radiation", *Dokl. Akad. Nauk SSSR* **14** (1937).

[54] J. V. Jelley, "Čerenkov radiation and its applications", Pergamon, London, 1958.

[55] J. R. Klein, "Realistic simulated charge spectrum for SNO and the prediction of tube-by-tube efficiencies", SNO internal report: http://manhattan.sno.laurentian.ca/sno/ananoteb.nsf/URL/MANN-6EX424, August 2005.

[56] J. Maneira, Private communication, February 2007.

[57] R. Boardman, "The detection of Čerenkov radiation from neutrino interactions", PhD thesis, 1992.

[58] S. D. Biller, N. A. Jelley, M. D. Thorman, N. P. Fox, and T. H. Ward, "Measurements of photomultiplier single photon counting efficiency for the Sudbury Neutrino Observatory", *Nucl. Instrum. Meth.* **A432** (1999) 364–373.

[59] J. C. Zwinkels, W. F. Davidson, and C. X. Dodd, "Optical properties of UV transmitting acrylics for use in a heavy water Cerenkov detector", *Appl. Opt.* **29** (1990) 3240–3248.

[60] S. A. Sullivan, "Experimental study of the absorption in distilled water, artificial sea water, and heavy water in the visible region of the spectrum", *J. Opt. Soc. Am.* **53** (1963) 962–968.

[61] A. C. Tam and C. K. N. Patel, "Optical absorptions of light and heavy water by laser optoacoustic spectroscopy", *Appl. Opt.* **18** (1979) 3348–3358.

[62] L. P. Boivin, W. F. Davidson, R. S. Storey, D. Sinclair, and E. D. Earle, "Determination of the attenuation coefficients of visible and ultraviolet light in heavy water", *Appl. Opt.* **25** (1990) 877–882.

[63] R. M. Pope and E. S. Fry, "Absorption spectrum (380–700 nm) of pure water. II. Integrating cavity measurements", *Appl. Opt.* **36** (1997) 8710–8723.

[64] F. M. Sogandares and E. S. Fry, "Absorption spectrum (340–640 nm) of pure water. I. Photothermal measurements", *Appl. Opt.* **36** (1997) 8699–8709.

[65] J. W. Strutt, "On the light from the sky, its polarization and colour", *Phil. Mag.* **XLI** (1871) 107120.

[66] A. Einstein, "Theorie der Opaleszenz von homogenen Flüssigkeiten und Flüssigkeitsgemischen in der Nähe des kritischen Zustandes", *Ann. Physik* **338** (1910) 1275–1298.

[67] J. R. Wilson, "A measurement of the ^{8}B solar neutrino energy spectrum at the Sudbury Neutrino Observatory", PhD thesis, 2008.

[68] M. G. Boulay, "Direct evidence for weak flavor mixing with the Sudbury Neutrino Observatory", PhD thesis. UMI-NQ-80984.

[69] N. McCauley, "ANxx updates", SNO internal report: http://manhattan.sno.laurentian.ca/sno/ananoteb.nsf/URL/MANN-69GLAV, February 2005.

[70] M. Huang, C. Kyba, and N. McCauley, "ANxx update: Determination of bad PMT channels for D_2O and salt phases", SNO internal report: http://manhattan.sno.laurentian.ca/sno/ananoteb.nsf/URL/MANN-6AWM3T, March 2005.

[71] W. H. Press, S. A. Teukolsky, W. T. Vetterling, and B. P. Flannery, "Numerical recipes in Fortran 77: The art of scientific computing", Cambridge, 2nd ed., 1992.

[72] E. Hecht, "Optics", Addison Wesley, New York, 3rd ed., 1998.

[73] M. J. Thomson, "The ^{222}Rn spike source calibration of the Sudbury Neutrino Observatory", Master's thesis.

[74] C. W. Howard, "Injection of a uniform ^{24}Na radioactive source into the Sudbury Neutrino Observatory", Master's thesis.

[75] J. R. Klein *et al.*, "Low energy threshold analysis (LETA) unidoc", SNO internal report: http://manhattan.sno.laurentian.ca/sno/ananoteb.nsf/URL/MANN-7R5LC8, April 2009.

[76] M. R. Dragowsky *et al.*, "The ^{16}N calibration source for the Sudbury Neutrino Observatory", *Nucl. Instrum. Meth.* **A481** (2002) 284–296, `nucl-ex/0109011`.

[77] M. Lay, "Creation and detection of Čerenkov light in the Sudbury Neutrino Observatory", PhD thesis.

[78] N. J. Tagg *et al.*, "The ^{8}Li calibration source for the Sudbury Neutrino Observatory", *Nucl. Instrum. Meth.* **A489** (2002) 178–188, `nucl-ex/0202024`.

[79] A. W. P. Poon *et al.*, "A compact ^{3}H(p,γ)^{4}He 19.8-MeV gamma-ray source for energy calibration at the Sudbury Neutrino Observatory", *Nucl. Instrum. Meth.* **A452** (2000) 115–129, `physics/9910011`.

[80] *MCNP—A general Monte Carlo code for neutron and photon transport, version 4-A*, 1986. Los Alamos National Laboratory, LA-7396-M.

[81] A. Fasso, A. Ferrari, P. R. Sala, and J. Ranft, "FLUKA: Status and prospects for hadronic applications", 2001, Prepared for International Conference on Advanced Monte Carlo for Radiation Physics, Particle Transport Simulation and Applications (MC 2000), Lisbon, Portugal, 23–26 Oct 2000.

[82] W. R. Nelson, H. Hirayama, and D. W. O. Rogers, *THE EGS4 CODE SYSTEM*, December 1985. SLAC-0265.

[83] J. R. Klein, "Uncertainties on threshold and gain for LETA", SNO internal report:
http://manhattan.sno.laurentian.ca/sno/ananoteb.nsf/URL/MANN-72QTZD, April 2007.

[84] J. Secrest, "Energy systematics for phase III", SNO internal report:
http://manhattan.sno.laurentian.ca/sno/ananoteb.nsf/URL/MANN-7CPS49, April 2008.

[85] K. Graham, "Energy systematics for the salt phase", SNO internal report:
http://manhattan.sno.laurentian.ca/sno/ananoteb.nsf/URL/MANN-5M9UN7, May
2003.

[86] M. Dunford, "Determining ^{16}N energy systematic uncertainties using the most probable electron energy fit", SNO internal report: http://manhattan.sno.laurentian.ca/sno/ananoteb.nsf/URL/MANN-6QFNJW, August 2006.

[87] K. Graham, "Energy systematics for the salt phase", SNO internal report:
http://manhattan.sno.laurentian.ca/sno/ananoteb.nsf/URL/MANN-5M9UN7, May
2003.

[88] A. S. Hamer, "Energy calibration of SNO for measurement of the charged current neutrino reaction", PhD thesis. UMI-NQ-54416.

[89] M. D. Lay, D. L. Wark, and R. J. Boardman, "Producing Čerenkov photons from low energy electrons with EGS4", SNO-STR-91-047, June 1991.

[90] O. Klein and Y. Nishina, "Über die Streuung von Strahlung durch freie Elektronen nach der neuen relativistischen Quantendynamik von Dirac", *Z. für Physik* **52** (1929) 853–868.

[91] G. W. Grodstein, "X-ray attenuation coefficients from 10 keV to 100 MeV", *Natl. Bur. Stand. (U.S.) Circ. No. 583*, 1957.

[92] E. Storm and H. Israel, "Photon cross sections from 1 keV to 100 MeV for elements Z=1 to Z=100", *Nucl. Data Tables* **A7** (1970) 565–681.

[93] W. Heitler, "The quantum theory of radiation", Oxford, Great Britain, 3rd ed., 1954. page 223.

[94] J. W. Motz, H. A. Olsen, and H. W. Koch, "Pair production by photons", *Rev. Mod. Phys.* **41** (1969) 581–639.

[95] H. W. Koch and J. W. Motz, "Bremsstrahlung cross-section formulas and related data", *Rev. Mod. Phys.* **31** (1959) 920–955.

[96] H. Messel and D. F. Crawford, "Electron-photon shower distribution function: tables for lead, copper, and air absorbers", Pergamon, New York, 1970.

[97] J. Detwiler, N. McCauley, K. Rielage, G. Tesic, and F. Zhang, "Live-time for the full NCD data set", SNO internal report: http://manhattan.sno.laurentian.ca/sno/ananoteb.nsf/URL/MANN-7APU7D, January 2008.

[98] P.-L. Drouin, "Partially constrained unbinned extended log-likelihood function", SNO internal report: http://manhattan.sno.laurentian.ca/sno/ananoteb.nsf/URL/MANN-6HSSAX, November 2005.

[99] B. Jamieson, "SNO NCD phase signal extraction on unblinded data with integration over systematic nuisance parameters by Markov-chain Monte Carlo", SNO internal report: http://manhattan.sno.laurentian.ca/sno/ananoteb.nsf/URL/MANN-7NCU9S, May 2008.

[100] F. James and M. Winkler, *MINUIT User's Guide*. CERN, Geneva, June 2004.

[101] K. O. Ondar, ed., "The correspondence between A. A. Markov and A. A. Chuprov on the theory of probability and mathematical statistics", Springer-Verlag, New York, 1991. Translated by Charles and Margaret Stein from the original text: *O Teorii Veroiatnostei I Matematicheskoi Statistike (perepiska A. A. Markov u A. A. Chuprov)* by Nauka, Moscow, 1977.

[102] N. Metropolis, A. W. Rosenbluth, M. N. Rosenbluth, A. H. Teller, and E. Teller, "Equation of state calculations by fast computing machines", *J. Chem. Phys.* **21** (1953) 1087–1092.

[103] W. K. Hastings, "Monte Carlo sampling methods using Markov chains and their applications", *Biometrika* **57** (1970) 97.

[104] P. C. Gregory, "Bayesian logical data analysis for the physical sciences", Cambridge, 2005.

[105] S. Oser, "Biases in signal extraction", SNO internal report: http://manhattan.sno.laurentian.ca/sno/ananoteb.nsf/URL/MANN-7C6MS7, May 2008.

[106] W. T. Winter, S. J. Freedman, K. E. Rehm, and J. P. Schiffer, "The ^{8}B neutrino spectrum", *Phys. Rev.* **C73** (2006) 025503, `nucl-ex/0406019`.

[107] A. Valassi, "Combining correlated measurements of several different physical quantities", *Nucl. Instrum. Meth.* **A500** (2003) 391–405.

[108] Z. Maki, M. Nakagawa, and S. Sakata, "Remarks on the unified model of elementary particles", *Prog. Theor. Phys.* **28** (1962) 870.

[109] M. Chen *et al.*, "PhysInt unidoc 2.1", SNO internal report: http://manhattan.sno.laurentian.ca/sno/ananoteb.nsf/URL/LANL-59AHQ2, April 2002.

[110] M. Chen, F. Duncan, and Y. Takeuchi, "QPhysics updates", SNO internal report: http://manhattan.sno.laurentian.ca/sno/ananoteb.nsf/URL/MANN-5NEUWG, June
2003.

[111] **SNO** Collaboration, Q. R. Ahmad *et al.*, "Measurement of day and night neutrino energy spectra at SNO and constraints on neutrino mixing parameters", *Phys. Rev. Lett.* **89** (2002) 011302, `nucl-ex/0204009`.

[112] A. Y. Smirnov, "Neutrino-2008: Where are we? Where are we going?", *J. Phys. Conf. Ser.* **136** (2008) 012002, 0810.2668.

Appendix A

Photon timing distribution

The optical path taken by photons reflected off of the acrylic vessel or the PSUP is complicated to track. Generally only prompt photons are used when analyzing events. In order to minimize the uncertainties introduced by late photons, a timing window around the prompt arrival time of photons is applied. The distribution of hit PMT times about the prompt peak is depicted in figure A.1 for a central ^{16}N source calibration run. The PMT time residual $t_{\rm res}$ is calculated

$$t_{\rm res} = t_{\rm PMT} - \frac{|\vec{p} - \vec{r}|}{\overline{c}_{\rm grp}} - t_{\rm event},$$

where $t_{\rm PMT}$ is the time the PMT triggers, $|\vec{p} - \vec{r}|$ is the direct path length from the event position to the PMT, and $\overline{c}_{\rm grp}$ is a weighted average photon group velocity over the three wavelength-weighted indices of refraction (table 3.1). Also indicated in figure A.1 are pre-pulsing and late pulsing of the PMTs and 35° reflections from the PMTs reflectors[1].

[1]For a complete discussion of PMT reflections see Moffat [48].

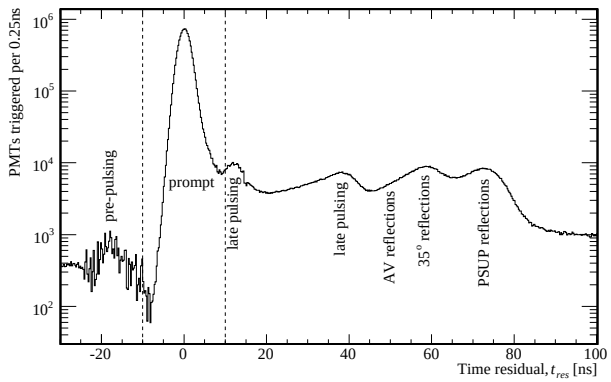

Figure A.1: Timing distribution of triggered PMTs corrected for the time-of-flight of an average photon from the reconstructed position directly to the triggered PMT. The data was collected during an ^{16}N calibration run near the centre of the detector.

Appendix B

Iterative maximum likelihood Gaussian fit

The measure of detector energy response and event energy are primarily based on the integer number of triggered PMTs. The integer nature becomes a problem when data is binned too finely in histograms. It becomes especially difficult over the large range of calibrated energies. In order to extract the mean and width, or resolution, of energy related quantities in the data or simulation it was favourable to develop an unbinned maximum likelihood fit. In general the distributions are well approximated by a Gaussian function, especially around the mean. The standard Gaussian function,

$$f(x) = \mathrm{erf}\left(\frac{\alpha}{\sqrt{2}}\right)^{-1} \frac{1}{\sqrt{2\pi}\sigma} \exp\left[-\frac{(x-\mu)^2}{2\sigma^2}\right], \tag{B.1}$$

is used but normalized over a finite range of $\alpha\sigma$ around the mean μ. The range of the fit is normally chosen to be between 1.6 and 1.7σ to incorporate most of the data while excluding any non-Gaussian tails. The fit is performed iteratively until the fit range converges.

Appendix C

Particle Data Group unconstrained averaging

This section summarizes the method that the Particle Data Group uses to determine unconstrained averages as described by Yao et al. [24]. For the measurements x_i, with uncorrelated uncertainties δx_i, the mean $\overline{x}$, with an uncertainty of $\delta\overline{x}$, is simply

$$\overline{x} \pm \delta\overline{x} = \frac{\sum_i w_i x_i}{\sum_i w_i} \pm \left(\sum_i w_i\right)^{-\frac{1}{2}}, \tag{C.1}$$

where

$$w_i = \left(\frac{1}{\delta x_i}\right)^2.$$

Then the χ^2 between the weighted mean and the data is

$$\chi^2 = \sum_i w_i \left(\overline{x} - x_i\right)^2. \tag{C.2}$$

This is expected to be equal to $N-1$ for the N measurements of x_i. If $\chi^2/(N-1)$ is greater than 1.0, *but not greatly so* [24], due either to an underestimation of the uncertainty δx_i or to the model assumption that x_i are necessarily sampling the same distribution, the error on the mean δx is increased by a factor S defined by

$$S \equiv \left[\chi^2/(N-1)\right]. \tag{C.3}$$

This would be the result of scaling the individual uncertainties δx_i by S to yield a χ^2 per degree of freedom of exactly 1.0.

One caveat to this procedure that the Particle Data Group recommends is to use only the measurements with smaller δx_i when determining S. They somewhat arbitrarily propose to use only data with uncertainty less than $\delta_\circ$ given by

$$\delta_\circ = 3\sqrt{N}\delta\overline{x}, \tag{C.4}$$

where $\delta\overline{x}$ is as calculated above for all the measurements.

Appendix D

An additional contribution to the energy scale uncertainty

The spatial variation error is introduced in subsection 5.5.1. The procedure outlined in that section attempts to calculate any potential discrepancy between the energy scale of calibration data and the simulation in a way that properly averages over the expected distribution of the neutrino signals: namely one that is homogeneous within the D_2O. The calibration data is limited to the positions that may be reached by the calibration source manipulator system discussed in section 2.6 and also limited by the finite amount of time in which to perform the calibrations. The latter requires extrapolation between the calibrations that were done while the former led to a substantial volume of the detector not being properly calibrated. The following describes attempts to quantify the effect of omitting the uncalibrated region from the determination of the energy scale error for the NCD phase.

The simplest estimate of the additional energy scale uncertainty is to assume some energy scale error and RMS spread for the volume element in question and recalculate the energy scale error; the difference between the error with and without the added contribution being the added uncertainty. For the likely worst case scenario depicted in figure D.1a the maximum energy scale error is selected and assigned an RMS spread of a comparable volume element in the lower hemisphere of the detector. The resulting energy scale error in this case would be $0.017 \pm 0.281\%$, implying an additional energy scale uncertainty of -0.541% (the difference between the nominal value of -0.524% and

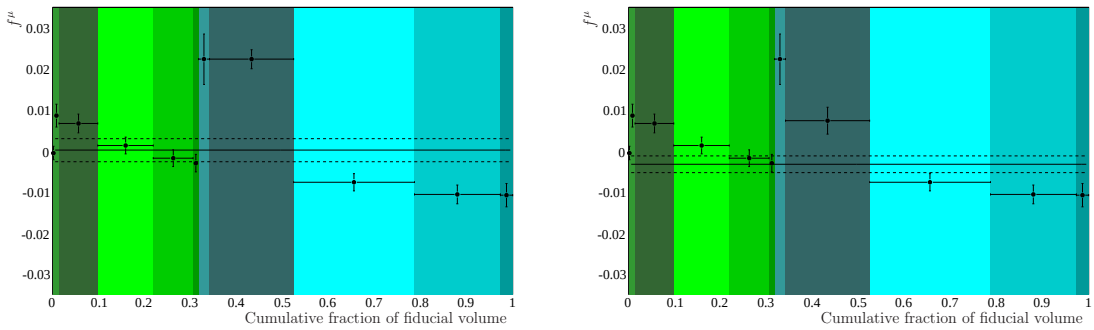

(a) Worst case assumption.

(b) Average of adjacent volume elements.

Figure D.1: NCD phase energy scale spatial variation error including an approximation of the error in the uncalibrated region spanning 0.4–0.5.

0.017%). A more realistic approximation is to consider an average of the energy scale errors buffering the calibration deficient region. Using the average of the buffering regions, the result of which is plotted in figure D.1b, results in an energy scale error of $-0.328 \pm 0.205\%$. This latter measurement, which is most likely representative of the actual situation, implies an additional energy scale uncertainty of 0.196%. This may be compared to the total energy scale error of $-0.46 \pm 0.49\%$.

It has been suggested by Hallin [41] that the RMS of the points in figure 6.14 should be treated as the distribution of energy scale error within a given volume element. This is in contrast to using the RMS as the uncertainty when calculating the volume weighted mean energy scale error. The distribution of energy scale errors within each bin has therefore been approximated by a Gaussian; the mean of which is set to the weighted mean (F^μ from equation 5.3), the width to the RMS, and the area to correspond to the volume of the element that the Gaussian represents. Figure D.2a plots the sum of the contributions from each volume element in the NCD phase save the one that has not been calibrated. The mean of the distribution (-0.382%) is shown along with that calculated in subsection 6.4.3 ($-0.524 \pm 0.187\%$). Figure D.2b includes the added contribution of the uncalibrated region as depicted in figure D.1b.

Table D.1 lists the estimated errors derived above as well as those for the pure D_2O and salt phases. The nominal values listed are those obtained in the main body

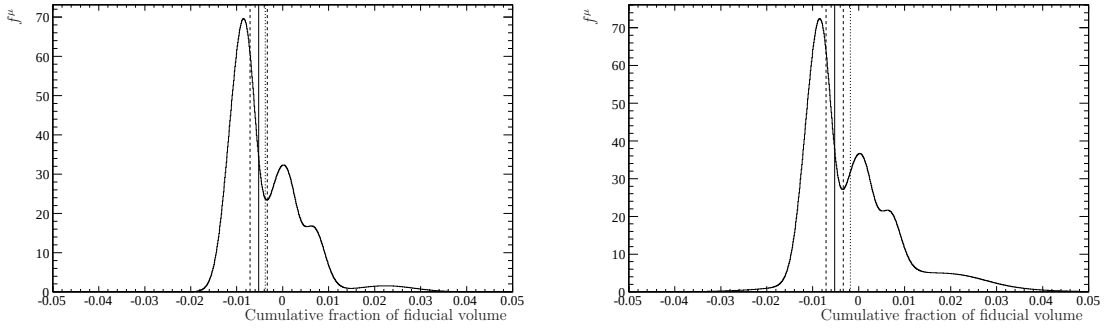

(a) Nominal data points.

(b) Including an approximation for the uncalibrated region.

Figure D.2: The NCD phase energy scale spatial variation error using an alternative volume weighting: the contribution of each volume element is distributed with a Gaussian distribution with a width equal to the RMS of the errors in that element. The solid line with dashed error bars represents the error as determined in chapter 6 while the dotted line is the mean of the plotted distribution.

		Additional region		Volume weighting over RMS	
Phase	Nominal	worst case	average	without region	with region
D_2O	0.304 ± 0.169	0.596 ± 0.265	0.434 ± 0.193	0.289	0.539
Salt	-0.067 ± 0.255	0.205 ± 0.294	0.228 ± 0.261	-0.174	0.071
NCD	-0.524 ± 0.187	0.017 ± 0.282	-0.328 ± 0.205	-0.382	-0.179

Table D.1: Volume weighted energy scale error including a contribution from the uncalibrated region (spanning 0.4–0.5 in figures 5.18, 5.34 and 6.15) and distributing the volume weighting within a given volume element according to the RMS of the points in that region (see text). The "worst case" scenario uses the data points shown in figure D.1a while the "average" and "with region" use the data points as shown in figure D.1b. All values are in percent.

Phase	Uncalibrated region	Alternative volume weighting	Total
D_2O	0.130	0.150	0.304 ± 0.261
Salt	0.295	0.107	-0.067 ± 0.404
NCD	0.196	0.142	-0.524 ± 0.306

Table D.2: The additional energy scale uncertainty as a result of the variation from the nominal values presented in table D.1. All values are in percent.

of this work according to the procedure described in subsection 5.5.1. A good estimate of the additional uncertainty on the nominal energy scale error is the difference between it and the error calculated using an average of the adjacent regions to approximate the uncalibrated volume element[1]. This difference should be comparable to the difference between the last two columns. The difference between the nominal energy scale error and that calculated using the alternative volume weighting scheme should also be considered as and additional contribution to the energy scale uncertainty. These values and the total energy scale error that would result from including these additional uncertainties are listed in table D.2.

Neither the low energy threshold analysis (LETA) nor the NCD phase analysis include a contribution for the effects of these additional sources of uncertainty. Since the uncertainty introduced is significant, future NCD phase analysis should take then into account and preferably obtain a more precise measurement of their magnitude. These additional uncertainties are likely a less significant contribution to the energy reconstruction as utilized by LETA given that a correction is applied to reduce the spatial variation between the calibration data and the simulation.

[1]The worst case scenarios are presented only for completeness. However, in the salt phase the average of the adjacent regions would constitute a smaller additional uncertainty. This effect is due to the tighter constraint placed on the average than that on the outlier used for the worst case scenario.